

Ultrafast control of emergent quantum matter probed by electron microscopy

Présentée le 26 mai 2023

Faculté des sciences de base
Laboratoire pour la microscopie et la diffusion d'électrons
Programme doctoral en physique

pour l'obtention du grade de Docteur ès Sciences

par

Benoît Guilhem Michel Binh TRUC

Acceptée sur proposition du jury

Prof. P. Ricci, président du jury
Prof. F. Carbone, directeur de thèse
Prof. C. Ropers, rapporteur
Prof. D. Fausti, rapporteur
Prof. H. Rønnow, rapporteur

1+1=3.

Cela signifie que l'union des talents dépasse leur simple addition. Cela signifie que la fusion des principes masculin et féminin, de petit et de grand, de haut et de bas, qui régissent l'univers, donne naissance à quelque chose de différent de l'un et de l'autre et qui les dépasse.

99.9% des gens qui parlent de physique quantique ne savent pas de quoi parle la physique quantique.

— Bernard Werber

To my parents and my sister...

Remerciements

Tout d'abord, je tiens à exprimer ma gratitude envers mon directeur de thèse, Fabrizio, ainsi que mon comité de jury pour leur temps et leur précieux feedback sur mon travail. J'ai été ravi de travailler avec Fabrizio, qui s'est toujours montré disponible et de bon conseil. Son expression favorite ? *low-hanging fruit*. C'est vrai, je ne suis pas très grand, néanmoins, il m'aurait fallu bien des chutes avant de réussir une cueillette dont je suis très fier.

Avant de commencer mon doctorat, un professeur m'a dit : "Ce que j'évalue chez un candidat, ce n'est pas s'il va réussir à ne pas tomber, mais comment il va se relever". Après ces quatre années d'expériences, cette phrase dont je comprends désormais toute sa signification m'est restée. Heureusement, je n'étais pas seul. Merci Alexey avec qui j'ai commencé le même jour cette aventure. Construire ce nouveau laboratoire à partir de rien et apprendre ensemble a été un grand plaisir. Quelques mois plus tard, Phoebe, skieuse émérite et marathonnienne, a rejoint nos rangs, apportant avec elle sa précieuse connaissance de la photonique. Nous formions ainsi l'équipe dédiée au magnétisme. Merci pour tout ces jours passés ensemble au laboratoire avec une petite pensée à tout ces moments de *galère* à nous creuser la tête sur nos observations inattendues.

Plus tard, j'ai eu la chance de faire partie d'une autre équipe travaillant sur une technique expérimentale différente. Je tiens à remercier en particulier Siham pour sa supervision et son enthousiasme, Paolo notre MacGyver du laboratoire et Rémi, qui a réalisé que nous mesurions le signal de l'air climatisé au lieu d'un *vrai* signal. Je remercie également Francesco mon partenaire de conférence pour nos nombreuses discussions. Je suis reconnaissant envers Thomas, Ivan, Ghil et Gianmaria pour m'avoir guidé et formé. Bien que je n'aie pas été directement impliqué dans des projets avec eux, je tiens à remercier tous mes autres collègues et amis de LUMES, Veronica, Simone, Lukas, Paolo, Hui-Yuan, Kjeld, Michele, Bruce, Le, Oliviero, Samuele, Serhii, Leonor, Christine et Hugo, Michele.

Dans mon domaine, la réussite d'une expérience dépend de nombreux facteurs expérimentaux, à commencer par la réalisation d'un échantillon de bonne qualité. Ce travail nécessite des compétences uniques. Je tiens à remercier l'équipe de crystallogénèse de l'EPFL, David et Yong, pour leur précieuse contribution. Je souhaite également adresser une attention particulière à Arnaud, qui m'a introduit au monde de la recherche scientifique depuis mes débuts et sur qui j'ai toujours pu compter, ainsi qu'à Priya, qui complète un sacré trio. Nos activités favorites? Labo, badminton, Sat!

Une fois le cristal obtenu, il est nécessaire de le modifier pour obtenir une lamelle très fine, pouvant être analysée à l'aide d'un microscope électronique. Cette étape requiert des opéra-

Remerciements

tions délicates d'une précision chirurgicale, et je tiens à remercier Thomas, Ping, Colette et Barbora pour leur expertise et leur soutien dans ce domaine.

Enfin, une fois les données expérimentales analysées, de nombreuses discussions scientifiques sont entreprises pour clarifier la nature du phénomène découvert. Je tiens à remercier Achim, Emil, Nina, Lingyao, Jiadong, Claudio et Angel pour leur support théorique et computationnel, qui ont grandement contribué à la réussite de mes recherches. Côté EPFL, mes remerciements vont également à deux figures dans le domaine du magnétisme, Dirk, responsable de la *swiss skyrmionic force* et Henrik superviseur de mon projet de master et qui m'a initialement introduit à Fabrizio. L'élaboration du nouveau laboratoire n'aurait pas pu se faire sans le soutien de différents services de l'EPFL. J'aimerais chaleureusement remercier Patrick, Clive du domaine de l'infrastructure, Damien et Amelia responsables en sécurité, Luc et Gilles de l'atelier mécanique.

Avant de remercier mes amis qui m'accompagnent depuis déjà de nombreuses années, je tiens à saluer toutes les nouvelles personnes incroyables que j'ai pu rencontrer lors des différentes conférences. En particulier merci à Dante, Elsa, Kenneth, Janine, et Martina pour vos conseils. La thèse, c'est rencontrer de nouvelles personnes, mais c'est aussi garder contact et évoluer en parallèle avec ses amis. J'aimerais commencer par remercier le groupe *Road to PhD* initialement nommé autrement (les vrais le savent ;)). J'appelle Aymeric, Eric et Etienne. Plus de dix ans maintenant à avoir refait le monde milles fois et bien que nos domaines respectifs ne soient pas identiques, nos discussions et débats m'ont grandement appris. Durant ce travail, j'ai compris ce que voulait dire le "Ph" de Ph.D. Non ce n'est pas *physics*, mais bien *philosophy*. J'ai réalisé qu'importe le sujet de recherche, il y a certaine universalité de questionnement tout au long du parcours doctoral. Merci pour ces discussions passionnantes. Merci Désirée pour nos chocolats chauds, Claire pour nos parties de badminton, Loïc pour tes histoires folles, Clément et Victor qui eux aussi ont monté un nouveau dispositif expérimental et avec qui j'ai partagé les hauts et les bas liés aux problèmes techniques.

Je tiens à remercier Laureline une colocataire exemplaire qui est venue me donner un coup de main à Noël à visser des miroirs et aligner un laser. Merci pour ton énergie et ta motivation. Merci Carla pour tes encouragements. Merci Gaëlle l'organisatrice d'évènements insolites. Parce qu'il est bientôt 4h du matin lorsque j'écris ces quelques lignes et que la deadline est toute proche (on change pas une équipe qui gagne !), je n'ai malheureusement pas le temps d'écrire une petite attention pour tout le monde (je commence à voir floooooou). Néanmoins sachez que vous comptez beaucoup à mes yeux et je vous remercie du fond du coeur d'être là à mes côtés. Dans l'ordre alphabétique, je tiens à remercier (j'espère n'oublier personne!) : Ambroise, Cécile, Chléa, Clara, Daniel, Diane, Eloïc, Estelle, Flavio, Flore, Foucauld, Gabriel, Isabelle, Jérémie, Justine, Laurane, Loane, Marko, Mathilde, Max, Michael, Nicolas, Noémie, Quentin, Sandra, Sévane, Stan, Stéphane, Tim, Valentine. J'aimerais faire une dédicace spéciale à Brigitte, Frédéric et Stéphane qui me suivent depuis mon enfance et à qui je dois beaucoup. Almost last but not least, merci à ma famille qui m'a toujours soutenu et m'a poussé à donner le meilleur de moi. Merci à ma soeur pour son soutien et tous les gossips qu'on a partagé. En plus de ça, je pense qu'elle est l'une si ce n'est pas la personne la plus patiente au monde. Merci à ma mère qui s'est intéressée de très près au monde la physique quantique et qui est

venue m'aider à faire des mesures au laboratoire. Merci à mon père pour le côté business et gestion de projets qui a été d'une grande aide, lors de mon doctorat, mais aussi en dehors.

Merci à Fabrizio, Francesco, Phoebe, Aymeric, Karim, Eric et Gaëlle pour leur aide lors de la relecture et des différents conseils lors de l'écriture de cette thèse.

Pour terminer, je remercie chaleureusement le fond européen pour la recherche qui a financé ce projet via une ERC consolidator grant intitulée "Imaging, Spectroscopy and Control of Quantum states in advanced Materials".

Lausanne, 17 avril 2023

B. T.

Preface

The magnetic phase diagram of topological magnets can be extraordinarily rich, showing intricate spatial textures of spins that can be stable, metastable, or fluctuating. This behavior emerges from the interplay between thermodynamic and topological fluctuations. In these systems the magnetic free-energy landscape is full of local minima, each corresponding to a particular spatial spin distribution and emergent magnetic properties. Jumping between these minima can occur upon tipping the balance between topology and thermodynamics via external stimuli. The most common ones are magnetic field, temperature, electric field, mechanical strain, and, recently, optical excitation. The latter has the peculiarity of being able to induce ultrafast modifications of the material's electronic structure, temperature, and/or mechanical strain. Therefore, light is a unique tool to drive the system out-of-equilibrium and force it to evolve along exotic paths in the free-energy landscape that cannot be crossed in adiabatic conditions. As a result, new magnetic phases can be discovered, some of which are even metastable or stable, and new ways of controlling the arrangement of spins can be achieved. This thesis focuses on using light to manipulate magnetic materials out-of-equilibrium. Its main results are:

- to show that tailored sequences of laser pulses can manipulate a handful of spins deterministically, i.e., genuinely engineering their amplitude and direction of motion at an extremely fast (fs) and small (nm) scales.
- to show that different electronic excitations triggered by laser pulses of different colors can make magnetite, the oldest known magnetic material, evolve through very different out-of-equilibrium paths encompassing different metastable structural phases.

Overall, this work demonstrates the possibility of using light to manipulate strongly correlated materials out-of-equilibrium to obtain different phases with different emergent properties.

Lausanne, 7 April 2023

Fabrizio Carbone.

Abstract

In the quest for controlling materials' properties, light as an external stimulus has a special place as it can create new states of matter and enable their ultrafast manipulation. In particular, spintronics, an exciting emergent field relying on the electron spin property, has tremendous potential as it breaks ground for high-density, high-speed, and low-power-consuming memory devices. Skyrmion, a specific magnetic texture of whirling spins, has attracted broad interest due to its unique topological properties. Skyrmion-based devices stand out as they combine ultra-efficient control and robustness on nanometer scales. More fundamentally, skyrmions offer an exclusive tabletop playground to study emergent fields, topological phase transitions, cosmology, and black holes, to mention a few. Optical manipulation of skyrmions is hence crucial as it paves the way for efficient ultrafast control and provides a direct approach to studying low-energy collective modes and topological fluctuations in real space.

In this thesis, I show the manipulation of quantum materials through three groundbreaking experiments. First, I used in-situ Lorentz transmission electron microscopy, a magnetic imaging technique, and showed the laser-induced skyrmion formation in the multiferroic Cu_2OSeO_3 compound. I, therefore, provide the first demonstration of the magnetic free energy landscape manipulation leading to a topological phase transition. Notably, a new recipe is revealed that allows the control of the magnetic phase diagram on a picosecond timescale by transiently modifying the material's inherent magnetic interactions. This study has profound consequences on out-of-equilibrium topological phase transition investigation and technological applications as it marks an important milestone for efficient ultrafast spintronic devices.

Furthermore, I established a new protocol using femtosecond light to coherently control a skyrmion crystal eight orders of magnitude faster than previously achieved by exploiting the collective nature of the skyrmion lattice. Remarkably, as the process relies on a collective periodic mode, it can be coherently manipulated by adjusting the time delay between laser pulse sequences. Consequently, the skyrmion orientation can be deterministically chosen. In other words, I present the manipulation in real space of a few spins orientation in an ultrafast and energy-efficient way, vital for next-generation devices. In addition, our observations demonstrate emergent properties of the skyrmion interactions at the mesoscale, opening exciting perspectives for investigating the collective skyrmion dynamics at a large scale which might be relevant for unconventional superconductors where magnetic vortices similar to skyrmions exist at similar length scales.

Last but not least, I show the importance of the different electronic excitations in Magnetite

Abstract

(Fe_3O_4), the prototypical metal-insulator system, and the oldest known magnetic material. The structural response along the specific crystallographic [110] axis is investigated using ultrafast electron diffraction, providing sub pm/ps spatio-temporal resolution. By tuning the photon energy, thus triggering different electronic transitions, two distinct lattice responses are unveiled, unattainable thermodynamically. This work paves the way to establishing novel hidden phases in quantum materials via specific electronic excitations in a strongly correlated environment.

Résumé

Dans la quête du contrôle des propriétés des matériaux, la lumière en tant que stimulus externe occupe une place particulière car elle peut créer de nouveaux états de la matière et permettre leur manipulation ultrarapide. En particulier, la spintronique, un domaine émergent passionnant qui repose sur la propriété de spin des électrons, a un potentiel énorme car elle ouvre la voie à des dispositifs de mémoire à haute densité, à grande vitesse et à faible consommation d'énergie. Le skyrmion, une texture magnétique spécifique de spins tourbillonnants, a suscité un large intérêt en raison de ses propriétés topologiques uniques. Les dispositifs basés sur le skyrmion se distinguent car ils combinent contrôle ultra-efficace et robustesse à l'échelle nanométrique. Plus fondamentalement, les skyrmions offrent un terrain de jeu exclusif pour étudier les champs émergents, les transitions de phase topologiques, la cosmologie et les trous noirs, pour n'en citer que quelques-uns. La manipulation optique des skyrmions est donc cruciale car elle ouvre la voie à un contrôle ultrarapide efficace et fournit une approche directe dans l'étude des modes collectifs de basse énergie et des fluctuations topologiques dans l'espace réel.

Dans cette thèse, je montre la manipulation des matériaux quantiques à travers trois expériences novatrices. Premièrement, j'ai utilisé la microscopie électronique à transmission de Lorentz in-situ, une technique d'imagerie magnétique, et j'ai montré la formation de skyrmions induite par laser dans le composé multiferroïque Cu_2OSeO_3 . Je fournis donc la première démonstration de la manipulation du paysage de l'énergie libre magnétique conduisant à une transition de phase topologique. En particulier, une nouvelle recette est révélée qui permet de contrôler le diagramme de phase magnétique à l'échelle de la picoseconde en modifiant de manière transitoire les interactions magnétiques inhérentes au matériau. Cette étude a des conséquences profondes sur l'étude des transitions de phase topologiques hors équilibre et sur les applications technologiques, car elle marque une étape importante pour les dispositifs spintroniques ultrarapides efficaces.

De plus, j'ai établi un nouveau protocole utilisant la lumière femtoseconde pour contrôler de manière cohérente un cristal de skyrmion huit ordres de grandeur plus rapidement que ce qui avait été réalisé auparavant en exploitant la nature collective du réseau de skyrmion. De façon remarquable, comme le processus repose sur un mode périodique collectif, il peut être manipulé de façon cohérente en ajustant le délai entre les séquences d'impulsions laser. Par conséquent, l'orientation du skyrmion peut être choisie de manière déterministe. En d'autres termes, je présente la manipulation dans l'espace réel de l'orientation de quelques spins d'une manière ultrarapide et économe en énergie, vitale pour les dispositifs de prochaine généra-

Résumé

tion. En outre, nos observations démontrent des propriétés émergentes des interactions des skyrmions à l'échelle mésoscopique, ouvrant des perspectives passionnantes pour l'étude de la dynamique collective des skyrmions à plus grande échelle, ce qui pourrait être pertinent pour les supraconducteurs non conventionnels où des tourbillons magnétiques similaires aux skyrmions existent à des échelles de longueur similaires.

Enfin, je montre l'importance des différentes excitations électroniques dans la magnétite (Fe_3O_4), le système métal-isolant prototypique, et le plus ancien matériau magnétique connu. La réponse structurelle le long de l'axe cristallographique spécifique [110] est étudiée à l'aide de la diffraction ultrarapide des électrons, qui offre une résolution spatio-temporelle inférieure à pm/ps. En ajustant l'énergie des photons, déclenchant ainsi différentes transitions électroniques, deux réponses distinctes du réseau sont dévoilées, inatteignables thermodynamiquement. Ce travail ouvre la voie à l'établissement de nouvelles phases cachées dans les matériaux quantiques via des excitations électroniques spécifiques dans un environnement fortement corrélé.

Prefazione

La luce come stimolo esterno gioca un ruolo speciale nel cercare di controllare le proprietà dei materiali, in quanto può creare nuovi stati della materia e consentirne la manipolazione ultraveloce. In particolare, la spintronica, un campo emergente ed entusiasmante che si basa sulla proprietà dello spin dell'elettrone, ha un enorme potenziale in quanto apre la strada a dispositivi di memoria ad alta densità, alta velocità e basso consumo energetico. Lo skyrmion, una particolare struttura magnetica di spin disposti a vortice, ha suscitato un ampio interesse grazie alle sue proprietà topologiche uniche. I dispositivi basati sullo skyrmion si distinguono perché combinano controllo ultra-efficiente e robustezza su scala nanometrica. Fondamentalmente, gli skyrmioni offrono un terreno fertile per studiare in laboratorio campi emergenti, transizioni di fase topologiche, cosmologia e buchi neri, per citarne alcuni. La manipolazione ottica degli skyrmioni è quindi cruciale in quanto permette un efficiente controllo ultraveloce e fornisce un approccio diretto allo studio dei modi collettivi a bassa energia e delle fluttuazioni topologiche nello spazio reale.

In questa tesi, ho mostrato la manipolazione dei materiali quantistici attraverso tre esperimenti innovativi. In primo luogo, ho utilizzato la microscopia elettronica a trasmissione in-situ di tipo Lorentz, una tecnica di imaging magnetico, e ho mostrato la formazione di skyrmioni indotta dal laser nel composto multiferroico Cu_2OSeO_3 . Ho fornito quindi la prima dimostrazione del controllo del profilo dell'energia magnetica libera che porta a una transizione di fase topologica. In particolare, ho proposto una nuova procedura che permette di controllare il diagramma di fase magnetico su una scala temporale di picosecondi, modificando in modo transiente le interazioni magnetiche intrinseche del materiale. Questo studio ha profonde conseguenze sull'indagine delle transizioni di fase topologiche fuori dall'equilibrio e sulle applicazioni tecnologiche, poiché segna un'importante pietra miliare per la realizzazione di efficienti dispositivi spintronici ultraveloci.

In secondo luogo, ho stabilito un nuovo protocollo che utilizza la luce a femtosecondi per controllare coerentemente un cristallo di skyrmioni otto ordini di grandezza più velocemente di quanto ottenuto in precedenza, sfruttando la natura collettiva del loro reticolo. In particolare, poiché il processo si basa su un'oscillazione periodica collettiva, è possibile manipolarla coerentemente regolando il ritardo temporale tra le sequenze di impulsi laser. In tal modo, è possibile scegliere l'orientamento degli skyrmioni in modo deterministico. In altre parole, ho dimostrato la manipolazione dell'orientamento di alcuni spin nello spazio reale in modo ultrarapido ed efficiente dal punto di vista energetico, che è fondamentale per i dispositivi di prossima generazione. Inoltre, le osservazioni sperimentali dimostrano le proprietà emergenti

Prefazione

delle interazioni tra gli skyrmioni a livello di meso-scala, aprendo prospettive interessanti per lo studio delle dinamiche collettive degli skyrmioni su larga scala. Queste potrebbero essere rilevanti per i superconduttori non convenzionali in cui esistono vortici magnetici simili agli skyrmioni su scale di lunghezza simili.

Infine, ho mostrato l'importanza delle diverse eccitazioni elettroniche nella magnetite (Fe_3O_4), prototipo di un sistema metallo-isolante e più antico materiale magnetico conosciuto. Ho studiato la risposta strutturale lungo lo specifico asse cristallografico [110] utilizzando la diffrazione elettronica ultraveloce, che fornisce una risoluzione spazio-temporale inferiore al pm/ps. Regolando l'energia dei fotoni e attivando così diverse transizioni elettroniche, ho investigato due distinte risposte reticolari, irraggiungibili dal punto di vista termodinamico. Questo lavoro apre la strada alla creazione di nuove fasi nascoste nei materiali quantistici attraverso specifiche eccitazioni elettroniche in un sistema fortemente correlato.

Kurzzusammenfassung

Auf der Suche nach der Kontrolle von Materialeigenschaften nimmt Licht als externer Stimulus einen besonderen Platz ein, da es neue Zustände der Materie erzeugen und deren ultraschnelle Manipulation ermöglichen kann. Insbesondere die Spintronik, ein aufregender neuer Bereich, der sich auf die Spin-Eigenschaft von Elektronen stützt, hat ein enormes Potenzial, da sie den Weg für Speichergeräte mit hoher Dichte, hoher Geschwindigkeit und geringem Stromverbrauch ebnet. Ein Skyrmion, eine spezielle magnetische Textur aus wirbelnden Spins, hat aufgrund seiner einzigartigen topologischen Eigenschaften großes Interesse geweckt. Auf Skyrmionen basierende Bauelemente zeichnen sich dadurch aus, dass sie extrem effiziente Kontrolle und Robustheit im Nanometerbereich kombinieren. Im Wesentlichen bieten Skyrmionen einen exklusiven Spielplatz für die Untersuchung von aufstrebenden Wissenschaftsgebieten, topologischen Phasenübergängen, Kosmologie und schwarzen Löchern, um nur einige Beispiele zu nennen. Die optische Manipulation von Skyrmionen ist daher von entscheidender Bedeutung, da sie den Weg für eine effiziente ultraschnelle Kontrolle ebnet und einen direkten Angriffspunkt zur Untersuchung von kollektiven Moden mit niedriger Energie und topologischen Fluktuationen im realen Raum bietet.

In dieser Arbeit zeige ich die Manipulation von Quantenmaterialien durch drei bahnbrechende Experimente. Zunächst habe ich die In-situ-Lorentz-Transmissionselektronenmikroskopie, eine magnetische Bildgebungstechnik, verwendet und die laserinduzierte Skyrmionenbildung in der multiferroischen Cu_2OSeO_3 -Verbindung gezeigt. Damit konnte ich erstmalig zeigen, wie eine Manipulation der magnetischen freien Energielandschaft zu einem topologischen Phasenübergang führt. Insbesondere wird eine neue Vorgehensweise etabliert, welche die Kontrolle des magnetischen Phasendiagramms auf einer Pikosekunden-Zeitskala ermöglicht, indem die dem Material eigenen magnetischen Wechselwirkungen vorübergehend verändert werden. Diese Studie hat tiefgreifende Auswirkungen auf die Untersuchung topologischer Phasenübergänge außerhalb des Gleichgewichts, sowie auf technologische Anwendungen, da sie einen wichtigen Meilenstein für effiziente ultraschnelle spintronische Bauelemente darstellt.

Darüber hinaus habe ich ein neues Protokoll entwickelt, welches Lichtpulse im Femtosekundenbereich nutzt, um ein Skyrmionen-Gitter kohärent zu kontrollieren. Dies geschieht acht Größenordnungen schneller als bisher gezeigt und macht von der kollektiven Natur des Skyrmion-Gitters gebrauch. Da der Prozess auf einem kollektiven periodischen Mode beruht, kann er kohärent beeinflusst werden, indem die Zeitverzögerung zwischen den Laserpulssequenzen angepasst wird. Folglich kann die Ausrichtung des Skyrmions deterministisch

Kurzzusammenfassung

gewählt werden. Mit anderen Worten: Ich präsentiere die ultraschnelle und energieeffiziente Manipulation der Ausrichtung einiger weniger Spins im realen Raum, die für die nächste Generation von Geräten unerlässlich ist. Darüber hinaus zeigen unsere Beobachtungen neue Eigenschaften der Skymion-Wechselwirkungen auf der Mesoskala. Dies eröffnet eine spannende Perspektive für Untersuchungen der kollektiven Skymion-Dynamik, welche unter anderem auch relevant für unkonventionelle Supraleiter sind, da diese den Skymionen ähnliche magnetische Wirbel auf vergleichbaren Längenskalen beherbergen.

Zu guter Letzt zeige ich die Bedeutung der verschiedenen elektronischen Anregungen in Magnetit (Fe_3O_4), dem prototypischen Metall-Isolator-System und dem ältesten bekannten magnetischen Material. Die strukturelle Reaktion entlang der kristallographischen [110]-Achse wird mit Hilfe der ultraschnellen Elektronenbeugung untersucht, die eine räumliche und zeitliche Auflösung im sub- pm/ps Bereich ermöglicht. Durch die Anpassung der Photonenenergie an unterschiedliche elektronische Übergänge auslöst, werden zwei unterschiedliche Gitterreaktionen enthüllt, die thermodynamisch nicht erreichbar sind. Diese Arbeit ebnet hier den Weg zur Entdeckung neuer verborgener Phasen in Quantenmaterialien durch spezifische elektronische Anregungen in einer stark korrelierten Umgebung.

Contents

Remerciements	i
Preface	v
Abstract (English/Français/Italiano/Deutsch)	vii
I Controlling and visualizing the microscopic world	1
1 Introduction	3
1.1 Emergence and quantum matter	3
1.2 A route to control quantum materials	5
1.3 Ultrafast and nonthermal pathways	5
2 Free electrons enable atomic, meV and attosecond resolution	9
2.1 The rise of electron microscopy	10
2.2 Lorentz transmission electron microscopy & magnetic imaging	15
2.2.1 Energy-filtered transmission electron microscopy	18
2.3 4D ultrafast transmission electron microscope	19
2.4 Ultrafast reflective high-energy electron diffraction	21
2.5 Conclusion and perspectives	24
II Manipulation of a topological magnetic texture	25
3 Topology and emergence in modern magnetism	27
3.1 Topology and magnetic skyrmion	28
3.1.1 Topological invariant and winding number	28
3.1.2 Stabilization mechanism	30
3.2 The Berry phase, Berry curvature and emergent fields	32
3.2.1 Geometrical phase and Berry curvature	34
3.2.2 Weyl nodes & magnetic monopole	36
3.2.3 Emergent electromagnetic fields	37
3.2.4 Quantized emergent fields	40
3.3 Quantum interferometry using topological magnetic field	42

4	Light-induced topological phase transition in the multiferroic Cu_2OSeO_3	43
4.1	When multiferroicity meets topology	44
4.2	History and properties of Cu_2OSeO_3	47
4.2.1	Quantum nature and origin of the ferroelectricity	47
4.2.2	Magnetic phase diagram & the skyrmion phase	52
4.3	Light for manipulating the magnetic order	54
4.3.1	Experimental methods	54
4.3.2	266 nm and 780 nm photoexcitation	55
4.3.3	Polarization, Field and pulse duration and wavelength dependence	57
4.3.4	Ultrafast skyrmion photo-creation via transient DMI modulation	61
4.4	Observation of a long-dynamics process after photoexcitation	73
4.5	Experimental limitations	76
4.6	Open questions	78
4.7	Conclusion	78
5	Road to ultrafast topological emergent magnetism	79
5.1	Light for efficient ultrafast control in spintronics	80
5.2	Ultrafast coherent control of a skyrmion crystal in Cu_2OSeO_3	81
5.3	Open questions & perspectives	103
5.3.1	Quantitative simulation and Topological inverse Faraday effect	103
5.3.2	What defines the rotation direction of the skyrmion crystal	103
5.3.3	Breakdown of the skyrmion crystal and skyrmion lattice expansion	105
5.3.4	Controlling the rotation direction using ultrafast OAM optical beam	107
5.4	Conclusion	110
6	Open questions in the skyrmion host material Cu_2OSeO_3	111
6.1	Real space exploration under various magnetic field conditions	111
6.1.1	Surface spiral state and skyrmion elongation with $\mathbf{H} \parallel [1\bar{1}0]$	112
6.1.2	low-temperature skyrmion phase with $\mathbf{H} \parallel [001]$	118
6.1.3	Black and white skyrmions and shrinking of the skyrmion pocket with $\mathbf{H} \parallel [111]$	126
6.2	Conclusion	130
III	Ultrafast generation of hidden phases	131
7	Magnetite Fe_3O_4 as the prototypical MIT system	133
7.1	History of the oldest magnetic material	134
7.1.1	The Verwey transition and trimerons	135
7.2	Tracking the Verwey transition with electron diffraction	138
7.2.1	Elastic theory and the shear mode	141
7.2.2	Ginzburg-Landau & group theory analysis	143
7.2.3	Further analysis and open questions	146
7.3	Hidden phases on demand using selective electronic excitations	147

7.4	Results	149
7.4.1	800 nm / 1.55 eV photon energy	149
7.4.2	400 nm / 3.10 eV photon energy	152
7.5	Discussion	155
7.5.1	Inter-site d-d electronic transitions	155
7.5.2	Ligand-Metal charge transfer	157
7.6	Limitation and perspectives	158
7.6.1	Twinning and domain morphology considerations	158
7.6.2	Open questions and further investigation	161
7.7	Conclusion	164
 List of acronyms		 165
 A Crystal growth and characterization		 169
A.1	Fe[SeO ₄]OH	169
 Bibliography		 179
 Curriculum Vitae		 209
 Publication lists		 213
 International conferences and schools		 215
 Academic involvement		 217

List of Figures

1.1	Route to control quantum materials	4
1.2	Light-induced control of quantum matter	6
2.1	Real space atomic resolution achieved with electron microscopy	10
2.2	Image formation in an optical and electron microscope	11
2.3	TaS ₂ EFTEM micrograph and electron diffraction	12
2.4	4D Ultrafast Transmission Electron Microscope at LUMES	13
2.5	TEM enables energy and momentum resolution.	14
2.6	Principles of Lorentz transmission electron microscopy	16
2.7	Skyrmion magnetization retrieval using TIE in FeGe	19
2.8	LTEM image of magnetic domain walls in Fe ₃ O ₄	20
2.9	Bragg law and ultrafast electron diffraction	22
2.10	RHEED pattern for various surface states	22
2.11	Schematic representation of the experimental setup	23
3.1	Topological classes in real space	29
3.2	Stereographic projections of topological solitons	31
3.3	Skyrmion configuration according to their vorticity and helicity	31
3.4	Beyond conventional skyrmions	33
3.5	Emergent monopole of Berry curvature	36
3.6	Anti-monopole as a zipper	37
3.7	Effective magnetic field of different topological solitons	37
3.8	Illustration of the local gauge transformation and potential vector	39
3.9	Topological and Skyrmion Hall effects due to emergent fields	41
4.1	Time reversal and spatial inversion broken symmetries in multiferroics	46
4.2	Cu ₂ OSeO ₃ crystal structure	48
4.3	Magnetic skyrmion in Cu ₂ OSeO ₃	49
4.4	Effective magnetic moment and electronic excitation in Cu ₂ OSeO ₃	50
4.5	Magnetically induced electric dipole and quadrupole polarization in Cu ₂ OSeO ₃	51
4.6	Tuning the magnetic skyrmion pocket	53
4.7	Stability comparison of the 266 nm, 780 nm and metastable skyrmions	56
4.8	Polarization dependence for 780 nm and 1200 nm skyrmion photo-creation process	58

List of Figures

4.9	Pulse duration and field dependences of the skyrmion photo-creation process	59
4.10	Temperature vs. magnetic field map of the absorbed fluence threshold	61
4.11	Skyrmion creation with the presence of a magnetic field	73
4.12	Fourier transform analysis and long-lived skyrmion fluctuation	75
4.13	Clockwise and anticlockwise rotation of the photo-created skyrmion lattice	76
4.14	780 nm-skyrmion reordering and decay in -18 mT field	77
5.1	Driving coherent magnetic modes using inverse Faraday effect	104
5.2	Skyrmion crystal rotation and skyrmion polarity	104
5.3	Illustration of Bloch-type skyrmion	105
5.4	Spatial dependence on the skyrmion rotation	106
5.5	Variation of the skyrmion lattice pitch length after photoexcitation	107
5.6	Generation of an ultrafast OAM beam	108
5.7	Skyrmion rotation controlled by ultrafast OAM beam	109
6.1	Observation of a spiral surface state and non-symmetric skyrmion crystals	114
6.2	Magnetic phase diagram and surface spiral spin state	115
6.3	Magnetic reorientation and skyrmion photo-creation	116
6.4	Instability of the skyrmion state	117
6.5	Light-induced magnetic phase transition	118
6.6	Observation of an independent skyrmion phase at LT	119
6.7	Comparison of the MT-skyrmion and the LT-skyrmion phases	120
6.8	TEM lamella and MT-skyrmion to LT-skyrmion phase transition	121
6.9	LT-skyrmion phase from low-fields to high-fields	123
6.10	LT-skyrmion phase from high-fields to low-fields	124
6.11	Stability of the MT-skyrmions and fluctuation of the LT-skyrmion phase	125
6.12	Skyrmion polarity/chirality reversal	127
6.13	Shrinking of the skyrmion phase with the presence of an in-plane magnetic field	129
7.1	Fe ₃ O ₄ Magnetite is everywhere in magnetism	135
7.2	Manifestation of the Verwey transition	136
7.3	Trimeron structure and its emergent network	138
7.4	Fe ₃ O ₄ sample characterization	139
7.5	Magnetite and the Verwey transition probed by RHEED	140
7.6	Rocking curve of Fe ₃ O ₄ in RHEED	140
7.7	Signature of the Verwey transition in RHEED	141
7.8	Shear deformation and its associated elastic energy	144
7.9	Possible structural transformation from the initial cubic phase	146
7.10	Optical electronic excitations in Fe ₃ O ₄	148
7.11	Ultrafast structural dynamics in Fe ₃ O ₄ upon 800 nm - 1.55 eV photoexcitation	151
7.12	Metastability a signature of hidden phases	152
7.13	Correlation plots upon 800 nm photoexcitation in the LT phase	153
7.14	Ultrafast structural dynamics in Fe ₃ O ₄ upon 400 nm - 3.10 eV photoexcitation	155

7.15 Sketch of the different photo-induced structural dynamics pathway 158
7.16 Beam stability and diffuse scattering 159
7.17 Transmission electron diffraction simulations and the broadening twinning effect 161

List of Tables

4.1	Pros and cons of mechanism candidates of the skyrmion photocreation process	60
5.1	Controlling skyrmion crystal with an ultrafast OAM beam	109
7.1	Characters table for O_h point group	144
7.2	Product table of the O_h point group	145
7.3	Correlation coefficients depending on the different compression and relaxation phases and photon energy	152

Controlling and visualizing the microscopic world

Part I

1 Introduction

1.1 Emergence and quantum matter

Controlling properties of materials *on demand* has always been an important challenge for both fundamental and applied studies [1]. Such control requires a deep understanding of the underlying microscopic interactions to harness and tailor their functionalities and an external stimuli that enable state manipulation on request.

Materials showing intertwined degrees of freedom are particularly fascinating as exotic phenomena can arise from the strong interaction environment. At the microscopic level, the system is described by the law of quantum mechanics. In independent and non-interacting systems composed of N particle, the wave function Ψ describing the system is simply the product of each independent single-particle wave function, expressed as:

$$\Psi(x_1, x_2, \dots, x_N, t) = \psi_1(x_1, t)\psi_2(x_2, t) \dots \psi_N(x_N, t)$$

where x is the position particle and t the time.

This simple description breaks down when introducing interactions between the different degrees of freedom proper to the microscopic system. In a solid-state system, four degrees of freedom are usually considered, and all are emerging from the fundamental Coulomb force. Three originate from the electron properties bound to a nucleus, forming the crystal lattice: the charge, spin, and orbital. The fourth degree of freedom is the lattice vibration (phonon) that encodes the structural properties of the crystal. When coupled, the marriage of the electronic and structural properties intrinsic to each material can give birth to a new form of degree of freedom, named quasi-particle. This notion of *greater entity* is called *emergence* and goes much beyond condensed matter systems. For example, intelligence emerges from the interaction of neurons, created by a specific arrangement of atoms, ultimately composed of elementary particles. Although the laws of quantum mechanics govern the evolution of a quantum system at the microscopic level, the transition to describing a larger emergent system is highly non-trivial. Nonetheless, in condensed matter systems, emergence can be

Chapter 1. Introduction

exploited to create new functionalities, such as superconductivity and complex magnetic order, crucial for next-generation device technologies (see Fig. 1.1).

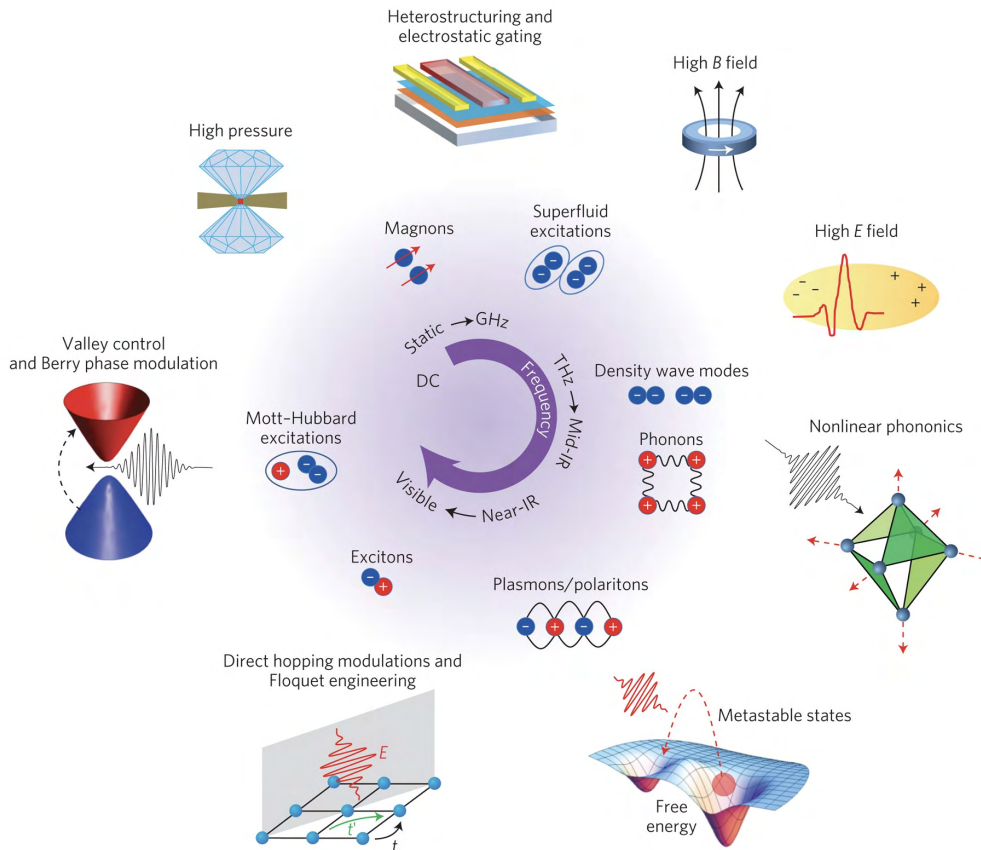


Figure 1.1 – **Route to control quantum materials.** Illustration of different excitations according to their natural energy in quantum materials and possible control techniques. Image reproduced from [1].

Quantum Materials are the generic term that encompasses such interactions. Their essential properties cannot be explained without invoking quantum effects or non-generic quantum effects like topology [2]. Furthermore, strong electronic correlations are usually present, giving rise to new phases of matter, and intense efforts to comprehend their nature are currently undertaken [1, 3]. For example, electronic order ensues charge density wave [4–7] and superconductivity [8–12], while magnetic order leads to magnetic skyrmions [13, 14] to name a few.

1.2 A route to control quantum materials

Inside most materials, the different degrees of freedom do not interact and are at thermodynamic equilibrium. However, some materials exhibit spontaneous phase transitions when the system is cooled or heated. To understand such a change, the minimization of the energy is invoked. In this representation, the system evolves in an energy landscape shaped by its inherent interactions and, depending on the thermal energy, sits in one minimum potential energy. Other external parameters, such as the magnetic field, can drive the system to undergo a phase transition. Interestingly a phase transition can occur even in the absence of thermal energy, where instead quantum fluctuation takes place [15–19]. A second strategy to control phases of matter is to directly modify the energy landscape, which is typically achieved by chemical doping or applying high-pressure inducing lattice distortion and consequently changing the microscopic interactions. Lastly, in 2D materials, Moiré engineering, named twistrionics have become possible. In that field, a twist angle is used as a knob to tune the electronic coupling and induces exotic phases such as unconventional superconductivity [20, 21]. In cold atoms system, the natural atomic lattice is replaced by an optical lattice that controls the effective interaction parameters mimicking condensed matter systems in a more straightforward approach as strong-correlations are suppressed [22]. Cavitronics and Floquet engineering harness light-matter interaction to induce emergent phenomena [23]. In those systems an external driving laser field optically dresses the electronic responses. Even without any driving field, coupling with the vacuum field has been realized in a cavity-enhanced interaction [24, 25]. It appears that triggering excitation using light radiation is a promising approach to activate quantum phenomena [3, 26–28] and generate new states of matter [9, 29, 30]. With recent developments of ultrafast lasers, light as external stimuli is particularly appealing as it unlocks femtosecond (10^{-15} s) control and out-of-equilibrium states. Indeed, all the abovementioned methods rely on adiabatic and thermodynamic equilibrium conditions. Driving the system out-of-equilibrium unleashes a plethora of new phenomena that can not be reached by other means.

1.3 Ultrafast and nonthermal pathways

In the femtosecond regime, heat that is incoherent lattice vibration does not have the time to form. By exploiting the instantaneous high-peak-power ($\sim 10^{19}$ W/m²) of an ultrafast laser beam, the system can be driven out-of-equilibrium without damaging the sample. Different mechanisms can be triggered depending on the materials, the fluence, and the photon energy (wavelength) used. For example, transient demagnetization [31], structural phase transitions [32], superconductivity [9, 10, 29] and magnetic order manipulation [33, 34] have been demonstrated. Generally, when electronic excitations are triggered, hot electrons are generated and relaxed through electron-electron scattering and electron-phonon coupling. During the process, the electronic temperature can reach a few thousand kelvins and act as a transient thermal-like response. In such cases, the system explores its complex free energy landscape and, while relaxing, can be trapped in one of the local minima, giving rise to a metastable state, also named hidden phases (see Fig. 1.2) [35–37].

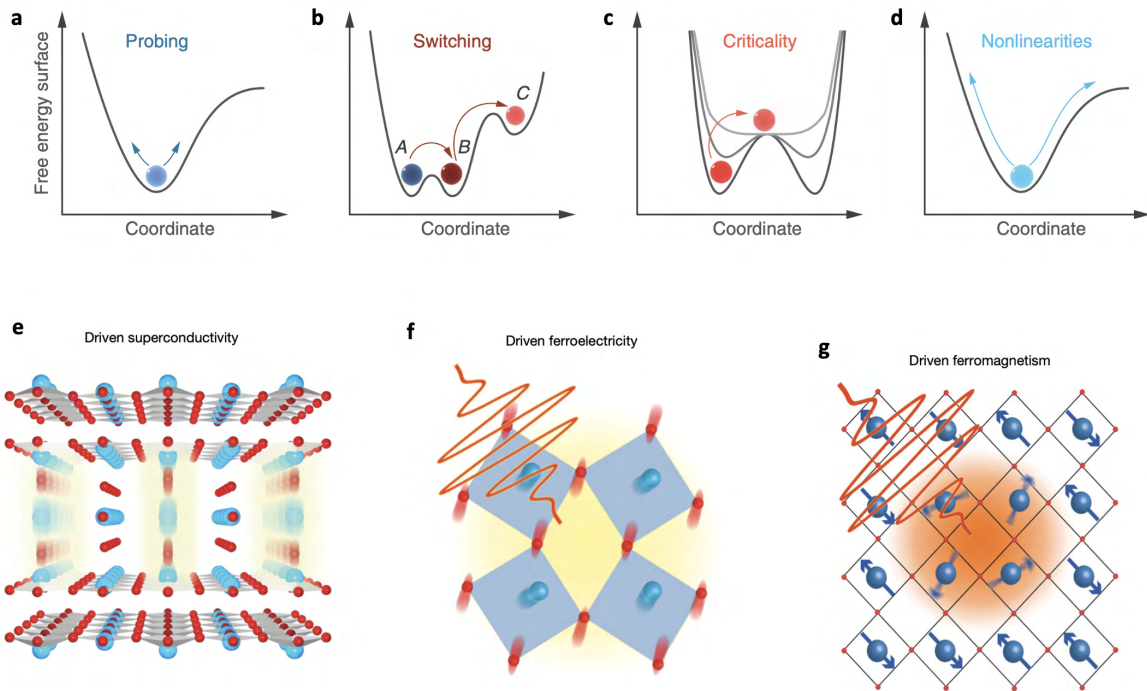


Figure 1.2 – **Light-induced control of quantum matter.** **a-d:** Illustration of different pathways upon photoexcitation. The color ball represents the evolution of the system state within the energy landscape that depends on the intrinsic degrees of freedom proper to the system. From left to right, the fluence is increased, inducing different types of mechanisms. Representation of light-induced ordering and cooperative effects, **(e)** in superconductivity and ferroic orders such as **(f)** ferroelectricity and **(g)** ferromagnetism. Images **a-d** adapted from [30]. Images **e-g** adapted from [3].

Most ultrafast experiments are done in visible light and the near-infrared as it corresponds to the laser fundamental frequency. The energy range corresponding is sufficiently high to drive those phases through electron-phonon coupling or in a thermal-like way [38]. However, this mechanism is poorly selective and causes heating [39]. Indeed, many modes are excited at the same time and prevent coherent control. Nonetheless, selectivity becomes possible by reducing the excitation energy in the mid-infrared and THz domains. Hence, low-energy collective modes can be coherently triggered [40–42]. For example, by exciting desired phonon modes, nonlinear phononics mechanisms can be reached. In this case, The coupling goes through lattice anharmonicities and generates a net displacement in the crystal, reshaping the free energy landscape and leading to a new equilibrium [43–47]. Going into the mid-infrared and THz regimes is technically challenging as it requires advanced ultrafast nonlinear optics and a humidity-free environment. For these reasons, low-energy photo-excitation is currently restricted to optical probes, although considerable effort has been undertaken to extend such attractive control to other probes [48, 49].

In this work, we demonstrate three approaches that do not require low-energy photons to drive the system in a Nonthermal way. In particular, we harness the strongly correlated environment naturally present in quantum matter. The first system investigated is the multiferroic skyrmion host materials Cu_2OSeO_3 . We show two distinct out-of-equilibrium magnetic responses, depending on the initial magnetic state, using near-infrared radiation (NIR) with 1.03 eV (1200 nm) photon energy. One induces a topological phase transition by transiently modifying the magnetic energy landscape through a phonon-mediated process. In the second study, a skyrmion crystal is coherently controlled at ultrafast timescales through the inverse Faraday effect. As the photon energy used in both cases is far below the optical bandgap of the materials, heat effects are drastically reduced, supporting the Nonthermal pathway. The second system under investigation is the prototypical metal-to-insulator system, Magnetite (Fe_3O_4). In that compound, strong electronic and structural correlations exist, hindering the precise mechanism involved in the phase transition for almost a century. We photo-excite the system with energies far above the optical bandgap (few hundreds of meV) with 1.55 eV (800 nm) and 3.10 eV (400 nm) photon energies that trigger specific electronic transitions. In the hot-electron picture discussed previously, both photo-excitation should lead to the same structural response. However, we observe two opposite behaviors demonstrating the importance of the triggered electronic excitation. Thus, paving the way for selective control with visible light. Some of these effects can be observed macroscopically, but their fundamental interactions occur at the atomic scale. To access the high resolution needed, the most powerful technique is probably the electron microscopy (EM). Recently, progress has led to the conception of 4D Ultrafast Electron Microscopy, where nanoscale and femtosecond resolutions have been attained for reversible magnetic processes [50]. This new generation of microscopes combines the capability to track the dynamics of these excitations in real and reciprocal space with an unprecedented resolution [51, 52]. An attractive variant of EM is Reflective High-Energy Electron Diffraction (RHEED). Indeed, its experimental configuration allows investigating structural dynamics with sub pm/ps spatio-temporal resolution without the need for ultrathin lamella. Both techniques are used in this thesis and are presented in the next Chapter.

This thesis is organized into three parts:

1. **Controlling and visualizing the microscopic world:** Two chapters compose this part. The introduction (this current Chapter) and an overview of electron microscopy techniques discussed in Chapter 2. In particular, I cover the unique capabilities and the operational principle of electron microscopy techniques that I exploit to comprehend the microscopic interaction of the two quantum materials.
2. **Manipulation of a topological magnetic texture:** In Chapter 3, I first introduce the notion of *topology* and *emergence* in magnetism. This brings us to Chapter 4, where an overview of the current knowledge of the multiferroic skyrmion host material Cu_2OSeO_3 is presented, and novel light-induced topological transition phenomenon is reported. In the spirit of controlling exotic magnetic phases, I reveal a new protocol to achieve such manipulation. The recipe is discussed in Chapter 5. During the investigation, many intriguing magnetic anomalies have been detected and their exact origin remains to be clarified. Nevertheless, they merit being presented; hence, Chapter 6 is dedicated to present futures perspectives in Cu_2OSeO_3 .
3. **Ultrafast generation of hidden phases:** In this last part, I show how to generate structural phases impossible to reach thermodynamically by tuning the photon energy such as it triggers specific electronic excitation. Magnetite (Fe_3O_4) is the ideal strongly correlated system as it exhibits electronic and structural intertwined degrees of freedom. The results are discussed in Chapter 7.

2 Free electrons enable atomic, meV and attosecond resolution

The typical size of an atom is about 10^{-10} m, also written 1 Å. In solid state of matter, the atoms arrange themselves to form a crystalline structure. The specific structure consists of a repeating motif possessing the overall symmetry of the crystal. The smallest group of atoms forming the motif is called the *unit cell* and has a typical size of a few Å. To understand and investigate the microscopic world, we need tools to resolve such spatial dimensions. Optical microscopes use light with a wavelength of around 500 nm. Consequently, they can not resolve smaller objects that $\lambda/(2n \sin \theta) \sim \lambda/2 = 250$ nm due to Abbe diffraction limit, where λ is the optical wavelength, n the refractive index of the media and θ the half-angle of the focusing beam. Nevertheless, this limit is valid only in the far-field, neglecting near-field effects and evanescent fields. For example, super-resolution microscopy [53–56] and scanning near-field optical microscopy [57–59] exploit such near-fields to circumvent the Abbe diffraction limit and have a resolution around ~ 10 nm. Still too low to achieve atomic resolution, another approach consists of reducing the photon wavelength going into the hard x-ray range. In this regime, the photon has a wavelength ~ 1 Å and an energy of few keV. In a diffractometer, an x-ray tube is used to generate the x-ray beam. Inside electrons from a hot cathode are accelerated to collide with a Copper or Cobalt target producing the x-ray beam. However, the wavelength of the x-ray emitted by the tube corresponds to a specific electronic transition proper to the materials and can not be tuned. For example, in copper K_{α_1} and K_{α_2} edges produced an x-ray beam with a wavelength $\lambda = 1.54$ Å (8.04 keV). Synchrotron radiation is needed to obtain a broad spectrum allowing spectroscopy and resonant x-ray scattering technique, where x-rays are generated through the bremsstrahlung effect. Such large facilities exist worldwide (around 70 in various stages of development) and provide high brightness and highly polarized x-ray photons. Depending on the measurement desired (spectroscopy, diffraction, imaging), a specific beamline with the corresponding geometry and detection instruments is used. To reach femtosecond (fs) temporal resolution, a free electron laser (FEL) is needed. Around twenty FELs are currently operational worldwide.

2.1 The rise of electron microscopy

Instead of using high-energy photons, another strategy to go into the sub-Å is to use the free electrons. Indeed, electrons are easy to manipulate and accelerate, thus reaching hundreds of keV easily to MeV [60, 61], thus a wavelength of the picometre (10^{-12} m or pm). In the 1920s-1930s, German scientists developed electromagnetic lens technology and started to build the first electron microscope at the Berlin Technische Hochschule. In 1933, the electron microscope's performance exceeded the optical microscope and established the beginning of a new era in the microscopic world. Today, sub-ångström is possible, enabling atomic resolution [62]. In particular, electron ptychography demonstrates spatial resolution only limited by lattice vibrations (see Fig. 2.1a) [63, 64].

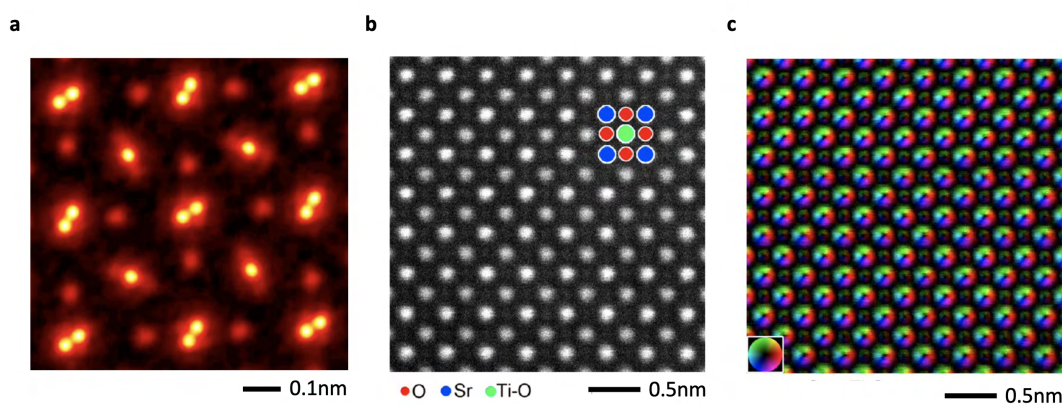


Figure 2.1 – **Real space atomic resolution achieved with electron microscopy.** **a:** Electron ptychography resolution-limited by lattice vibration in PrScO_3 demonstrating the best spatial resolution ever achieved [64]. **b:** Annular dark-field scanning transmission electron microscope (STEM) micrograph showing the atomic arrangement of SrTiO_3 and **(c)** the projected electric field vector map retrieved constructed from segmented detector micrographs, see ref. [65].

An transmission electron microscope (TEM) operates on a similar principle as optical microscopes. Indeed, the photon beam translates into an electron beam, the optical lens system into an electromagnetic lens system and ray optics relate to electron optics. Three sets of electromagnetic lenses are used in a conventional TEM. A condenser lens system shapes the energetic electron beam produced by the cathode and gun assembly. The objective lenses form the image of the sample with the transmitted electrons. Finally, the projector lenses magnify and focus the image onto the detector (see Fig. 2.2).

To fully comprehend the properties of complex matter microscopically, three complementary types of probes are usually used; neutron, photon, and electron. Neutrons and high-energy photons require a large facility to be produced, and although they are extremely precise probes, long exposure time and sizeable samples are usually needed due to the weak cross-section. On the other hand, electrons, as charged particles, interact substantially with matter. The

2.1. The rise of electron microscopy

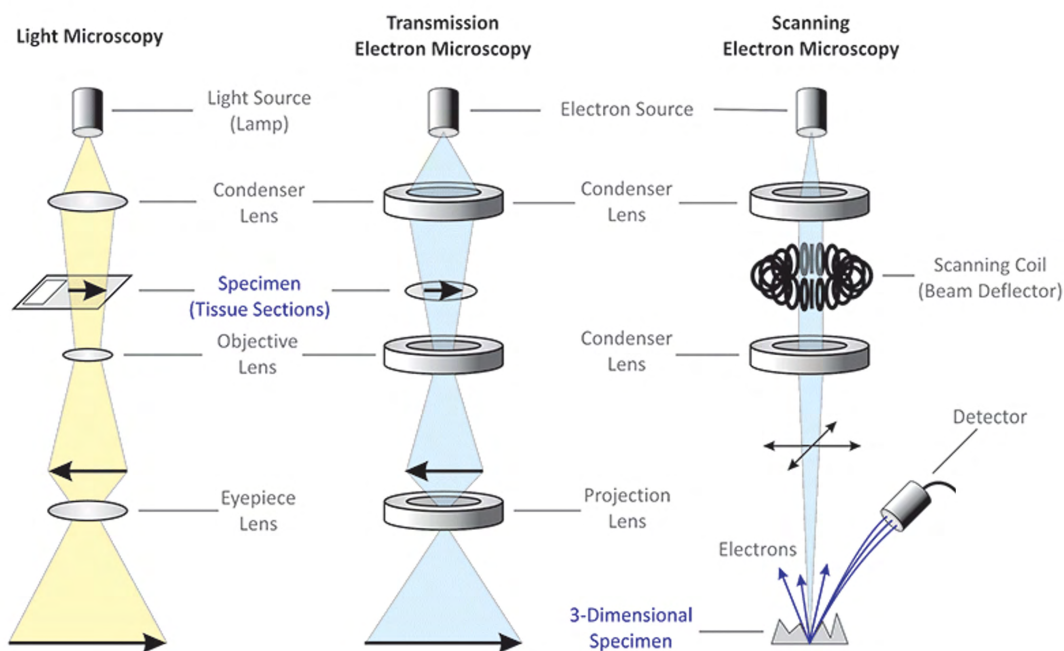


Figure 2.2 – **Image formation in an optical and electron microscope.** Left: Sketch of an optical microscope. Middle: Sketch of a TEM and its analogy with its older brother, the optical microscope. Right: Sketch of an scanning electron microscope (SEM), in that configuration, the electron beam scanned the sample surface, and a detector collected the back-reflected electrons. An image is then reconstructed. Image from MicrobiologyInfo.com

scattering cross-section is about six to seven orders larger than its x-ray analog, leading to faster acquisitions and access to advanced characterization methods. The strong electron-matter interaction leads to dynamical effects complexifying the analysis, and nanometres samples are required for the electrons to be transmitted and detected. Nevertheless, we can take advantage of the different electron-matter interactions to retrieve precious sample information such as its internal structural state, electronic properties, oxidation states, and compute real space quantitative elemental mapping [66–69]. Electrons are scattered by the positive potential inside the electronic cloud via the Coulomb interaction. Consequently, in addition, to being highly sensitive to the atomic structure, free electrons are an excellent probe to detect charged modulation in charged-ordered systems (see Fig. 2.3d-f) [6, 70–73] and can even resolve the atomic electric field [65, 74, 75].

Another type of deflection emerges in magnetic systems. In those materials, the electrons are deviated due to the Lorentz electromagnetic force applied by the sample in-plane magnetization instead of the electrostatic Coulomb potential. Classically, the electron trajectory is bent according to the spatial dependent magnetization, and the presence of non-homogeneous magnetic texture leads to different paths, forming a magnetic contrast. Hence, it allows us to visualize magnetic domains in real space with nanometre spatial resolution [76–80]. The technique is named Lorentz-TEM, and its quantum description is presented in the next part.

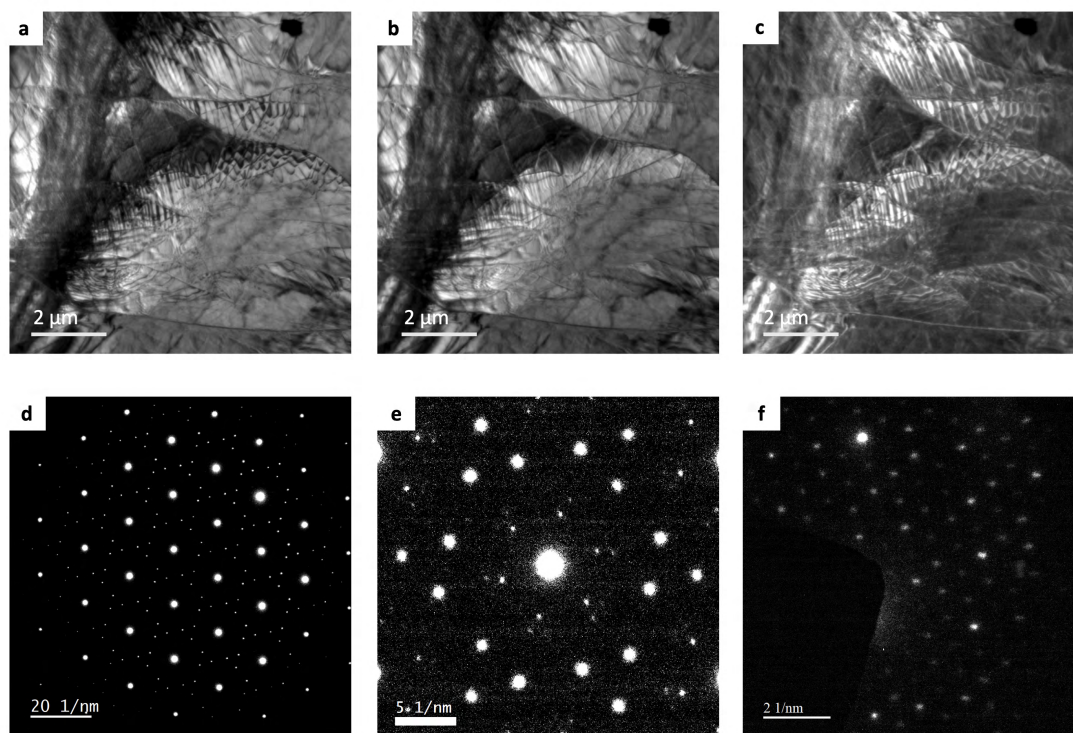


Figure 2.3 – TaS₂ energy-filtered transmission electron microscopy (EFTEM) micrograph and electron diffraction. **a-c:** Series of EFTEM micrograph showing anomalies in the electronic contrast taken at -5 eV, 0 eV and 10 eV, respectively. The slit had a energy width of 10 eV and the energy resolution is sub-eV. **d:** Diffraction pattern at room temperature. Intense spots are the Bragg spot from the structural lattice. The smaller spots show the nearly commensurate charge-density wave (CDW) at room temperature. **e:** Zoom in close to a Bragg spot adjusting the dynamical range. A second CDW phase similar as the *H-state* is observed at room temperature. **f:** Diffraction pattern taken at 5 K showing the commensurate CDW.

2.1. The rise of electron microscopy

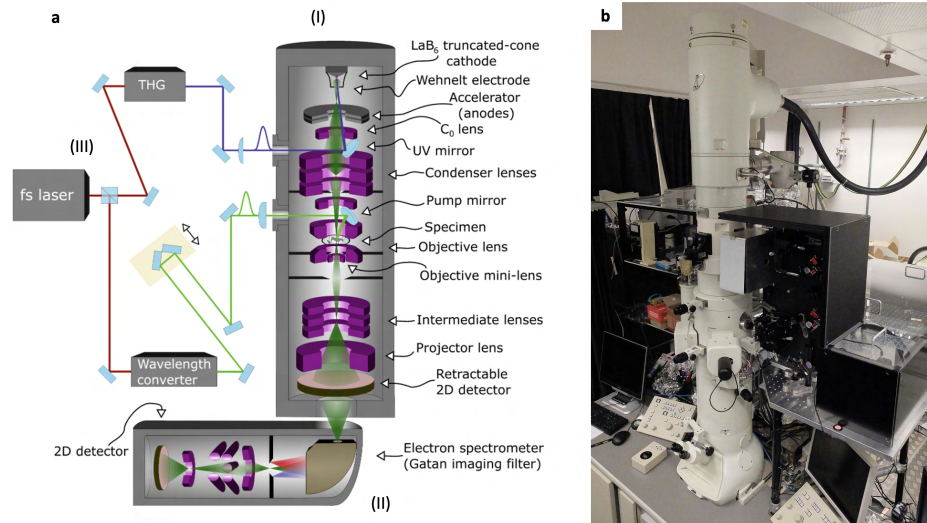


Figure 2.4 – **4D Ultrafast Transmission Electron Microscope at LUMES.** **a:** (I) Column of the electron microscope; the electromagnetic lens system (purple) is used to prepare the electron beam (condenser lenses), create the image (objective lenses), and finally magnify and focus the image (intermediate and projective lenses). The electron beam is represented in green. (II) Electron GIF spectrometer; a magnetic prism disperses the electrons in function of their energy enabling electron energy loss spectroscopy (EELS) and EFTEM. (III) Optical setup providing the ultrafast temporal resolution; A femtosecond laser beam is splitted in two optical path. One is frequency tripled and photo-induces the electron pulses. The second brings the sample out-of-equilibrium. Sketch reproduced from [81]. **b:** Picture of the 4D ultrafast TEM at LUMES - EPFL.

Chapter 2. Free electrons enable atomic, meV and attosecond resolution

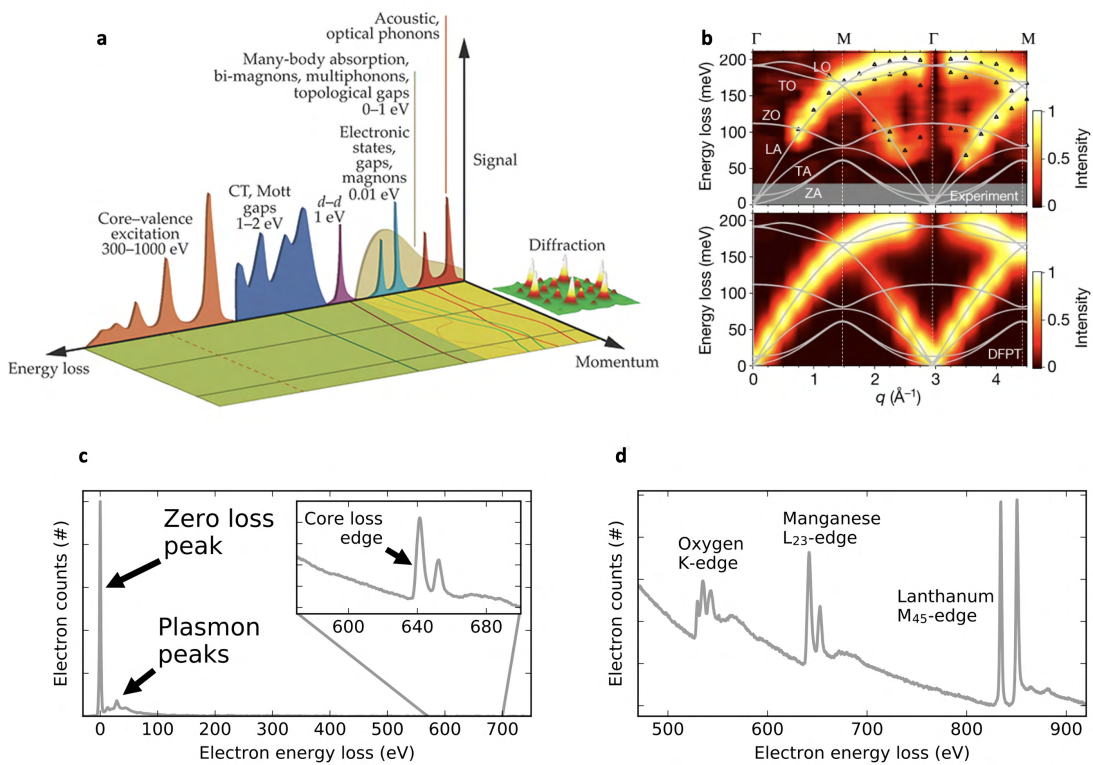


Figure 2.5 – TEM enables energy and momentum resolution.. **a**: Map of the different energy excitation in condensed matter system and their corresponding momentum dispersion. **b**: Phonons dispersion of graphite resolved by scanning-TEM. **c** and **d**: Typical EELS spectrum. The zero loss peak correspond to the elastic beam. At low-energy surface and bulk plasmon are usually dominant. At higher energy sharp peaks appear and corresponds to core-valence electronic transitions. Image **a** of courtesy by F. Carbone. Image **b** reproduced from [82], images **c** and **d** are from Wikimedia Commons.

2.2 Lorentz transmission electron microscopy & magnetic imaging

Several methods are available to understand the complex magnetic order in magnetic materials. Neutron scattering techniques are a powerful method to investigate the low-energy magnetic excitation spectrum and the underlying magnetic interactions. However, it requires large single crystals sample as the neutron cross section is pretty low. Furthermore, neutron scattering techniques do not provide real space information, which is essential to comprehend the emergent magnetic order interplay. Among the real space magnetic imaging techniques such as Kerr microscopy and spin-polarized scanning tunneling microscopy, Lorentz transmission electron microscopy (LTEM) is probably one of the most powerful approaches as it combines nanometre spatial resolution, short exposure time (infeasible for scanning probe), table-top instrument and can be performed in time-resolved mode with femtosecond temporal resolution. Lorentz transmission electron microscopy [83] takes advantage of the magnetic interaction (Lorentz force) between the electron beam and the specimen. Hence, depending on the in-plane component of the local magnetization, the electron beam is deflected, and magnetic contrast arises in the image plane. Two different modes exist. In the Foucault mode, the image stays in focus, and the objective aperture is shifted to block certain spots in the diffraction plane. Therefore, only electrons deflected by a specific angle given by the in-plane magnetization are selected and create the magnetic contrast. This technique has a high spatial resolution since the sample remains in focus. However, due to its technical challenges, the second mode is usually preferred as it gives a good compromise between spatial resolution (few nm) and implementation and allows magnetic phase retrieval.

Fresnel mode is based on acquiring a defocused (overfocus or underfocus) image of the specimen. The electron beam converges or diverges at the regions of the sample where the spin direction changes and therefore creates bright or dark contrast as depicted in Fig.2.6c,d. Since the image is defocused, the spatial resolution is reduced to a few nanometres, yet, higher magnetic contrast is achieved. In addition, Fresnel mode allows to retrieve the map of the magnetic phase by acquiring a series of images at different focus and using the transport-of-intensity equation (TIE), described below.

Phase retrieval and Transport of Intensity Equation

Let us consider an initial energetic and coherent electron beam that can be described by a plane wave in the *weak phase object approximation*, which assumes elastically scattered electrons and no absorption by the sample. The wave function that describes the electron evolved accordingly to the relativistic time-dependent Schrödinger equation, also named the Dirac equation. In particular, for high-energy electron beam and crystalline structure, its solution is given by [85]:

$$\phi_{obj}(\mathbf{r}) = a(\mathbf{r})e^{i\phi(\mathbf{r})}, \quad (2.1)$$

Chapter 2. Free electrons enable atomic, meV and attosecond resolution

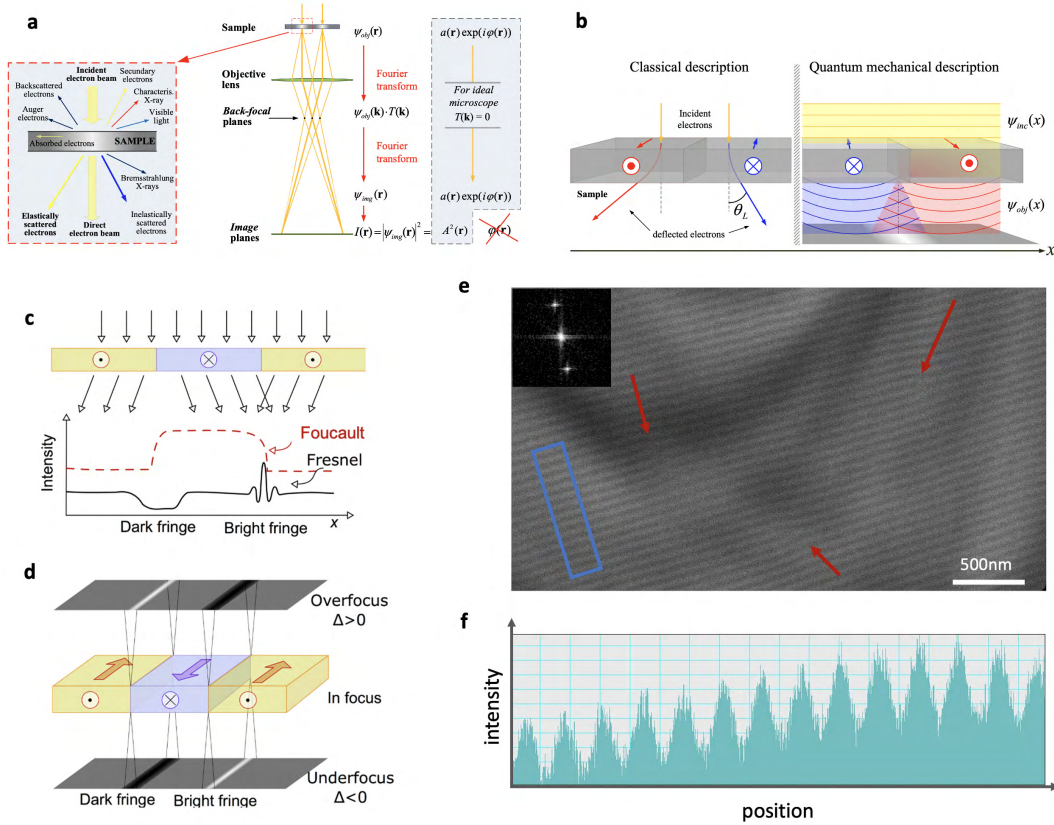


Figure 2.6 – **Principles of Lorentz transmission electron microscopy.** **a**: Sketch of different steps of the image wave function transformation. The left panel shows different electron-matter interactions present in electron microscopy. **b**: Classical and quantum description of the Lorentz force acting on the electron beam, leading to a magnetic contrast. **c**: Sketch of the intensity variation depending on the mode used. **d**: In Fresnel mode, the image is acquired out-of-focus giving bright and dark contrast or vice-versa. **e**: Energy-filtered LTEM image of the helical phase in Cu_2OSeO_3 . The red arrows show defects in the helical order, only visible in real space. No signature can be observed in the corresponding Fourier transform shown in the inset. **f**: Intensity profile of the blue rectangle in image **e**, a clear contrast is observed. The continuous background is due to sample thickness inhomogeneity. Image **a** and **b** reproduced from [84], images **c** and **d** from [81].

where ϕ_{obj} is the *object electron wave* that described the exit wave function after the interaction with the specimen and has an amplitude $a(\mathbf{r})$ and a phase shift $\phi(\mathbf{r})$, where \mathbf{r} is the spatial coordinate vector $\mathbf{r} = (x, y, z)$. After having traversed the lamella, the objective lens projects the electron into first its back-focal plane and then creates the image in its image plane as depicted in Fig. 2.6a. Mathematically, these two transformations are described by the Fourier transform F . In the back-focal plane, a reciprocal representation of the sample is created, more commonly named a diffraction pattern. The corresponding transformation is expressed as:

$$\Psi_{obj}(\mathbf{k}) = F\{\Psi_{obj}(\mathbf{r})\}, \quad (2.2)$$

2.2. Lorentz transmission electron microscopy & magnetic imaging

where \mathbf{k} is the wave vector and the Fourier transform F is defined as:

$$\Psi_{obj}(\mathbf{k}) = \int \Psi_{obj}(\mathbf{r}) e^{(2\pi i \mathbf{k} \cdot \mathbf{r})} d\mathbf{r}^3. \quad (2.3)$$

During the electron propagation and the image formation, spherical and chromatic aberrations emerged due to the lens's imperfection and the polychromatic e-beam. Such artefacts are microscope dependent and are expressed in a *transfer function* $T(\mathbf{k})$, that is generally expressed as follow

$$T(\mathbf{k}) = A(\mathbf{k}) e^{i\chi(\mathbf{k})} e^{-g(\mathbf{k})}. \quad (2.4)$$

The first term encompasses the cut-off aperture, and magnification effects, $g(\mathbf{k})$ accounts for the microscope instabilities, and $\chi(\mathbf{k})$ is the *phase contrast function* representing phase shifts induced by the lens aberration such as astigmatism, defocus, spherical aberrations. Considering the first order, the *phase contrast function* writes

$$\chi(\mathbf{k}) = \frac{2\pi}{\lambda} \left(\frac{C_s}{4} \lambda^4 k^4 + \frac{\Delta_z}{2} \lambda^2 k^2 - \frac{C_a}{2} \lambda^2 (k_y^2 - k_x^2) \right) \quad (2.5)$$

where C_s and C_a are the spherical aberrations and axial astigmatism coefficient, respectively, λ the electron wavelength, and Δ_z the defocus. Hence, the final image wave function is given by the two consecutive transformations and writes

$$\Psi_{img}(\mathbf{r}) = F\{\Psi_{dif}(\mathbf{k})\} = F\{\Psi_{obj}(\mathbf{k}) T(\mathbf{k})\}. \quad (2.6)$$

For an ideal microscope free of aberrations with zero defocus, i.e., $T(\mathbf{k}) = 1$, the relation simplifies, and the measured intensity given by the modulus of the image wave function is

$$\begin{aligned} I(\mathbf{r}) &= |\Psi_{img}(\mathbf{r})|^2 \\ &= |a(\mathbf{r})|^2. \end{aligned} \quad (2.7)$$

In that case, the phase contrast information is lost as the intensity is not phase dependent (see eq. (2.7)). If we consider now the case where the defocus is nonzero, the intensity will be modulated by the phase shift induced. In particular, considering no aperture, neglecting magnification effect, i.e., $A(\mathbf{k}) = 1$ and no phase shift due to spherical aberration and astigmatism, i.e., $C_s = 0$ and $C_a = 0$, the image wave function writes

$$\Psi_{img}(\mathbf{r}) = F^{-1} \left\{ F[\Psi_{obj}(\mathbf{r})] \cdot e^{(i\pi \Delta_z \lambda k^2)} \right\}. \quad (2.8)$$

For small defocus value, we apply a Taylor expansion, and after some algebra, we derive the following relation:

$$-\frac{2\pi}{\lambda} \frac{\partial I(x, y, \Delta_z)}{\partial \Delta_z} \Big|_{\Delta_z \rightarrow 0} = \nabla \cdot [I(x, y, 0) \nabla \phi(x, y)] \quad (2.9)$$

known as the transport-of-intensity equation, where $\phi(x, y)$ is the phase distribution of the transmitted electron wave that encoded the electromagnetic interaction of the electron wave and the specimen. From the Maxwell-Ampere equation, the phase $\phi(x, y)$ and the magnetization \mathbf{M} are related through

$$\nabla \phi(x, y) = -\frac{e}{\hbar} (\mathbf{M}(x, y) \times \mathbf{n}_z) t \quad (2.10)$$

where \hbar is the reduced Planck constant, e is the elementary charge, t the thickness, and \mathbf{n}_z the vector normal to the sample surface-

Hence, by acquiring a series at different defocus lengths, the phase encoding the magnetization can be retrieved. Finally, using eq. (2.10), the specimen magnetization can be extracted. Note that the typical deflection angle from Lorentz interaction β_L is small, around three orders of magnitude weaker than the Bragg angle (β_{Bragg}). The deflection angles are given by [86]

$$\beta_L = \frac{e\lambda B t}{h} \sim 10^{-5} \text{ rad}, \quad \beta_{Bragg} \sim 10^{-2} \text{ rad},$$

where B the magnetic field, and h the Planck constant. Further information about the full mathematical derivation can be found in refs. [79, 80, 84, 86]. An example of the magnetic phase retrieval of Bloch-type skyrmion is presented in Fig. 2.7.

2.2.1 Energy-filtered transmission electron microscopy

We distinguish two kinds of transmitted electrons. Elastic electrons, which have conserved their initial energy, and inelastic electrons that have exchanged some energy and momentum with the sample, through multiple scattering effects or plasmonic interaction, for instance. By adding to the microscope, a magnetic prism (spectrometer, see Fig. 2.4) that dispersed the electrons depending on their energy EELS become possible, and additional information can be retrieved, such as low energy excitations, plasmonic excitations, and core-valence excitations (see Fig. 2.5a) [87–89]. Such a microscope is named 4D electron microscope as it explores three spatial dimension and the energy dimension. In electron microscopy, spatial resolution is not limited by the electrons' wavelength (few pm) but from spherical aberrations that cumulate along the electron path caused by the electromagnetic lenses and the initial polychromatic electron beam. The energy resolution depends essentially on the initial energy spread given by the electron gun. The recent development of field emission gun technology has made possible meV energy resolution compared to the sub-eV resolution obtained with thermionic gun [90]. Notably, the energy-momentum dispersion of low-energy phonon modes has been recently demonstrated [82]. In imaging mode, the micrograph quality depend substantially of the sample thickness as dynamical and inelastic effects arise. Four-

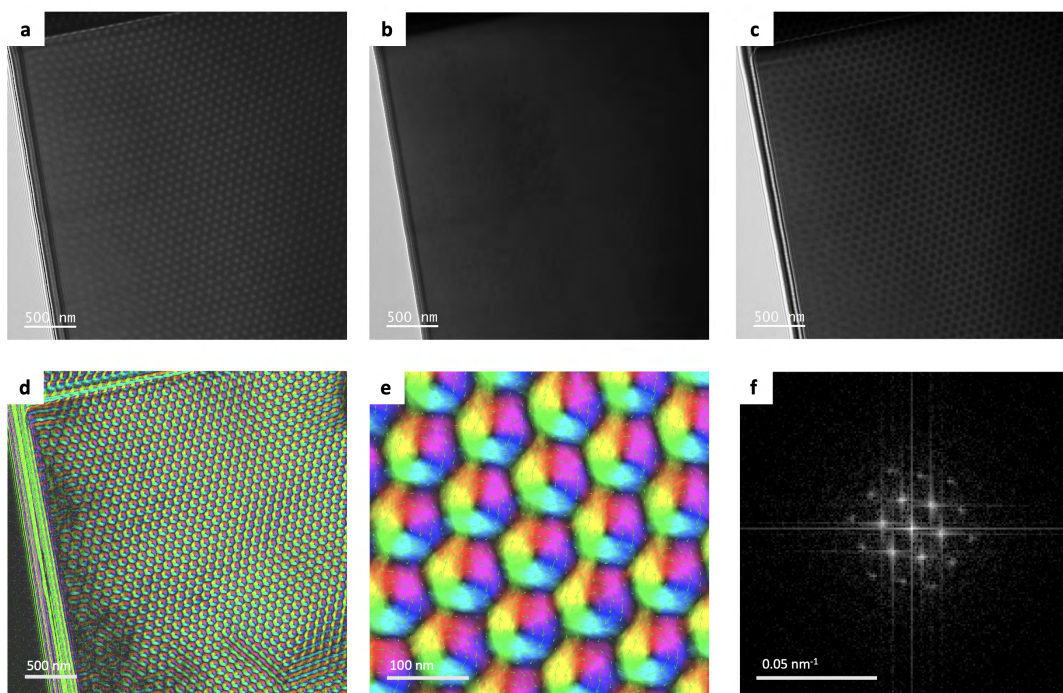


Figure 2.7 – **Skyrmion magnetization retrieval using TIE in FeGe.** TEM micrograph taken (a) underfocus ($\Delta_z = -0.8$ mm), (b) at focus, and (c) overfocus ($\Delta_z = +0.8$ mm) of a FeGe thin lamella, showing a magnetic contrast due to the present skyrmion in-plane magnetization. **d:** magnetic phase retrieval using TIE. **e:** Zoom in showing Bloch-type skyrmion. **f:** Corresponding Fourier transform of image **a**.

dimensional electron microscopy can suppress such undesirable effects as it is possible to form an image with electrons having a specific energy. This technique is called EFTEM. In addition to enhance considerably the image quality by keeping only elastic electrons, EFTEM can uncover in real space elusive states, such as Moiré excitons [91], or evanescent fields [92, 93]. In this thesis, we use energy-filtered cryo-LTEM to get insight into the magnetic properties of the skyrmion host multiferroic Cu_2OSeO_3 out-of-equilibrium. Specifically, a femtosecond laser pulse with different wavelength is used to pump the specimen. Although we operate the microscope in in-situ conditions i.e. single optical pump pulse and continuous electron probe, our microscope at LUMES can achieve time-resolved measurement and allows ultrafast pump-probe techniques, overviewed in the next section.

2.3 4D ultrafast transmission electron microscope

Since the last decade, a growing interest of ultrafast TEM has appeared. Such table-top setup exploits the unique versatility and resolution of 4D transmission electron microscope coupled with an ultrafast laser providing femtosecond temporal resolution, competing synchrotron

Chapter 2. Free electrons enable atomic, meV and attosecond resolution

techniques [94]. Today, state-of-the-art electron microscopy allows fs/nm spatio-temporal magnetic imaging [95] and recent developments have opened attosecond perspectives [96–99]. The stroboscopic approach also called pump-probe technique is used to achieve such a temporal resolution. Practically, the initial laser beam, typically produced by a femtosecond Ti:sapphire amplifier having a wavelength of 780 nm (1.59 eV), is split into two parts. The first part is used to excite the sample out-of-equilibrium and is called the pump. Different photon energies can be used depending on the optical setup that requires non-linear optics such as an optical parametric amplifier (OPA). The second part is converted into ultraviolet (UV) (260 nm / 4.77 eV) to illuminate a LaB₆ cathode of the microscope and photocreate a bunch of electrons used as the probe (see Fig. 2.8c). To avoid space-charge effect, the UV beam fluence is attenuated enough to photoexcite on average a single electron per pulse. The time delay between the pump and the probe pulses is realized with a delay stage. The concept is illustrated in Fig.2.4a. Note that, only reversible phenomena can be investigated by stroboscopic techniques since the sample must return to its equilibrium state before arrival of the next pump pulse. Nevertheless, recently single shot imaging has been demonstrated as well [61, 100–103], which opens a new way for exploring irreversible events. Regrettably, single-shot magnetic imaging is far beyond state-of-the-art, and thus indirect method must be used to get insight of ultrafast irreversible magnetic process. We recently achieve such demonstration [104], exploiting three key ingredients: threshold behaviour, irreversible and coherent process.

In summary, these properties enable performing ultrafast imaging, diffraction and spectroscopy with Å/meV/as resolution. Combined in one tabletop instrument, they offer an unique powerful tool to investigate and track dynamical processes in real and reciprocal space.

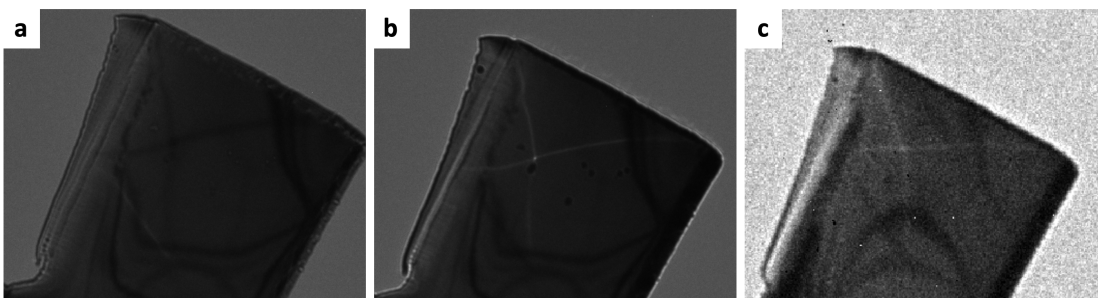


Figure 2.8 – LTEM image of magnetic domain walls in Fe₃O₄. Micrograph taken, at room temperature, with no external magnetic field, with thermionic electrons (a) over focus (b) under focus (c) with photoelectrons at 300 kHz repetition rate. The size of the sample is 5x5 μm².

2.4 Ultrafast reflective high-energy electron diffraction

Probably one of the major drawbacks of transmission electron microscopy is the need for ultra-thin lamella, which is challenging to produce. The reflective High-Energy Electron Diffraction technique circumvents this constraint using reflected electrons (RHEED). A second advantage of such a configuration is to exploit the electron penetration depth that is extremely small, with few Å. Hence, the electron beam only probes a few atomic layers depending on the grazing angle, allowing surface investigation where intriguing effects emerge [105–109]. An example of the RHEED pattern associated with the surface state of the corresponding sample is presented in Fig. 2.10. In addition, the RHEED setup is cost-effective and modular compared to its TEM older brother. In particular, for ultrafast time-resolved measurement, the one electron per bunch limitation can be overcome by using a GHz compression stage, allowing a temporal resolution of ~ 100 fs with up to 10^6 electrons per bunch [110–113]. Similarly, as a 4D ultrafast TEM, Ultrafast Reflective High-Energy Electron Diffraction (URHEED) relies on a femtosecond laser. The laser beam is split into two beams. One beam photo-creates the electron bunches that are accelerated with a nominal 30 kV high-voltage. The second beam is front-tilted to match the electron group velocity allowing sub pm/ps spatio-temporal resolution [111] and thus ideal for investigating structural dynamics. Indeed, by tracking the Bragg spot evolution, the structural distortion can be retrieved. Indeed, the strain ε along a certain direction $[hkl]$ at a time delayed t is defined by

$$\varepsilon^{hkl} = \frac{d(t_0) - d(t)}{d(t_0)}, \quad (2.11)$$

where d is the atomic lattice spacing for the plane (hkl) , and the h, k, l are the Miller indices. Using the Bragg law that relates the lattice atomic distance and the Bragg angle θ for a given wavelength λ expressed as:

$$2d \sin \theta = n\lambda \quad (2.12)$$

with n is diffraction order. For clarity, we drop the explicit time dependence and consider the first-order diffraction, using eq. (2.12), the strain rewrites

$$\varepsilon = \frac{d_0 - d}{d_0} = 1 - \frac{\sin \theta_0}{\sin \theta} = \frac{\sin \theta - \sin \theta_0}{\sin \theta} \simeq \frac{\theta - \theta_0}{\theta} \quad (2.13)$$

where we use the sample angle approximation. In practice, we measured the amplitude of the scattering vector S that directly relates (see Fig. 2.9c) to the Bragg angle through the relation

$$\arctan 2\theta = \frac{S}{CL} \longrightarrow \theta \simeq \frac{S}{2CL}, \quad (2.14)$$

Chapter 2. Free electrons enable atomic, meV and attosecond resolution

where CL is the camera length. Finally combining eq. (2.13) and eq. (2.14), we find

$$\varepsilon \simeq \frac{\theta - \theta_0}{\theta} \simeq \frac{S - S_0}{S}. \quad (2.15)$$

Hence, we can retrieve the specific strain along the corresponding axis by tracking the Bragg peak position, i.e., the scattering vector. This method is particularly effective in investigating sub-ps and pm structural dynamics [114, 115]. For these reasons, we employ URHEED to study the light-induced structural dynamics in Magnetite (Fe_3O_4) as this system shows a structural phase transition around from a high symmetry cubic phase to a lower monoclinic symmetry.

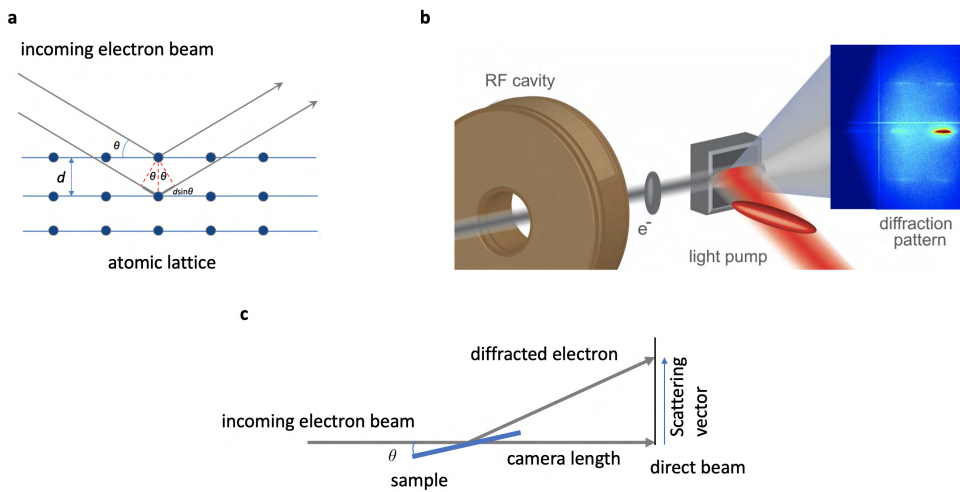


Figure 2.9 – **Bragg law and ultrafast electron diffraction.** **a:** Classical representation of the Bragg law. **b:** Sketch of the experimental setup. A radio frequency cavity compressed the electron bunch to achieve sub-ps temporal resolution. The laser pump is front tilted to compensate for the electron group velocity mismatch. **c:** Sketch of the experimental setup. The experimental camera length is ~ 30 cm and the grazing angle 2θ varies from 0.5 to 5° .

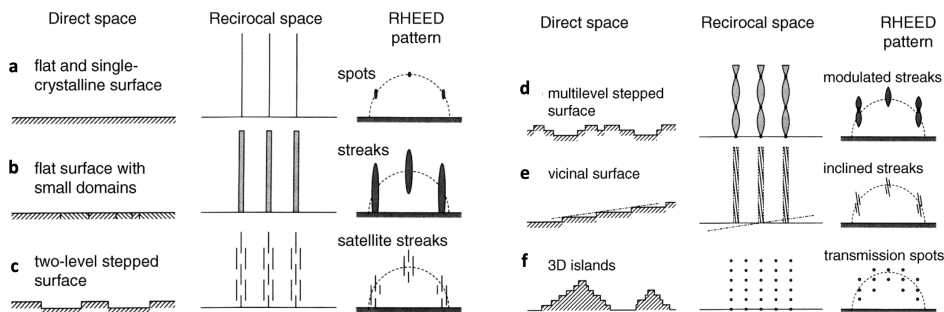


Figure 2.10 – **RHEED pattern for various surface states.** **a-f:** Illustration of various RHEED patterns associated with different possible surface morphology. Image adapted from [116].

2.4. Ultrafast reflective high-energy electron diffraction

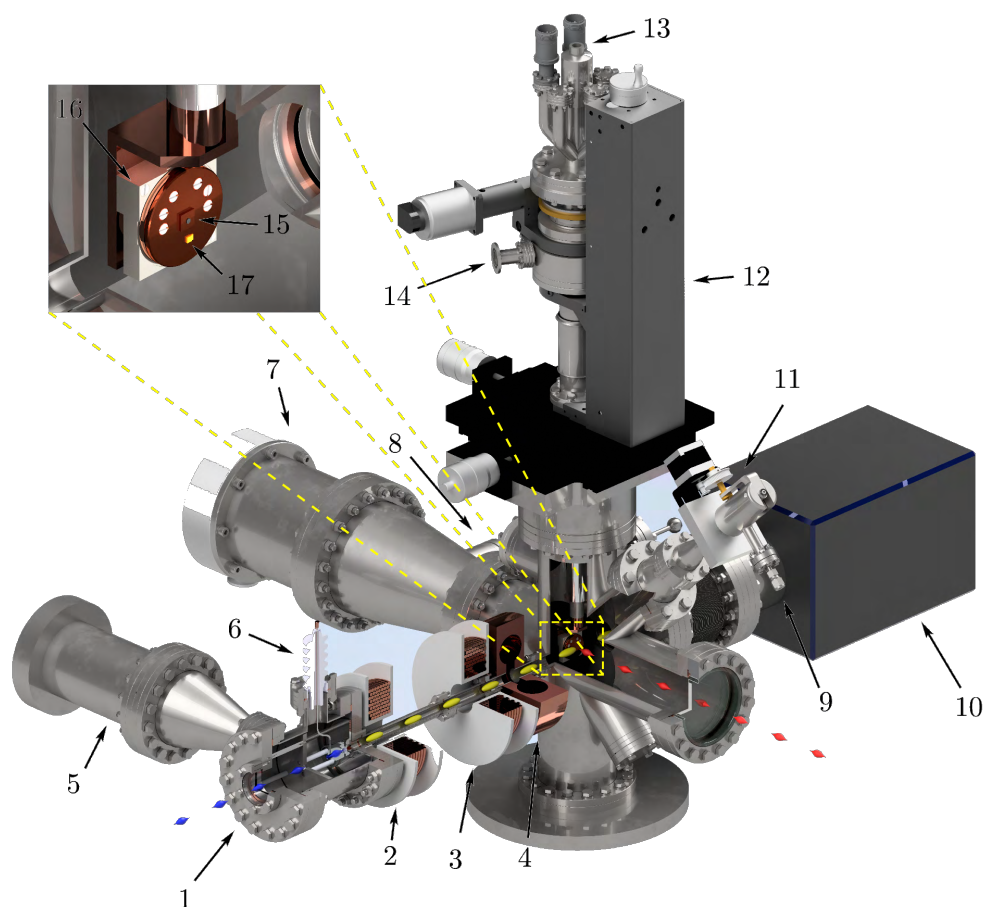


Figure 2.11 – **Schematic representation of the experimental setup.** 1) DC gun, 2) collimation solenoid, 3) focusing solenoid, 4) RF cavity, 5) DC gun turbo pump, 6) HV connection, 7) main turbo pump, 8) ion gauge, 9) gas inlet, 10) detector, 11) leak valve, 12) 4-axis manipulator, 13) flow cryostat entrance, 14) cryostat vacuum port, 15) sample position, 16) 5th-axis housing, 17) sample temperature sensor. Image of courtesy P. Usai.

2.5 Conclusion and perspectives

Using free electrons to probe matter provides powerful methods to investigate the atomic scale and high and low-energy excitations with femtosecond temporal resolution. Going beyond being an extremely versatile characterization tool, electron microscopes offer a unique playground to test fundamental particle physics with free electrons and explore the quantum future of microscopy [117]. For example, engineering of the electron wave function [97, 118–121], as well as generating electron-photon pairs [122] have been recently demonstrated. Furthermore, the pioneer works have shown the possibility of controlling electrons at the attosecond timescale [96–99]. Finally, let us mention that with the recent development of the vitrification protocol for biological samples, a new playground is accessible where ultrafast phenomena have been shown to play an important role [123, 124].

Manipulation of a topological magnetic texture

Part II

3 Topology and emergence in modern magnetism

In solids, magnetic order emerges from the interplay between magnetic interactions inherent to the hosting material that can be tuned using external parameters such as temperature, magnetic field, or pressure. Magnetic phase transitions can be described by spontaneous symmetry breaking. For example, in the case of a paramagnetic to ferromagnetic transition, the time-reversal symmetry is broken and is well described by critical scaling mean-field theories [125–128]. Present-day, magnetic materials present an ideal and rich playground to investigate criticality [16, 129], quantum phase transition [15, 130], and emergent fields application [131]. Notably, in the last decades, many efforts have been put into the quest of finding a quantum spin liquid host material, as its theoretical many-body entangled interacting system does magnetically order down to the lowest temperature and might be intimately linked to superconductivity [132–135].

Recently, a novel class of magnetic ordering has brought substantial interest theoretically and experimentally for its peculiar real space topological properties. Initially predicted more than sixty years ago, using particle physics theory to describe nucleon, Tony Skyrme found that topological solitons are solutions of the non-linear sigma model [136, 137]. In solid-state physics, more precisely in magnetic systems, this topological soliton can be realized in real space and is named a magnetic skyrmion in honor of the physicist. A skyrmion consists of a whirling vortex-like spin texture with topological protection and exists in different variants. In 2009, a small angle neutron scattering experiment in bulk MnSi, a non-centrosymmetric metallic B20 compound, provided the first experimental evidence of the skyrmion's existence [138], and was then confirmed in real space by Lorentz-Transmission electron microscopy [139]. Since then, skyrmions have been discovered in many other systems, such as insulators and multilayered materials, and can either form a skyrmion lattice (SkL), named also a skyrmion crystal (SkX), or exist individually [14]. Skyrmions are usually stabilized by the Dzyaloshinskii-Moriya interaction (DMI), which originates either from bulk properties and can create both Bloch-type and Néel-type skyrmions depending on the local point group symmetry [14], or arises from interfacial interaction leading to Néel-type skyrmions in multilayered system [140]. Due to its specific spin arrangement, a skyrmion has non-trivial topological properties and offers a

unique platform to study fundamental interactions including magnetic monopoles phenomena in emergent fields and gauge theories [141–144], light-matter interaction [104, 145–147], and Abrikosov vortices in type-II superconductors [148, 149]. In addition, skyrmions are of great interest in spintronics applications, where their nanometre size, robustness against external perturbations, and highly efficient coupling to spin currents are leveraged [14, 150].

In the following sections, we overview how skyrmions emerge from magnetic interactions and how to classify their different variants. Then, the notions of the Berry phase and Berry curvature are introduced. From this theory, we derive the existence of emergent fields, which elegantly explains the origin of the topological Hall effect and predicts an emergent magnetic monopole realized as a point defect in the skyrmion lattice. Finally, we conclude by showing that skyrmion topological properties can be harnessed to perform quantum interferometry, opening new understanding in the quantum origin of the Berry phase.

3.1 Topology and magnetic skyrmion

Borrowed from mathematicians, the concept of *topology* has revised our modern approach to physics. Driven by this enthusiasm, many discoveries and advances in condensed matter physics have emerged, such as surface states in a topological insulator [151, 152], topological superconductors [11] and Majorana zero-mode in topological quantum computing [153]. Recently discovered, magnetic skyrmions, as an exotic magnetic texture is probably one of the most investigated topological objects [14, 138, 139, 150], as they offer a unique playground to study magnetism [14], emergent fields [144, 154], Topological phase transition (TPT) [19, 155, 156], and are a promising candidate for spintronic devices [13, 157, 158] and in neuromorphic computing applications [159–161]. Furthermore, skyrmion's topology is widely investigated in other research fields where singularities arise or can be manipulated, such as in black holes [162–164], topological dark matter [165], plasmonics [166, 167], and optics [168].

3.1.1 Topological invariant and winding number

In a nutshell, without involving mathematical details, mathematicians usually characterize objects using geometrical properties and classify them with respect to their symmetries. Typically during a phase transition, some geometrical properties change and consequently break some symmetries of the system. In the concept of Topology, geometrical symmetry does not directly play a role. Instead, the object is characterized by a topological invariant. Two objects are topologically equivalent if we can apply a geometrical transformation such that we can contract one into the other by a smooth continuous deformation, i.e., neither introducing nor removing singularities. For example, a cup of coffee is topologically equivalent to a torus due to its handle. The torus has a different topological class compare to a sphere, as we must introduce a singularity to make the transformation, inducing a TPT. Examples of different topological classes are presented in Fig. 3.1.

Topologist's Morning Routine

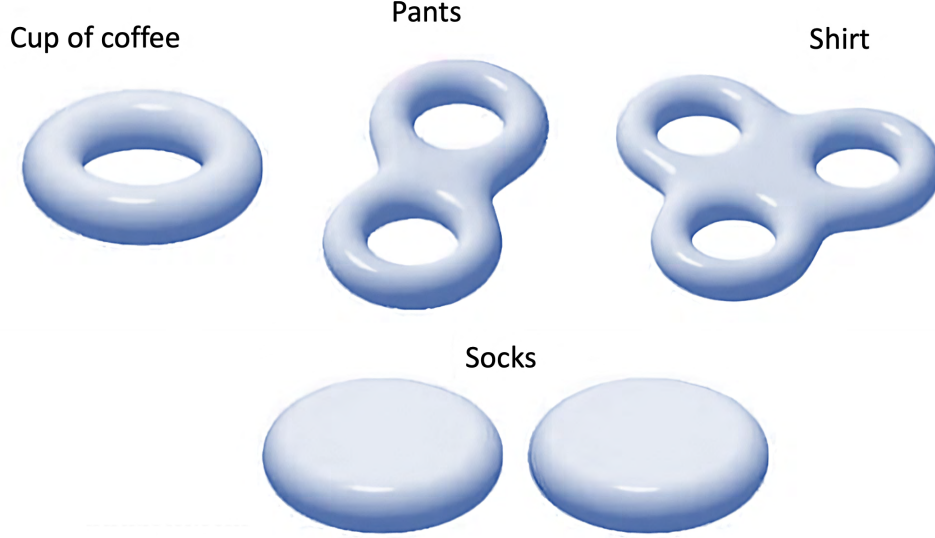


Figure 3.1 – **Topological classes in real space.** Example of different topological classes used in a topologist's morning routine. Note the socks are topologically trivial, as their topological invariant is defined as zero. Image adapted from www.reddit.com.

Here, we focus on topological magnetic textures, specifically a magnetic skyrmion. The topological invariant, named the topological charge, also defined as skyrmion number or winding number, characterizes the skyrmion twisted spin structure and is defined as:

$$\mathcal{W} = \int n_{Sk}(\mathbf{r}) d^2r \quad (3.1)$$

with n_{Sk} the topological charge density. The topological charge density expresses

$$n_{Sk}(\mathbf{r}) = \frac{1}{4\pi} \mathbf{m}(\mathbf{r}) \cdot \left[\frac{\partial \mathbf{m}(\mathbf{r})}{\partial x} \times \frac{\partial \mathbf{m}(\mathbf{r})}{\partial y} \right], \quad (3.2)$$

where $\mathbf{m}(\mathbf{r})$ is the local magnetization with unity amplitude, i.e. $|\mathbf{m}(\mathbf{r})| = 1$. To compute the topological charge, we use the spherical coordinates with the azimuthal angle θ and polar angle ϕ and express the position vector in polar coordinates $\mathbf{r} = r(\cos \phi, \sin \phi)$. Thus, the topological density expresses in spherical coordinate

$$n_{Sk}(\mathbf{r}) = (\cos \Phi(\mathbf{r}) \sin \Theta(\mathbf{r}), \sin \Phi(\mathbf{r}) \sin \Theta(\mathbf{r}), \cos \Theta(\mathbf{r})). \quad (3.3)$$

By substituting eq. (3.2) in eq. (3.1) and using spherical coordinate, we obtain [169]

$$\mathcal{W} = \frac{1}{4\pi} \int_0^\infty dr \int_0^{2\pi} d\phi \frac{\partial\Phi(\phi)}{\partial(\phi)} \frac{\partial\theta(r)}{\partial r} \sin\theta(r) \quad (3.4)$$

$$= \underbrace{-\frac{1}{2} \cos\theta(r)}_{\text{polarity}} \Big|_{r=0}^\infty \cdot \underbrace{\frac{1}{2\pi} \Phi(\phi)}_{\text{vorticity}} \Big|_{\phi=0}^{2\pi}. \quad (3.5)$$

We define the polarity p and the vorticity m . Let us suppose at the skyrmion center ($r = 0$) the spins point down; therefore, the spins point up at its edge ($r \rightarrow \infty$). In other words, the spin's orientation is reversed from the center to the edge and is characterized by the polarity, which can take two values $p = \pm 1$. The vorticity m determines the topological charge, and due to continuity in the magnetization, the polar angle can only wrap the Bloch sphere in multiple of 2π , therefore

$$m = \frac{1}{2\pi} \Phi(\phi) \Big|_{\phi=0}^{2\pi} = 0, \pm 1, \pm 2, \dots \quad (3.6)$$

If the azimuthal angle of the moment changes monotonically with the azimuthal direction ϕ , we can define the helicity γ , which represents a phase in the relation

$$\Phi(\phi) = m\phi + \gamma. \quad (3.7)$$

Hence, we can describe different types of skyrmion using their winding number, vorticity, and helicity properties. For example, $(\mathcal{W}, m, \gamma) = (1, -1, -\pi/2)$, $(1, -1, -0)$, and $(-1, 1, -\pi/2)$ corresponds to Bloch-type, Néel-type and anti-skyrmion, respectively. The three spin configurations are depicted in Fig. 3.2, which illustrates their corresponding mapping onto a sphere. More generally, the different types of skyrmions can be expressed with the following magnetization profile

$$\mathbf{m}_{Sk}(\mathbf{r}) = \begin{pmatrix} \left(\frac{x}{r} \cos \gamma - m \frac{y}{r} \sin \gamma \right) \sin \left(\frac{\pi}{r_0} r \right) \\ \left(\frac{x}{r} \sin \gamma + m \frac{y}{r} \cos \gamma \right) \sin \left(\frac{\pi}{r_0} r \right) \\ p \cos \left(\frac{\pi}{r_0} r \right) \end{pmatrix} \quad (3.8)$$

for $0 < r < r_0$, and r_0 the radius of the skyrmion. Additional examples skyrmion configuration with different vorticity and helicity are shown in Fig. 3.3. Some configurations are energetically preferred, as discussed in the next section.

3.1.2 Stabilization mechanism

The stable magnetic configuration is determined by minimizing the magnetic free energy, which is material dependent. Skyrmions emerge from the competition among the different magnetic interactions of the system. One can distinguish two kinds of interactions. One favors the spins to be aligned parallelly with respect to each other, like the ferromagnetic exchange or the Zeeman coupling. The second interaction category forces the spins to be noncollinear,

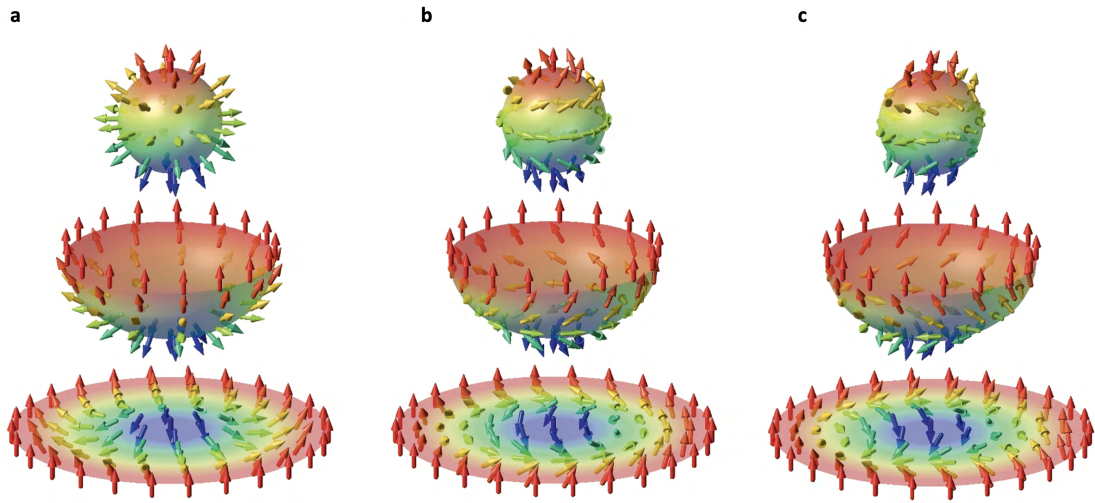


Figure 3.2 – **Stereographic projections of topological solitons.** Stereographic projection of (a) a Néel-type, (b) a Bloch-type skyrmion and (c) a anti-skyrmion and their corresponding mapping on the unit sphere (hedgehog configuration) The color code indicates the value of the z-component of the magnetization with red (blue) representing $m_z = +1(-1)$ ". Image reproduced from [170].

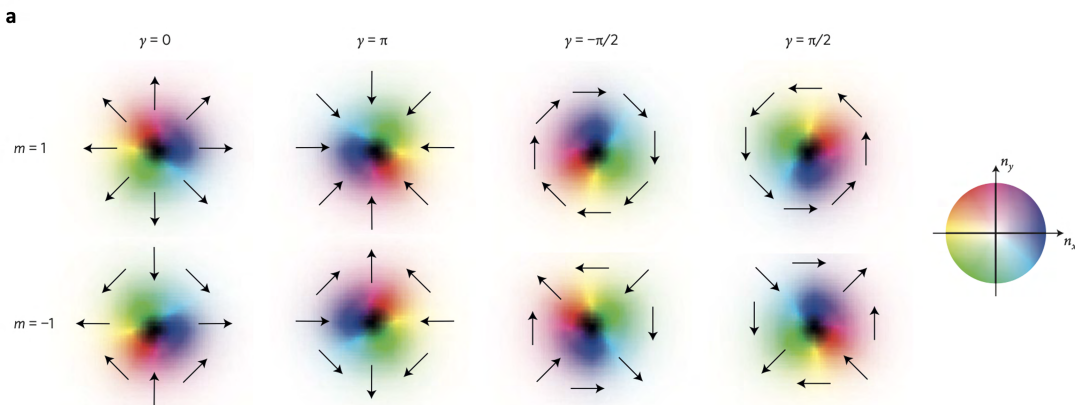


Figure 3.3 – **Skyrmion configuration according to their vorticity and helicity.** a: Representation of different skyrmion magnetic arrangements classified by their vorticity and helicity. Note all anti-skyrmion ($m = -1$) with different helicity are equivalent and correspond to an in-plane rotation. The black arrows denote the in-plane magnetization, and the colors express the out-of-plane component, with black pointing down and white pointing up. Image taken from [169].

inducing canting and twisting. Such interaction naturally exists in non-centrosymmetric systems and produces the so-called Dzyaloshinskii-Moriya interaction (DMI). The skyrmion vorticity and helicity are defined by the crystallographic point-group symmetry of the host

material [14]. The basic interaction terms sufficient to stabilize skyrmions are described in this Hamiltonian:

$$\mathcal{H} = -J \underbrace{\sum_{i,j} \boldsymbol{\sigma}_i \cdot \boldsymbol{\sigma}_j}_{\text{Exchange}} - \mathbf{B} \underbrace{\sum_i \boldsymbol{\sigma}_i}_{\text{Zeeman}} - \underbrace{\mathbf{D}_{ij} \sum_{i,j} \boldsymbol{\sigma}_i \times \boldsymbol{\sigma}_j}_{\text{Dzyaloshinskii-Moriya}}. \quad (3.9)$$

Due to its high computational cost, theoretical simulations generally use a continuous field approximation to minimize the Free energy functional, including higher orders using the Ginzburg-Landau theory framework. The Free energy functional expresses as:

$$F[\mathbf{m}] = \int [\underbrace{J(\nabla \mathbf{m})^2}_{\text{Exchange}} + \underbrace{\mathbf{Dm} \cdot (\nabla \times \mathbf{m})}_{\text{Dzyaloshinskii-Moriya}} - \underbrace{\mathbf{B} \cdot \mathbf{m}}_{\text{Zeeman}} + \underbrace{a\mathbf{m}^2 + b\mathbf{m}^4 + \dots}_{\text{Higher orders}}] \text{dr}. \quad (3.10)$$

Depending on the material, additional terms must be included to describe the magnetic system accurately. For instance, magnetic anisotropy has been shown to play an essential role in forming a second skyrmion phase in Cu_2OSeO_3 [171]. Moreover, thermal fluctuations are usually required to stabilize the skyrmion phase [138, 139, 172], and are usually omitted in simulations. Magnetic fluctuations can also be significant in the stabilization mechanism [173].

Even in the absence of DMI in centrosymmetric systems, magnetic skyrmions have recently been observed [174, 175]. A long-range exchange interaction has been shown to be responsible, represented by the Runderman-Kittel-Kasuya-Yosida (RKKY) model and causes magnetic frustrations favorable to skyrmions formation. The exact skyrmion profile depends also on the sample geometry, defects, and the potential presence of other quasiparticles.

Since this thesis focuses on the generation and control of a skyrmion magnetic texture using ultrashort photon pulses, such optical manipulation opens intriguing directions to investigate (out-of-equilibrium) topological phase transition and dynamical emergent fields, to mention only a few. Therefore, before diving into the experimental results and interpretation of this work, it is instructive to present some key concepts of the emergent fields physics in a skyrmion and its relation with real-space topological (Berry) physics.

3.2 The Berry phase, Berry curvature and emergent fields

It is well known that electrons flowing in a magnetic material can induce various fascinating effects. The material's resistivity directly reflects the electrons' ability to propagate. In particular, in the presence of an external magnetic field, the electrons deviate and accumulate at an edge creating a Hall voltage. However, even in the absence of an external magnetic field, Hall voltage can still appear due to intrinsic magnetization; this effect and its quantized version are named the Anomalous Hall and Quantum Anomalous Hall effect. The Kondo effect describes anomalies in the resistivity at low-temperature and occurs due to magnetic

3.2. The Berry phase, Berry curvature and emergent fields

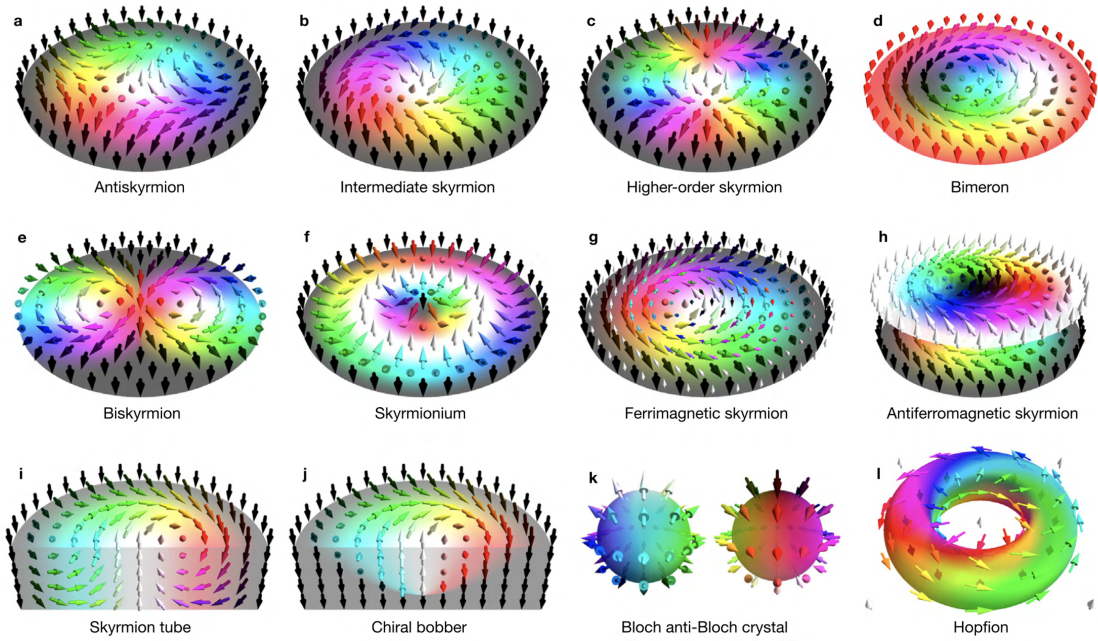


Figure 3.4 – **Beyond conventional skyrmions.** Zoo of exotic magnetic textures with different topological charge and helicity, some have been experimentally demonstrated while others remain to be discovered. In this thesis, we investigated Bloch-type skyrmion tube (i). Image reproduced from [176].

impurities. In superconductivity, magnetism is also closely related as antiferromagnetic order has been reported close to the superconducting phase in high- T_c superconductor cuprates [177, 178] and spin-spin interactions mediate Cooper pair formation in heavy fermion superconductors [179]. Nonetheless, all previous systems host only trivial topological magnetic textures. From this observation, a natural question arises: What happens to an electron flowing through a non-trivial topological spin texture like a skyrmion, and how should we understand it? This question was addressed recently, theoretically, and experimentally. It turns out that the electron is deflected, giving an additional contribution to the total Hall resistance [154, 180]. Moreover, the skyrmion is also pushed forward with a deflection angle [181, 182]. Both effects are named the Topological Hall effect (THE) and the skyrmion Hall effect (SHE), respectively. Predicted theoretically by Bruno *et al.* [183], this phenomenon has a pure topological origin and can be explained in the adiabatic limit, which is generally a good approximation as the electron's wavelength is much smaller compared to the magnetic unit cell of hundreds of Angstroms. While traversing a *fixed* skyrmion, the electron's spin constantly aligns with the local magnetization and picks up a Berry phase. Consequently, the electrons feel a "fictitious" magnetic field that emerges and is quantized due to the topological nature of the skyrmion. Before diving into the emergent fields derivation, described in Section 3.2.3, we need to introduce the notion of Berry phase and Berry curvature, presented in the next section.

3.2.1 Geometrical phase and Berry curvature

Let us consider the strong interaction case in which the itinerant electron's spin aligns constantly adiabatically with a non-uniform magnetic field while evolving. The system can be described by a time-dependent Hamiltonian \mathcal{H} with parameters $\mathbf{R} = (R_1, R_2, \dots)$ i.e.

$$\mathcal{H} = \mathcal{H}(\mathbf{R}), \quad \mathbf{R} = \mathbf{R}(t). \quad (3.11)$$

As the system evolves adiabatically, i.e., the Hamiltonian's parameters vary slowly along a path C in the parameter space, the system will follow instantaneous eigenstates with their respective time-evolved energies. This is expressed:

$$\mathcal{H}(\mathbf{R})|\phi_n(\mathbf{R})\rangle = \varepsilon_n(\mathbf{R})|\phi_n(\mathbf{R})\rangle, \quad \langle\phi_n(\mathbf{R})|\phi_n(\mathbf{R})\rangle = 1 \quad (3.12)$$

where ϕ_n and E_n are the instantaneous normalized eigenstates, and their associated eigenenergies are assumed to be non-degenerate, respectively.

Let us suppose that initially at time t_0 the wave function $|\Psi\rangle$ describing the system is prepared in the n^{th} instantaneous eigenstate i.e. $|\Psi(t_0)\rangle \propto |\phi_n(\mathbf{R}(t_0))\rangle$. The time-dependent Schrödinger equation describes the time evolution of the system

$$i\hbar \frac{\partial}{\partial t} |\Psi(t)\rangle = \mathcal{H}(\mathbf{R})|\Psi(t)\rangle. \quad (3.13)$$

We make the Ansatz

$$|\Psi(t)\rangle = e^{i\gamma_n(t)} e^{-\frac{i}{\hbar} \int_0^t \varepsilon_n(\mathbf{R}(t')) dt'} |\phi_n(\mathbf{R}(t))\rangle. \quad (3.14)$$

During the adiabatic evolution, the system acquires an extra phase (first exponential term) in addition to the dynamical phase (second exponential term). This extra phase represents the gauge freedom and depends on the path C that follows in the parameter space during the evolution. The geometrical phase factor γ_n is retrieved by inserting eq. (3.14) in eq.(3.13) and expresses as:

$$\gamma_n = \int_C A_n(\mathbf{R}) \cdot d\mathbf{R}, \quad (3.15)$$

where $A_n(\mathbf{R})$ is the Berry connection or Berry vector potential in analogy to electrodynamics with

$$A_n(\mathbf{R}) = i\langle\phi_n|\nabla_{\mathbf{R}}|\phi_n\rangle. \quad (3.16)$$

In general, the Berry connection is gauge dependent, indeed if we make a gauge transformation of the eigenstates

$$|\phi_n(\mathbf{R})\rangle \rightarrow e^{i\alpha_n(\mathbf{R})} |\phi_n(\mathbf{R})\rangle \quad (3.17)$$

3.2. The Berry phase, Berry curvature and emergent fields

where $\alpha_n : \mathbf{R} \rightarrow \mathbb{R}$ are arbitrary differentiable functions, thus the Berry connection transforms to

$$A_n(\mathbf{R}) \rightarrow A_n(\mathbf{R}) - \frac{\partial \alpha_n(\mathbf{R})}{\partial \mathbf{R}}. \quad (3.18)$$

Hence, the phase γ_n will change by $\alpha_n(\mathbf{R}(t = t_0)) - \alpha_n(\mathbf{R}(t = T))$, where $\mathbf{R}(t_0 = 0)$ and $\mathbf{R}(T)$ are the initial and final points of the path C in the parameter space. Fock (1928) concludes that it was possible to choose a path such that γ_n cancels out [184]. For this reason, the geometrical phase has been neglected in time-dependent theoretical treatments until Berry (1984) reconsidered the cyclic evolution case corresponding to a *close* path C , with $\mathbf{R}(0) = \mathbf{R}(T)$ [185]. This implies that

$$\alpha_n(\mathbf{R}(0)) - \alpha_n(\mathbf{R}(T)) = 2\pi \times \text{integer} \quad (3.19)$$

and shows that γ_n can not be removed. Therefore, the geometrical phase, also named Berry phase γ_n , becomes a gauge-invariant physical quantity under a close path (cyclic evolution) and is written

$$\gamma_n = \oint_C \mathbf{A}_n(\mathbf{R}) \cdot d\mathbf{R}. \quad (3.20)$$

If the parameter space is three-dimensional and by using Stokes theorem, then the path integral transforms into a surface integral, which defines the Berry curvature Ω_n in a vector form as

$$\Omega_n(\mathbf{R}) = \nabla_{\mathbf{R}} \times A_n(\mathbf{R}) \quad (3.21)$$

and

$$\gamma_n = \oint_C \mathbf{A}_n(\mathbf{R}) \cdot d\mathbf{R} = \int_S \Omega_n(\mathbf{R}) \cdot d\mathbf{S}. \quad (3.22)$$

The generalization of Berry curvature to an arbitrary-dimensional parameter space is given by anti-symmetric rank-2 gauge-field tensor $\Omega_{\mu\nu}^n(\mathbf{R})$

$$\Omega_{\mu\nu}^n(\mathbf{R}) = \frac{\partial}{\partial \mathbf{R}^\mu} A_\nu^n(\mathbf{R}) - \frac{\partial}{\partial \mathbf{R}^\nu} A_\mu^n(\mathbf{R}) \quad (3.23)$$

$$= i \left[\left\langle \frac{\partial \phi_n(\mathbf{R})}{\partial \mathbf{R}^\mu} \middle| \frac{\partial \phi_n(\mathbf{R})}{\partial \mathbf{R}^\nu} \right\rangle - (\nu \leftrightarrow \mu) \right] \quad (3.24)$$

which can also be written as a summation over the eigenstates:

$$\Omega_{\mu\nu}^n(\mathbf{R}) = i \sum_{n \neq m} \frac{\langle \phi_n | \frac{\partial \mathcal{H}}{\partial \mathbf{R}^\mu} | \phi_m \rangle \langle \phi_m | \frac{\partial \mathcal{H}}{\partial \mathbf{R}^\nu} | \phi_n \rangle - (\nu \leftrightarrow \mu)}{(\epsilon_n - \epsilon_m)^2}. \quad (3.25)$$

The Berry curvature (see eq. (3.21)) has a similar expression to a magnetic field and acts as a fictitious magnetic field. In that respect, the Berry phase in eq. (3.22) represents the Berry curvature flux.

3.2.2 Weyl nodes & magnetic monopole

The expression eq. (3.25) shows that the Berry curvature can become singular when the two energies ε_n and ε_m converge to the same value. This case corresponds to a monopole in the parameter space where the degenerated points act as sources and drains of the Berry curvature flux. Further details with their explicit derivation can be found in refs. [142, 186, 187]. In condensed matter physics, systems are described either in real space or reciprocal (momentum) space. In momentum space, Berry curvature monopole arises as Weyl nodes [188–190], where the strong spin-orbit coupling is present (see Fig. 3.5). For magnetism, this indicates the possibility of constructing real space emergent magnetic monopoles and is currently under active investigation. Magnetic monopoles have been reported in spin-ice systems [191, 192]. A skyrmion is also closely related to a magnetic monopole as it is the stereographic projection from a 3D Bloch sphere or hedgehog behaving as a magnetic monopole [193]. In 3D materials, the skyrmion lattice forms tubes. In the skyrmion tube arrangement, topological defects can appear at the junction of two tubes shown in Fig. 3.6a, and corresponds to an emergent magnetic monopole that can zip and unzip the skyrmion structure [141]. Beyond its fundamental interest in topological field theories [143, 194–196], these emergent topological magnetic structures offer appealing perspectives in spintronics [144]. Examples of non-trivial magnetic structures present in doped $\text{MnSi}_{1-x}\text{Ge}_x$ with their respective effective (emergent) magnetic field are illustrated in Fig. 3.7 [194].

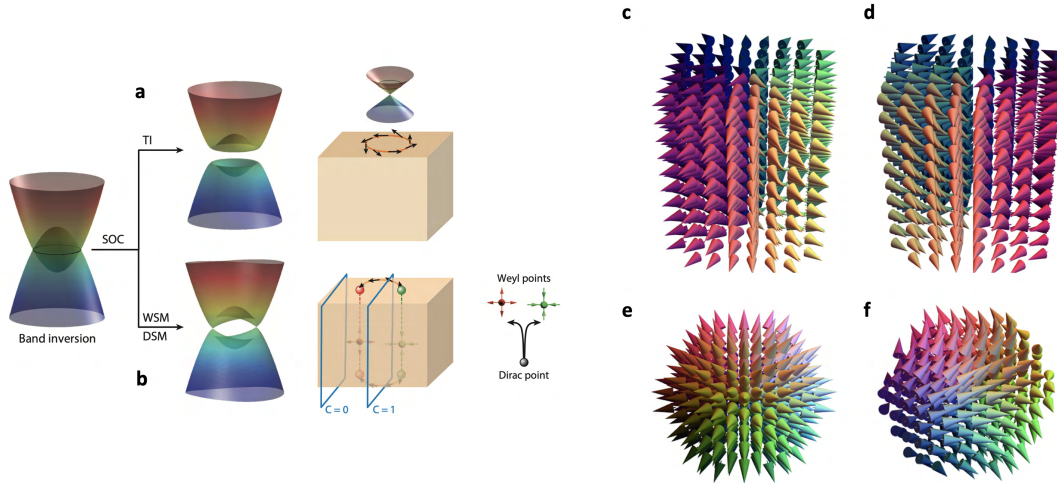


Figure 3.5 – **Emergent monopole of Berry curvature.** In reciprocal space, spin-orbit coupling leads to two cases in band inversion system: (a) a topological insulator and (b) Weyl and Dirac semimetal, where monopole and anti-monopole emerge at the band crossing points, image from [189]. Examples of singular vector fields are shown, namely (c) vortex and (d) anti-vortex. e and f spin distributions correspond to a hedgehog and anti-hedgehog, respectively, and are topologically non-trivial, image from [195].

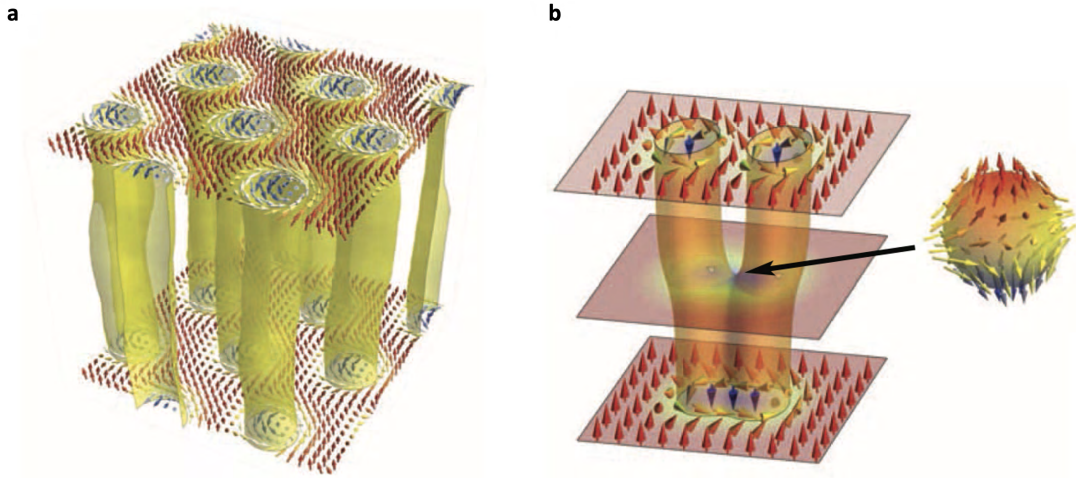


Figure 3.6 – **Anti-monopole as a zipper**. **a**: representation of the skyrmion tubes formed in 3D materials. **b**: A topological anti-monopole emerges at the interface of two merged skyrmion tubes. Image adapted from [141].

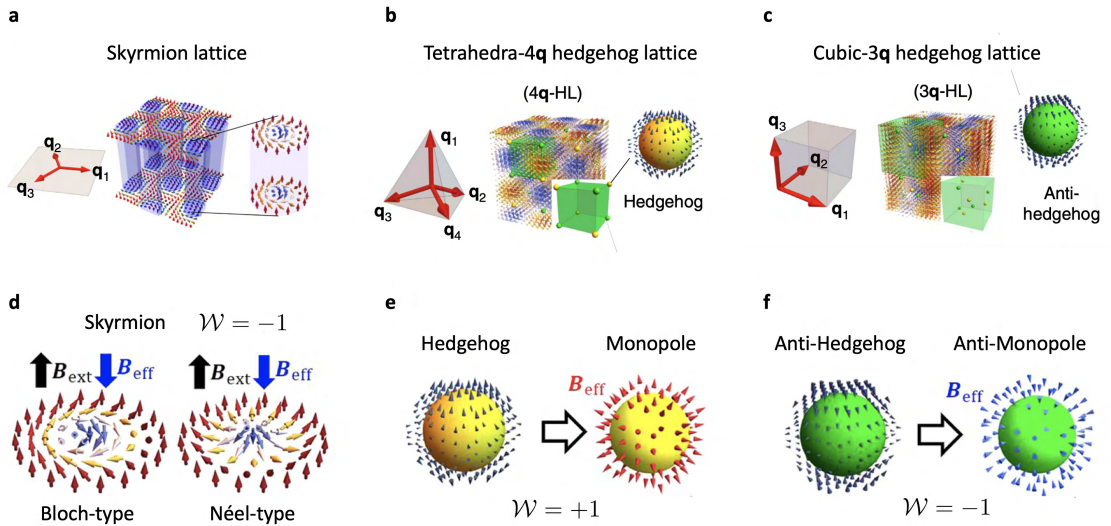


Figure 3.7 – **Effective magnetic field of different topological solitons**. **a**, **b**, and **c** show the three topological magnetic textures present in doped $\text{MnSi}_{1-x}\text{Ge}_x$ [194] with their corresponding \mathbf{q} -vectors describing the magnetic lattice. **d**, **e**, and **f** illustrate their corresponding effective field and winding number, adapted from [144].

3.2.3 Emergent electromagnetic fields

In this part, we derive the emergence of effective electromagnetic fields due to non-vanishing real space Berry curvature, felt by an itinerant electron. Note that the realization of a non-vanishing Berry curvature requires breaking either time-reversal symmetry, inversion sym-

metry, or both. As time-reversal symmetry implies $\Omega(-\mathbf{r}) = -\Omega(\mathbf{r})$, and inversion symmetry implies $\Omega(-\mathbf{r}) = \Omega(\mathbf{r})$, it is thus evident that at least one symmetry must be broken. This is typically realized in magnetic systems as time-reversal symmetry is broken.

Let us consider the simplest interaction model where the conduction electron's spin couples to the local non-uniform magnetization $\mathbf{m}(\mathbf{r}, t)$, which has a constant amplitude, i.e., $|\mathbf{m}(\mathbf{r}, t)| = 1$, and can point in any direction. In that case, we can write the Hamiltonian as:

$$\mathcal{H} = \left[\frac{\mathbf{p}^2}{2m_e} \mathbb{1} - J\boldsymbol{\mu} \cdot \mathbf{m}(\mathbf{r}, t) \right], \quad (3.26)$$

where the first term is the kinetic energy of the electron and the second term is its interaction with the local magnetic texture, $\mathbb{1}$ is the 2×2 identity matrix, $J > 0$ is the coupling constant, $\boldsymbol{\mu}$ the magnetic moment of the electron. For an electron of mass m_e , charge e and Landé factor g , the magnetic moment and the spin s are related by

$$\boldsymbol{\mu} = -\frac{ge}{2m} \mathbf{s} = -\frac{g\mu_B}{2} \boldsymbol{\sigma} \quad (3.27)$$

with μ_B the Bohr magneton and $\boldsymbol{\sigma}$ the vector of Pauli matrices.

The evolution of the system described by the wave function $|\Psi(t)\rangle$ is given by the time-dependent Schrödinger's equation and is written:

$$i\hbar \frac{\partial}{\partial t} |\Psi(\mathbf{r}, t)\rangle = \left[\frac{\mathbf{p}^2}{2m_e} \mathbb{1} - J\boldsymbol{\mu} \cdot \mathbf{m}(\mathbf{r}, t) \right] |\Psi(\mathbf{r}, t)\rangle. \quad (3.28)$$

To simplify the second term of the Hamiltonian, we can perform a local SU(2) gauge transformation $|\Psi(t)\rangle = U(\mathbf{r}, t)|\Phi(t)\rangle$, such as the local magnetization aligns parallel to a fixed axis (\hat{e}_z) sketched in Fig. 3.8. The second term becomes trivial as

$$J\boldsymbol{\mu} \cdot \mathbf{m}(\mathbf{r}, t) \xrightarrow{U(\mathbf{r}, t)} \tilde{J}\sigma_z, \quad (3.29)$$

with $\tilde{J} = Jg\mu_B(\hbar/2)$. The local transformation is given by the unitary operation U

$$U(\mathbf{r}, t) = \exp\left(-i\frac{\theta(\mathbf{r}, t)}{2}\sigma \cdot \hat{n}(\mathbf{r}, t)\right), \quad (3.30)$$

where $\hat{n}(\mathbf{r}, t) = \frac{\hat{e}_z \times \mathbf{m}(\mathbf{r}, t)}{|\hat{e}_z \times \mathbf{m}(\mathbf{r}, t)|}$ is the axis of rotation to align the magnetization along the arbitrary axis \hat{e}_z , and $\theta(\mathbf{r}, t) = \arccos(\mathbf{m}(\mathbf{r}, t) \cdot \hat{e}_z)$ the angle of rotation. Multiplying from the left by U^\dagger eq. (3.28), using $|\Psi(t)\rangle = U(\mathbf{r}, t)|\Phi(t)\rangle$, and dropping the explicit space and time notation, we obtain:

$$i\hbar \frac{\partial}{\partial t} |\Phi\rangle = \left[q^e V^e + \frac{(\mathbf{p}\mathbb{1} - q^e \mathbf{A})^2}{2m} + \tilde{J}\sigma_z \right] |\Phi\rangle \quad (3.31)$$

3.2. The Berry phase, Berry curvature and emergent fields

with the 2×2 matrices as the emergent scalar V^e and vector \mathbf{A}^e potentials, given by:

$$\begin{cases} \mathbf{A}^e = \frac{i\hbar}{q^e} U^\dagger \nabla U, \\ V^e = -\frac{i\hbar}{q^e} U^\dagger \partial_t U. \end{cases} \quad (3.32)$$

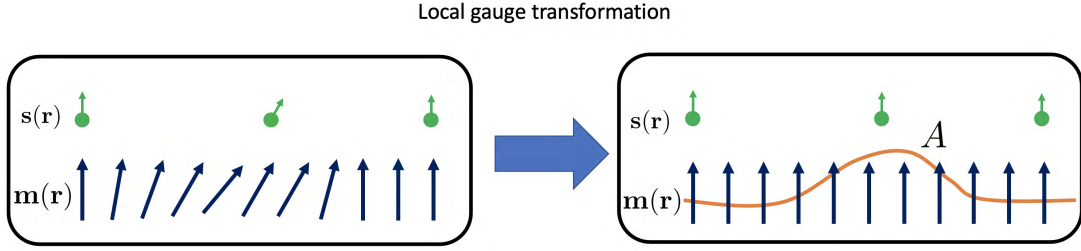


Figure 3.8 – Illustration of the local gauge transformation and potential vector.

For a magnetization texture that varies smoothly in space and time, we can treat the emergent scalar and vector potential as a perturbation of the unperturbed Hamiltonian $\mathcal{H}_0 = \frac{\mathbf{p}^2}{2m} + \tilde{j}\sigma_z$, describing two spin-up and two spin-down bands. In the adiabatic approximation, the emergent scalar and vector potential can be projected on these two spin bands and give the emergent electromagnetic potential

$$\begin{cases} \mathbf{A}_\sigma^e = \langle \sigma | \mathbf{A}^e | \sigma \rangle = \frac{i\hbar}{q^e} \langle \Psi_\sigma | \nabla | \Psi_\sigma \rangle, \\ V_\sigma^e = \langle \sigma | V^e | \sigma \rangle = -\frac{i\hbar}{q^e} \langle \Psi_\sigma | \partial_t | \Psi_\sigma \rangle \end{cases} \quad (3.33)$$

with $\sigma = \text{spin-up and spin-down}$ and $|\Psi_\sigma\rangle = U|\sigma\rangle$. We recognize the same form of the Berry connection introduced in eq. (3.16). Here, the real space Berry curvature acts as an emergent magnetic field, while mixed space-time Berry curvature acts like an emergent electric field, written respectively as:

$$\begin{cases} (\mathbf{B}_\sigma^e)_i = \nabla \times \mathbf{A}_\sigma^e = \mp \frac{\hbar}{2q^e} \frac{\varepsilon_{ijk}}{2} \mathbf{m} \cdot (\partial_j \mathbf{m} \times \partial_k \mathbf{m}), \\ (\mathbf{E}_\sigma^e)_i = -\nabla V_\sigma^e - \partial_t \mathbf{A}_\sigma^e = \mp \frac{\hbar}{2q^e} \mathbf{m} \cdot (\partial_i \mathbf{m} \times \partial_t \mathbf{m}) \end{cases} \quad (3.34)$$

where ε_{ijk} is the Levi-Civita symbol, the upper (lower) sign stands for spin-up and spin-down bands, and the subscript (i, j, k) denote the spatial coordinate (x, y, z) . As the sign of the Berry phase depends on the spin's orientation, we define the emergent charge $-1/2$ ($1/2$) for spin-up (spin-down) bands. Finally, we obtain the emergent (effective) magnetic and electric fields *felt*

by the conduction electron.

$$\begin{cases} \mathbf{B}_i^e = \frac{\hbar}{2} \varepsilon_{ijk} \mathbf{m} \cdot (\partial_j \mathbf{m} \times \partial_k \mathbf{m}), \\ \mathbf{E}_i^e = \hbar \mathbf{m} \cdot (\partial_i \mathbf{m} \times \partial_t \mathbf{m}) \end{cases} \quad (3.35)$$

In that model, we did not impose any restriction on the magnetic structure except its normalization for simplicity. Therefore any noncollinear magnetic texture that varies smoothly in space and time would lead to an emergent electromagnetic field.

3.2.4 Quantized emergent fields

Skyrmions are of particular interest as they ensure the topological quantization of the emergent fields since the skyrmion spin arrangement covers exactly one Bloch sphere represented by its winding number \mathcal{W} defined in eq. (3.1). Consequently, a skyrmion offers an ideal playground to study quantitatively emergent electromagnetic fields underlying the charge and magnetism interaction [154, 197]. Moreover, Abrikosov vortices in type-II superconductors also carry a quantized magnetic flux. Therefore, we can speculate that a skyrmion lattice would provide a real space simulation platform to investigate Abrikosov vortex dynamics that are more challenging to observe.

In analogy to the magnetic flux, the emergent magnetic flux is given by integrating the emergent magnetic fields within a magnetic unit cell (*MUC*)

$$\phi_0^e = \int_{MUC} \mathbf{B}^e \cdot d\mathbf{S} = 4\pi\hbar\mathcal{W} = \frac{2\pi\hbar}{|q^e|} \mathcal{W}, \quad (3.36)$$

which is quantized and proportional to the skyrmion winding number.

An emergent electric field arises only if the local magnetization varies in time. In this case, let us suppose the drift of a rigid magnetic texture at a constant drift velocity \mathbf{v}_d with $\mathbf{m}(\mathbf{r}, t) = \mathbf{m}(\mathbf{r} - \mathbf{v}_d t)$. The time derivative in eq. (3.35) becomes nonzero with $\partial_t \mathbf{m} = -(\mathbf{v}_d \cdot \nabla) \mathbf{m}$, producing an emergent electric field expressed

$$\mathbf{E}^e = -\mathbf{v}_d \times \mathbf{B}^e. \quad (3.37)$$

This relation reflects Faraday's induction law; a change in the magnetic flux produces an electric field. The effect of the emergent electric field in eq. (3.37) acts in opposition to the emergent magnetic field, reducing the Hall signal [154, 197]. For obtaining quantitative agreement with experiments, correction must be applied due to non-adiabatic processes and magnetic fluctuation background, etc.

To summarize, a conduction electron propagating through noncollinear and time-dependent magnetic texture experiences effective electromagnetic forces which emerge from the non-vanishing Berry curvature. In the case of topological magnetic texture, such as in a skyrmion

3.2. The Berry phase, Berry curvature and emergent fields

lattice, the emergent fields are quantized. The deflection that undergoes the electron gives rise to an additional Hall signal measured experimentally (see Fig. 3.9c,d) [154, 180, 198]. In addition, the electron through spin-transfer torque *pushes* the skyrmion in the opposite direction [181], both effects are depicted in Fig. 3.9a. Further details can be found in the refs. [169, 187, 199].

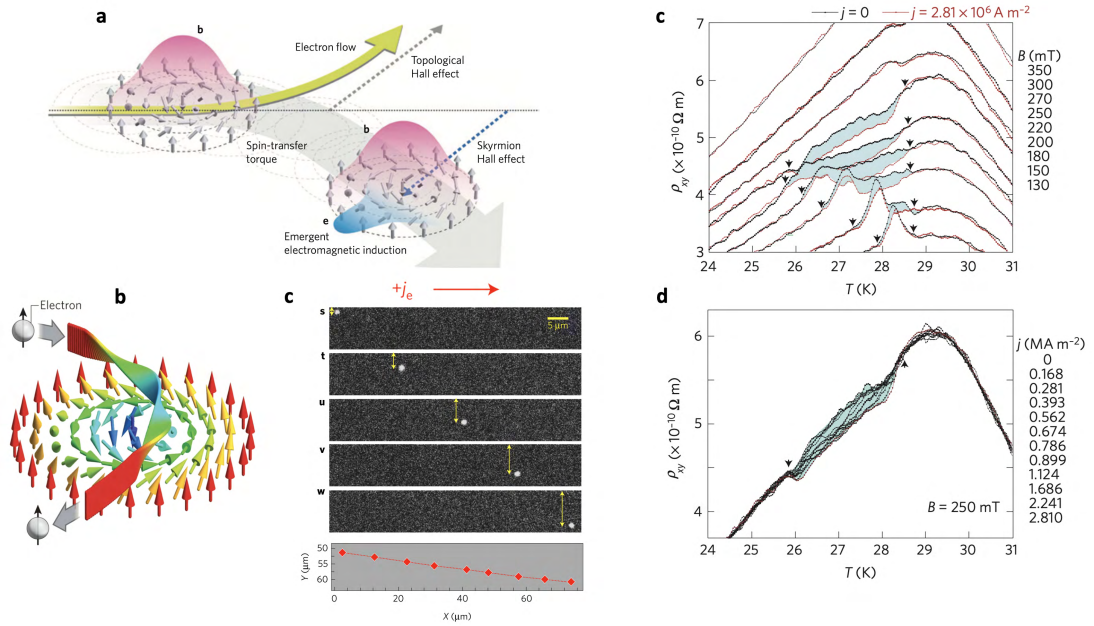


Figure 3.9 – **Topological and Skyrmion Hall effects due to emergent fields.** **a:** Sketch illustrating the deflection of the electron flow and the skyrmion. The pink (blue) area represents the emergent magnetic (electric) field. Image from [169]. **b:** The electron's spin constantly aligns to the local skyrmion magnetization and consequently picks a Berry phase. Image reproduced from [200]. **c:** Real space observation of the SHE using Magneto-Optical Kerr effect (MOKE) microscopy and a $+2.8 \times 10^6 \text{ A cm}^{-2}$ current density. Image from [182]. **c:** Topological Hall resistivity emerging in the Skyrmion phase of MnSi. **d:** Hall resistivity for different applied current densities. Image adapted from [154].

3.3 Quantum interferometry using topological magnetic field

Although beyond the scope of this thesis, here I propose an experiment using the skyrmion field to perform quantum interferometry of the electron wave function. Quantum interferometry (QI) is a powerful method to validate and test the foundation of quantum mechanics by confronting experiments with current theoretical models. Neutrons are broadly used to perform such experiments as it provides access to the four fundamental interactions [201]. In the seventies, a famous series of neutron interferometry experiments were undertaken to demonstrate the 4π -periodicity in Fermions, where an external magnetic field or the Earth's gravitational field was used to rotate the neutron's spin [202–206]. Recently, Danner *et al.* have demonstrated that the phase shift on the neutrons' wave function has a pure quantum origin [207]. Besides testing the fundamentals law of physics, quantum interferometry has been recently used to probe Bloch band topology in a graphene-type optical lattice [208] and is proposed to spot anyonic excitation [209]. Destructive quantum interferences, analog to the double-slit experiment, in the electron's wave function have been reported in scattering experiment [210], transport measurements within molecules [211] and were used to probe spin dynamics in semi-conductors [212]. However, to date, quantum interferometry using spinor properties of electron's spin has not been demonstrated. Indeed, the electron's wave function must have a 4π -symmetry under rotation in real space. As discussed in the previous sections, the conduction electron's spin that traverses a skyrmion undergoes exactly a 2π -rotation. Consequently, skyrmion field is a promising topological platform to test quantum interferometry on the electron's wave function. The question I propose to address is threefold:

1. Can we demonstrate the 4π -symmetry electron interferometry experiments using instead topological magnetic texture as the phase shift element of the electron's wave function?
2. How do the Topological and Skyrmion Hall effects relate to the anti-symmetric operation of the wave function followed by a 2π -rotation?
3. What about bosonic QI such as magnon QI?

While the two first questions can be addressed in metallic skyrmion host materials, the third requires the use of an insulating skyrmion host material, where magnon currents and Topological magnon hall effect have been reported [213–215]. Bloch-type skyrmions exist in the Mott insulator Cu_2OSeO_3 [172], as this type of skyrmions have in-plane magnetization, it is therefore possible to visualize them using Lorentz-Transmission electron microscopy. The next Chapter introduces some intriguing properties and observation of the multiferroic Cu_2OSeO_3 , that will be under investigation upon ultrafast photo-excitation and discussed in Chapter 4 and Chapter 5.

4 Light-induced topological phase transition in the multiferroic Cu_2OSeO_3

Multiferroics are fascinating materials that possess coexisting ferroic phases. This unique property is exciting as it allows to control the magnetic order using electric fields without heat dissipation, as multiferroics are insulators. Combining topology and multiferroic orders breaks ground for many novel intriguing effects. In such systems, out-of-equilibrium phenomena are expected to give spectacular responses as the ultrafast excitation has the ability to favor one degree of freedom in the complex intertwined electronic, magnetic, and structural interactions, thus reshaping the energy landscape. Here we use single near-infrared (NIR) femtosecond laser pulses to drive a distinctly nonequilibrium topological phase transition: creating a skyrmion crystal in the Mott insulator Cu_2OSeO_3 at exceptionally low magnetic field values (lower values than we find is possible through an adiabatic field-cooling protocol). Due to their real space topological properties, magnetic skyrmions are of great interest for both fundamental science and future technological applications. The generation of skyrmions was recently demonstrated in metallic skyrmion-hosting materials using electrical current pulses [216] or laser pulses [217, 218]. In these previous studies, thermal effects were shown to be the primary driving mechanism where metallicity plays an important role. However, insulating multiferroic materials offer an intriguing option for potentially more direct and energy-efficient control. A natural question arises: can we induce a skyrmion phase in an insulator by femtosecond light pulses, which provide the fastest way for modifying the magnetic state? In this chapter, we address this unsolved fundamental question by demonstrating the photo-creation of a skyrmion crystal using a single NIR femtosecond laser pulse far below the bandgap of the insulating material Cu_2OSeO_3 , where the light absorption is very low. The new photo-induced skyrmion phase exists at a lower critical magnetic field than is required to stabilize the equilibrium skyrmion phase. In other words, this phase cannot be generated adiabatically, and its creation requires a brief nonequilibrium excitation which we accomplish through an ultrashort NIR laser pulse. The long lifetime of this nonequilibrium skyrmion phase and the fact that it is achieved through optical control demonstrates the significant relevance of our discovery for future device physics. Finally, we report a strong dependence of this nonequilibrium photo-creation process on the photon energy used to drive the excitation. We can understand this wavelength dependence and the mechanism behind the photo-creation process by a phonon-mediated mechanism and

support this with atomistic spin calculations. To visualize this phase, we generate high-quality magnetic images with extraordinary spatial resolution in a transmission electron microscope operated in cryo-Lorenz force mode. We send femtosecond NIR laser pulses to excite the samples directly into the microscope. This experimental configuration is unique. Only five such experimental setups in the world exist to date: Göttingen, Lawrence Berkeley National Lab, Technion, Stockholm, and our microscope. The ultrafast generation of skyrmions at low magnetic fields has important applications in future computing schemes (e.g., non-volatile artificial synapses for neuromorphic computing, see [159]). More broadly, this work can significantly contribute to the current understanding and utilization of out-of-equilibrium phenomena and topological phase transitions.

The content of this Chapter is an extension from the preprint, "Observation of a new light-induced skyrmion phase in the Mott insulator Cu_2OSeO_3 " by A. A. Sapozhnik*, B. Truc*, P. Tengdin*, E. V. Boström, T. Schönenberger, S. Gargiulo, I. Madan, T. LaGrange, A. Magrez, C. Verdozzi, A. Rubio, H. M. Rønnow, F. Carbone, arXiv:2212.07878 [219]. *These authors have equally contributed.

Contribution

I contributed to this work by participating in all the experimental aspects. From the laser beam line installation to the data acquisition. The experimental investigation was carried out along with A. A. Sapozhnik and P. Tengdin. I helped processing, analyzing and interpreting the data. A. A. Sapozhnik compiled the photocreation data, while I compiled and developed a Matlab code to analyze the magnetic order dynamics observed (not presented in the arXiv preprint). I. Madan and T. LaGrange gave experimental support. For the theory, atomistic spin calculations were performed by E. V. Boström, a collaboration with A. Rubio and C. Verdozzi. Simulation of the thermal load response was performed by S. Gargiulo. The TEM lamellae were provided by T. Schönenberger, and the crystals are grown by A. Magrez. F. Carbone supervised this work.

4.1 When multiferroicity meets topology

Materials can exhibit *ferroic* phase, which is the generic term to designate ferromagnetic, ferroelectric, ferroelastic, and, more generally, their *anti* counterpart. For example, antiferroelectrics are materials that have ordered electric polarization, which exactly cancels out within the crystallographic unit cell. Note that metallicity destroys ferroelectricity as an electric field is not allowed in bulk. Thence, multiferroics have an insulating nature. These phases appear spontaneously below a critical temperature where some symmetries break. Indeed, magnetic ordering breaks time-reversal symmetry, while ferroelectricity requires the breakdown of spatial inversion symmetry, and broken rotational symmetry leads to ferroelasticity (see Fig. 4.1). Notably, in some materials, more than one ferroic property can coexist in the same phase giving birth to intriguing inter-coupled effects depicted in Fig. 4.1a. For instance,

the piezoelectric effect is the induction of an electric polarization when stress is applied to the multiferroic material. This phenomenon and its inverse effect are widely used today for converting sound waves into electrical impulsion or in speaker technology, respectively. Development in multiferroic systems as functional materials is an active field of research as they hold promises for a large variety of technological applications [220], ranging from clean-energy harvesting [221–224], targeted drug delivery in biomedical application [225], energy-efficient device physics [226, 227] and dark matter detection [228]. Moreover, multiferroics offer the unique possibility to study the combination of different types of symmetry breaking. Remarkably, this allows investigating at the laboratory scale fundamental processes in cosmology and high-energy physics where similar space/time symmetries properties are observed [229].

The magnetoelectric effect is of particular interest in future data storage technology. It combines miniaturization and enables electric field-controlled magnetic states with low-energy consumption as heat dissipation is drastically reduced. Designing materials that possess both ferromagnetism and ferroelectricity is a challenging task. Indeed, this requires a fundamental understanding of the coexistence of the two orders in the same phase and advanced growth and characterization techniques. For these reasons, many theoretical and experimental studies have been conducted since the beginning of this Millennium which has led to veritable breakthroughs [220, 230–236]. Furthermore, with the recent development of femtosecond lasers, optical manipulation of the spontaneous magnetization and polarization orders have become possible, giving even more appealing prospects as it paves the way for ultrafast control [237, 238]. This period is sometimes called the "Renaissance of Magnetoelectric Multiferroics" [239]. At the same time, spontaneous topological magnetization has been demonstrated with the discovery of skyrmions in a B20 crystal structure compound [138]. Due to their topological properties, skyrmions can be efficiently controlled using electrical and spin currents (see Chapter 3). Since then, physicists have wondered about the possibility of having such material in which topological magnetic properties would coexist with electric polarization, thus, combining topological character and multiferroic properties advantages in a single system. For example, in that system, magnetic skyrmion would exist and carry an electric dipole. Consequently, we could control skyrmion with an electric field rather than an electrical current taking advantage of the insulating character of multiferroics, thus opening the perspective for ultra-low consumption devices. Cu_2OSeO_3 is a good candidate, as it belongs to the B20 compound family, and spontaneous magnetization along with magnetoelectric effect have been reported [240–242]. In 2012, a Japanese team made the breakthrough and reported the discovery of Bloch-type skyrmion along with spontaneous electric polarization in the multiferroic Cu_2OSeO_3 [172] (see Fig. 4.3).

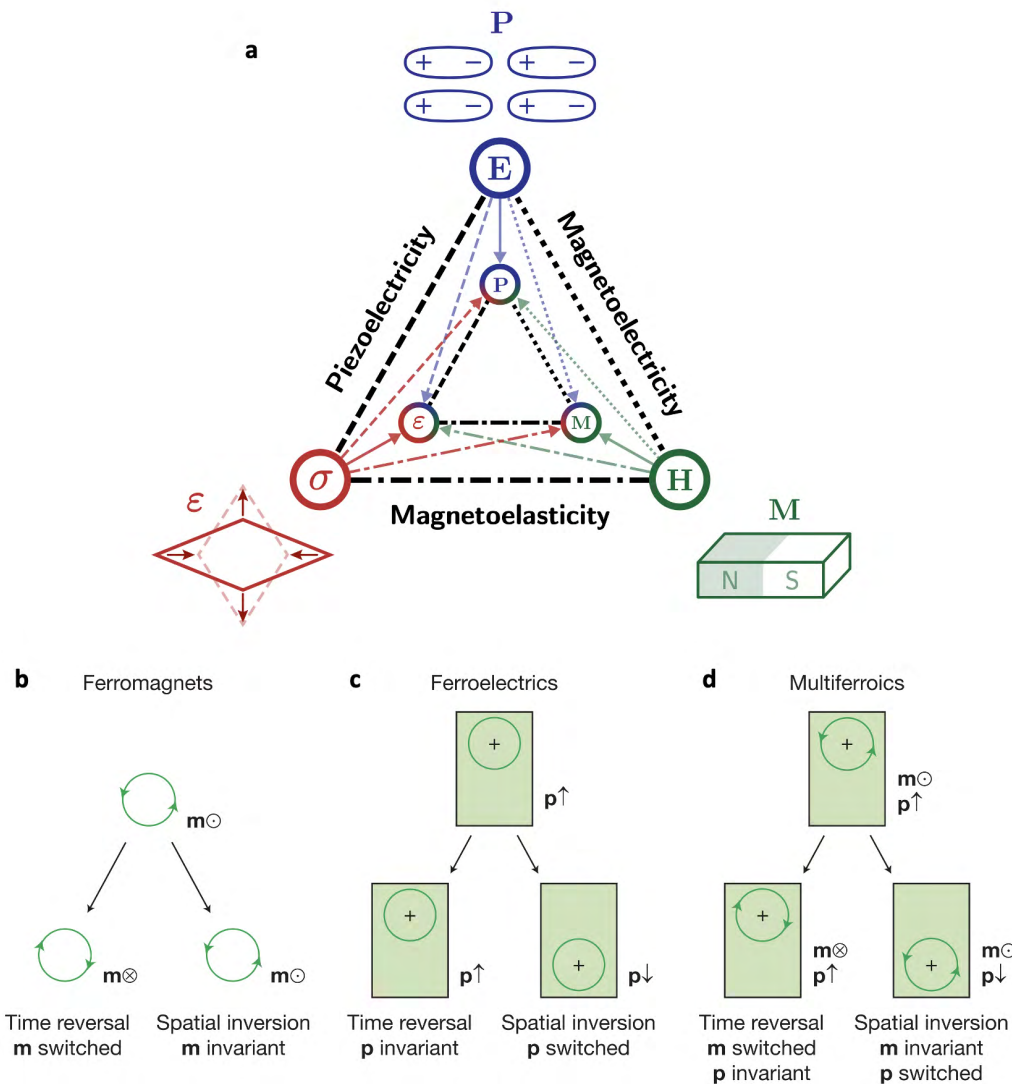


Figure 4.1 – **Time reversal and spatial inversion broken symmetries in multiferroics.** **a:** Representation of the different possible interactions between the external parameter and their corresponding response giving rise to piezoelectric, magnetoelectric and magnetoelastic effects. External parameters are stress (σ), electric field (E) and magnetic field (H) and their associated linear response the strain (ϵ), electric polarization (P) and magnetization (M), respectively. **b:** Local magnetic moment is classically equivalent to circular electrical current flowing clockwise or anti-clockwise depending on the direction of the magnetic moment. Reversing time leads to the current flowing in the opposite direction, thus inverting the magnetic moment direction. **c:** Displacing the charge density localization by inverting its spatial coordinate induces a sign change in the electric dipole moment. **d:** In multiferroics possessing spontaneous magnetization and electric polarization, both symmetries illustrated in **b** and **c** are broken. Note that ferroelasticity breaks rotational symmetry, which is not represented here. Illustration **a** was realized by A. Galan. Images **b-d** are reproduced from [232].

4.2 History and properties of Cu_2OSeO_3

Copper oxide selenide was first synthesized in 1976 by Meunier, and Bertaud [240] and has $P2_13$ cubic structure as the other B20 compounds presented in Fig. 4.2c. Shortly after, Kohn reported a spontaneous magnetization below 59 K and showed that Cu_2OSeO_3 is ferrimagnetic at low-temperature with 0.5 Bohr magneton per Cu ion [241]. He also suggested the possible presence of a magnetoelectric effect as the system lacks an inversion center, which consequently allows such an effect by symmetry. Unlike most of the discovered multiferroic materials, Cu_2OSeO_3 does not undergo any reduction in the symmetry group and remains metrically cubic as proven by high-resolution x-ray experiment down to 10 K [242]. However, below the Curie temperature, the magnetic space group has to undergo a symmetry lowering as ferromagnetic/ferrimagnetic orders are not allowed in a cubic magnetic space group. It transforms to the sub-space group $R3$ [242]. The magnetic model proposed and supported by the neutron diffraction experiment consists of four Cu_4 triplet tetrahedra embedded in the cubic unit cell, forming a distorted pyrochlore structure. Each unit has three spin-1/2 from the Cu^{2+} ion ferromagnetically aligned and one anti-ferromagnetically aligned illustrated in Fig. 4.4a. This specific magnetic arrangement, as well as the absence of reduction of symmetry lowering, were further supported by various techniques, including nuclear, electron, and muon spin resonances [243–246], as well as far-infrared [247], and Raman optical [248] studies. Consequently, Cu_2OSeO_3 possesses the unique properties to allow piezoelectric, linear magnetoelectric, and piezomagnetic coupling. Furthermore, in a multiferroic material which breaks spatial inversion and time-reversal symmetry such as in magnetic chiral material like Cu_2OSeO_3 , magnetochiral effect can appear and the phonon magnetochiral effect has been recently demonstrated [249].

In 2012, Seki *et al.* reported the discovery of Bloch-type skyrmions in Cu_2OSeO_3 (see Fig. 4.3) along with spontaneous electric polarization, in the same phase [172]. The only one known to date multiferroic skyrmion host material. Since this major discovery, in addition to the existing extensive investigations on the ferrimagnetic ground state, ensues a detailed magnetic [246, 251, 253, 254] and electronic [255, 256] characterization exploiting different multiferroic effects such as the magneto-optical susceptibility [256]. Moreover, the breakthrough has opened new horizons to investigate and control topological magnetic objects. In particular, the abovementioned electric-field skyrmion control has been demonstrated [14, 257–259] and has inspired new theoretical development in the characterization of skyrmion using the magnetoelectric effect [260]. Before diving into the light-induced skyrmion demonstration, we must understand the microscopic quantum nature of Cu_2OSeO_3 from which the skyrmion phase originates and its multiferroic properties, covered in the next part.

4.2.1 Quantum nature and origin of the ferroelectricity

Cu_2OSeO_3 is a Mott insulator with an electronic bandgap of ~ 2.3 eV (~ 539 nm), around 1.5 eV lie the electronic crystal field excitations, detected in the optical conductivity in Fig. 4.4e.

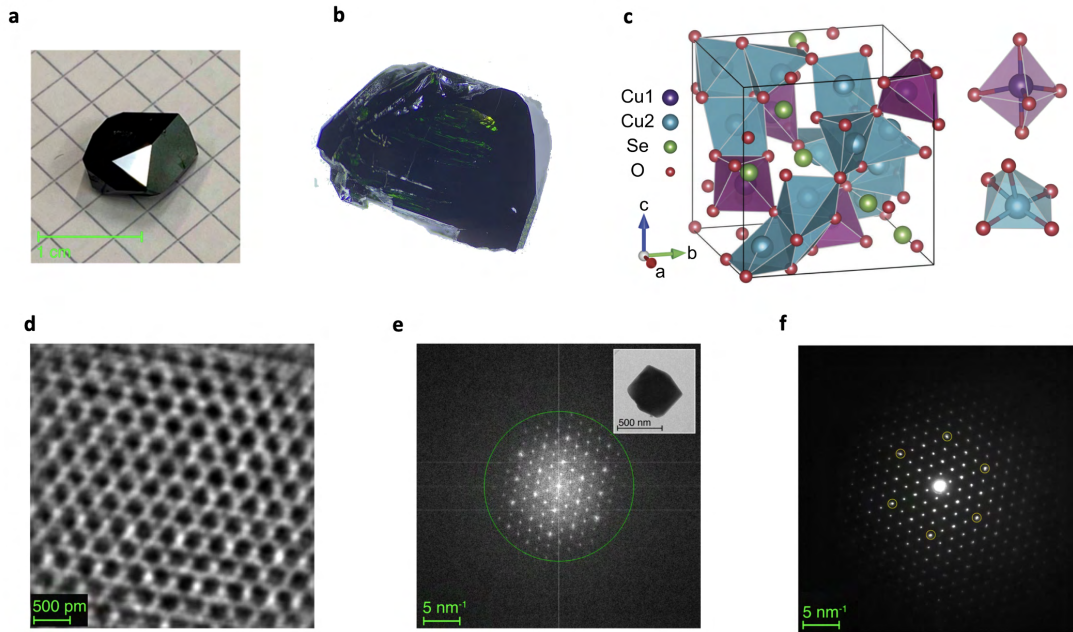


Figure 4.2 – Cu_2OSeO_3 crystal structure. **a** and **b**: Typical Cu_2OSeO_3 single crystals grown at EPFL using chemical vapor deposition. The crystal size varies from a few mm^3 to one cm^3 for the largest, ideal for neutron studies. During the growth, specific crystal planes such as the (111) plane crystallize preferably. This is nicely observable in the crystal **a** (triangular facet). Note also the dark green reflection visible on crystal **b** characteristic of the ~ 2.3 eV (~ 539 nm) bandgap. **c**: Representation of the Cu_2OSeO_3 cubic crystal structure with $P2_13$ space group, with a lattice constant $a = 8.925 \text{ \AA}$ at ambient conditions [250]. Micrograph **d** shows an high-resolution transmission electron microscopy (HRTEM) image of the Cu_2OSeO_3 probed along the [111] zone axis. Its corresponding Fast Fourier Transform (FFT) pattern is presented in **e**. **f**: selected area electron diffraction (SAED) pattern of the same crystallite shows the single crystal's excellent crystallinity. Images **a** and **d-f** are taken from [251], **c** from [252].

Charge transfer excitations starts above ~ 2.3 eV and peaks at 3.2 eV and 4.0 eV [256]. The complex magnetic phase diagram emerges from the effective magnetic moment carried by each Cu_4 tetrahedra unit rather than individual Cu spins. Four rigid, highly entangled, and weakly coupled Cu_4 clusters are embedded in a cubic unit cell depicted in Fig. 4.4a,c [246, 262]. In the ferrimagnetic ground state, two kinds of Cu^{2+} ions are distinguished. Cu-I are ferromagnetically aligned and possess spin-up configuration, while Cu-II has spin-down and is antiferromagnetically aligned with respect to the Cu-I spins. The different exchange couplings have been computed using density functional theory (DFT), including the Colomb interaction [255]. Five relevant, effective spin exchanges J are identified with opposite signs and represented in Fig. 4.4c. The superexchange interaction between Cu-I sites is ferromagnetic with $J_1 = -1.132$ meV and $J_3 = -3.693$ meV, while the couplings between Cu-I and Cu-II have

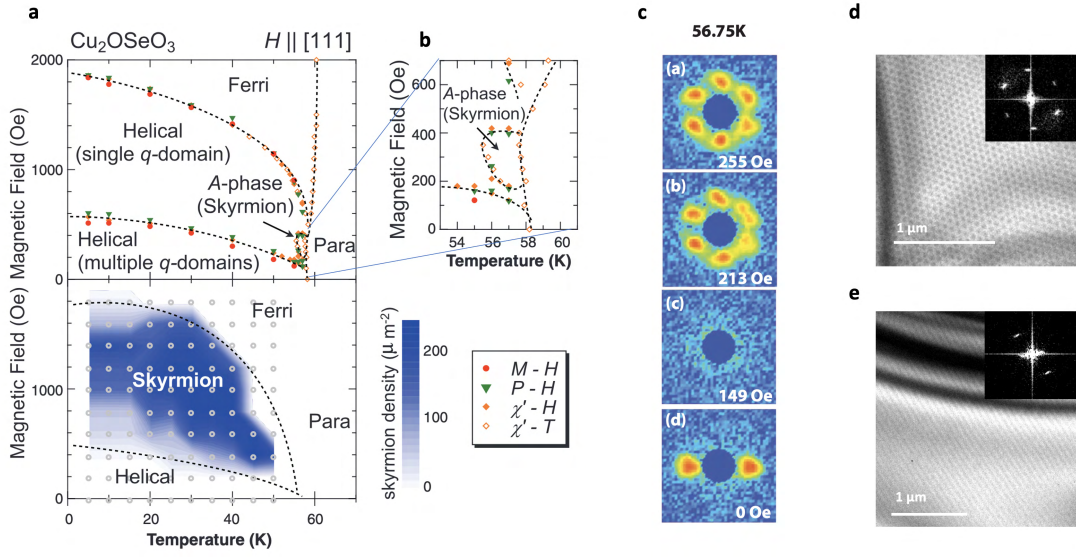


Figure 4.3 – **Magnetic skyrmion in Cu_2OSeO_3 .** **a:** Magnetic phase diagram of the Cu_2OSeO_3 compound measured by electric polarizability, magnetic susceptibility, and real space imaging techniques [172]. **b:** Zoom in on the newly discovered skyrmion phase in bulk Cu_2OSeO_3 . **c:** Example of small-angle neutron scattering (SANS) profiles; (a) and (b) in the skyrmion phase showing a distinctive six-fold symmetry and (d) in the helical phase at zero field [253], where only two-fold symmetry is observed. **d** and **e** show real space LTEM images taken in our laboratory at 5 K in the skyrmion and helical phases, respectively. Each black *dot* is a skyrmion. The inset corresponds to the FFT of the image.

antiferromagnetic nature with positive exchange constants 6.534 meV, 0.900 meV for J_2 , J_4 , respectively. The only relevant super-superexchange interaction is between the Cu-I and Cu-II inter-cluster at a distance of 6.35 Å with $J_5 = 0.984$ meV. This peculiar atomic arrangement gives birth to a spectacular DMI where the $|D_4/J_4|$ ratio is 1.95, much larger than in other materials [255, 263]. This model is in excellent agreement with experimental data. Furthermore, it successfully reproduces the complex emergent magnetic behavior of Cu_2OSeO_3 existing on the nanometres scale [264]. Regarding the ferroelectricity origin, Seki *et al.* invoked the spin-dependent $d-p$ hybridization model of the Copper and Oxygen orbitals, already used to describe the ferroelectricity in $\text{Ba}_2\text{XGe}_2\text{O}_7$ ($X = \text{Mn}, \text{Co}, \text{Cu}$) family [265]. The microscopic model originating from spin-orbit coupling (SOC) catches the main polarization features as well as the complex sign change (see Fig. 4.5d) and agrees roughly with experimental value [255]. Hence, the relativistic SOC effect is responsible for the multiferroic nature in Cu_2OSeO_3 , where it induces an electric polarization in the presence of magnetic order. From the model, Yang *et al.* computed the electric polarization and charge distribution within a single skyrmion as shown in Fig. 4.5. It suggests that each skyrmion carries an electric dipole or quadrupole, allowing skyrmion manipulation using electric fields.

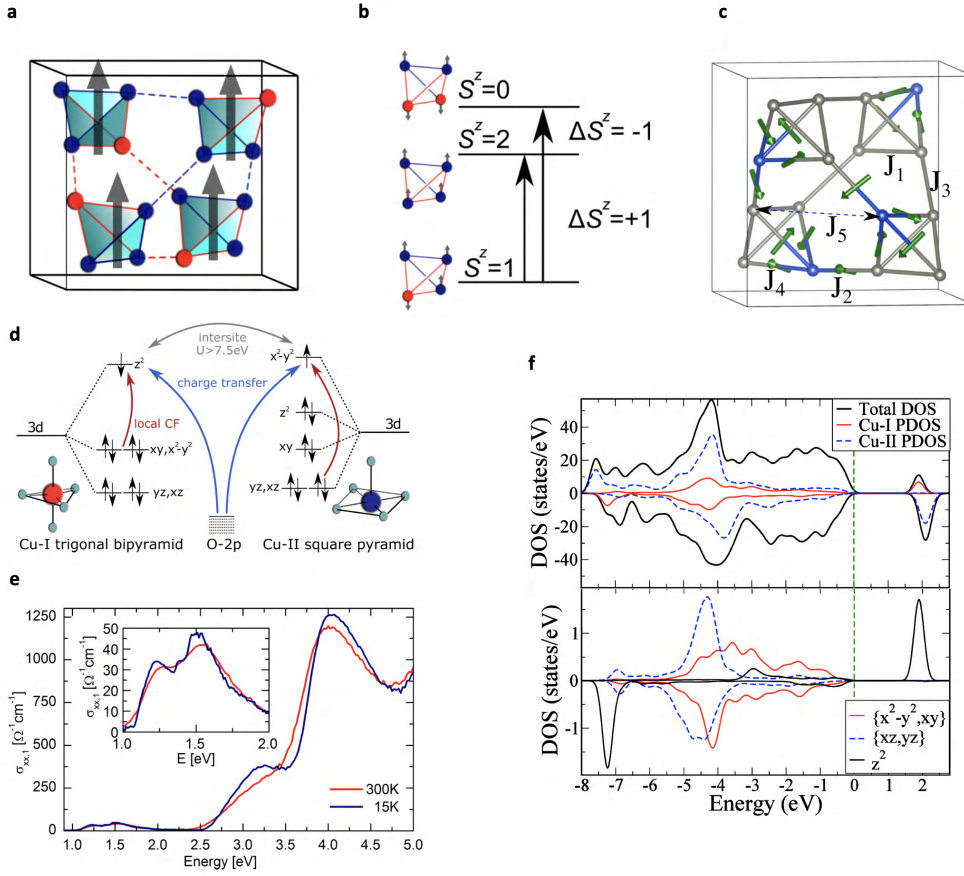


Figure 4.4 – **Effective magnetic moment and electronic excitation in Cu_2OSeO_3 .** For clarity, only the Copper atoms are represented in the cubic unit cell. **a:** The magnetic moments with $S = 1/2$ are localized on two kind of Copper ions. Three Cu-I align ferromagnetically, while the spin of Cu-II has an antiferromagnetic exchange, giving the ferrimagnetic nature. The spin arrangement in the distorted pyrochlore structure, blue (red) corresponds to spin-up (spin-down), approximated by an effective magnetic moment (black arrow). The solid blue (red) lines show the strong (anti)ferromagnetic exchange within the Cu_4 tetrahedra. The dashed blue (red) lines show the weak (anti)ferromagnetic inter-cluster interaction. The longer-range super-superexchange between Cu-I and Cu-II is not illustrated here. **b:** Sketch of the energy levels and total S^z moment associated to possible spin-flip configurations. **c:** The green arrows show the DMI vectors between the Cu ions and the different exchange interactions relevant. J_1 and J_3 are ferromagnetic, while the superexchange interactions J_2 and J_4 are antiferromagnetic. J_5 is positive. Thus, the interaction between the Cu-I and Cu-II inter-cluster is antiferromagnetic. In this drawing, grey (blue) balls represent Cu-I (Cu-II) atoms. **d:** Sketch of different possible electronic excitations. Crystal field excitations lie around 1.5 eV, while charge transfer starts above 2 eV and peaks at 3.2 eV and 4.0 eV as demonstrated by the optical conductivity in **e**. **f** shows the density of state retrieved from Generalized gradient approximation + U (GGA+U) calculation for the two different kinds of Cu ions present in the unit cell [255]. The bottom panel shows the orbital contribution for the Cu-I type. Images reproduced from [255, 256, 261].

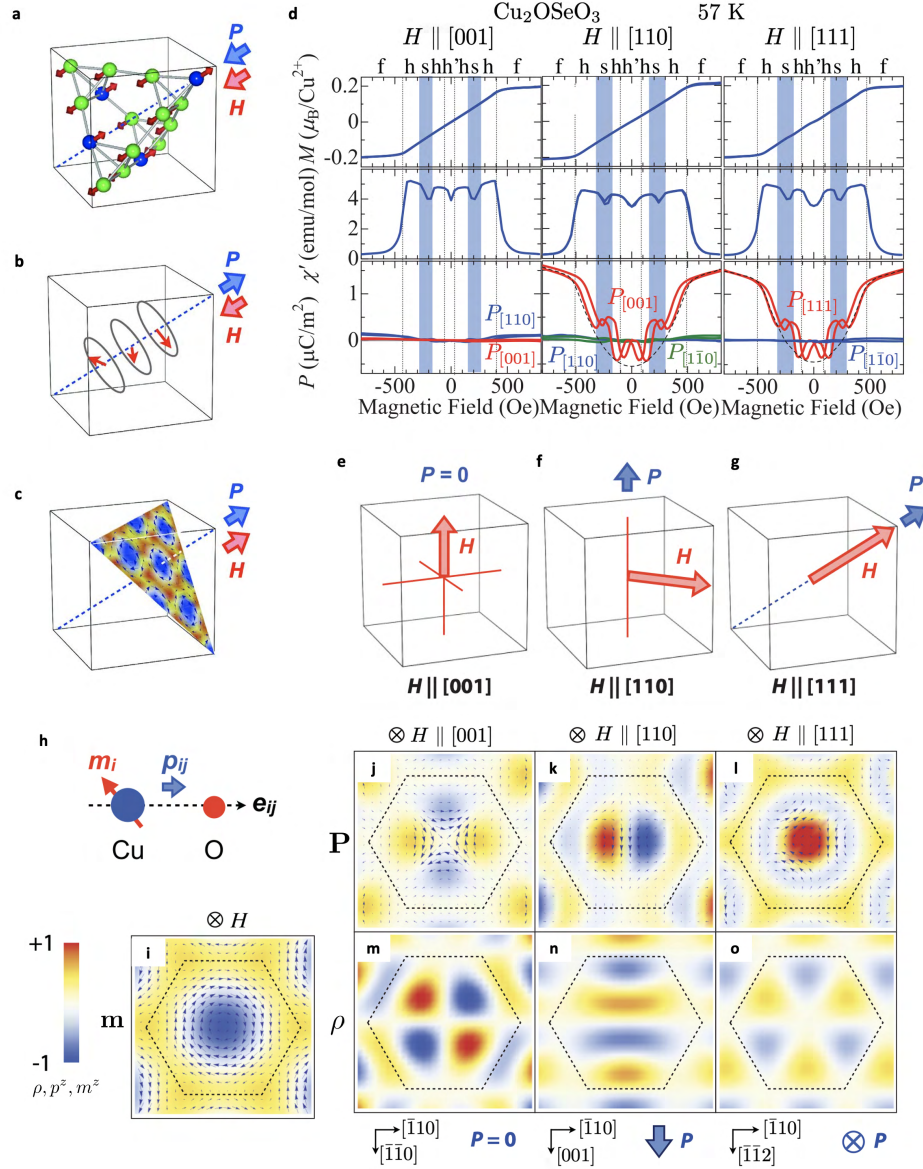


Figure 4.5 – **Magnetically induced electric dipole and quadrupole polarization in Cu_2OSeO_3 .** **a-c:** Representation of the electric polarization \mathbf{P} direction under an external applied magnetic field \mathbf{H} in the ferrimagnetic, helical, and skyrmion phases, respectively. **d** shows the magnetization, ac magnetic susceptibility, and electric polarization magnetic field dependence along different crystallographic directions. The dashed lines show the theoretical prediction of the electric polarization obtained from the $d-p$ hybridization model. **e-g:** Prediction of the magnetically induced electric polarization \mathbf{P} according to the $d-p$ hybridization model and symmetry argument. **h:** The magnetic moment is localized on the Cu at site i , while the electric dipole p_{ij} arises from $d-p$ hybridization between the Copper and the Oxygen at site j orbitals. **i:** Vector field of the magnetization of a Bloch-type skyrmion and (**j-o**) the corresponding electric polarization field (top panels) and spatial charge distribution (bottom panels) under different external field direction. Images reproduced from [172, 266].

4.2.2 Magnetic phase diagram & the skyrmion phase

Beyond its ferroelectric properties, the magnetic phase diagram of Cu_2OSeO_3 has been recently under intense investigation. Indeed, although sharing similar magnetic features with the original B20 skyrmion-host compound MnSi, as the stabilization of the skyrmion phase by thermal fluctuation, and the existence of a helical and conical phases, it turns out that applying the field along different high axes symmetry reveals novel magnetic phases and scaling properties [171, 267, 268]. Moreover, Cu_2OSeO_3 magnetic phase diagram can be manipulated by other means such as electric fields [258] only possible in a multiferroic compound.

In bulk Cu_2OSeO_3 , the skyrmion phase only exists in a narrow pocket of a few kelvins (~ 56 - 59 K) and tens of millitesla (~ 20 - 50 mT) as shown in the phase diagram in Fig. 4.3a. Controlling the magnetic ground state using external parameters is thus essential as it opens broader skyrmion regions and gives insight into the underlying magnetic and electronic interactions. While chemical doping leads to the generation of a second skyrmion phase and the shrinking of the initial one [269], applying pressure turns out to be beneficial for the stabilization of the skyrmion phase [270, 271], where skyrmion signature reached room-temperature [272]. In addition to controlling the skyrmion crystal orientation [257], the electric field modifies the magnetic energy landscape, reducing or enlarging the skyrmion pocket [273]. The corresponding modification of the magnetic phase diagram are summarized in Fig. 4.6. Without involving external parameters, the question of size-effect and geometrical effect has been recently addressed; in particular, skyrmion does not exist below 300 nm nano crystal [274], while in thin lamella the skyrmion pocket is modified [172, 268] and reciprocal space tomography has revealed a transformation from Néel-type to Bloch-type skyrmion at the surface [275].

Due to the Mott character, disorder effects and the emergent magnetism involved, theoretical and computational studies are challenging. From one side the atomistic spin calculations allowing a true microscopic investigation relies on the study of only one to few skyrmion units, as it becomes too computationally expensive. From the other side, micromagnetic simulation can capture the large size of a skyrmion crystal and its collective behavior. However, it completely neglect any atomic effect as it is construct on the continuum approximation. Nevertheless, more theoretical studies are anticipated as DFT and mean-field approach is an effective trade-off to approach the skyrmion physics [264] and more generally the multiferroics properties in Cu_2OSeO_3 . Including a complete picture of out-of-equilibrium phenomena is currently nearly impossible as the simulation must capture dynamical effects spanning ten order of magnitude (see below in section 4.3.2).

In the meantime, a more phenomenological approach have been undertaken to understand the nature of the Cu_2OSeO_3 magnetic phase diagram and its (topological) phase transitions underlying fundamental interactions at the microscopic and mesoscopic scales. In particular, further investigations have revealed new phases [171, 267, 276] at low-temperature where magnetic anisotropy interactions become relevant. Additionally, the vast complexity of the skyrmion phase diagram allows us to investigate topological phase transition, as the helical and

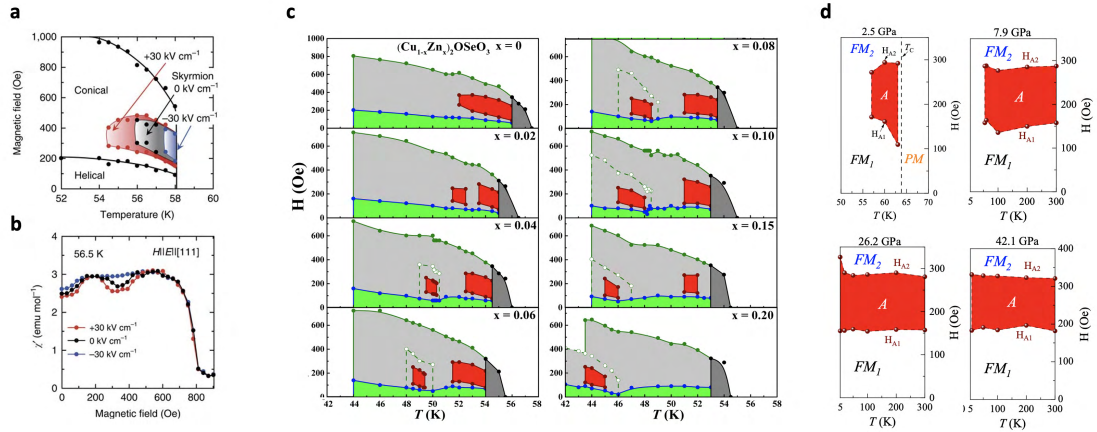


Figure 4.6 – **Tuning the magnetic skyrmion pocket.** Controlling the range in the temperature-magnetic field space in which skyrmions exist at equilibrium has been recently achieved. Using different external parameters, the intrinsic properties of Cu_2OSeO_3 change leading to distinct magnetic phase diagrams. In particular, the phase diagram under external (a) electric field [273], (c) chemical doping [269] and (d) pressure [272] have been studied. b: Example of the change in the magnetic susceptibility response under the presence of an electric field [273]. The red area corresponds to the skyrmion phase in c and d.

conical phase are topologically trivial. Specifically, Topological melting of the skyrmion crystal leads to an intermediate hexatic phase [155], while strong dissipation processes have been spotted close to the TPT from the skyrmion phase to the other topologically trivial magnetic phases [277]. The first evidence of the Kibble–Zurek mechanism has been recently reported suggesting that Cu_2OSeO_3 belongs to the Kibble-Zurek universality class [278]. Nevertheless, many open questions remain to be addressed theoretically and experimentally, as the origin of the strong dissipation remains unclear and new effects have been identified in this work discussed in Chapter 6.

Cu_2OSeO_3 is a quantum material par excellence to study in a single system multiferrocity and topology. While the magnetic phase diagram and the topological phase transition has been broadly investigated in thermodynamic equilibrium, the manipulation of the magnetic order using light remains to be explored. Manipulation of magnetic orders using laser excitation is particularly appealing as it breaks ground for ultrafast control [279]. The skyrmion photo-creation using femtosecond laser pulses have been recently demonstrated in our laboratory with the B20 FeGe compound [217] and in a multilayered system where the nucleation occurs on few hundreds of ps [218]. Both studied considered metallic materials and the skyrmion creation was attributed to laser-induced heat effect providing an upper limit for ultrafast skyrmion generation. Such limitation can be overcome in an insulating material, as non-thermal process can be easily triggered by tuning the photon energy. In this Chapter, we investigated the possibility of photo-inducing a topological phase transition in the multiferroic insulating Cu_2OSeO_3 compound. We reported the skyrmion photo-creation for

three different photon energies both above and below the optical bandgap of 2.3 eV triggering distinct possible excitations. The NIR with 1200 nm (1.03 eV) the lowest photon energy tested provide the most efficient way to generate a skyrmion phase and corresponds to the lowest value known reported. The newly photo-induced state differs from the equilibrium skyrmion phases and it can only be reached by laser illumination. To understand the precise mechanism underlying we examined the photo-creation process under different experimental conditions, changing the fluence, wavelength, polarization, pulse duration, magnetic field strength and orientation. The results disregarded our simple scenario proposed. Hence, to understand the microscopic nature of the effect, we performed atomistic spin calculation and showed that a phonon-assisted skyrmion process is responsible for the skyrmion generation, consistent with our wavelength dependence data. In addition to the demonstration of the skyrmion photo-creation in an insulating material, we unveiled a long-lived fluctuating and rotating skyrmion state that depends on the applied magnetic field, from which its origin remains to be elucidated.

4.3 Light for manipulating the magnetic order

Ultrafast light can be coupled to magnetic orders in various ways [279]. For example, in Cu_2OSeO_3 where spin-orbit interaction is pronounced inverse Faraday effect (IFE) leads to the excitation of the magnetic state [280]. However, the importance of the topological nature of the magnetic order remains to be clarified. Indeed, even in the absence of SOC, circularly polarized light is predicted to induce an effective through the topological nature of the skyrmion spin texture [145]. Furthermore, ultrafast x-ray scattering studies have revealed a deviation in the spin scattering response in the skyrmion phase associated with its topological order [281]. In this Chapter, we present a new microscopic mechanism to control at the ps timescale the magnetic energy landscape. First, let us introduce the experimental conditions and the initial results that have led us to this conclusion.

4.3.1 Experimental methods

To study the magnetic response after ultrashort photoexcitation. We first reached the helical phase by cooling down the sample at a nominal temperature of 5 K under an external field lower than the metastable skyrmion critical field of 25 mT. The upper critical field is 75 mT. Then, we imaged the initial magnetic state using LTEM before the illumination of the sample by the single laser pulse. A second image was taken after the photoexcitation, allowing us to compare the two states. We used a modified in-situ TEM JEOL 21000HR, the electrons emitted from a thermionic gun are accelerated to an energy of 200 keV. The magnetic contrast is obtained in Lorentz imaging mode with a 2 mm defocus length, and the external magnetic is applied by the objective lens of the microscope. Most of the images were acquired in EFTEM mode, removing the diffuse electron scattering, thus increasing the image quality. A K2TM camera, a direct detection electron camera, was used to record the images. A liquid

helium sample holder controls the temperature.

Harnessing the insulating character of Cu_2OSeO_3 , we tested three photon energies that can trigger different excitations (see Fig. 4.4d). Ultraviolet photon energy (266 nm (4.66 eV)) is above the bandgap and triggers charge transfer, NIR 780 nm (1.59 eV) although below the optical bandgap can induce electronic crystal field transitions. The longest wavelength investigated is 1200 nm (1.03 eV). The corresponding energy is below both aforementioned excitation and has a penetration depth of $\sim 30 \mu\text{m}$. Hence, the lamella with a thickness of approximately 150 nm behaves as a transparent media, and a very low amount of energy is introduced in the system, exciting lower energy modes, such as phonons. The UV 266 nm laser beam was generated using a frequency tripler of the 780 nm laser fundamental. The 1200 nm radiation was obtained using the signal beam of an OPA. A series of optical choppers were used to reduce the 4 kHz repetition rate of the laser amplifier enabling a single-shot experiment. The pulse duration is tuned using a grating pair and is measured with an autocorrelator. To obtain the absorbed fluence, first, the fluence was computed by measuring the circular beam spot size using a beam profiler and the average power at 4 kHz using a thermal power sensor. A photodiode was then calibrated and used to retrieve the energy contained within a single pulse. Corrections were applied to account for the optical properties of the different optical elements, like the TEM window. Finally, the absorbed fluence was computed by extracting the absorption coefficient from ref. [256]. The main uncertainties of the fluence estimation come from the laser beam footprint determination, as it is not determined directly at the sample location. Although providing an accurate estimation is technically challenging, 10-15% uncertainties are a good first approximation since the depth-of-focus is relatively large compared to the sample vertical position uncertainties. Further information can be found in ref. [219].

4.3.2 266 nm and 780 nm photoexcitation

As a reference point, we used the skyrmion photo-creation in metallic FeGe demonstrated recently in our lab [217] and compared in the first place 266 nm and 780 nm photoexcitation. Both photon energies deposited energy in the system but in fundamentally different ways, as the electronic bandgap separates them. We found that both wavelengths can photo-induce skyrmions. Nevertheless, the absorbed fluence required is around five times higher for the 266 nm case compared to 780 nm photoexcitation. In addition, higher magnetic fields compared to the lower critical field must be applied to establish a skyrmion phase. Depending on the sample region, it ranges from 40 mT to 74 mT. After a 780 nm flash, the skyrmion phase immediately appears. On the contrary, the skyrmion phases induced by the UV illumination slowly appear on a few minutes' timescales (see Fig. 4.7a). Our observations suggest that both skyrmion phases are different. We performed for both skyrmion phases a field cycling by ramping up the field at 133 mT, as it should erase the skyrmions that go into a trivial topological phase (conical or field polarized state). The results are presented in Fig. 4.7. As expected, the magnetic contrast progressively vanishes while increasing the field, indicating the presence

of the conical or field-polarized state. Interestingly, after the field cycling loop, around half of the 266 nm-skyrmions survived, while 780 nm-skyrmions entirely relaxed to the helical state. The same result is obtained for metastable skyrmions. Combining the long-timescale of the 266 nm-skyrmion expansion and their robustness against high fields suggests that the 266 nm-skyrmions have a different nature compared to the 780 nm-skyrmion, and metastable skyrmions, that are associated with the electronic excitation triggered. The exact mechanism remains to be clarified as a pure thermal effect can not be assigned due to the higher magnetic fields required. As more efficient, we focused on the 780 nm photoexcitation. We reported

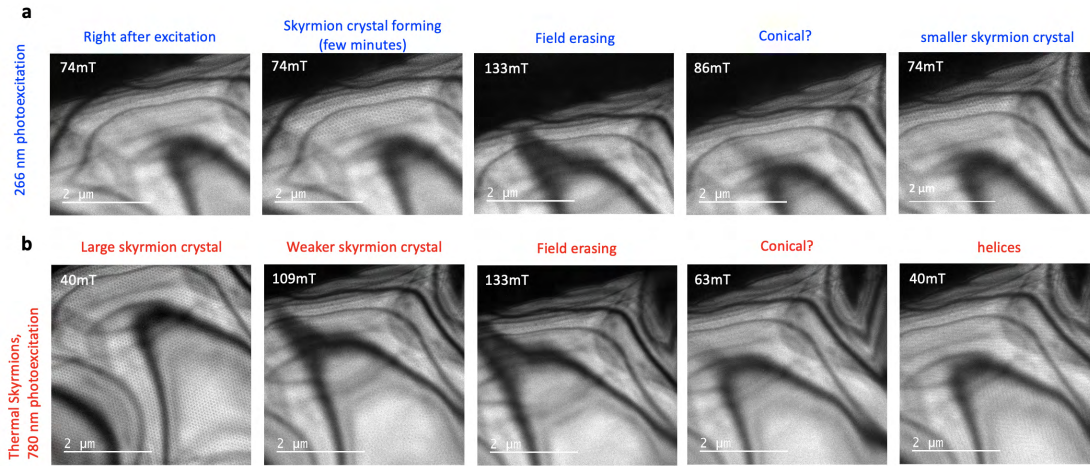


Figure 4.7 – **Stability comparison of the 266 nm, 780 nm and metastable skyrmions.** **a:** Evolution of the photo-created 266 nm-skyrmions upon field cycling. After one loop, around half of the 266 nm-skyrmions have survived. **b:** Evolution of the photo-created 780 nm-skyrmions upon field cycling. No trace of skyrmions is visible after the process. The exact result is obtained with metastable skyrmions. All datasets were acquired at 5 K.

two noteworthy phenomena. One, after photoexcitation, skyrmions are not static as in the metastable case. Instead, we observed fluctuating and skyrmion lattice rotation dynamics on seconds timescale that relaxed after approximately one minute. Second, we discovered the possibility of photo-creating the skyrmion phase at lower magnetic fields (14 mT) than the lower critical field (25 mT). Those observations are highly reproducible and were reproduced in three other lamellae. The two phenomena are most likely decoupled due to the considerable timescale difference. The photo-creation process is expected to happen on hundreds of ps timescale, while the observed long-lived dynamics occur on the second timescale, ten orders of magnitude difference. Thus, we focused our attention on the initial trigger, which is the photo-creation mechanism. The second long-lived fluctuating process is discussed in Section 4.4.

A pure thermal process like in ref. [217] is not compatible with our observation. Hence, we need to investigate other potential mechanisms. We consider four scenarios in which the

skyrmion generation is triggered by an external parameter induced by the ultrashort laser pulse.

1. **Electric-field generation:** Intense and focus laser pulse generated an electric field. Skyrmion creation in Cu_2OSeO_3 via an electric field has been demonstrated [282]. Moreover, rotation of the skyrmion lattice can be controlled by electric fields [257] and could explain our dynamical observations.
2. **Combination of heating-effect and magnetic-field induction:** In that case, instead of going only along the temperature axis to reach the equilibrium skyrmion phase as done in ref. [217], a vertical component (field) is added, enabling the state to reach the equilibrium skyrmion phase. The additional magnetic field component would be induced by the inverse Faraday effect or azimuthal polarization potentially present in our laser beam that has been shown to generate intense magnetic fields [283]. Furthermore, skyrmion lattice rotation can be induced by a magnetic field gradient [284].
3. **Strain assisted:** Bend contours directly reflect the inherent strain of the lamella. After photoexcitation, we observed displacement of the bend contours that returned to their initial position after a few seconds. Thus, it indicates that strain is present in the fluence used. Moreover, lattice distortion effects have been shown to stabilize the skyrmion phase in Cu_2OSeO_3 [270–272].
4. **Temperature effect via crystal field excitation:** The 780 nm photoexcitation triggers crystal field excitation, thus heating the sample by approximately ~ 600 K, according to our numerical simulations. We could imagine a related skyrmion generation process in which the crystal field excitation would change the magnetic energy landscape. Moreover, a continuous skyrmion rotation was observed in the presence of a temperature gradient [213].

To get insights into the complicated mechanism, we investigate the skyrmion photo-creation process varying the laser pulse parameters and the applied magnetic field. The results are discussed in the next part.

4.3.3 Polarization, Field and pulse duration and wavelength dependence

We investigated four laser beam parameters (fluence, polarization, pulse duration, and wavelength) and two external parameters: magnetic strength and orientation. As the magnetic field orientation is fixed in a TEM, the fabrication of a specific TEM lamella with adjusted crystallographic axes is required. Due to time constrain, as the lifetime of one sample is below 15 hours at cryogenics temperature in our instrument (see section 4.5), we did not investigate the entire space parameters and followed a discovery-based approach. In other words, the leftover (not shown in the submitted preprint) results exposed below can not be rigorously

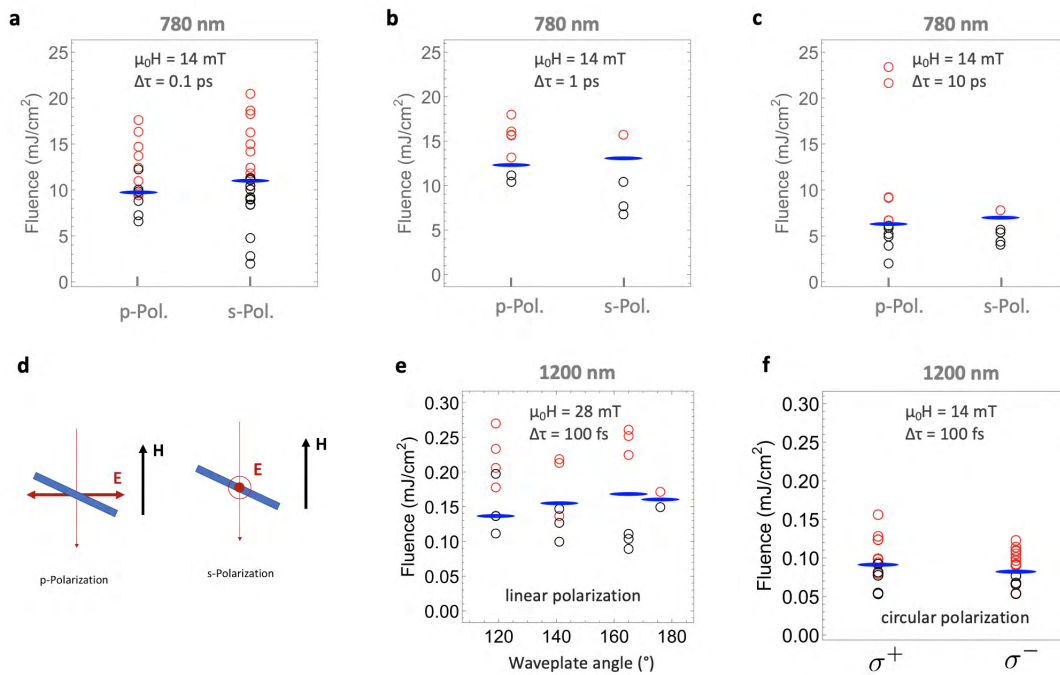


Figure 4.8 – **Polarization dependence for 780 nm and 1200 nm skyrmion photo-creation process.** **a-c,e-f** present the resulting magnetic state after single pulse photoexcitation. Red dots indicate the skyrmion creation, while in black dots trials, no skyrmion was observed. The blue bar indicates the absorbed fluence threshold to induce the skyrmion phase. **a-c** show the result upon 780 nm photoexcitation with a single linearly polarized pulse for different pulse durations. **d**: Illustration of the experimental geometry and its corresponding s-polarization and p-polarization. The blue rectangle denotes the sample look at the cross-section, and the red arrow indicates the laser beam propagation. **e-f** show the polarization dependence result upon 1200 nm photoexcitation with a single pulse for linear and circular polarization. This study was carried out at 5 K, in the initial helical phase reached upon zero-field-cooled (ZFC) protocol.

compared among them as some parameters might differ. Nevertheless, they contain precious information that merits being presented and discussed.

First, we noted that once the fluence threshold is crossed, skyrmions almost always appear, thus demonstrating the strong deterministic nature of the process. No upper fluence limit was reached, supporting the idea of a non-thermal process, as the temperature increase is far above the Curie temperature. To have a precise idea of the heat deposited by the single laser pulse in the system, we need to perform a multiphysics simulation reproducing our experimental conditions. We used the same numerical model described in the Supplementary Information of ref. [104] (see Chapter 5). This model considers the sample geometry, the beam spatio-temporal profile, and time-dependent heat dissipation effects. For 780 nm with an incident fluence of 60 mJ/cm^2 (absorbed fluence $\sim 7.8 \text{ mJ/cm}^2$), the temperature of the lamella increase

4.3. Light for manipulating the magnetic order

by approximately 600 K, far above the Curie temperature (~ 50 K in our lamella), consistent with a non-purely thermal effect. The temperature increase is less pronounced for 1200 nm light since this photon energy is barely absorbed (see Fig. 4.4d). The temperature increase is ~ 50 K for an incident fluence of 20 mJ/cm^2 (absorbed fluence $\sim 0.1 \text{ mJ/cm}^2$). In both cases, the system rapidly cooled down and returned to its initial value on a μs timescale. Hence, the long-lived dynamics process occurring on the second timescale, six orders of magnitude longer, can not be directly assigned to thermal effects.

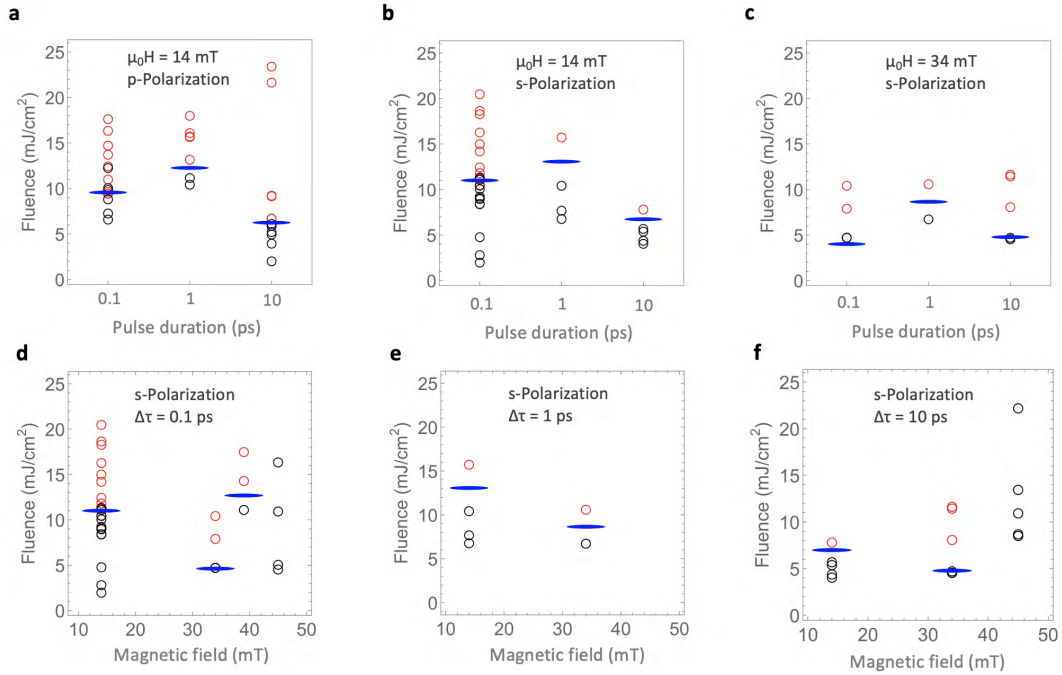


Figure 4.9 – Pulse duration and field dependences of the skyrmion photo-creation process. **a-c:** Investigation of the pulse duration dependence for different polarization and applied fields indicated on the corresponding panel. Although no striking effect is observed, we noted that 10 ps can induce the skyrmion phase, indicating that the mechanism must occur on similar or longer timescales. **d-e:** Investigation of magnetic field effect on the skyrmion photo-creation for 0.1 ps, 1 ps, and 10 ps pulse duration, respectively. At 45 mT, it is not possible to generate skyrmion within the fluence investigated for the 0.1 ps, and 10 ps cases. Red dots indicate the skyrmion creation, while in black dots trials, no skyrmion was observed. The blue bar indicates the absorbed fluence threshold to induce the skyrmion phase. This study was carried out with 780 nm ultrashort single pulse, at 5 K, in the initial helical phase reached upon ZFC protocol.

No evident dependence appears in the polarization (Fig. 4.8), pulse duration (Fig. 4.9), and the magnetic field orientation (section 6.1.1) investigated. However, the magnetic field strength and the wavelength show both a striking effect. Indeed, above a field around 45 mT, the skyrmion photo-generation with 780 nm-light become unattainable (see Fig. 4.9d,f) and an

optimal magnetic field around 34 mT exists. Note that we observed an opposite behavior for 266 nm photoexcitation as the field must be increased to higher fields to photo-create skyrmions. Furthermore, distinct long-lived dynamics are observed depending on the magnetic field amplitude (see below, in section 4.4). Our observation strongly suggests that the external magnetic field is a key parameter in the two mechanisms process. Nonetheless, it must be an intrinsic property, as the laser pulse polarization has shown to not affect the threshold fluence. Consequently, the two scenarios of the electric and magnetic fields induced by the laser pulse are disregarded. By tuning the wavelength to lower energy, we observed an increase in the skyrmion photo-creation efficiency by two orders of magnitude. The average absorbed fluence threshold for 780 nm-light (1.59 eV) is around 10 mJ/cm^2 , while this value decreases to $\sim 0.1 \text{ mJ/cm}^2$ for 1200 nm (1.03 eV) photon energy. Investigating the potential thermal energy contribution to the mechanism, we examined the 1200 nm-photo-creation process with a based temperature of 34 K, around 16 K below the Curie temperature (see Fig. 4.10). Although no quantitative result in the fluence threshold can be identified as the fluence difference value is close to our uncertainties, we remarked that the skyrmion phase does not exist at high temperatures and low magnetic fields. Indeed, at 34 mT above the critical field, the photo-induced skyrmion phase is stable across all the temperature ranges. On the other hand, at 14 mT below the critical field and 34 K, no skyrmion formation was ever observed, which leads to three hypotheses; the fluence required to induce the skyrmion phase is above the tested fluence, the skyrmions decay faster than our time resolution, and no skyrmion can be photo-generated in this part of the phase diagram. This shows direct evidence of the competition between the laser-induced out-of-equilibrium states and the inherent thermodynamic equilibrium state.

The wavelength dependence discards scenarios 3 (strain) and 4 (temperature), leaving none of the scenarios considered. A recap of investigated potential mechanism pros and cons are displayed in Tab. 4.1. As no straightforward photo-creation mechanism was unveiled, we performed atomistic spin calculations to understand the microscopic process. The results presented in the next part show strong modulation of the DMI by phonons that can be triggered with our laser pulse. In this regard, the access of the skyrmion phase is fostered as the instantaneous DMI changes the magnetic energy landscape. Once formed, the skyrmion phase remains in a metastable state.

potential mechanism	E-Field	H-Field	Strain	Temperature
Cons	Pulse duration, polarization	Pulse duration, Polarization	wavelength	1200 nm, Applied H-field
Pros	Rotation, 1200 nm	Rotation, magnetic field	Bend contours shaking	780 nm, Rotation

Table 4.1 – **Pros and cons of mechanism candidates in the skyrmion photocreation process.**

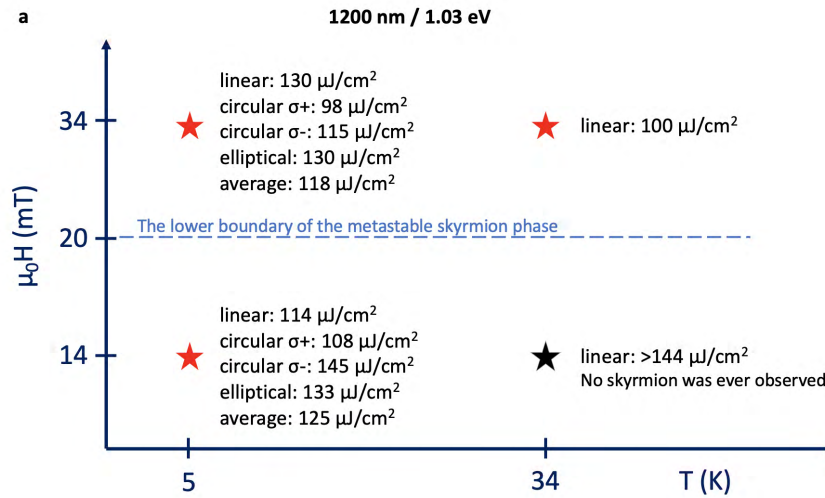


Figure 4.10 – **Temperature vs. magnetic field map of the absorbed fluence threshold.** **a:** Stars indicate the position in the temperature versus magnetic field diagram at the threshold absorbed fluence we found depending on the polarization. No skyrmion was observed in the low field - high-temperature region. Note that the lamella under investigation is different from the previously presented results.

4.3.4 Ultrafast skyrmion photo-creation via transient DMI modulation

To date, two experimental work creating skyrmion using ultrafast laser light has been recently achieved [217, 218]. In both cases, the laser pulse induces heat responsible for the skyrmion formation. In FeGe, the transient temperature increase enables the magnetic system to visit the high-temperature skyrmion phase, which then relaxes at its initial low temperature forming a metastable skyrmion phase [217]. For the multilayered systems (Pt/CoFeB/MgO and Pt/Co), the laser provokes an ultrafast demagnetization and a non-crystalline skyrmion phase mediated by transient fluctuations states [218]. The two studies rely on exploiting the intrinsic properties of the skyrmion host materials. However, inducing a topological phase transition by direct manipulation of the inherent magnetic energy landscape remains to be reported. In this work, we addressed such challenges and demonstrated that by triggering phononic excitation, the magnetic energy landscape is transiently modified. Consequently, the magnetic phase diagram is transiently renormalized and enables efficient skyrmion formation. Our discovery answers our initial question "Can we induce a skyrmion phase in an insulator by femtosecond light pulses, which provide the fastest way for modifying the magnetic state?" and open new perspectives for magnetic order manipulation without the need for invasive parameters such as chemical doping or pressure and out-of-equilibrium topological phase transition. The work synthesized in ref.[219] is presented below.

Observation of a new light-induced skyrmion phase in the Mott insulator Cu_2OSeO_3

Alexey A. Sapozhnik,^{*} Benoit Truc,^{*} Phoebe Tengdin,^{*} Simone Gargiulo, Ivan Madan, Thomas LaGrange, and Fabrizio Carbone[†]
*Laboratory for Ultrafast Microscopy and Electron Scattering (LUMES), Institute of Physics,
École Polytechnique Fédérale de Lausanne (EPFL), Lausanne, Switzerland.*

Thomas Schönenberger and Henrik M. Rønnow
*Laboratory for Quantum Magnetism (LQM), Institute of Physics,
École Polytechnique Fédérale de Lausanne (EPFL), Lausanne, Switzerland.*

Arnaud Magrez
Crystal Growth Facility, Institute of Physics, École Polytechnique Fédérale de Lausanne (EPFL), Lausanne, Switzerland.

Emil Viñas Boström
Max Planck Institute for the Structure and Dynamics of Matter, Hamburg, Germany

Angel Rubio
*Max Planck Institute for the Structure and Dynamics of Matter, Hamburg, Germany and
Center for Computational Quantum Physics (CCQ), The Flatiron Institute, New York, USA.*

Claudio Verdozzi
Division of Mathematical Physics and ETSF, Lund University, Lund, Sweden
(Dated: December 16, 2022)

We report the discovery of a novel skyrmion phase in the multiferroic insulator Cu_2OSeO_3 for magnetic fields below the equilibrium skyrmion pocket. This phase can be accessed by exciting the sample out of equilibrium with near-infrared (NIR) femtosecond laser pulses but can not be reached by any conventional field cooling protocol. From the strong wavelength dependence of the photocreation process and via spin dynamics simulations, we identify the magnetoelastic effect as the most likely photocreation mechanism. This effect results in a transient modification of the magnetic interaction extending the equilibrium skyrmion pocket to lower magnetic fields. Once created, the skyrmions rearrange and remain stable over a long time, reaching minutes. The presented results are relevant for designing high-efficiency non-volatile data storage based on magnetic skyrmions.

I. INTRODUCTION

Magnetic skyrmions are topologically nontrivial magnetic textures where the spins twist in a vortex-like fashion around the skyrmion core. Their small size and high speed of current-induced motion make them prospective for various spintronics applications [1–4]. Implementing these concepts requires solving multiple fundamental and technological challenges, such as stabilizing room temperature and zero-field skyrmion phases necessary for practical applications in modern information technology. However, in most of the discovered skyrmion-hosting compounds, skyrmions exist only at low temperatures and require external magnetic fields [5]. Searching for topologically nontrivial phases at ambient conditions and exploring the ways for their ultrafast manipulation can lead to a different data storage paradigm, allowing for faster data processing without ohmic losses.

Insulating skyrmion hosting compounds are of high interest due to low Gilbert damping [6], which allows for

studying the propagation of magnons through a skyrmion crystal [7, 8] or thermal-gradient induced skyrmion motion [9]. However, such materials are very rare, including multiferroic Cu_2OSeO_3 [10] and $\text{Tm}_3\text{Fe}_5\text{O}_{12}$ (TmIG), where the topological Hall effect was detected at room temperature in Pt/TmIG heterostructures [11]. Cu_2OSeO_3 is the ideal candidate for studying the light-induced effects due to its bulk Dzyaloshinskii–Moriya interaction (DMI) and a rich phase diagram containing various low-temperature magnetic phases [12]. The material exhibits a bandgap of 2.5 eV [13] and a local maximum of absorption around 1.5 eV corresponding to the transitions between the 3d levels of Cu split by crystal field effects [14]. The equilibrium skyrmion phase in Cu_2OSeO_3 can be tuned by an external electric field [15, 16], and the electric field-induced creation of skyrmions was recently demonstrated [17]. The mechanical strain plays an important role in stabilizing skyrmions in Cu_2OSeO_3 , which was evidenced by a significant expansion of the skyrmion phase at high pressures [18].

Light stimulation provides a fast and versatile way to control the structural and magnetic properties of the materials [19]. The coupling between light and the magnetic state of a sample occurs via several mechanisms. These

^{*} The authors have contributed equally

[†] fabrizio.carbone@epfl.ch

include coupling between the magnetic and the electronic subsystems at an elevated temperature [20], nonlinear phononics [21], or a transient magnetic field generated via the inverse Faraday effect [22]. The previous experiments on the photocreation of topological magnetic textures focused on metallic compounds, where the transient heating of the material was identified as the primary microscopic mechanism [23–25].

In this work, we demonstrate the photoinduced creation of skyrmions by a single NIR femtosecond pulse outside the adiabatically accessible regime. We visualized the skyrmions by the Lorentz transmission electron microscopy (TEM) technique, which provides a high spatial resolution for studying the magnetic materials on the nanoscale [26–28]. We successfully generated the skyrmions at low magnetic fields below the equilibrium skyrmion pocket in Cu_2OSeO_3 by 780-nm and 1200-nm pulses. Considering the low absorption of Cu_2OSeO_3 at 1200-nm, the reported results are relevant for low-power skyrmion-based memory [14].

II. EXPERIMENTAL TECHNIQUES AND METHODS

Single crystals of Cu_2OSeO_3 were grown by chemical vapor transport in a horizontal two-zone furnace. The precursor for the growth was a stoichiometric mixture of CuO and SeO_2 sealed in a quartz ampule. The ampule was filled with HCl at a pressure of 100 mbar, acting as the transport agent. A slab of material with a [111] direction normal to it was cut from a Cu_2OSeO_3 single crystal and polished to a thickness of $10\ \mu\text{m}$. A TEM lamella was prepared by further thinning down a $5\times 5\ \mu\text{m}^2$ to a thickness of approximately 150 nm by Ga ions using the focused ion beam (FIB) technique. The thickness of the sample was determined by electron-energy loss spectroscopy (EELS) log-ratio method [29].

The measurements were performed in a TEM JEOL 2100HR (acceleration voltage of 200 kV) equipped with a thermionic gun. The microscope is modified to provide laser light onto the sample [30]. The setup was operated at saturation conditions with an electron energy distribution width of 1 eV. The images were recorded on a K2 camera (GATAN) in energy-filtered mode, and the width of the energy-selective slit was set to 10 eV. Magnetic contrast was achieved using Lorentz transmission electron microscopy (LTEM) with an underfocus of 2 mm [31].

A Ti:Sapphire regenerative amplifier RAEA HP (KM-Labs) was used to produce 35 fs pulses with a bandwidth centered at 780 nm at a repetition rate of 4 kHz. A modified OPA TOPAS (Light Conversion) was utilized for converting them into NIR pulses with a wavelength of 1200 nm. The duration of the 1200-nm pulses was fixed at 100 fs, and that of the 780-nm pulses could be changed from 100 fs to 10 ps. A set of optical choppers was implemented for reducing the repetition rate down to 4 Hz

necessary for performing single pump pulse experiments enabled by a fast mechanical shutter.

III. RESULTS

The equilibrium phase diagram of the Cu_2OSeO_3 lamella was measured by field cooling (FC) the sample from 65 K at different magnetic fields and is presented in Fig. 1a. The cooling rate was $\sim 1\ \text{K}/\text{sec}$. Field cooling in magnetic fields lower than 24 mT results in the appearance of a helical phase below the ordering temperature T_C . Magnetic fields exceeding 50 mT correspond to the conical or field polarized (FP) states that are indistinguishable in the LTEM images. The boundary between these two phases is indicated by a dashed line in Fig. 1a and d. The measured T_C of 40 K is lower than the value of 59 K reported earlier [10]. This discrepancy might be explained by the difference in the actual sample temperature and the temperature measured by the thermocouple of the sample holder or by the fact that we studied a thin lamella (150 nm) that may have a different T_C and phase diagram than the bulk crystal measured in Ref. [10].

The skyrmion photocreation experiment below the equilibrium skyrmion pocket was conducted according to the protocol shown in Fig. 1a. First, the sample was cooled from 65 K (above the T_C) in a field of 14 mT, which is the remanent field of the TEM objective lens, following the blue arrow. The initial state of the sample after FC is helical (Fig. 1b). After reaching a temperature of 5 K, the sample was irradiated with a single 780-nm femtosecond pulse resulting in the formation of a skyrmion lattice (Fig. 1c). The absorbed fluence in this experiment was $15\ \text{mJ}/\text{cm}^2$.

We tested the possibility of creating the low-field skyrmion phase shown in Fig. 1c by slow field cooling. Fig. 1d indicates the path followed within the phase diagram. First, the sample is cooled in a field of 40 mT from 65 K to 5 K at a cooling rate of $\sim 1\ \text{K}/\text{sec}$, resulting in the formation of a skyrmion lattice (Fig. 1e). However, after decreasing the magnetic field to 14 mT, the skyrmion lattice transforms into helices (Fig. 1f). Thus, the photoinduced skyrmion phase in the Cu_2OSeO_3 lamella at 14 mT and 5 K is a manifestation of a unique magnetic phase, which can be accessed only via photoexcitation of the sample.

The discovered low-field skyrmion phase exhibits a long lifetime exceeding several tens of seconds (Fig. 2). We have also observed the skyrmions present in the sample minutes after the excitation (not shown). The helical and the skyrmion domains coexist in the sample for a few seconds after the optical excitation (Fig. 2b), and on a longer time scale, the skyrmion lattice expands prevailing over the helical domains (Fig. 2c).

We studied the pulse duration dependence of the skyrmion photocreation process at 5 K and a field of 14 mT. The final magnetic states of the Cu_2OSeO_3 lamella are reported in Fig. 3a for the excitation with a

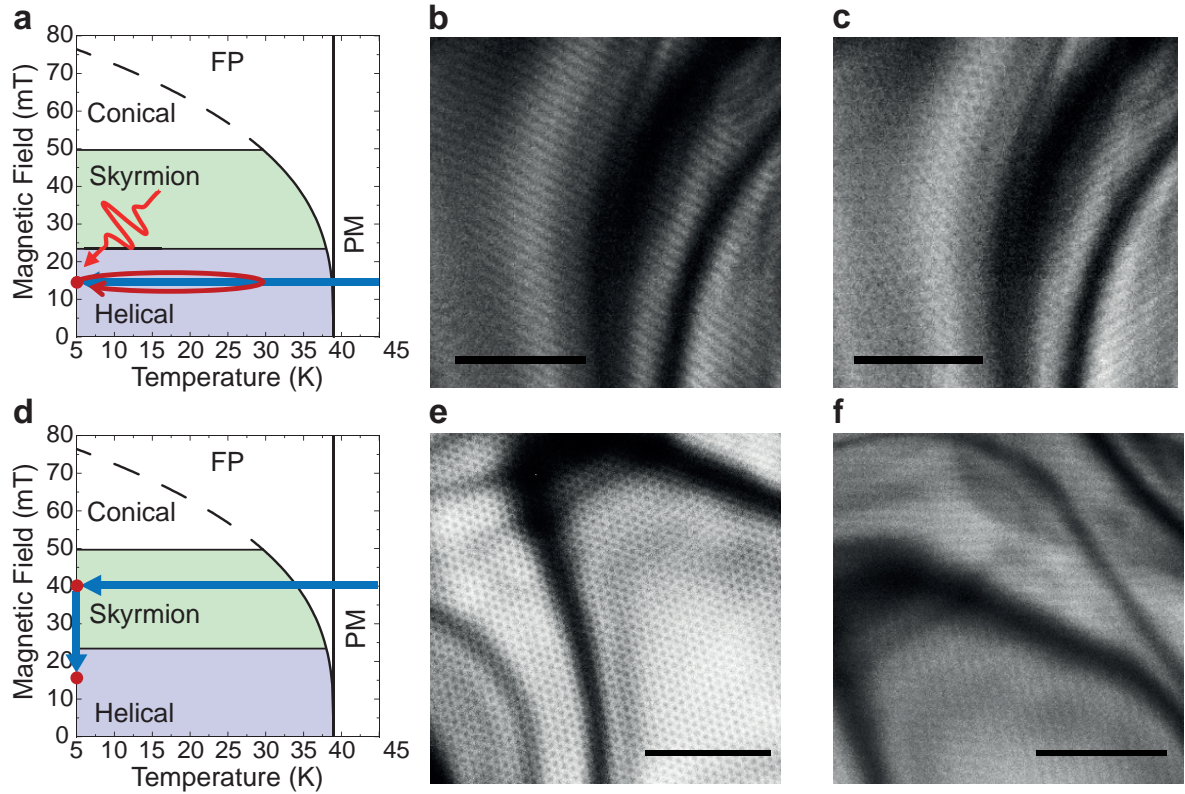


FIG. 1. **New skyrmion phase below the equilibrium skyrmion pocket in Cu_2OSeO_3 .** **a** The field cooling phase diagram of the Cu_2OSeO_3 lamella. FP is the field polarized state, and PM denotes the paramagnetic state. **b** After FC the sample below the equilibrium skyrmion pocket (14 mT), only the helical state is visible in the real-space LTEM image measured at 5 K. **c** After the arrival of a single 780-nm laser pulse, the magnetic state of the sample contains coexisting skyrmion and helical phases. **d** Protocol followed to attempt accessing the novel skyrmion phase at low magnetic fields by FC. **e** The skyrmion phase at 5 K and 40 mT generated by field cooling the sample through the Curie temperature. **f** After decreasing the magnetic field to 14 mT, the skyrmions disappear and the helical phase emerges. The scale bars in panels **b**, **c**, **e**, **f** are $1\ \mu\text{m}$.

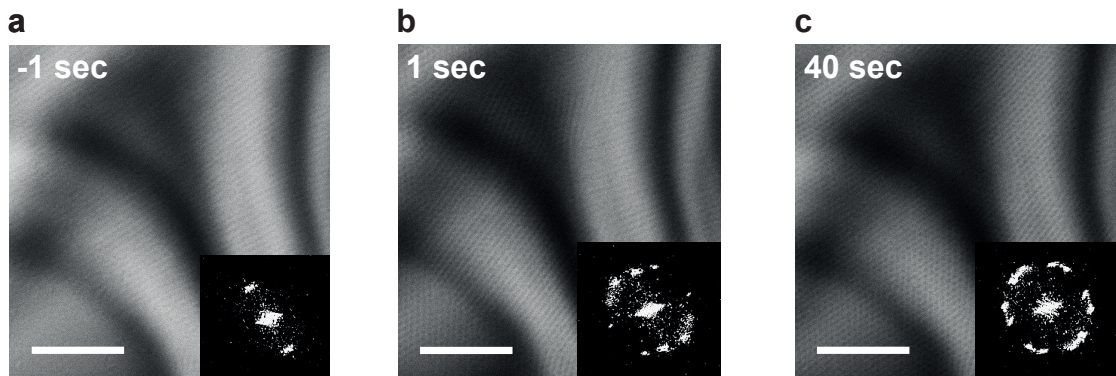


FIG. 2. **The stability of the photocreated skyrmion phase.** The LTEM images of the Cu_2OSeO_3 lamella at 5 K and 14 mT **a** one second before, **b** one second after, and **c** 40 seconds after the irradiation of the sample by an optical pulse. The insets show the Fourier Transform (FT) patterns calculated over the corresponding images. The scale bar is $1\ \mu\text{m}$.

single 780-nm pulse. Before each measurement, the sample was reset to the single-domain helical state by briefly applying an out-of-plane magnetic field of 1 T. Note that resetting by going above the Curie temperature and following field cooling did not result in any change. The vertical axis corresponds to the fluence absorbed in the thin 150-nm part of the sample (see Supplementary Information). The sample remains in the helical state for lower fluences, as indicated by the black circles. Occasionally, a reorientation of the helix wave vector \mathbf{Q} was observed after the arrival of a pulse, but no skyrmions were created. A skyrmion lattice was generated as higher fluences, corresponding to the red circles. The skyrmion generation threshold marked by the blue lines shows only weak dependence on the pulse duration.

Tuning the photon energy below the crystal field excitation regime allows for achieving an outstanding efficiency in generating the skyrmions as demonstrated in Fig. 3b. The absorbed threshold fluence required for generating the skyrmions with 780-nm pulses at 5 K and 14 mT is 11 mJ/cm², and for 1200-nm photons, this value reduces to 0.06 mJ/cm². Although the absolute values varies slightly among the samples tested, we reproduced this result in four different samples. To the best of our knowledge, it is a record-low fluence necessary for generating skyrmions in a magnetic material. The fluence threshold shows only a weak polarization dependence for a wavelength of 1200 nm (Fig. 3c). This behavior is expected from the cubic symmetry of the material point group and is consistent with the simulations discussed below.

IV. DISCUSSION

The low-temperature skyrmion phase identified in our experiments can only be accessed by laser excitation (Fig. 1c) and is absent under adiabatic field cooling of the sample (Fig. 1f). It indicates that the photocreation of skyrmions in this regime cannot be explained solely by the transient heating of the sample and that other non-thermal effects play a central role. To gain further insight into the microscopic processes underlying skyrmion photocreation in Cu₂OSeO₃, we performed extensive spin dynamics simulations. Due to the multiferroic nature of the material, there is a large number of mechanisms by which the laser electric field can affect magnetization. Since our measurements were performed at wavelengths inside the bulk band gap and low to moderate fluences, real (as opposed to virtual) electronic excitations can be assumed negligible. In addition, as indicated by Fig. 3b, a much lower fluence is needed to create skyrmions for $\lambda = 1200$ nm than for $\lambda = 780$ nm. It is likely due to the electronic crystal field excitations present at shorter wavelengths [14], which hinder energy from reaching the magnetic subsystem and are detrimental to skyrmion creation.

As illustrated in Fig. 4a, the possible light-matter cou-

pling mechanisms are the Raman excitation of phonons and magnons, an effective magnetic field generated by the inverse Faraday effect, and direct magnetoelectric coupling to the spontaneous polarization [32–34]. The magnetoelectric effect, originating from the coupling between the laser electric field and the electronic polarization of Cu₂OSeO₃, is proportional to the amplitude of the electric field [17]. Thus, the fluence threshold is expected to show a strong dependence on the pulse duration and a crystal orientation dependence that we did not observe. In contrast, our experimental data only exhibits a weak dependence of the fluence threshold on the pulse duration (Fig. 3a). Thus, the magnetoelectric coupling is likely not the main mechanism driving the observed photocreation below the equilibrium skyrmion pocket. The inverse Faraday effect is also expected to play a small role in the photocreation process due to the weak polarization dependence for 1200-nm light [22].

In contrast, static mechanical strain is known to modify the shape of the magnetic phase diagram of Cu₂OSeO₃ and similar materials. An increase of the T_C and an expansion of the skyrmion pocket were demonstrated in a bulk crystal of Cu₂OSeO₃ under compressive stress [18]. Moreover, a negative uniaxial strain can shift the equilibrium skyrmion pocket to lower magnetic fields via magnetoelastic coupling [35], and mechanical strain can modify the Dzyaloshinskii-Moriya interaction (DMI) constant of a skyrmion hosting compound [36], or both the DMI constant and the anisotropy constant [37]. Since a modest strain of 0.3 % can induce a modulation of the DMI of up to 20 % [38, 39], a transient strain mediated by long-wavelength acoustic phonons is expected to have a significant impact on the DMI [40].

To make the above arguments quantitative we consider a time-dependent interaction Hamiltonian $H_I(t)$ accounting for all of the discussed mechanisms. This Hamiltonian is

$$H_I(t) = \sum_{\langle ij \rangle} [J_{ij}(t) \mathbf{m}_i \cdot \mathbf{m}_j + \mathbf{D}_{ij}(t) \cdot (\mathbf{m}_i \times \mathbf{m}_j)] \quad (1) \\ + \sum_i [\mathbf{B}(t) \cdot \mathbf{m}_i - \mathbf{E}(t) \cdot \mathbf{P}_i],$$

where J_{ij} is the exchange interaction between magnetic moments \mathbf{m}_i and \mathbf{m}_j , \mathbf{D}_{ij} is the DMI, \mathbf{B} and \mathbf{E} are the external magnetic and electric fields, and \mathbf{P}_i the electronic polarization. Each microscopic process is associated with a characteristic energy scale, denoted by g_R for the magnon Raman process, g_{IFE} for the inverse Faraday effect, $g_{\text{m-el}}$ for the magneto-electric coupling, and $g_{\text{m-ph}}$ for the magneto-phonon coupling. Further, each mechanism only affects a given term in Eq. (1), such that the exchange depends on g_R , the DMI on $g_{\text{m-ph}}$, the magnetic field on g_{IFE} and the polarization on $g_{\text{m-el}}$. A detailed discussion of the values of these energies is provided in the Supplemental Material.

To account for the time-dependence of the magnetic interactions, we note that the magnon Raman process, the inverse Faraday effect, and the magneto-electric effect

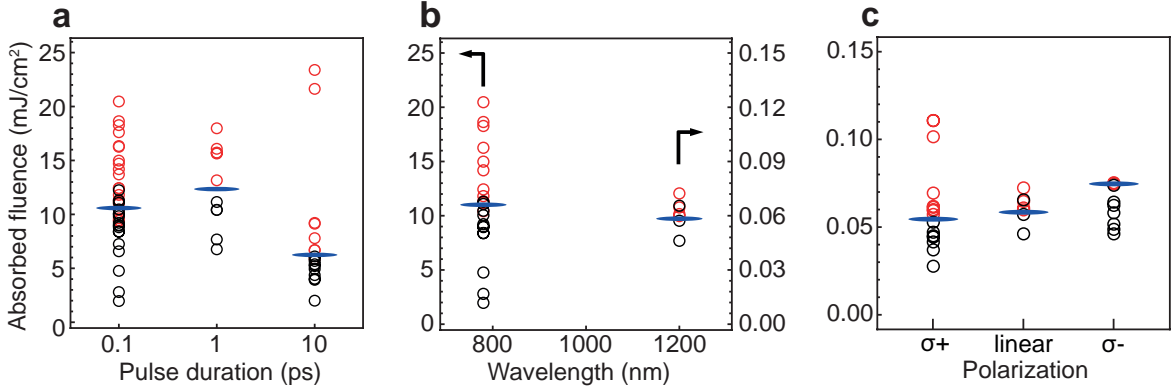


FIG. 3. **Absorbed fluence threshold for the photoinduced generation of skyrmions with NIR photons.** **a** The pulse duration dependence of the skyrmion photocreation in Cu_2OSeO_3 at 5 K and 14 mT for a 780-nm single-pulse photoexcitation. **b** Comparison of the photocreation threshold between 780-nm and 1200-nm optical excitation. **c** The photocreation of skyrmions with single femtosecond pulses having a wavelength of 1200 nm for different polarizations. The vertical axis indicates the absorbed fluence. The red and black circles display the final state of the sample exhibiting skyrmions and helices, respectively. The blue horizontal lines indicate the skyrmion generation threshold. The vertical axes in all panels correspond to the absorbed fluence in the thin part of the sample.

only modify the spin parameters during the action of the pulse (assumed to be a Gaussian of width τ). In contrast, the phonon modulation of the DMI is expected to persist for as long as there are phonons present in the system. The time-dependent part of the DMI is therefore assumed to have an onset time given by the pulse width τ , and an exponential decay set by the phonon lifetime τ_{ph} . This time dependence is described by a log-normal function as further discussed in the Supplemental Material.

To describe the skyrmion photocreation process we simulated the time-evolution governed by Eq. (1) following laser excitation (see Supplemental Material for a discussion of the equilibrium spin parameters and phase diagram as well as the spin equations of motion). In line with our experiments, the magnetic field was chosen such that the system is initially in the helical state and close to the phase boundary to the conical state. By exploring a significant portion of the parameter space defined by Eq. (1), the dominant mechanism leading to skyrmion photocreation in Cu_2OSeO_3 was identified as the transient modulation of the DMI by long-wavelength acoustic phonons. This identification is in line with several previous studies that have found a strong dependence of the Dzyaloshinskii-Moriya interaction (DMI) on strain [38, 39] as well as on a dynamical coupling to acoustic phonons [40].

In agreement with our experimental results, our simulations predict a skyrmions phase to appear upon laser irradiation for magnetic parameters below the equilibrium skyrmion pocket. Heuristically, the skyrmion photocreation process as emerging from our simulations can be understood as follows (see Fig 4b). The coupled spin-phonon system is excited into a non-equilibrium state through Raman and magneto-electric processes. Simultaneously, the modulation of the DMI by acoustic

phonons leads to a change in the free energy landscape, allowing the system to relax into a quasi-stationary state defined by the instantaneous phonon-modulated Hamiltonian. At a time-scale set by the phonon lifetime τ_{ph} the free energy landscape returns to its original form, while the magnetic system stays trapped in the meta-stable skyrmion crystal state.

To substantiate this picture we show in Fig. 4c the non-equilibrium magnetic phase diagram as a function of pulse duration and laser fluence, and shows the topological charge \mathcal{Q} of magnetic state at the final time of our simulations (corresponding to about 300 ps). The topological charge $\mathcal{Q} = 0$ in the helical or ferromagnetic state, and becomes $\mathcal{Q} = -1$ and 1 for skyrmions and antiskyrmions, respectively. Thus the topological charge counts skyrmions and antiskyrmions and is non-zero only when a net imbalance of such excitations is present. Our simulation shows that photoexcitation strongly favors skyrmion creation, and thus \mathcal{Q} in Fig. 4c is equal to the total skyrmion number N_{sk} . Clearly, above a threshold fluence of $F \approx 1 \text{ mJ/cm}^2$, the non-equilibrium steady state changes character from a helical to a skyrmion crystal state. Similarly Fig. 4d shows the topological charge \mathcal{Q} as a function of DMI modulation.

We note that Fig. 4c predicts an approximately linear relation between the threshold fluence and the pulse duration. For this to be consistent with Fig. 3a, we have to assume that the spins are insensitive to processes on time-scales shorter than about 1 ps. More precisely, assuming that the laser energy is transferred to the acoustic phonons faster than some excitation time τ_{exc} , and that this time is shorter than the characteristic magnetic time-scale τ_{spin} , the resulting spin dynamics is expected to be independent of pulse duration for $\tau < \tau_{\text{exc}}$.

To assess the stability of the non-equilibrium skyrmion

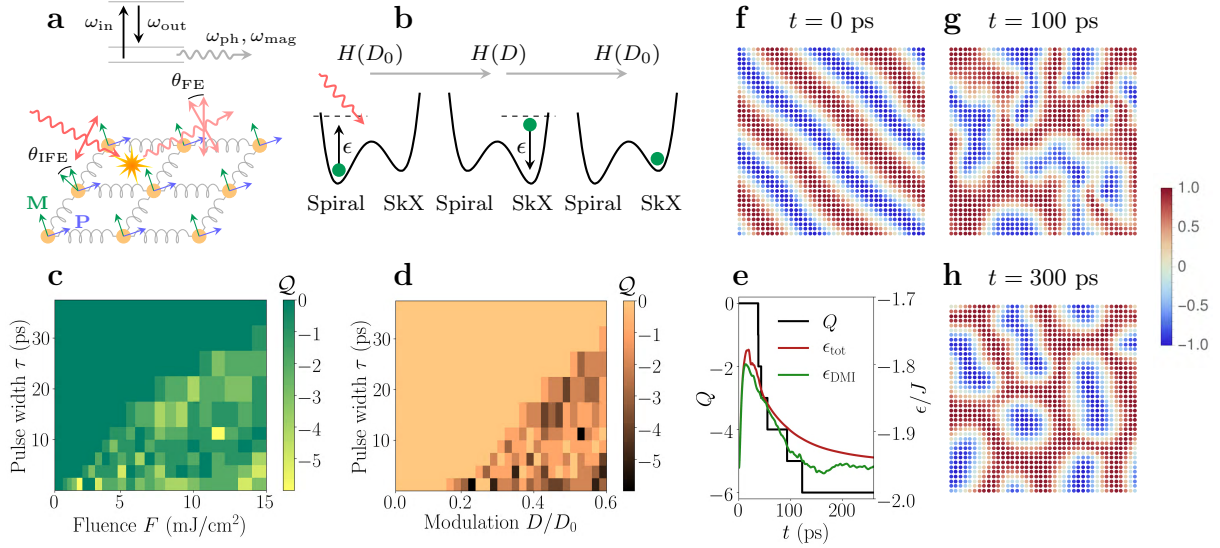


FIG. 4. Microscopic mechanism of skyrmion photocreation. **a**, Schematic of the light-matter interaction mechanisms contributing to skyrmion photocreation in Cu_2OSeO_3 . Top panel: Raman scattering processes involving virtual electronic states lead to emission of magnons and phonons. Main panel: The inverse Faraday effect and a direct magneto-electric coupling to the polarization (blue arrows) leads to a change in laser polarization and a torque on the magnetic moments (green arrows). **b**, Heuristic rendering of the mechanism of skyrmion photocreation: (1) Raman and magneto-electric processes lead to excitation of the coupled spin-phonon system and a change in the free energy landscape. (2) The system relaxes into a quasi-stationary state defined by the photon-modulated Hamiltonian (3) The system returns to equilibrium trapped in the meta-stable skyrmion crystal state. **c**, Non-equilibrium magnetic phase diagram as a function of laser fluence and pulse duration. The areas with a non-zero value of the topological charge Q correspond to skyrmion photocreation. **d**, Topological charge Q as a function of phonon-modulated Dzyaloshinskii-Moriya interaction D . **e**, Time-dependence of the topological charge and the total energy per spin during skyrmion creation. **f-h**, Instantaneous spin configurations at different times t for the pulse duration $\tau = 10$ ps and a fluence $F = 10$ mJ/cm^2 . The equilibrium spin parameters of the normalized spin model are taken as $J = 48.2$ meV, $D = 10.8$ and $B = 0.63$ meV (corresponding to $B = 20.7$ mT), in accordance with literature. The strength of the light-matter coupling constants are taken as $g_R = 0.1J$, $g_{\text{IFE}} = 0$, $g_{\text{m-el}} = 0.01J$ and $g_{\text{m-ph}} = 0.5D$ for a laser electric field of $E = 10^9$ V/m.

state, we further investigated the time-evolution of the magnetic system. Fig. 4f-h shows the instantaneous magnetization $\mathbf{m}_i(t)$ at a number of different times t , for a pulse length τ leading to a meta-stable skyrmion state. As seen from Fig. 4e, the topological charge changes during the initial part of the excitation and relaxation process, which can be identified from total energy per spin $\epsilon_{\text{tot}} = E/N$. However, after a time $t = 150$ ps, corresponding roughly to the phonon lifetime τ_{ph} , the topological charge is constant. Within the spin model the skyrmion state remains stable indefinitely, since additional energy would have to be supplied to bring the system back into the helical ground state. This is in good agreement with the experimental finding of a meta-stable skyrmion state surviving for several minutes.

V. CONCLUSION

In conclusion, we demonstrated the possibility of generating skyrmions in Cu_2OSeO_3 at low magnetic fields below the equilibrium skyrmion pocket by NIR

femtosecond laser pulses. Supported by the wavelength dependence and spin dynamics calculations, we claim that the irradiation of the sample results in the triggering of low-energy phonons which transiently change the DMI. As a consequence, these effects modify the free energy landscape of the material and enable the transformation of the magnetic state into the skyrmion lattice. The lifetime of the low-field skyrmion phase after the light-induced generation exceeds minutes, which is important for future magnetic data storage. The threshold fluences for the skyrmion photocreation at 5 K and 14 mT are 11 mJ/cm^2 and 0.06 mJ/cm^2 for 780 nm and 1200 nm, respectively. The latter is the lowest reported fluence required for generating skyrmions. Thus, our experiment marks a milestone in the development of energy-efficient skyrmion-based spintronics devices.

ACKNOWLEDGMENTS

We acknowledge support from the ERC consolidator grant ISCQuM and SNSF via sinergia nanoskyrmionics

grant 171003. The authors would like to gratefully acknowledge Prof. A. Rosch, Dr. N. del Ser, and Prof. J. Zang for helpful discussions and the comments related to the theory part of the manuscript.

-
- [1] S. Woo, K. Litzius, B. Krüger, M.-Y. Im, L. Caretta, K. Richter, M. Mann, A. Krone, R. M. Reeve, M. Weigand, P. Agrawal, I. Lemesch, M.-A. Mawass, P. Fischer, M. Kläui, and G. S. D. Beach, *Nature Materials* **15**, 501 (2016).
- [2] A. Fert, N. Reyren, and V. Cros, *Nature Reviews Materials* **2** (2017).
- [3] C. Back, V. Cros, H. Ebert, K. Everschor-Sitte, A. Fert, M. Garst, T. Ma, S. Mankovsky, T. L. Monchesky, M. Mostovoy, N. Nagaosa, S. S. P. Parkin, C. Pfleiderer, N. Reyren, A. Rosch, Y. Taguchi, Y. Tokura, K. von Bergmann, and J. Zang, *Journal of Physics D: Applied Physics* **53**, 363001 (2020).
- [4] S. Luo and L. You, *APL Materials* **9**, 050901 (2021).
- [5] Y. Tokura and N. Kanazawa, *Chemical Reviews* **121**, 2857 (2020).
- [6] I. Stasinopoulos, S. Weichselbaumer, A. Bauer, J. Waizner, H. Berger, S. Maendl, M. Garst, C. Pfleiderer, and D. Grundler, *Applied Physics Letters* **111**, 032408 (2017).
- [7] C. Schütte and M. Garst, *Physical Review B* **90**, 10.1103/physrevb.90.094423 (2014).
- [8] J. Iwasaki, A. J. Beekman, and N. Nagaosa, *Physical Review B* **89**, 10.1103/physrevb.89.064412 (2014).
- [9] X. Yu, F. Kagawa, S. Seki, M. Kubota, J. Masell, F. S. Yasin, K. Nakajima, M. Nakamura, M. Kawasaki, N. Nagaosa, and Y. Tokura, *Nature Communications* **12**, 10.1038/s41467-021-25291-2 (2021).
- [10] S. Seki, X. Z. Yu, S. Ishiwata, and Y. Tokura, *Science* **336**, 198 (2012).
- [11] Q. Shao, Y. Liu, G. Yu, S. K. Kim, X. Che, C. Tang, Q. L. He, Y. Tserkovnyak, J. Shi, and K. L. Wang, *Nature Electronics* **2**, 182 (2019).
- [12] A. Chacon, L. Heinen, M. Halder, A. Bauer, W. Simeth, S. Mühlbauer, H. Berger, M. Garst, A. Rosch, and C. Pfleiderer, *Nature Physics* **14**, 936 (2018).
- [13] N. Ogawa, S. Seki, and Y. Tokura, *Scientific Reports* **5** (2015).
- [14] R. B. Versteeg, I. Vergara, S. D. Schäfer, D. Bischoff, A. Aqeel, T. T. M. Palstra, M. Grüninger, and P. H. M. van Loosdrecht, *Physical Review B* **94** (2016).
- [15] Y. Okamura, F. Kagawa, S. Seki, and Y. Tokura, *Nature Communications* **7** (2016).
- [16] A. J. Kruchkov, J. S. White, M. Bartkowiak, I. Živković, A. Magrez, and H. M. Rønnow, *Scientific Reports* **8** (2018).
- [17] P. Huang, M. Cantoni, A. Kruchkov, J. Rajeswari, A. Magrez, F. Carbone, and H. M. Rønnow, *Nano Letters* **18**, 5167 (2018).
- [18] I. Levatić, P. Popčević, V. Šurija, A. Kruchkov, H. Berger, A. Magrez, J. S. White, H. M. Rønnow, and I. Živković, *Scientific Reports* **6** (2016).
- [19] D. N. Basov, R. D. Averitt, and D. Hsieh, *Nature Materials* **16**, 1077 (2017).
- [20] B. Koopmans, G. Malinowski, F. D. Longa, D. Steiauf, M. Fähnle, T. Roth, M. Cinchetti, and M. Aeschlimann, *Nature Materials* **9**, 259 (2009).
- [21] D. Afanasiev, J. R. Hortensius, B. A. Ivanov, A. Sasani, E. Bousquet, Y. M. Blanter, R. V. Mikhaylovskiy, A. V. Kimel, and A. D. Caviglia, *Nature Materials* **20**, 607 (2021).
- [22] A. V. Kimel, A. Kirilyuk, P. A. Usachev, R. V. Pisarev, A. M. Balbashov, and T. Rasing, *Nature* **435**, 655 (2005).
- [23] M. Finazzi, M. Savoini, A. R. Khorsand, A. Tsukamoto, A. Itoh, L. Duò, A. Kirilyuk, T. Rasing, and M. Ezawa, *Physical Review Letters* **110** (2013).
- [24] G. Berruto, I. Madan, Y. Murooka, G. Vanacore, E. Pomarico, J. Rajeswari, R. Lamb, P. Huang, A. Kruchkov, Y. Togawa, T. LaGrange, D. McGrouther, H. Rønnow, and F. Carbone, *Physical Review Letters* **120** (2018).
- [25] F. Büttner, B. Pfau, M. Böttcher, M. Schneider, G. Mercurio, C. M. Günther, P. Hensing, C. Klose, A. Wittmann, K. Gerlinger, L.-M. Kern, C. Strüber, C. von Korff Schmising, J. Fuchs, D. Engel, A. Churikova, S. Huang, D. Suzuki, I. Lemesch, M. Huang, L. Caretta, D. Weder, J. H. Gaida, M. Möller, T. R. Harvey, S. Zayko, K. Bagschik, R. Carley, L. Mercadier, J. Schlappa, A. Yaroslavtsev, L. L. Guyard, N. Gerasimova, A. Scherz, C. Deiter, R. Gort, D. Hickin, J. Zhu, M. Turcato, D. Lomidze, F. Erdinger, A. Castoldi, S. Maffessanti, M. Porro, A. Samartsev, J. Sinova, C. Ropers, J. H. Mentink, B. Dupé, G. S. D. Beach, and S. Eisebitt, *Nature Materials* **20**, 30 (2020).
- [26] M. Möller, J. H. Gaida, S. Schäfer, and C. Ropers, *Communications Physics* **3** (2020).
- [27] N. R. da Silva, M. Möller, A. Feist, H. Ulrichs, C. Ropers, and S. Schäfer, *Physical Review X* **8** (2018).
- [28] G. Cao, S. Jiang, J. Åkerman, and J. Weissenrieder, *Nanoscale* **13**, 3746 (2021).
- [29] T. Malis, S. C. Cheng, and R. F. Egerton, *Journal of Electron Microscopy Technique* **8**, 193 (1988).
- [30] L. Piazza, D. Masiel, T. LaGrange, B. Reed, B. Barwick, and F. Carbone, *Chemical Physics* **423**, 79 (2013).
- [31] C. Phatak, A. Petford-Long, and M. D. Graef, *Current Opinion in Solid State and Materials Science* **20**, 107 (2016).
- [32] J. H. Yang, Z. L. Li, X. Z. Lu, M.-H. Whangbo, S.-H. Wei, X. G. Gong, and H. J. Xiang, *Phys. Rev. Lett.* **109**, 107203 (2012).
- [33] S. Seki, S. Ishiwata, and Y. Tokura, *Phys. Rev. B* **86**, 060403 (2012).
- [34] Y.-H. Liu, Y.-Q. Li, and J. H. Han, *Phys. Rev. B* **87**, 100402 (2013).
- [35] J. Wang, *Annual Review of Materials Research* **49**, 361 (2019).
- [36] Y. Ba, S. Zhuang, Y. Zhang, Y. Wang, Y. Gao, H. Zhou, M. Chen, W. Sun, Q. Liu, G. Chai, J. Ma, Y. Zhang, H. Tian, H. Du, W. Jiang, C. Nan, J.-M. Hu, and Y. Zhao, *Nature Communications* **12** (2021).

- [37] C. Feng, F. Meng, Y. Wang, J. Jiang, N. Mehmood, Y. Cao, X. Lv, F. Yang, L. Wang, Y. Zhao, S. Xie, Z. Hou, W. Mi, Y. Peng, K. Wang, X. Gao, G. Yu, and J. Liu, *Advanced Functional Materials* **31**, 2008715 (2021).
- [38] K. Shibata, J. Iwasaki, N. Kanazawa, S. Aizawa, T. Tanigaki, M. Shirai, T. Nakajima, M. Kubota, M. Kawasaki, H. S. Park, D. Shindo, N. Nagaosa, and Y. Tokura, *Nature Nanotechnology* **10**, 589 (2015).
- [39] L. Deng, H.-C. Wu, A. P. Litvinchuk, N. F. Q. Yuan, J.-J. Lee, R. Dahal, H. Berger, H.-D. Yang, and C.-W. Chu, *Proceedings of the National Academy of Sciences* **117**, 8783 (2020).
- [40] T. Nomura, X.-X. Zhang, S. Zherlitsyn, J. Wosnitza, Y. Tokura, N. Nagaosa, and S. Seki, *Phys. Rev. Lett.* **122**, 145901 (2019).
- [41] O. Janson, I. Rousochatzakis, A. A. Tsirlin, M. Belesi, A. A. Leonov, U. K. Rößler, J. van den Brink, and H. Rosner, *Nature Communications* **5**, 10.1038/ncomms6376 (2014).
- [42] E. V. Boström and C. Verdozzi, *Phys. Status Solidi B* **256**, 1800590 (2019).
- [43] S. Buhrandt and L. Fritz, *Phys. Rev. B* **88**, 195137 (2013).
- [44] M. Lakshmanan, *Philos. Trans. Royal Soc. A* **369**, 1280 (2011).
- [45] V. G. Baryakhtar and B. A. Ivanov, *Low Temp. Phys.* **41**, 663 (2015).
- [46] P. Depondt and F. G. Mertens, *Journal of Physics: Condensed Matter* **21**, 336005 (2009).
- [47] B. Berg and M. Lüscher, *Nucl. Phys. B* **190**, 412 (1981).
- [48] B. S. Shastry and B. I. Shraiman, *Phys. Rev. Lett.* **65**, 1068 (1990).
- [49] P. A. Fleury, S. P. S. Porto, and R. Loudon, *Phys. Rev. Lett.* **18**, 658 (1967).
- [50] P. A. Fleury and R. Loudon, *Phys. Rev.* **166**, 514 (1968).
- [51] E. V. n. Boström, T. S. Parvini, J. W. McIver, A. Rubio, S. V. Kusminskiy, and M. A. Sentef, *Phys. Rev. B* **104**, L100404 (2021).
- [52] N. Ogawa, S. Seki, and Y. Tokura, *Sci. Rep.* **5**, 9552 (2015).
- [53] R. Khoshlahni, A. Qaiumzadeh, A. Bergman, and A. Brataas, *Phys. Rev. B* **99**, 054423 (2019).
- [54] S. V. Kusminskiy, *Quantum Magnetism, Spin Waves, and Optical Cavities* (Springer International Publishing, 2019).

SUPPLEMENTAL METHODS

Calculation of the absorbed fluence

To determine the absorbed fluence, we consider a sample thickness $t = 150$ nm and an absorption length of either $l_{780\text{ nm}} = 1.5$ μm and $l_{1200\text{ nm}} = 30$ μm . Since $t \ll l_{780\text{ nm}}, l_{1200\text{ nm}}$, the absorbed fluence fraction can be approximated as t/l_λ . Thus, 10% and 0.5% of the incident fluence are absorbed at 780 nm and 1200 nm, respectively.

Equilibrium spin Hamiltonian

The magnetic structure of Cu_2OSeO_3 consists at the microscopic level of 16 Cu ions per unit cell, each carrying a magnetic moment of $|\mathbf{s}_i| \approx \hbar/2$. However, due a hierarchy of magnetic interaction strengths [41], the four spins on each pyramid of the pyrochlore lattice bind together to form effective magnetic moments of size $|\mathbf{S}_i| = \hbar$ living on a trillium lattice. After an additional coarse graining step, valid for magnetic structures where the magnetization is constant over distances comparable with the lattice size ($\nabla \cdot \mathbf{M} \ll a$), the effective spin Hamiltonian in equilibrium is

$$H_0 = \sum_{\langle ij \rangle} [J \mathbf{m}_i \cdot \mathbf{m}_j + \mathbf{D}_{ij} \cdot (\mathbf{m}_i \times \mathbf{m}_j)] \quad (2)$$

$$+ \sum_i \mathbf{B} \cdot \mathbf{m}_i.$$

For Cu_2OSeO_3 the skyrmion radius is $r = 50.89$ nm, compared to the lattice parameter $a = 8.91$ Å, such that the coarse graining procedure is justified. To describe the magnetization dynamics we employ a three-dimensional square lattice with $40 \times 40 \times 10$ lattice points. The magnetic moments are normalized to $|\mathbf{m}_i| = 1$, and all interaction parameters are measured in units of the exchange interaction $J_0 = 48.2$ meV. This gives the effective parameters $J = 1$, $D = 0.224$ and $B = 0.013$, corresponding to 20.7 mT, in agreement with previous work [41].

Simulated annealing and Metropolis Monte Carlo

The equilibrium magnetic phase diagram is found by simulated annealing down to a target temperature $k_B T/J_0 = 0.02$ using the Metropolis Monte Carlo algorithm [42], corresponding to $T \approx 1$ K. To minimize stochastic effects in the phase diagram and the subsequent dynamics, each step involves 2000 thermalization sweeps followed by an average over 2000 Monte Carlo realizations with 40 sweeps each. In agreement with previous work [43], we find four competing equilibrium phases: a ferromagnetic phase, a helical spiral phase, a conical phase and a skyrmion crystal (SkX) phase.

Equations of motion

The magnetization dynamics is governed by the Landau-Lifshitz-Gilbert (LLG) equation [44, 45], which in the present case reads

$$\frac{\partial \mathbf{m}_i}{\partial t} = -\gamma \mathbf{m}_i \times \frac{\delta H}{\delta \mathbf{m}_i} - \lambda \mathbf{m}_i \times \left(\mathbf{m}_i \times \frac{\delta H}{\delta \mathbf{m}_i} \right). \quad (3)$$

Here the effective magnetic field acting on magnetic moment \mathbf{m}_i is given by the functional derivative of the total Hamiltonian H with respect to \mathbf{m}_i . The parameters $\gamma = 1/(1 + \alpha^2)$ and $\lambda = \alpha/(1 + \alpha^2)$ take into account the phenomenological damping constant α , which for Cu_2OSeO_3 is on the order of 10^{-4} . The LLG equation is solved by geometric Depondt-Mertens algorithm [46].

Light-matter coupling

The dominant light-matter coupling mechanisms considered here are Raman excitation of phonons and magnons, an effective magnetic field generated by the inverse Faraday effect, and a direct magneto-electric coupling via the spontaneous polarization [10, 32, 34]. Several studies have found a strong dependence of the Dzyaloshinskii-Moriya interaction (DMI) on strain [38, 39] as well as on a dynamical coupling to acoustic phonons [40]. To describe such mechanisms we consider the total Hamiltonian $H(t) = H_0 + H_I(t)$, with the time-dependent interaction Hamiltonian

$$H_I(t) = \sum_{\langle ij \rangle} [J_{ij}(t) \mathbf{m}_i \cdot \mathbf{m}_j + \mathbf{D}_{ij}(t) \cdot (\mathbf{m}_i \times \mathbf{m}_j)] \quad (4)$$

$$+ \sum_i [\mathbf{B}(t) \cdot \mathbf{m}_i - \mathbf{E}(t) \cdot \mathbf{P}_i],$$

The exchange interaction $J_{ij} = g_R(t)(\mathbf{e}_{\text{sc}} \cdot \mathbf{d}_{ij})(\mathbf{e}_{\text{in}} \cdot \mathbf{d}_{ij})$ is modified to take into account magnon Raman processes, the inverse Faraday effect generates an effective field $\mathbf{B}(t) = g_{\text{IFE}} \mathbf{E}^*(t) \times \mathbf{E}(t)$, and the magneto-electric effect is described by a coupling to the polarization $\mathbf{P}_i = g_{\text{m-el}}(S_i^y S_i^z, S_i^z S_i^x, S_i^x S_i^y)$. Assuming a uniform excitation of acoustic phonons with momenta $\mathbf{k} \approx 0$ gives an isotropic modification of the DMI strength $\mathbf{D}(t) = \mathbf{D}(1 - g_{\text{m-ph}}(t))$, where $g_{\text{m-ph}}(t)$ is proportional to the time-dependent average phonon amplitude. Since the phonon dynamics of Cu_3OSeO_2 is very complex, we here use a phenomenological description of $g_{\text{m-ph}}(t)$ as a log-normal function, with an onset determined by the laser electric field and a decay related to the phonon lifetime τ_{ph} . The laser electric field is described by a normalized Gaussian envelope of width σ and peak time τ .

Time-dependence of the magnetic parameters

The excitation mechanisms discussed above are associated with different characteristic time-scales. In particu-

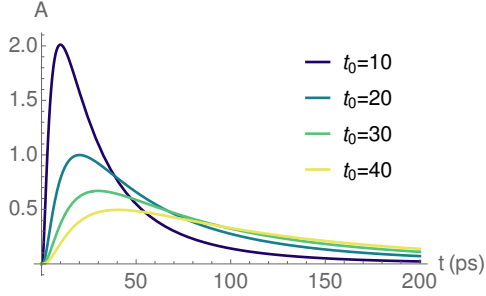


FIG. S1. **Time-dependence of magnon-phonon interaction.** Examples of log-normal functions with peak time t_0 as used to model time-dependence of the magnon-phonon interaction.

lar, both the magnon Raman processes, inverse Faraday effect and magneto-electric effects are impulsive in the sense that they only are present during the action of the laser pulse. In contrast, the magnon-phonon coupling is expected to persist for as long as there are phonons in the system. Since the magnetic moments have a characteristic time-scale of about 1 ps, while a single optical cycle of the laser is around 1 fs, the magnetic moments are assumed to only respond to the average field given by the pulse envelope.

Under these assumptions, the first three mechanisms satisfy $g_i(t) = g_i f(t)$ for $g_i \in \{g_R, g_{\text{IFE}}, g_{\text{m-el}}\}$ and can be described by a Gaussian time-dependence of the form

$$f(t) = \frac{1}{\tau\sqrt{2\pi}} \exp[-(t - t_0)^2 / (2\tau^2)], \quad (5)$$

where τ is the pulse width and t_0 the time of peak intensity. In contrast, the magnon-phonon coupling is modeled by the log-normal function

$$g_{\text{m-ph}}(t) = \frac{g_{\text{m-ph}}}{t\sigma\sqrt{2\pi}} \exp[-(\ln t - \mu)^2 / (2\sigma^2)] \quad (6)$$

Here the peak time is given by $t_0 = e^{\mu - \sigma^2}$, and the effective width (or skewness) by $\tau = (e^{\sigma^2} + 2)\sqrt{e^{\sigma^2} - 1}$. The width is assumed to be related to the phonon lifetime, which is assumed to be of the order of 100 ps. A few examples of the log-normal function for $\sigma = 1$ and different t_0 is given in Fig. S1.

A. Definition of the topological charge

To quantify the topology of the spin texture we use the lattice topological charge Q defined by [47]

$$Q = \frac{1}{4\pi} \sum_{\Delta} \Omega_{\Delta}. \quad (7)$$

In this definition the lattice is triangulated and Ω_{Δ} corresponds to the signed area of the spherical triangle

spanned by three neighboring spins, given by [47]

$$\exp(i\Omega_{\Delta}/2) = \frac{1}{\rho} (1 + \mathbf{m}_i \cdot \mathbf{m}_j + \mathbf{m}_j \cdot \mathbf{m}_k + \mathbf{m}_k \cdot \mathbf{m}_i) \quad (8)$$

$$+ i\eta_{ijk} \mathbf{m}_i \cdot [\mathbf{m}_j \times \mathbf{m}_k]$$

$$\rho = \sqrt{2(1 + \mathbf{m}_i \cdot \mathbf{m}_j)(1 + \mathbf{m}_j \cdot \mathbf{m}_k)(1 + \mathbf{m}_k \cdot \mathbf{m}_i)},$$

where $\eta_{ijk} = +1$ (-1) if the path $i \rightarrow j \rightarrow k \rightarrow i$ is positively (negatively) oriented. The surface area Ω_{Δ} is well-defined everywhere except at the zero-measure set $\mathbf{m}_i \cdot (\mathbf{m}_j \times \mathbf{m}_k) = 0$ and $1 + \mathbf{m}_i \cdot \mathbf{m}_j + \mathbf{m}_j \cdot \mathbf{m}_k + \mathbf{m}_k \cdot \mathbf{m}_i < 0$, where $\exp(i\Omega_{\Delta}/2)$ has a branch cut.

The topological charge is a compact, convenient indicator of the presence of a non-trivial spin texture: For a single skyrmion $Q = -1$, for a single antiskyrmion $Q = 1$, and for a cluster of skyrmions and antiskyrmions $Q = \sum_i Q_i$ with Q_i their individual charges.

SUPPLEMENTAL NOTE: ESTIMATED MAGNITUDE OF LIGHT-MATTER COUPLINGS

As discussed in detail in the following sections, the magnon Raman coupling gives a modulation ~ 10 % of the equilibrium exchange, the inverse Faraday effect is likely negligible, the magneto-electric effect gives a contribution of around ~ 1 % of the equilibrium exchange, while the spin-phonon coupling can give a modulation on the order of ~ 50 % of the equilibrium DMI.

Magnon Raman processes

An isotropic light-matter interaction arises due to the coupling of the laser to the charge of the electrons underlying the magnetic moments. For spin-1/2 systems, this coupling can be derived by considering a half-filled Mott insulator subject to an external electric field. The weak-field limit of this coupling reproduces the Raman vertex derived by Fleury and Loudon from general symmetry arguments [48–50], and is described by the Raman Hamiltonian [51]

$$H_R = \sum_{qq'} R_{\mathbf{q}\mathbf{q}'} a_{q'}^\dagger a_q \sum_{\langle ij \rangle} g_{ijqq'} \mathbf{m}_i \cdot \mathbf{m}_j \quad (9)$$

$$= \sum_{\langle ij \rangle} J_{ij} \mathbf{m}_i \cdot \mathbf{m}_j.$$

Here $R_{\mathbf{q}\mathbf{q}'} = J(ea/\hbar)^2 \gamma_{\mathbf{q}} \gamma_{\mathbf{q}'}$ is the strength of the Raman coupling, e is the electron charge, a the lattice parameter, \hbar Planck's constant, and J is the equilibrium exchange interaction. The function $\gamma_{\mathbf{q}}$ describes the strength of the one-photon vector potential, and the geometric factor $g_{ijqq'} = (\hat{\mathbf{e}}_q^* \cdot \mathbf{d}_{ij})(\hat{\mathbf{e}}_{q'} \cdot \mathbf{d}_{ij})$ encodes the underlying virtual electronic processes. To simplify the notation we have defined $q \equiv \{\mathbf{q}, s\}$ with s the polarization.

The leading order term of the Raman Hamiltonian describes a two-photon two-magnon process. To assess the strength of the light-matter coupling, we note that $\lambda_{R,\mathbf{q}} = R_{\mathbf{q}\mathbf{q}'}n_{\mathbf{q}}$ where $n_{\mathbf{q}}$ is the number of photons in the incident field. Using the fact that $n_{\mathbf{q}} = IV/(\hbar\omega_{\mathbf{q}}c)$ with the intensity $I = (cn\epsilon_0/2)E^2$, we have $\lambda_{R,\mathbf{q}} = (ea/\hbar\omega_{\mathbf{q}})^2(n/4)E^2$. Assuming that $a = 5 \text{ \AA}$, $E = 10^9 \text{ Vm}^{-1}$ and $n = 2.40$, we find $\lambda_R = 0.16$ with a characteristic energy scale $g_R = J\lambda_R = 7.7 \text{ meV}$.

Inverse Faraday effect

For a system with non-zero magnetization the dielectric tensor acquires nonzero off-diagonal elements and can be written as $\epsilon_{ij}(\mathbf{M}) = \epsilon_0(\epsilon_r\delta_{ij} - if\epsilon_{ijk}M_k)$. Here ϵ_0 is the vacuum permittivity, ϵ_r the relative permittivity, f is a small parameter related to the Faraday angle θ_F discussed below, and δ_{ij} and ϵ_{ijk} are the Kronecker and Levi-Civita tensors, respectively. Calculating the interaction energy in a volume V_c around each spin [52–54],

$$U(t) = -\frac{i\theta_F c\sqrt{\epsilon_r}\epsilon_0 a^3}{2\omega} \frac{\mathbf{M}(\mathbf{r})}{M_s} \cdot [\mathbf{E}^*(t) \times \mathbf{E}(t)], \quad (10)$$

the Faraday coupling is $\alpha_F = \theta_F V_c c\sqrt{\epsilon_r}$, where θ_F is the Faraday angle per unit distance, and $\mathbf{B}_F(t) = \epsilon_0/(2i\omega)[\mathbf{E}^*(t) \times \mathbf{E}(t)]$ is the effective optical spin density. The IFE coupling Hamiltonian is then written as

$$H_{\text{IFE}} = \alpha_F \mathbf{B}_F(t) \cdot \sum_i \mathbf{m}_i. \quad (11)$$

To estimate the light-matter coupling strength, we write the Faraday angle as $\theta_F = \mathcal{V}B$ where \mathcal{V} is the so-called Verdet constant, which is smaller than 100 rad/Tm. Taking $E = 10^9 \text{ V/m}$, $a = 5 \text{ \AA}$ and $\lambda = 1240 \text{ nm}$, giving $\hbar\omega = 1 \text{ eV}$, we find the characteristic energy scale $g_{\text{IFE}} = \alpha_F |\mathbf{B}_F| = 4.3 \times 10^{-4} \text{ meV}$.

Magnetoelectric coupling

Due to the multiferroic nature of Cu_2OSeO_3 there is a direct magnetoelectric coupling proceeding with $d-p$ hybridization [10]. The resulting magnetoelectric coupling Hamiltonian is

$$H_{\text{m-el}} = -\mathbf{E} \cdot \sum_i \mathbf{P}_i \quad (12)$$

$$\mathbf{P}_i = \gamma(S_i^y S_i^z, S_i^z S_i^x, S_i^x S_i^y).$$

In Refs. [10, 34] the coupling constant γ is estimated to the value $\gamma = 5.64 \cdot 10^{-27} \text{ \mu Cm}$ by comparison to experiment. This gives, for an electric field of $E = 10^9 \text{ Vm}^{-1}$, an interaction energy of $g_{\text{m-el}} \approx 10^{-23} \text{ J}$ or equivalently $g_{\text{m-el}} \approx 1 \text{ meV}$.

Magnon-phonon coupling

The spin-phonon coupling of Cu_2OSeO_3 has been discussed in the context of non-reciprocal magnon propagation [40], where a coupling Hamiltonian of the form

$$H_{\text{s-ph}} = \gamma D \partial_z u_x (S_i^y S_j^z - S_i^z S_j^y) + \gamma D \partial_z u_y (S_i^z S_j^x - S_i^x S_j^z)$$

was derived for a phonon propagating along the z -direction. Assuming acoustic phonons propagating along all cubic axes are excited with the same probability, this gives a spin-phonon coupling Hamiltonian

$$H_{\text{s-ph}} = \gamma \mathbf{D} \cdot (\mathbf{S}_i \times \mathbf{S}_j) \quad (13)$$

where the DMI vector has been shifted according to the following

$$\begin{aligned} D_x &= D_{x0}(1 + \gamma[\partial_y + \partial_z]u_x) \\ D_y &= D_{y0}(1 + \gamma[\partial_z + \partial_x]u_y) \\ D_z &= D_{z0}(1 + \gamma[\partial_x + \partial_y]u_z). \end{aligned} \quad (14)$$

To estimate the size of the DMI modulation, we note that in Ref. [40] the value of γ was estimated to be in the range $\gamma = 50 - 90$ by fitting the calculated magneto-chiral effect towards experiment. With an estimate of the phonon derivatives of $\partial_j u_i \approx k_j u_i \approx 0.01$, the spin-phonon coupling can still give a modulation of the DMI on the order of 50 %. This gives a characteristic energy scale of $g_{\text{m-ph}} = 0.5D = 5.4 \text{ meV}$. This large value is in line with previous studies, where the strain-induced modulation of the DMI has been found to be very large for a number of chiral magnets [38, 39].

Although the time-dependence of the phonon coordinate u could in principle be obtained by a full dynamical simulation of the coupled vibrational modes of Cu_2OSeO_3 , such a calculation becomes prohibitive in practice due to the complexity of the system. Here we instead take a phenomenological approach and parameterize the time-dependence of the DMI with a log-normal function, whose onset is determined by the pulse parameters of the laser electric field and whose decay is set by the lifetime of the phonon modes.

Considering the presence of an external magnetic field

As complementary information, we numerically investigated the skyrmion creation process with the presence of an in-plane magnetic field, which has been shown to reduce the skyrmion stability drastically [285] (discussed in section 6.1.3). To establish the role of magnetic fields for the skyrmion excitation, we compared the effect of adding either a normal or ab in-plane magnetic field pulse to the modulation of the DMI (see Fig. 4.11). While the direction of the magnetic field does not seem to be significant (at least in these calculations), having a magnetic field present increases the likelihood of creating skyrmions. However, it might be that there are parameter regimes where the direction of the field has more importance. More extensive calculations are therefore required to investigate this potential effect.

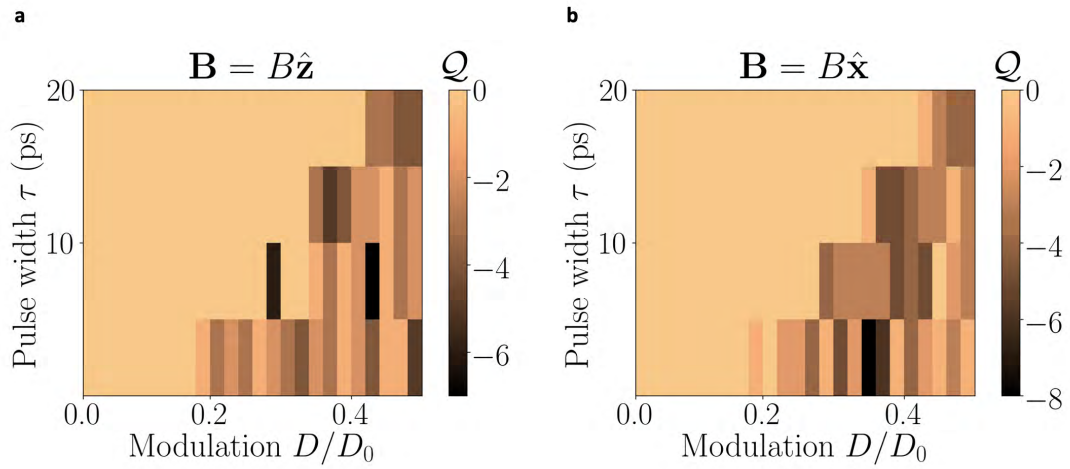


Figure 4.11 – **Skyrmion creation with the presence of a magnetic field.** Topological charge as a function of the phonon-modulated DMI D with (a) an out-of-plane magnetic field or with (b) an in-plane magnetic field.

4.4 Observation of a long-dynamics process after photoexcitation

At equilibrium, anomalous dissipation processes close to the topological phase transitions [277] have been identified. Furthermore, it is well known that strong magnetic fluctuations exist in Cu_2OSeO_3 assigned to substantial anisotropic effects [171, 267]. However, until now, information in real space has yet to exist, which is crucial for a complete understanding of both individual and collective magnetic behaviors. In addition, dissipating effects and relaxation dynamics across an out-of-equilibrium TPT remain elusive. In this thesis, we tackled both aspects and presented exciting preliminary results. In particular, we unveiled a permanent fluctuating skyrmion state close to the conical phase, discussed in section 6.1.2. After topological phase transition induced upon ultrafast excitation, the skyrmions crystallize in a skyrmion lattice. By taking a series of LTEM images after the photo-creation, we detect a

collective behavior of the skyrmions that depends on the applied magnetic field.

To analyze the collective magnetic order dynamics process, I developed a homemade code to visualize the skyrmion order. The protocol followed is illustrated in Fig 4.12a-d. We found that the long-lived dynamics depend on the applied field strength and orientation. At 14 mT, a dominant anticlockwise rotation of the skyrmion lattice is observed up to one minute after the photoexcitation (Fig. 4.13a). At -18 mT, a similar effect is noticed with both senses of rotation (Fig. 4.13b). The rotation rate is $\sim 1^\circ/\text{s}$. Using a higher magnetic field stabilizes the skyrmion lattice fixing its orientation. Still, a fluctuating character is observed as the magnetic state oscillates between the skyrmion phase and a helical-like state shown in Fig. 4.12e-h. Interestingly, although -18 mT, and +14 mT are close in absolute value, two distinct behaviors are distinguished in the skyrmion collective response. Continuous rotation skyrmion rotation exists in the presence of a radial thermal gradient [213], and we have recently demonstrated that skyrmion breathing mode can induce an ultrafast skyrmion rotation [104] (Chapter 5). However, none of the effects can adequately explain our long-dynamics observation. Indeed, according to our simulations, no thermal gradient is expected after a few μs , and the breathing mode relaxes on the nanoseconds timescale. Moreover, performing magnetic simulation on a minutes timescale is currently beyond state-of-the-art. We speculated that the skyrmion rotation originates from the weak but non-negligible role of the skyrmion periodic potential order that favors a specific alignment. In that scenario, the skyrmions are first induced by the phonon-mediated mechanism described above and trapped in a metastable potential well with a given orientation preferred in that instantaneous state in the free energy landscape. The topological nature of the skyrmion prevents them from collapsing, and the skyrmion crystal rearranges slowly. As skyrmions are solitons, the process should occur on a fast time scale as no energy cost is required. However, in a real material, defects induce disorder in the energy landscape, which has to be overcome by the skyrmion system to relax toward its ground state. Consequently, the characteristic relaxation time is defined by the fluctuation strength and the disorder present in the material.

A second observation differentiates the -18 mT and +14 mT photo-skyrmions. At -18 mT, the skyrmions, although initially forming a single crystal (see Fig. 4.14b), progressively relax towards its true equilibrium state (helical). While, at +14 mT, the photo-generated skyrmions remain stable, and no decay was observed for the same time window investigated. Magnetic anisotropy interactions are probably responsible for the effect and have been shown to be important in Cu_2OSeO_3 [171, 267].

4.4. Observation of a long-dynamics process after photoexcitation

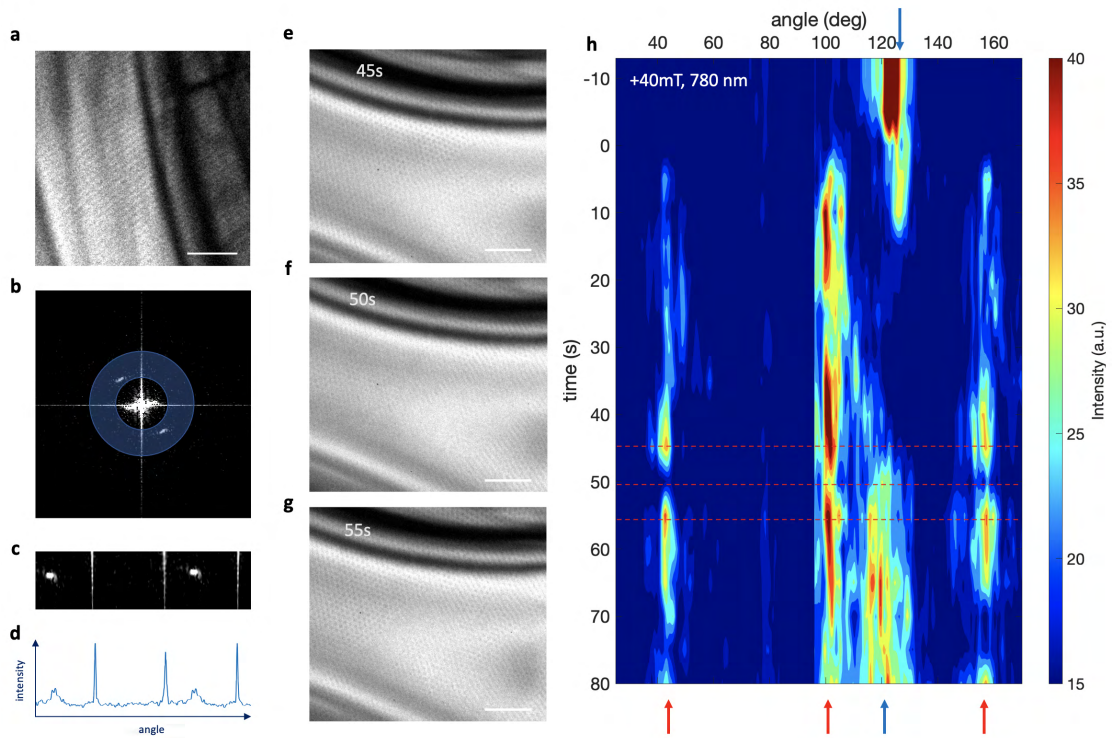


Figure 4.12 – **Fourier transform analysis and long-lived skyrmion fluctuation.** **a-d:** Example of the protocol followed in the Fourier transform analysis. First, the Fourier transform of the image **a** is computed. Using an annular mask shown in light blue in image **b** and unwrapping the obtained pattern, we obtained a strip containing the peak of the magnetic order (**c**). Finally, a vertical binning is applied to retrieve the profile illustrated in **d**. The white spikes are artifacts from the image edge, removed in our analysis. From the profile, we can construct a graph representing the time evolution of the profile, allowing us to visualize the evolution of the magnetic order. An example is given by the figure **h**. The blue (red) arrows show the signature of the helical (skyrmion) phase. **h:** Magnetic order dynamics following photoexcitation with an 780 nm single pulse of 80 fs and an incident fluence of 83 mJ/cm^2 . The system is initially prepared in the helical state. $t = 0$ corresponds to the pulse arrival. The skyrmion order appears and fluctuates, well represented by the intensity variation. Three real space LTEM images at three different times denoted by the red dashed line are shown in **e-g**. Image **f**, which corresponds to a weaker intensity in **h**, shows the presence of a conical phase and elongated skyrmions resembling to helices. The white scale bar corresponds to 500 nm. The dataset was acquired at 5 K and from the sample presented in Fig. 4.12h.

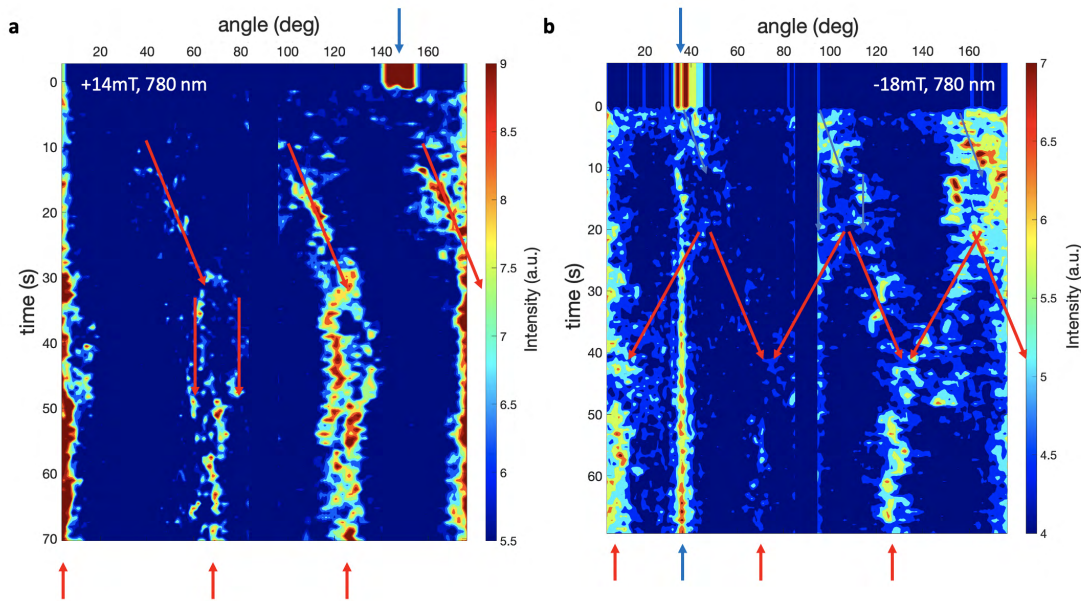


Figure 4.13 – **Clockwise and anticlockwise rotation of the photo-created skyrmion lattice.** Evolution of the magnetic order prepared initially in the helical state following photoexcitation with a 780 nm single pulse of 80 fs and an incident fluence of 83 mJ/cm^2 . The blue (red) arrows show the signature of the helical (skyrmion) phase. **a:** At 14 mT, positive field and below the critical field, an anticlockwise rotation and a splitting are observed. After 50 s, the lattice stabilizes. **b:** For the negative version also below the critical value, at -18 mT, the two senses of rotation are observed. Similarly, after 50 s, the lattice stabilizes. The incident fluence used in both cases is 83 mJ/cm^2 . All the dataset was acquired at 5 K.

4.5 Experimental limitations

The presented work was extremely challenging in many aspects as a large parameter space (wavelength, polarization, pulse duration, magnetic field amplitude, and orientation) was investigated, and due to contamination issues, different samples were investigated, increasing the analysis complexity, as the quantitative effect depends on the sample thickness and sample quality. Furthermore, each session is limited by the liquid helium holder to approximately 5 hours of measurement. The lifetime of each lamella is about 15 hours at cryogenic temperature as contamination starts to appear at the surface and hinders the magnetic contrast leading to measurement inconsistencies. In total, this work compiled more than two years of exploration and accounted for more than twenty cryo-LTEM sessions and ten different lamellae.

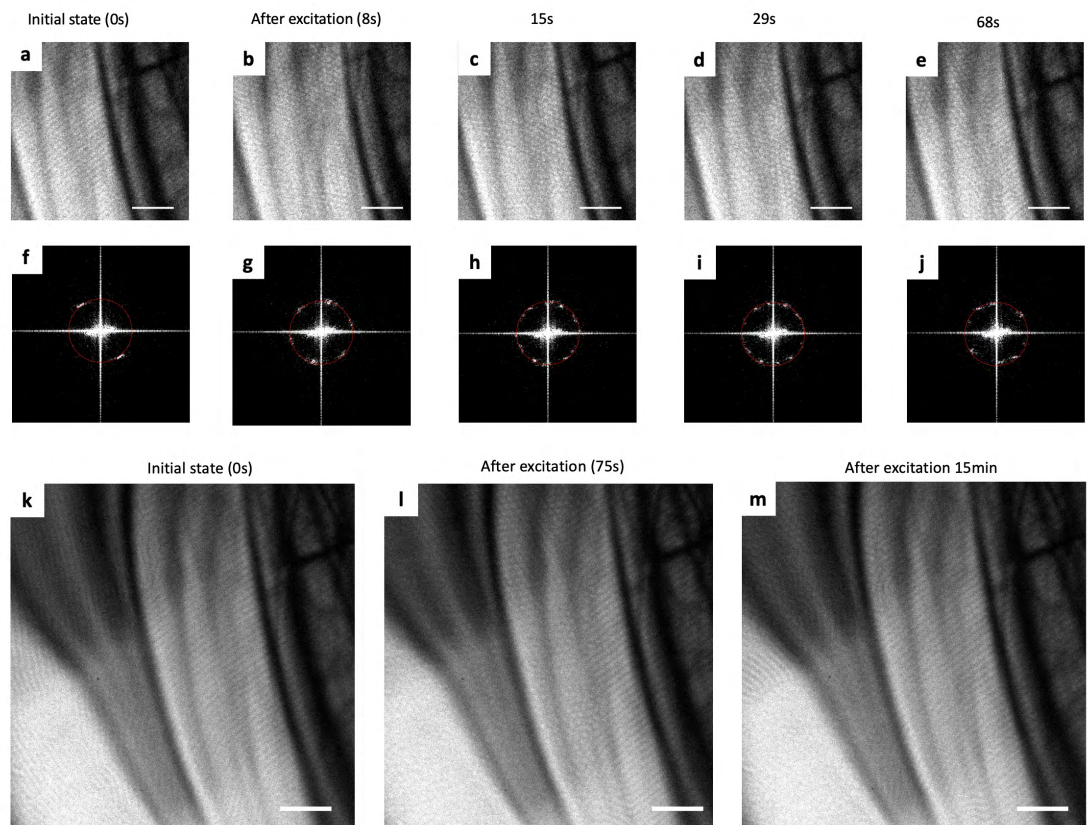


Figure 4.14 – **780 nm-skyrmion reordering and decay in -18 mT field.** **a-e:** Series of LTEM images, taken **a** before the photoexcitation and (**b-e**) after. After being created, the skyrmions rearranged and decayed back toward the helical phase. **f-j** shows the associated (upper image) FFT. **k-m** present a second data set with longer waiting time. Most skyrmions have decayed. The red circle has the same reciprocal length in all FFT figures. No change in pitch length is observed. The white scale bar corresponds to 500 nm. All images were acquired at 5 K.

4.6 Open questions

As pioneers in the out-of-equilibrium real space investigation of the complicated multiferroic Cu_2OSeO_3 , many questions have arisen along the study. To mention only a few, maybe the first question to address is how precisely the entire magnetic phase diagram is reshaped. In particular, can it quantitatively explain the skyrmion pocket shifting for the 1200 nm photo-excitation, and what about the 266 nm case? In the microscopic simulation, all acoustic phonons with near-zero momentum were considered; what would happen if we specifically trigger one phonon mode using lower energies in the mid-infrared range? The long-lived dynamics process merits clarification as it directly reflects the present disorder and the magnetic fluctuating energy. Finally, can we induce the reverse effect to erase the skyrmions? We tried to address the last question. Whereas using extremely high fluence, the skyrmion phase can be destroyed in some cases. We noticed that for a reasonably low-fluence regime, the laser pulse induced the skyrmion to rotate. This novel effect is presented in the next Chapter.

4.7 Conclusion

In this Chapter, we introduced and reviewed the remarkable Cu_2OSeO_3 properties. Harnessing its insulating nature, we investigated the skyrmion photo-creation using an ultrashort laser pulse. A strong wavelength dependence is observed that we associate with a phonon-mediated process using atomistic spin calculation. According to our simulation, the skyrmion formation established in approximately 120 ps, faster than the 500 ps reported in the metallic multilayered system [218]. We uncovered long-lived skyrmion dynamics that depend on the magnetic field. Although its clear origin must be clarified, we anticipate an essential role of the magnetic disorder in the magnetic free energy and the inherent magnetic fluctuation. In summary, our work provides the first demonstration of the magnetic free energy landscape manipulation that leads to a topological phase transition. Thus, we expect profound consequences in the study of out-of-equilibrium TPT and the Kibble-Zurek mechanism, as well as in technological application as we provide a milestone for future ultrafast energy-efficient spintronic devices.

5 Road to ultrafast topological emergent magnetism

In this work, we image the nanoscale dynamics of an irreversible magnetic process and show that they take place on picosecond timescales. In doing so, we control the rotation of a skyrmion crystal in a topological magnet with a timescale much faster than anything achieved before, using individual femtosecond laser pulses. To place our work in context, extensive experimental and theoretical studies on skyrmion dynamics previously demonstrated the capability to rotate the skyrmion crystal via electrical or spin currents applied either with electrical connections or a focused high-energy electron beam (much stronger than the one used in our microscope). Our work differs from these earlier studies (see for example ref. [213]) because femtosecond laser pulses offer the capability to perform the manipulation in an ultrafast, controlled and contact-free manner. Furthermore, tuning the laser pulse parameters: polarization, fluence, timing, and spatial distribution, provides us with a unique flexibility in achieving deterministic skyrmion control. Our discovery was made possible by the combination of the extremely high magnetic spatial resolution in a transmission electron microscope operated in Lorenz force mode with ultrafast and precise in-situ excitation using near infrared femtosecond laser pulses. The hysteretic nature of the material allowed us to manipulate the magnetic order in a stable manner, i.e. the magnetic ordering changes in a quantitative way after each laser pulse and remains in that configuration until the system is perturbed again. A new experimental protocol we designed based on this principle provided us with some truly spectacular results that yield insight into the fundamental mechanisms responsible. We then joined forces with several eminent theorists in the field to provide a convincing theoretical description of the observed dynamics. Together, this work will have a very significant impact on information technology and spintronics research, since the manipulation of skyrmions in an ultrafast, highly efficient, and contact-free manner has far reaching implications for state-of-the-art logical devices based on topological ordering such as racetrack memory. We are convinced that our work will guide the development of future spintronics devices. This work is the result of a many-years experimental effort and a true breakthrough in ultrafast spintronics and magnetic imaging.

Contribution

My contribution covers all the experimental aspects, from the laser beam line installation to the data acquisition. Furthermore, I had the chance to be the first to realize the effect during my analysis. The experimental investigation reported in ref. [104] was carried out along with P. Tengdin and A. A. Sapozhnik. The inverted polarity dataset was acquired by myself and F. Truc. OAM beam investigation was carried out by myself with the help of A. A. Sapozhnik. I performed the entire data analysis and contributed to the theoretical effort, as I proposed the conservation of angular momentum as the leading mechanism. I. Madan and T. LaGrange gave experimental support. The complete theory and micromagnetic simulation were performed by L. Kong and N. Del Ser under the supervision of our collaborators J. Zang and A. Rosch. Simulations of the thermal load response were performed by S. Gargiulo. The TEM lamellae were provided by T. Schönenberger and P. Che. Crystals were grown by P. R. Baral, and A. Magrez. F. Carbone supervised this work.

5.1 Light for efficient ultrafast control in spintronics

In 1947, an enormous breakthrough was achieved at Bell Laboratories in the field of semiconductors which will revolutionize our modern society. The first transistor has just been invented. Still used today, there are ubiquitously integrated into our daily electronic devices [286]. A permanent race rages between the various large semiconductor companies to increase the integrated transistor density, following Moore's law [287]. Indeed, more dense rhymes with more efficient. Today, miniaturization has exceeded the 100 million transistors per mm^2 , or 100 transistors per μm^2 , approaching the ultimate density defined by quantum effects that emerge in that spatial scale [288]. One possible way to overcome this issue and build the next-generation nanodevices is to reduce the dimensionality and use 2D materials [289–293]. On the other hand, using the electron spin property instead of his charge has tremendous potential as it provides low-power consumption, high-speed and high-density memory, and can also benefits from the ultimate thickness of 2D materials [294]. This breathtaking field is named spintronics. Beyond miniaturizing conventional electronic devices, manipulating spins has a profound impact on the Quantum World, as it can realize quantum functionalities. Indeed, many quantum applications rely on the spin properties such as quantum computing and information [295, 296], quantum sensing [297–301] and, quantum metrology [302, 303], to mention only a few. In data storage, spintronics has already found its place in our daily life [304–306] driven by the discovery of the giant magneto-resistance effect in 1988 [307, 308]. Nevertheless, with the constant production of data, which consequently induces a higher energy demand, we must upgrade our current technologies and pursue the hunt for energy-efficient, and ultra-dense development [309–311]. As this emerging field is at the nanometre level, quantum effects [312, 313] and defects [314] become relevant. Hence, a deep fundamental understanding of the underlying principles and advanced experimental realizations and demonstrations are required. In the last decades, a considerable effort has been engaged in the quest to master spin properties [294, 312, 315–317]. Manipulation of

spin state has been achieved using electrical current [318, 319], electric field [311, 320–322], magnetic field [312, 323, 324], or mechanical resonator [325, 326]. Among all means, optical control has a special place as it allows non-invasive ultrafast manipulation of individual spin [327–329] and larger spin complex forming a magnetic order [279, 280, 312]. Skyrmion, a specific spin arrangement consisting of whirling spins, has attracted the attention of physicists due to its peculiar topological properties (see Chapter 3). In spintronics, skyrmion-based devices stand out as magnetic unit as it combines efficient control, robustness, and nanometre size, ideal for ultra-dense and low-consumption devices [14] and neuromorphic computing [159]. Laser-induced skyrmion formation and deletion have been demonstrated in FeGe [217], multilayered system [218], ultrathin films [330] and recently in an insulating material [219] with a nucleation process in the sub-nanoseconds regime. In order to be useful in real devices, beyond creation and erasing, skyrmion control is needed. We can distinguish two categories to control the skyrmion lattice orientation. One modifies the intrinsic properties of the skyrmion host materials inducing a new equilibrium [257]. The second approach differs as a continuous skyrmion rotation is observed in the presence of the external trigger. In particular, such processes were experimentally demonstrated by using magnon-current induced by thermal gradient [213] and the combination of dissipation, temperature fluctuations, and magnetic field gradient [284]. Both processes lead to a rotation rate of 10^0 - 10^1 degrees per second, leaving a crucial question: Can we use light to rotate the skyrmion lattice non-thermally at an ultrafast timescale? Hence, paving the way for ultrafast topological magnetism.

5.2 Ultrafast coherent control of a skyrmion crystal in Cu_2OSeO_3

To address this question, we choose our favorite skyrmion host-materials Cu_2OSeO_3 as it reduces thermal effect drastically. Furthermore, in that materials, sub-ns collective spin excitations are known to be triggered by the inverse Faraday effect upon ultrafast NIR circularly polarized excitation [280]. Moreover, IFE has a non-thermal origin and enables coherent control [33]. Therefore, it is reasonable to expect triggering a skyrmion rotation by the spin current photo-induced, depending on the light polarization. Using LTEM, a real space magnetic imaging technique to investigate the proposed effect, we demonstrated the rotation of a skyrmion crystal at a speed of 10^8 - 10^{10} degrees per second. This high-speed rotation is possible by a novel mechanism exploiting the collective nature of the skyrmion lattice. In detail, the laser pulse drives a collective magnetic mode, named breathing mode, which progressively relaxes due to Gilbert damping. Invoking the conservation of angular momentum, a rotational torque is applied to the skyrmion lattice leading to the rotation. Remarkably, as the process relies on a collective periodic mode, it can be coherently manipulated by adjusting the time delay between a laser pulse sequence. Consequently, the skyrmion orientation can be deterministically defined and changed in an ultrafast and energy-efficient fashion. From another perspective, this work demonstrated the manipulation in real space of a few spins orientation at an ultrafast time scale, vital for next-generation spintronics devices. This work is synthesized in ref. [104], and is presented below.

Imaging the Ultrafast Coherent Control of a Skyrmion Crystal

Phoebe Tengdin^{1,*}, Benoit Truc^{1,*}, Alexey Sapozhnik^{1,*}, Lingyao Kong,² Nina del Ser³, Simone Gargiulo¹, Ivan Madan,¹ Thomas Schönenberger,⁴ Priya R. Baral⁵, Ping Che⁶, Arnaud Magrez⁵, Dirk Grundler,^{6,7} Henrik M. Rønnow,⁴ Thomas Lagrange,¹ Jiadong Zang,^{3,8} Achim Rosch,³ and Fabrizio Carbone^{1,†}

¹*Institute of Physics, LUMES, École Polytechnique Fédérale de Lausanne (EPFL), Lausanne, Switzerland*

²*School of Physics and Optoelectronics Engineering Science, Anhui University, Hefei 230601, China*

³*Institute for Theoretical Physics, University of Cologne, Köln, Germany*

⁴*Institute of Physics, LQM, École Polytechnique Fédérale de Lausanne (EPFL), Lausanne, Switzerland*

⁵*Institute of Physics, Crystal Growth Facility, Ecole Polytechnique Fédérale de Lausanne (EPFL), Lausanne, Switzerland*

⁶*Institute of Materials (IMX), Laboratory of Nanoscale Magnetic Materials and Magnonics, Ecole Polytechnique Fédérale de Lausanne (EPFL), Lausanne, Switzerland*

⁷*Institute of Electrical and Micro Engineering, Ecole Polytechnique Fédérale de Lausanne (EPFL), Lausanne, Switzerland*

⁸*Department of Physics and Astronomy, University of New Hampshire, Durham, New Hampshire, USA*



(Received 22 July 2022; revised 13 September 2022; accepted 16 November 2022; published 20 December 2022)

Exotic magnetic textures emerging from the subtle interplay between thermodynamic and topological fluctuation have attracted intense interest due to their potential applications in spintronic devices. Recent advances in electron microscopy enable the imaging of random photogenerated individual skyrmions. However, their deterministic and dynamical manipulation is hampered by the chaotic nature of such fluctuations and the intrinsically irreversible switching between different minima in the magnetic energy landscape. Here, we demonstrate a method to coherently control the rotation of a skyrmion crystal by discrete amounts at speeds which are much faster than previously observed. By employing circularly polarized femtosecond laser pulses with an energy below the band gap of the Mott insulator Cu_2OSeO_3 , we excite a collective magnon mode via the inverse Faraday effect. This triggers coherent magnetic oscillations that directly control the rotation of a skyrmion crystal imaged by cryo-Lorentz transmission electron microscopy. The manipulation of topological order via ultrafast laser pulses shown here can be used to engineer fast spin-based logical devices.

DOI: [10.1103/PhysRevX.12.041030](https://doi.org/10.1103/PhysRevX.12.041030)

Subject Areas: Condensed Matter Physics, Magnetism
Spintronics

I. INTRODUCTION

When an electron traverses a skyrmion's magnetic structure, the topological ordering causes the electron's spin to pick up a Berry phase. This produces a Lorentz force on the electron as well as a net force on the skyrmion oriented perpendicular to the flow of electric current, known as the Skyrmion Hall effect [1,2]. The effect provides a greatly enhanced coupling of electric current to the magnetic texture, much more efficient than for current-driven manipulation of domain walls [3,4]. In analogy to the case

of electric current, skyrmions present in an insulating host material are subject to similar forces when exposed to a pure spin current [5]. However, this process can proceed without the Ohmic losses that exist when using electrical current. Additionally, excitation of spins can be achieved in an ultrafast and contact-free manner using ultrafast lasers on femtosecond timescales [6,7].

The emergence of Cu_2OSeO_3 as a skyrmion hosting Mott insulating material with multiferroic properties and bulk Dzyaloshinskii-Moriya interaction opens the possibility to study and manipulate topological order and skyrmion dynamics purely under the influence of magnetic excitations or electric fields [8]. Additionally, spin currents and collective oscillations in Cu_2OSeO_3 are shown to have an exceptionally low damping and correspondingly long mean free path, making them effective candidates for manipulating spin order [9,10]. Recent works demonstrate the ability to rotate the skyrmion crystal in Cu_2OSeO_3 via thermally generated spin currents [11,12], electric fields

*These authors contributed equally to this work.

†fabrizio.carbone@epfl.ch

Published by the American Physical Society under the terms of the *Creative Commons Attribution 4.0 International license*. Further distribution of this work must maintain attribution to the author(s) and the published article's title, journal citation, and DOI.

[13,14], and a magnetic field gradient in doped crystals [15]. In Refs. [11,12], the spin currents are induced via the spin Seebeck effect with a strong local heat gradient generated from a high-power electron beam. For all previous experiments of this kind, the rotation proceeds on the timescale of hundreds of milliseconds to seconds. To increase the speed of these processes, faster excitation mechanisms are required.

Recent experiments show that circularly polarized femtosecond pulses of light can induce an effective magnetic field of up to 0.6 T in a material for timescales as short as 50–100 fs and drive switching of the magnetic order via the inverse Faraday effect [16–18]. Femtosecond light pulses can also generate spin excitations that have pulse widths in the femtosecond timescale and can travel up to ballistic speeds [19–23], and single pulses are used to trigger the generation of skyrmions in a ferromagnetic or helical background [24,25]. However, the microscopic details of spin excitation on ultrafast timescales are still not fully understood. Experiments investigating these excitations are ultimately constrained by a limited ability to directly image spins on the relevant length (nanometer) and time (femtosecond) scales and are furthermore limited by the inherently irreversible nature of many of the magnetic phenomena studied. The development of Lorentz force microscopy for imaging magnetic textures such as skyrmions coupled with ultrafast excitation of these structures constitutes a promising tool for enhancing the understanding of these spin excitations and their propagation.

In this work, we take advantage of the strong coupling between topological ordering and collective spin oscillations in Cu_2OSeO_3 to drive skyrmion rotational motion with single

femtosecond pulses of circularly polarized near-infrared light. After each individual laser pulse, we image the skyrmion crystal in real space via *in situ* cryo-Lorentz force transmission electron microscopy (LTEM). We show that with each laser pulse we rotate the skyrmion crystal by a controlled and irreversible amount. The magnitude of the rotation depends sensitively upon the polarization and fluence of the pulse. With time-varied double pulse measurements performed at the fluence threshold of the observed rotation, we show that this rotation process is driven by a collective magnon excitation that has a characteristic excitation period of approximately 175 ps. Furthermore, the rotation can be switched on and off in a coherent manner by changing the delay time between successive driving pulses with the appropriate polarization. Our conceptually new experimental protocol provides nanoscale images of irreversible modification of the skyrmion crystal orientation that correspond to picosecond dynamics in the material. Through real-space analysis of our images, we generate detailed mappings of the rotations present over macroscopic distances (tens of microns) with a precision that is limited only by the natural length scale of the skyrmions themselves (approximately 60 nm). Additionally, the energy of the light used for excitation (1 eV) is far beneath the band gap of the skyrmion host material, and, thus, control can be achieved with remarkably low values of absorbed fluence, potentially enabling future ultrafast and highly efficient devices.

II. EXPERIMENTAL RESULTS

Figures 1(a) and 1(b) show real-space cryo-LTEM underfocused images of the skyrmion crystal in Cu_2OSeO_3 discussed in this work. Figure 1(a) shows a

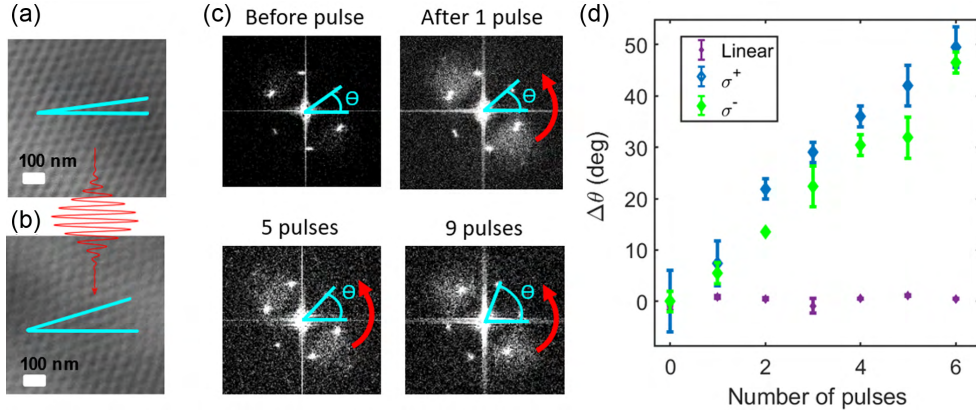


FIG. 1. Illustration and schematic of laser-driven skyrmion crystal rotation process. (a) Real-space images of skyrmion crystal in Cu_2OSeO_3 taken before excitation with the laser pulse and (b) after six successive near-infrared laser pulses each rotate the skyrmion crystal by a discrete amount. Note that the angle (depicted in blue) to the horizontal changes. (c) Fourier transforms of LTEM images following successive pulses of 8 mJ/cm² of near-infrared femtosecond laser excitation. The angle of the hexagonal ordering of the skyrmion crystal changes as a function of the number of pulses applied to the sample. (d) Tracking the position of a single peak in the FT of an image while pumping the sample with individual femtosecond laser pulses. Note that σ^+ and σ^- polarizations both rotate the skyrmion crystal in the same direction, while linear polarization does not rotate the skyrmion crystal. The error bars are 95% confidence intervals calculated from the data and multiplied by an uncertainty factor determined from the noise level in the data.

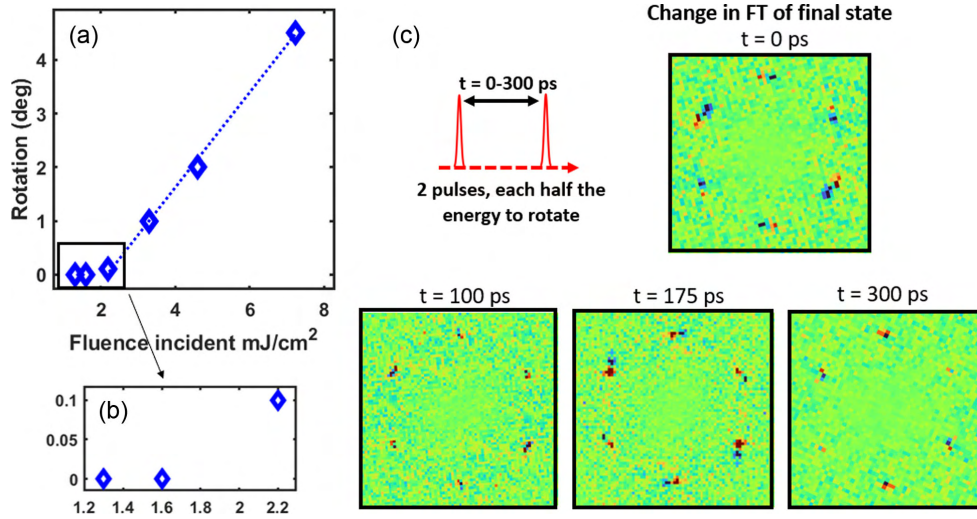


FIG. 2. Fluence and time dependence of skyrmion crystal rotation. (a) Fluence dependence of skyrmion crystal rotation. The dashed line is a linear fit to the data points with fluences from 1.6 to 8 mJ/cm². (b) Threshold value of fluence needed to drive rotation in the skyrmion crystal. This value of fluence (2.2 mJ/cm²) is split into two pulses and used to perform the double pulse time-resolved experiments described in (c). Two laser pulses, each with a fluence of 1.1 mJ/cm², are separated by a controlled delay. After the pulses excite the sample, a Lorentz image of the magnetization is recorded. The change in the Fourier transform of the images is shown for various time delays between pulses, illustrating that this time delay between the two pulses directly influences the observed rotation. For clarity, the observed changes are shown after the rotation is driven by 120 pairs of pulses.

metastable skyrmion crystal that forms when we cool the thin lamella from above the Curie temperature (approximately 60 K) to 5 K under an applied magnetic field of 34 mT. Further details of the complete phase diagram of the sample are provided in Supplemental Material [26]. Next, we irradiate the sample with individual femtosecond laser pulses having a waist much larger than the sample size (see Appendix A 1), after which we observe that the skyrmion crystal rotates. Figure 1(c) illustrates our procedure for tracking the rotation of the skyrmion crystal in the real-space TEM images. After each successive laser pulse, we take an image and then take the Fourier transform (FT) of the real-space image (or a subsection of an image) and calculate the angle of the FT in a polar coordinate system. We repeat this process, allowing us to map the change in the angle of the skyrmion crystal following a train of pulses of near-infrared radiation. Further details about the pulse train and imaging settings are given in Appendix A 1. In Fig. 1(d), we extract and plot the angle of a single peak in the FT of the skyrmion crystal after illuminating the sample with femtosecond pulses of light. For the circularly polarized light (both σ^+ and σ^-), each pulse rotates the skyrmion crystal by a discrete amount, with the direction of rotation being the same for both handednesses of polarization, while the linearly polarized light does not rotate the skyrmion crystal. This difference between the rotation of linear and circular polarizations implies that the circularly polarized pulses can drive excitation of magnons (the

quanta of spin current) on ultrafast timescales. The mechanism for this excitation is known to be inverse Faraday effect [27] and is discussed later in the text.

In Fig. 2(a), we plot the fluence dependence of the rotation process. We observe that the magnitude of rotation depends sensitively on the amount of laser fluence used in the experiment. In Fig. 2(b), we show that the threshold fluence needed to rotate the skyrmion crystal with circularly polarized light is >1.6 mJ/cm². Above this threshold, the rotation amount proceeds in a roughly linear fashion until 8 mJ/cm². We observe that pulses with energies above this value (approximately 10 mJ/cm²) can melt and reform the skyrmion crystal; thus, they cannot be used to rotate the crystal in a controlled way.

Following this fluence dependence, we study the threshold between rotation and nonrotation using a time-resolved technique. We split the photoexcitation pulse into two parts with equal value, and we measure the rotation of the skyrmion crystal as a function of the time delay between the two pulses, each with a fluence of 1.1 mJ/cm², corresponding to half of the required fluence for the skyrmion crystal rotation. When the pulses are combined into one pulse at time zero, the excitation is above the threshold where rotation occurs [see Fig. 2(a)]. In Fig. 2(c), we plot the difference in the Fourier transform of two images: one image taken before and one taken after two pulses are sent at the intervals indicated (0–300 ps). We observe that rotation occurs only when the pulses are sent at certain intervals.

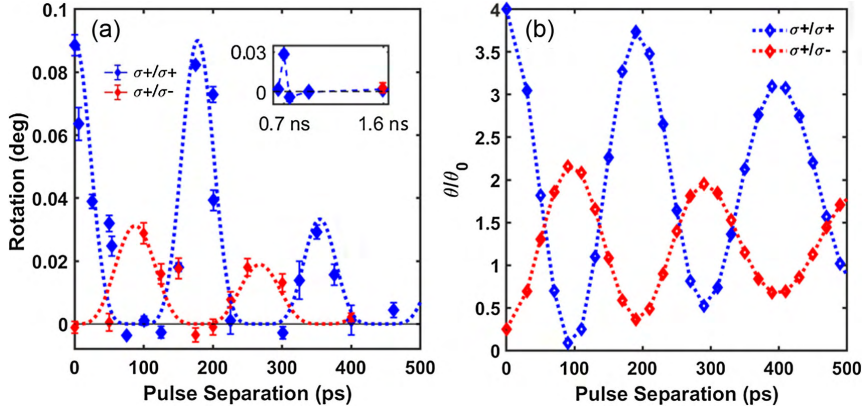


FIG. 3. Detailed time dependence of skyrmion crystal rotation. (a) Double pulse timed experiments showing the rotation of the skyrmion crystal observed as a function of the delay between the two pump pulses. The pulses either have both σ^+ polarization (blue points) or a sequence of σ^+/σ^- polarization (red points). For the blue points, we use pulses of equal amplitude (each with 1.1 mJ/cm^2) and observe a coherent oscillation in the amplitude of rotation with a period of 175 ps that damps out progressively over a nanosecond. For the case of σ^+/σ^- polarization, the second pulse of σ^- polarization has half the amplitude (0.6 mJ/cm^2) of the first one (1.1 mJ/cm^2 with σ^+ polarization). Here, we observe rotation with approximately half the amplitude out of phase with the previous oscillation. The blue and red dashed lines are a guide for the eye. Error bars (95% confidence intervals) are within the markers used. (b) Theoretical prediction of the rotation angle θ/θ_0 for such pulse sequences in a clean system where θ_0 is the rotation angle for a single pulse. The theory is based on the calculation of rotational torques arising from breathing-mode oscillations; see Supplemental Material [26].

This result is further investigated in Fig. 3. We plot the detailed time dependence of the skyrmion crystal rotation as a function of the pulse separation in Fig. 3(a). The blue data points are taken for a sequence of two right-handed circular (σ^+) polarized pulses. The time dependence of the rotation phenomenon shows an oscillation with a period of approximately 175 ps and a damping that takes place over the course of a nanosecond. This response can be attributed only to the launching of a coherent collective magnetic oscillation in the skyrmion crystal that drives the rotation process. For the red data points, we send one pulse with σ^+ polarization and a second pulse with left-handed circular polarization (σ^-) and slightly more than half the fluence value of the first pulse (0.6 mJ/cm^2). For a sequence of $\sigma^+ + \sigma^-$ pulses, we observe a coherent drive that is out of phase with the $\sigma^+ + \sigma^+$ sequence by 180° (approximately 87 ps). This is due to the polarization of the second pulse, which can excite a magnetic field with opposite direction to the first one via the inverse Faraday effect. The magnitude of the rotation also has a weaker amplitude due to the weaker amplitude of the second pulse, showing that the process roughly scales linearly as predicted in Figs. 2(a) and 2(b).

Next, we present a theoretical model that can help us to understand the origin of the collective excitation observed. We compute and show theoretically in Supplemental Material [26] that the combination of Gilbert damping, or another source of damping (e.g., disorder), and breathing-mode oscillations naturally leads to rotational torques, $T_{\alpha, \text{pump}}^R = -\alpha m_0 \int d^3\vec{r} (d\hat{n}/d\theta) \partial_t \hat{n} \propto (\delta M)^2$, where m_0 is the spin density, here we consider only Gilbert damping α ,

\hat{n} the direction of the magnetization, and $d\hat{n}/d\theta$ the change of the magnetization as a function of the rotation angle θ . For a clean system, we compute the rotation angle $\Delta\theta_{\alpha, \text{pump}}$ after a field pulse of amplitude δB and duration τ and obtain (see Supplemental Material [26])

$$\Delta\theta_{\alpha, \text{pump}} \approx \gamma_{\alpha, \text{pump}} \frac{1}{\alpha N_S} \left(\frac{\delta B}{B_0} \right)^2 \left(\frac{\tau}{T_0} \right)^2, \quad (1)$$

where T_0 is the period of the breathing mode, B_0 the static external magnetic field, N_S the number of skyrmions involved in the rotation, and $\gamma_{\alpha, \text{pump}} \approx 9.7^\circ$ a prefactor for a single pulse which we determine using numerical simulations; see Supplemental Material [26]. For a sequence of two pulses with relative delay time $\Delta\tau$, we show in Fig. 3(b) how the rotation angle changes as a function of $\Delta\tau$. This qualitatively reproduces the experimental result in Fig. 3(a). The remarkable match in the timescales of the experimental and theoretical data confirms that rotational torques induced by the breathing mode can explain our experiment.

Further analysis of our system shows that all rotations are well completed within 5 ns . If we assume a rotation timescale of $5\text{--}50 \text{ ns}$, we estimate an effective rotation rate of $2 \times 10^8\text{--}2 \times 10^7 \text{ deg/s}$; see Supplemental Material [26]. This rotation rate is more than 6 orders of magnitude faster than previously reported [11]. If we consider the case of coherent control, when the oscillations are stopped after a half period of 87 ps by a pulse of the appropriate amplitude, the effective rotation rate could even be increased to 2×10^{10} .

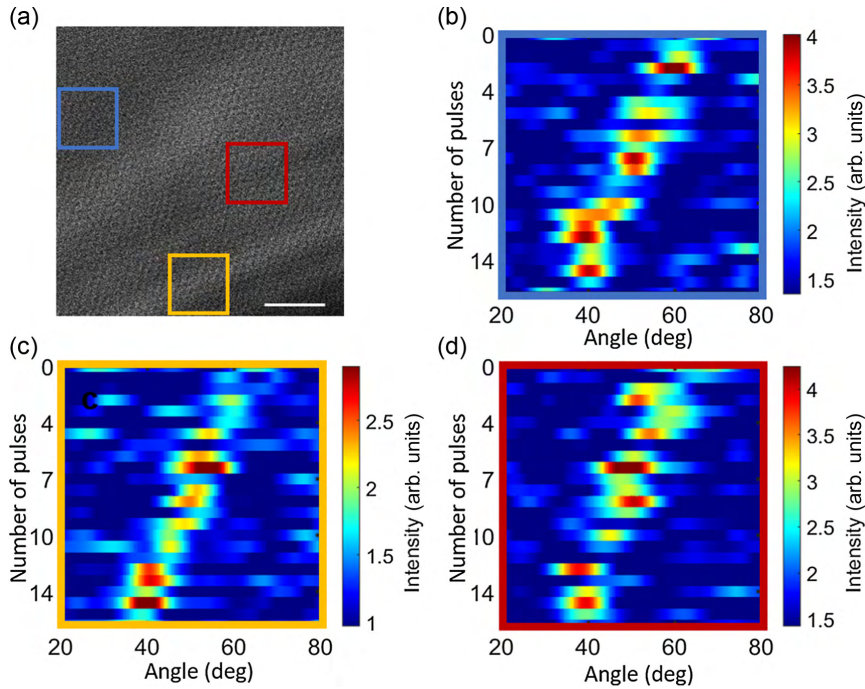


FIG. 4. Skymion crystal rotation in a real-space image from the TEM. (a) Real-space LTEM image of the magnetic structure in Cu_2OSeO_3 . The scale bar (bottom right) is 500 nm. Response of the skymion crystal after excitation by a femtosecond laser pulse train is shown for specific regions of the film in (b)–(d). Each pulse has an energy of 8 mJ/cm^2 . We take the FT of each subsection of the image and plot the angle of a single peak in the FT as a function of the number of pulses applied to the sample. The intensity corresponds to the intensity of the peak in the Fourier transform within a region of angles. See Supplemental Material [26] for rotational maps of the entire film.

In Fig. 4, we use our real-space image to map the rotation of the skymion crystal across macroscopic distances while again illuminating the sample with a train of femtosecond near-infrared (1 eV) laser pulses. We divide the real-space image in Fig. 4(a) into 25 individual boxes, for each of which we take the FT of the (sub)image and then plot the region around a single point in the FT. In Figs. 4(b)–4(d), we show cutouts of the rotation that takes place in different regions of the sample. See Supplemental Material [26] for additional plots of the rotation present in each subregion of a 5×5 grid of the sample. We find that, by analyzing subregions of the samples, we could better isolate the different regions of the skymion rotation, resulting in a higher-quality signal. For the data presented in Fig. 4, the grid size that leads to the best isolation of rotation regions corresponds to an analysis subregion of 460 nm . Since the skymion crystal period in this material is approximately 60 nm , this corresponds to a cluster of 7–8 skymions across, or approximately 50 skymions. We observe rotations as low as 0.05° per pulse in the Fourier transform of our images; here, taken after a sequence of 120 pulses, this corresponds to movements of the skymions in real space of about 0.4 nm (per pulse).

III. DISCUSSION

Several mechanisms have previously been identified as potential origins for the rotation of skymion crystals. Roughly, they can be grouped into two different classes. The first one is based on a manipulation of anisotropy terms, e.g., by electric fields [13,14], which leads to a rotation by a finite angle. In contrast, a continuous rotation can be induced using the Magnus force imprinted onto the skymions by electrical, spin, or heat currents. In an inhomogeneous system, these forces lead to a rotational torque. The inhomogeneity can arise from, e.g., a temperature gradient [4] or simply radial heat currents when the center of the skymion crystal is heated [11,12]. While the latter effect may be of relevance in our experiment at high fluence density, the polarization and time dependence of our two-pulse low-fluence experiments in Fig. 3(a) allow us to identify uniquely a new mechanism for the skymion rotation.

As shown in Fig. 3(a), the first pulse induces a collective oscillation of the skymion crystal with a period of $T = 175 \text{ ps}$ corresponding to a frequency of 5.7 GHz . The origin of these oscillations is already known [16,27]: Via the inverse Faraday effect, the polarized laser light induces an effective magnetic-field pulse which triggers the

breathing mode of the skyrmion crystal, i.e., a coherent oscillation of the size of each skyrmion. The magnetic-field pulse has an amplitude of ± 10 mT for left- or right-polarized light with a duration of $\tau = 50$ fs [16,28]; see Supplemental Material [26] for details. The coherent oscillations are enhanced if the second pulse is either in phase with the same polarization as the first pulse or out of phase with the opposite polarization, as seen for the red data points. Remarkably, the skyrmion rotation starts whenever the amplitude of the breathing-mode oscillation is sufficiently large. This is direct experimental evidence that collective oscillations induced by the inverse Faraday effect lead to rotations of the skyrmion crystal.

Previous numerical and analytical studies [29,30] show that collective magnetic oscillations can induce a translational motion of magnetic textures proportional to δM^2 , where δM is the amplitude of the oscillatory mode. In the current setting, such a translational motion is prohibited by symmetry. Quantitatively, however, Eq. (1) predicts—for a clean system and using the ultrashort pulse duration of our experiment—rotation angles about 6 orders of magnitude smaller than observed experimentally; see Supplemental Material [26]. This shows that the Gilbert damping is probably *not* the primary source of the rotational torques. Instead, the rotational torques are most likely induced because the breathing mode triggers a ratchetlike motion in the disorder potential of our sample. Disorder is furthermore responsible for the fact that the rotation angle is not proportional to δB^2 , instead following the typical threshold behavior [see Fig. 2(b)] expected for a disorder-pinned system. As the system is in a regime where pinning effects are much more important than effects from the very weak Gilbert damping, it is not surprising that disorder leads to substantially larger rotational torques than predicted for a clean system. As the forces from disorder are many orders of magnitude larger than the forces for damping ($\alpha \sim 10^{-4}$), it is highly plausible that many orders of magnitude larger rotational torques can arise from a disorder mechanism. This is also consistent with the numerical observation in Ref. [31] that boundaries can strongly enhance the ratchetlike motion of skyrmions in oscillating magnetic fields.

In conclusion, our experiment shows that single ultrafast laser pulses can trigger remarkably large rotations of skyrmions using rotational torques induced by collective spin oscillations and a ratchetlike motion in a disordered system. We show that fluence, polarization, and timing can directly control the rotation, while other parameters such as the beam shape have not yet been explored. To modify the spin currents and operate spin-based devices, we could imagine using spatially varied laser beam profiles such as Laguerre-Gaussian beams to generate tailored device frameworks as needed for logical operations. Tightly focusing these beams may also offer the possibility to generate individual skyrmions, as shown in Ref. [32], while the orbital angular momentum in the beams may lead to

even more efficient rotations [33,34]. Thus, our work offers the possibility to design new modifiable spintronic devices with logical bit sizes limited only by the spatial pattern of the light used for excitation and with temporal command sequences that can be modified on picosecond timescales. This demonstration of picosecond control over nanometer-scaled topological magnetic objects will lead to an array of new device physics and allow scientists to build new functionalities for skyrmions.

All data, code, and materials used in the analyses are available to readers on request.

ACKNOWLEDGMENTS

We acknowledge useful discussions with Ido Kaminer. We acknowledge support from the ERC consolidator grant ISCQuM and SNSF via sinergia nanoskyrmionics Grant No. 171003, the Humboldt Foundation, the DFG via SPP 2137 (Project No. 403505545) and Collaborative Research Center (CRC) 1238 359 (Project No. 277146847, subproject C04) and CRC 183 (Project No. 277101999, subproject A01), U.S. Department of Energy, Office of Basic Energy Sciences under Grant No. DE-SC0020221, the National Natural Science Foundation of China under Grant No. 11974021, and the SMART-electron project that has received funding from the European Union's Horizon 2020 Research and Innovation Program under Grant Agreement No. 964591. S. G. acknowledges support from Google Inc.

The authors declare no competing interests.

Conceptualization, P. T., B. T., A. S., and F. C.; data analysis, B. T.; experimental methodology, P. T., B. T., A. S., I. M., and T. L.; experimental investigation, P. T., B. T., and A. S.; visualization, P. T., B. T., A. S., and T. L.; sample preparation, T. S., P. B., P. C., and A. M.; theory and simulations, L. K., N. d. S., S. G., J. Z., and A. R.; supervision, A. M., D. G., J. Z., A. R., T. L., and F. C.; writing (original draft), P. T.; writing (review and editing), P. T., B. T., A. S., S. G., P. C., A. M., D. G., H. K., T. L., J. Z., A. R., and F. C.

APPENDIX: METHODS AND MATERIALS

1. Methods: Details of the experimental setup

The experiments are carried out in a modified JEOL JEM2100 TEM [35]. In this instrument, *in situ* cryo-LTEM can be performed in the Fresnel configuration [36] at camera-rate temporal resolution (ms) using a continuous wave electron beam generated thermionically, upon *in situ* pulsed optical excitation of the specimen with a tunable femtosecond source. The camera used for the detection of the electrons is a Gatan® K2 direct detection camera. The sample is cooled to 5 K using a helium-cooled sample holder from Gatan.

A Ti:sapphire regenerative amplifier is used to generate 35-fs pulses of light with a center wavelength at 800 nm and a 34-nm (FWHM) bandwidth. The pulse energy directly from the amplifier is 1.5 mJ per pulse at a 4-kHz repetition rate, and approximately 55% of this light (0.81 mJ) is used to convert to near-IR wavelength via an optical parametric amplifier. After conversion to 1200 nm/1.03 eV, the pulses have the duration of 50 fs, and we use a series of optical choppers to lower the repetition rate to 10 Hz. In this way, we are able to use a mechanical shutter to send individual pulses as desired or to send a train of pulses that has a repetition rate lower than the exposure time of our camera. For the pulse train measurements, the pulses have a repetition rate of either 10 Hz or 10 Hz with every 3rd pulse missing (to check for stability). The camera rate is 20 Hz. For the time-resolved measurements, pairs of pulses are either sent individually or at 4-Hz repetition rate, with total rotation recorded after 120 pulses and the rotation per pulse calculated by dividing the observed rotation angle by 120. The beam is then focused to a diameter of 40 μm (FWHM), which is much larger than the sample size. The magnetic field in the microscope is applied normal to the sample surface along the [111] direction.

2. Materials: Sample preparation

A high-quality single crystal of Cu_2OSeO_3 is grown by the chemical vapor transport method. 25 g of a stoichiometric mixture of CuO and SeO_2 are sealed in a 36-mm-diameter quartz ampule together with 100 mbar of HCl used as transport agent. The ampule is placed in a horizontal two-zone furnace. During the growth, source and sink temperatures are set at 635 $^\circ\text{C}$ and 545 $^\circ\text{C}$, respectively. The single crystal is aligned and cut into a cube so that the three main directions correspond to $[1\bar{1}0]$, $[111]$, and $[\bar{1}\bar{1}2]$, respectively. Then, choosing $[111]$ as the main surface, the cube is cut into slices of approximately 0.5 mm thickness. The sample is thinned to about 110 nm by a focused ion beam technique. The dimensions of the thinned lamella region of the sample are approximately 10 $\mu\text{m} \times 10 \mu\text{m} \times 100 \text{ nm}$.

-
- [1] K. Litzius *et al.*, *Skyrmion Hall Effect Revealed by Direct Time-Resolved X-Ray Microscopy*, *Nat. Phys.* **13**, 170 (2017).
- [2] W. Jiang *et al.*, *Direct Observation of the Skyrmion Hall Effect*, *Nat. Phys.* **13**, 162 (2017).
- [3] J. Grollier, P. Boulenc, V. Cros, A. Hamzić, A. Vaurès, A. Fert, and G. Faini, *Switching a Spin Valve back and forth by Current-Induced Domain Wall Motion*, *Appl. Phys. Lett.* **83**, 509 (2003).
- [4] F. Jonietz *et al.*, *Spin Transfer Torques in MnSi at Ultralow Current Densities*, *Science* **330**, 1648 (2010).
- [5] X. Yu *et al.*, *Real-Space Observations of 60-nm Skyrmion Dynamics in an Insulating Magnet under Low Heat Flow*, *Nat. Commun.* **12**, 5079 (2021).
- [6] T. Kampfrath *et al.*, *Terahertz Spin Current Pulses Controlled by Magnetic Heterostructures*, *Nat. Nanotechnol.* **8**, 256 (2013).
- [7] T. Seifert *et al.*, *Efficient Metallic Spintronic Emitters of Ultrabroadband Terahertz Radiation*, *Nat. Photonics* **10**, 483 (2016).
- [8] S. Seki, X. Z. Yu, S. Ishiwata, and Y. Tokura, *Observation of Skyrmions in a Multiferroic Material*, *Science* **336**, 198 (2012).
- [9] N. Prasai *et al.*, *Ballistic Magnon Heat Conduction and Possible Poiseuille Flow in the Helimagnetic Insulator Cu_2OSeO_3* , *Phys. Rev. B* **95**, 224407 (2017).
- [10] I. Stasinopoulos *et al.*, *Low Spin Wave Damping in the Insulating Chiral Magnet Cu_2OSeO_3* , *Appl. Phys. Lett.* **111**, 032408 (2017).
- [11] M. Mochizuki, X. Z. Yu, S. Seki, N. Kanazawa, W. Koshibae, J. Zang, M. Mostovoy, Y. Tokura, and N. Nagaosa, *Thermally Driven Ratchet Motion of a Skyrmion Microcrystal and Topological Magnon Hall Effect*, *Nat. Mater.* **13**, 241 (2014).
- [12] S. Pöllath *et al.*, *Dynamical Defects in Rotating Magnetic Skyrmion Lattices*, *Phys. Rev. Lett.* **118**, 207205 (2017).
- [13] J. S. White *et al.*, *Electric Field Control of the Skyrmion Lattice in Cu_2OSeO_3* , *J. Phys. Condens. Matter* **24**, 432201 (2012).
- [14] J. S. White *et al.*, *Electric-Field-Induced Skyrmion Distortion and Giant Lattice Rotation in the Magnetoelectric Insulator Cu_2OSeO_3* , *Phys. Rev. Lett.* **113**, 107203 (2014).
- [15] M. G. Han *et al.*, *Scaling, Rotation, and Channeling Behavior of Helical and Skyrmion Spin Textures in Thin Films of Te-Doped Cu_2OSeO_3* , *Sci. Adv.* **6**, 1 (2020).
- [16] A. V. Kimel, A. Kirilyuk, P. A. Usachev, R. V. Pisarev, A. M. Balbashov, and T. Rasing, *Ultrafast Non-thermal Control of Magnetization by Instantaneous Photomagnetic Pulses*, *Nature (London)* **435**, 655 (2005).
- [17] C. D. Stanciu, F. Hansteen, A. V. Kimel, A. Kirilyuk, A. Tsukamoto, A. Itoh, and Th. Rasing, *All-Optical Magnetic Recording with Circularly Polarized Light*, *Phys. Rev. Lett.* **99**, 047601 (2007).
- [18] F. Hansteen, A. Kimel, A. Kirilyuk, and T. Rasing, *Femtosecond Photomagnetic Switching of Spins in Ferrimagnetic Garnet Films*, *Phys. Rev. Lett.* **95**, 047402 (2005).
- [19] J. Hurst, P.-A. Hervieux, and G. Manfredi, *Spin Current Generation by Ultrafast Laser Pulses in Ferromagnetic Nickel Films*, *Phys. Rev. B* **97**, 014424 (2018).
- [20] A. B. Schmidt, M. Pickel, M. Donath, P. Buczek, A. Ernst, V. P. Zhukov, P. M. Echenique, L. M. Sandratskii, E. V. Chulkov, and M. Weinelt, *Ultrafast Magnon Generation in an Fe Film on Cu (100)*, *Phys. Rev. Lett.* **105**, 197401 (2010).
- [21] J. Kimling, G.-M. Choi, J. T. Brangham, T. Matalla-Wagner, T. Huebner, T. Kuschel, F. Yang, and D. G. Cahill, *Pico-second Spin Seebeck Effect*, *Phys. Rev. Lett.* **118**, 057201 (2017).
- [22] A. Alekhin *et al.*, *Femtosecond Spin Current Pulses Generated by the Nonthermal Spin-Dependent Seebeck*

- Effect and Interacting with Ferromagnets in Spin Valves*, *Phys. Rev. Lett.* **119**, 017202 (2017).
- [23] P. Tenggindin *et al.*, *Critical Behavior within 20 fs Drives the Out-of-Equilibrium Laser-Induced Magnetic Phase Transition in Nickel*, *Sci. Adv.* **4**, eaap9744 (2018).
- [24] G. Berruto *et al.*, *Laser-Induced Skyrmion Writing and Erasing in an Ultrafast Cryo-Lorentz Transmission Electron Microscope*, *Phys. Rev. Lett.* **120**, 117201 (2018).
- [25] T. Eggebrecht, M. Möller, J. Gregor Gatzmann, N. R. da Silva, A. Feist, U. Martens, H. Ulrichs, M. Münzenberg, C. Ropers, and S. Schäfer, *Light-Induced Metastable Magnetic Texture Uncovered by In Situ Lorentz Microscopy*, *Phys. Rev. Lett.* **118**, 097203 (2017).
- [26] See Supplemental Material at <http://link.aps.org/supplemental/10.1103/PhysRevX.12.041030> for more details.
- [27] N. Ogawa, S. Seki, and Y. Tokura, *Ultrafast Optical Excitation of Magnetic Skyrmions*, *Sci. Rep.* **5**, 9552 (2015).
- [28] J. P. Van Der Ziel, P. S. Pershan, and L. D. Malmstrom, *Optically-Induced Magnetization Resulting from the Inverse Faraday Effect*, *Phys. Rev. Lett.* **15**, 190 (1965).
- [29] C. Schütte and M. Garst, *Magnon-Skyrmion Scattering in Chiral Magnets*, *Phys. Rev. B* **90**, 094423 (2014).
- [30] N. del Ser, L. Heinen, and A. Rosch, *Archimedean Screw in Driven Chiral Magnets*, *SciPost Phys.* **11**, 009 (2021).
- [31] W. Chen, L. Liu, and Y. Zheng, *Ultrafast Ratchet Dynamics of Skyrmions by Defect Engineering in Materials with Poor Conductivity under Gigahertz Magnetic Fields*, *Phys. Rev. Appl.* **14**, 064014 (2020).
- [32] H. Fujita and M. Sato, *Ultrafast Generation of Skyrmionic Defects with Vortex Beams: Printing Laser Profiles on Magnets*, *Phys. Rev. B* **95**, 054421 (2017).
- [33] S. Ali, J. R. Davies, and J. T. Mendonca, *Inverse Faraday Effect with Linearly Polarized Laser Pulses*, *Phys. Rev. Lett.* **105**, 035001 (2010).
- [34] W. Yang, H. Yang, Y. Cao, and P. Yan, *Photonic Orbital Angular Momentum Transfer and Magnetic Skyrmion Rotation*, *Opt. Express* **26**, 8778 (2018).
- [35] L. Piazza, D. J. Masiel, T. Lagrange, B. W. Reed, B. Barwick, and F. Carbone, *Design and Implementation of a fs-Resolved Transmission Electron Microscope Based on Thermionic Gun Technology*, *Chem. Phys.* **423**, 79 (2013).
- [36] S. McVitie and M. Cushley, *Quantitative Fresnel Lorentz Microscopy and the Transport of Intensity Equation*, *Ultramicroscopy* **106**, 423 (2006).

Supplementary Text

Imaging the Ultrafast Coherent Control of a Skyrmion Crystal

CONTENTS

I. Theory of rotational torques	1
II. Estimation of inverse Faraday effect by pump beam	5
III. Phase diagram of the samples measured with TEM	6
IV. Details on the gridded analysis of skyrmion rotation in our image	6
V. Finite Element modelling of timescales and final temperature reached following laser pulse excitation	6
VI. Details of the phononic heat capacity and heat conductivity used in finite element method	11
VII. Additional time-varied data taken at 10K on different lamella	11
References	13

I. THEORY OF ROTATIONAL TORQUES

In this section, we develop a theory of rotational torques on skyrmion crystals. Operating on the Landau-Lifshitz-Gilbert equation with $\frac{1}{|\vec{\gamma}|}\hat{n}$, where \hat{n} is the direction of the magnetization and γ is the gyromagnetic ratio, we obtain the equation of motion

$$m_0\hat{n} \times \frac{d\hat{n}}{dt} = -\frac{\partial E}{\partial \hat{n}} - \alpha m_0 \frac{d\hat{n}}{dt} \quad (\text{S1})$$

where m_0 is the spin-density (with units of \hbar per volume), and $\vec{b} = -\frac{\partial E}{\partial \hat{n}}$ is an effective magnetic field defined by the (functional) derivative of the total energy with respect to \hat{n} . α parametrizes the Gilbert damping, which is the only damping term we consider here for simplicity. We parametrize the magnetic texture by a rotation angle θ and write

$$\frac{d\hat{n}}{dt} = \frac{d\hat{n}}{d\theta} \partial_t \theta + \partial_t \hat{n} \quad (\text{S2a})$$

with

$$\frac{d\hat{n}}{d\theta} = \hat{z} \times \hat{n} - (\hat{z} \times \vec{r}) \cdot \nabla \hat{n} \quad (\text{S2b})$$

The first term describes the rotations of the spin orientation, the second one the rotation of space. To obtain an equation for the rate of change of the total angular momentum, J_z , we multiply Eq. (S1) with $\frac{d\hat{n}}{d\theta}$ and integrate over

space. After identifying the left-hand side of the equation with the time-derivative of the total angular momentum, we obtain

$$\frac{d}{dt}J_z = -\frac{dE}{d\theta} - \alpha m_0 \int d^3\vec{r} \frac{d\hat{n}}{d\theta} \left(\frac{d\hat{n}}{d\theta} \partial_t \theta + \partial_t \hat{n} \right). \quad (\text{S3})$$

The total angular momentum, $J_z = S_z + L_z$, has two contributions, the first one, $S_z = m_0 \int d^3\vec{r} \hat{n}_z$, is simply the total spin in z -direction. The orbital angular momentum L_z instead can be computed from the topological charge density $\rho_T = \frac{1}{4\pi} \hat{n} \cdot (\partial_x \hat{n} \times \partial_y \hat{n})$. Up to surface terms, it can be written as, $-m_0 \int d^3\vec{r} 2\pi(x^2 + y^2) \rho_T(\vec{r})$.

To obtain an equation for the rotation angle, $\Delta\theta = \int dt \partial_t \theta$, after a field pulse, we simply integrate Eq. (S3) over time. Using that angular momentum is the same before and after the pulse, we obviously have $\int dt \frac{d}{dt} J_z = 0$. Furthermore, all rotationally invariant terms in the energy functional (exchange coupling, DMI interaction, dipolar interactions for spherical samples, magnetic fields in the z -direction) also do not contribute. In the limit of a weakly perturbed skyrmion crystal, we write the remaining terms as

$$\alpha D_{rot} \Delta\theta \approx \int dt (T_{an}^R + T_{\alpha,pump}^R + T_{dis}^R). \quad (\text{S4})$$

The term on the left-hand side arises from the friction connected with the rotation of the skyrmion crystal with $D_{rot} = m_0 \int d^3\vec{r} \left(\frac{d\hat{n}}{d\theta} \right)^2$ where we approximate \hat{n} by the unperturbed spin texture \hat{n}_0 .

The main contribution to this integral arises from the terms growing linear in \vec{r} in Eq. (S2)), giving rise to a contribution proportional to r^2 and thus linear in the number of skyrmions, N_s , involved in the rotation. Collecting those, we obtain for a roughly spherically shaped domain of a triangular skyrmion crystal

$$D_{rot} = m_0 \int d^3\vec{r} \left(\frac{d\hat{n}_0}{d\theta} \right)^2 \approx N_s A_s \frac{m_0}{2\pi} \int d^3\vec{r} (\nabla \hat{n}_0)^2, \quad (\text{S5})$$

where A_s is the area of the skyrmion unit cell. On the right-hand side of Eq. (S4) we collect different types of rotational torques. The first one, $T_{an}^R \propto 6\theta$ arises from weak anisotropy terms which, in a clean system, fix the relative orientation of skyrmion crystal and crystalline lattice. For our experiment these terms can be completely neglected as $\Delta\theta$ is much smaller than $\frac{2\pi}{6}$ (i.e., there is no ratchet motion from minimum to minimum of $E(\theta)$) and furthermore $\Delta\theta$ is independent of θ .

Remarkably, in the driven system, the Gilbert damping-term can give rise to rotational torques which *induce* a rotation with

$$T_{\alpha,pump}^R = -\alpha m_0 \int d^3\vec{r} \frac{d\hat{n}}{d\theta} \partial_t \hat{n}. \quad (\text{S6})$$

This term, evaluated below, vanishes in thermal equilibrium but is generically finite in a driven system. Finally, the disorder in the system and boundary terms also induces torques, T_{dis}^R , which include pinning terms counteracting a rotation and pumping terms supporting rotations, see below.

Expanding the magnetic texture around its equilibrium configuration, $\hat{n} = \hat{n}_0 + \delta\hat{n}$, we observe that for the time-integrated torque, $\int T_{\alpha,pump}^R dt$, the contribution linear in $\delta\hat{n}$ vanishes, thus the leading term is quadratic in $\delta\hat{n}$. We now consider the response to a magnetic field pulse parallel to the external magnetic field B_0 (i.e., perpendicular to the surface). τ is the duration of the pulse and δB its amplitude, such that $B(t) \approx B_0 + \delta B \tau \delta(\tau)$ describes a single pulse. Therefore, $\delta\hat{n}$ is linear in $\delta B \tau$. For the rotation angle after a single pulse we obtain in the absence of disorder

$$\Delta\theta_{\alpha,pump} \approx -\frac{2\pi}{N_s A_s} \frac{\int dt d^3\vec{r} \frac{d\delta\hat{n}}{d\theta} \partial_t \delta\hat{n}}{\int d^3\vec{r} (\nabla \hat{n}_0)^2} \approx \gamma_{\alpha,pump} \frac{1}{\alpha N_s} \left(\frac{\delta B}{B_0} \right)^2 \left(\frac{\tau}{T_0} \right)^2. \quad (\text{S7})$$

where we used the oscillation period T_0 of the breathing mode to obtain the dimensionless ratio $\frac{\tau}{T_0}$. The factor $\frac{1}{\alpha}$ reflects that the time integral is proportional to this factor as the life-time of the breathing mode is of the order of T_0/α . The remaining prefactor $\gamma_{\alpha,pump}$ with the unit of an angle depends only weakly on all remaining system parameters. It encodes both how efficient the field pulse is in inducing collective oscillations of the magnetic textures and how efficient these oscillations induce rotational torques using non-linearities in $T_{\alpha,pump}^R$.

A simple two dimensional schematic animation is shown in the supplementary movie, where only a single breathing mode is taken into account. To obtain a numerical estimate for $\gamma_{\alpha,pump}$, we perform a micromagnetic simulation using mumax. We use periodic boundary conditions, thus effectively simulating an infinitely large system. Thus, rotations are absent in the simulations but we compute directly $T_{\alpha,pump}^R$ and $\gamma_{\alpha,pump}$ from Eq. (S7). We simulate a slab with a thickness of 60 nm using a unit cell of $66 \text{ nm} \times 114 \text{ nm}$ discretized into cubes with a width of 2 nm. Magnetic parameters of Cu_2OSeO_3 are used in the simulation. The saturation magnetization is $M_s = 1.044 \times 10^5 \text{ Am}^{-1}$, the exchange parameter is $A = 3.547 \times 10^{13} \text{ Jm}^{-1}$, and the bulk DMI is $D = 7.43 \times 10^{-5} \text{ Jm}^{-2}$. The skyrmion crystal is stabilized by a static field of 0.06 T, and the skyrmion spacing is about 66 nm, leading to the unit cell area of the skyrmion crystal $A_s = 3.772 \times 10^3 \text{ nm}^2$. For these parameters, we find that a field pulse mainly excites two collective modes with frequencies 4.8 GHz and 5.0 GHz, see Fig. 1, roughly matching the experimentally observed frequency of 5.7 Gz. As shown in the supplementary animation, both modes can be viewed as breathing modes with an oscillating magnetization amplitude but the modes differ by the z -dependence of their amplitude.

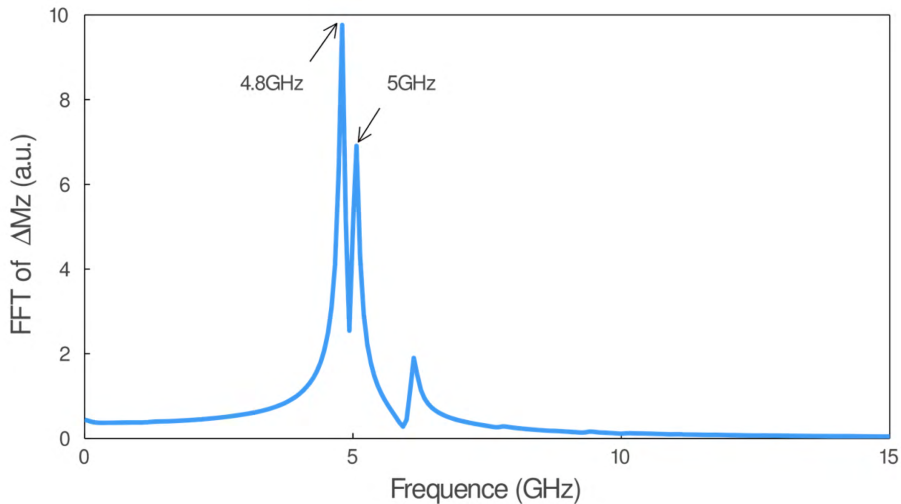


FIG. 1. Fast Fourier transformation of the total excited magnetization as a function of the excitation frequency obtained for $\alpha = 0.01$. Two collective breathing modes are labeled.

To make the simulations feasible, we use field pulses with a duration of 10 ps, 200 times longer than the experimental pulses, and also relatively large values of the Gilbert damping $\alpha \sim 0.01$, but use Eq. (S7) to extrapolate to experimental values. Under a pulse of 10 mT, typical time variations of $N_s \dot{\theta}(t) \approx -\frac{2\pi}{N_s A_s} \int dt d^3 r \frac{d\delta\hat{n}}{d\theta} \partial_t \delta\hat{n}$ and $N_s \theta(t) = \int_0^t \dot{\theta}$ as are shown in Fig. 2. A finite rotation angle builds up on the time scale of a few ns for $\alpha = 0.01$. In Fig. 3 we show that the rotation angle is proportional to $(\delta B)^2/\alpha$ as predicted by Eq. (S7). Fitting the results to Eq. (S7), we obtain for

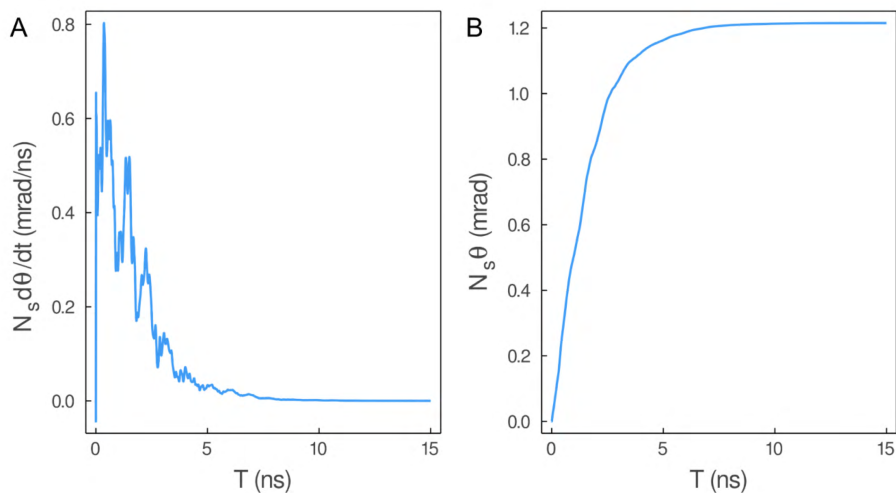


FIG. 2. Typical time variations of (a) the rotation rate and (b) total rotation angle $N_s \theta(t) = \int_0^t N_s \dot{\theta}$ for $\alpha = 0.01$, for a square-shaped pulse with a duration of 10 ps and an amplitude of 10 mT. The rotation builds up on a time scale of a few ns for these parameters.

a single pulse of square shape

$$\gamma_{\alpha,pump} \approx 9.7^\circ \quad (\text{S8})$$

Thus, we have shown that Gilbert damping is able to induce sizable rotational torques but the experimental effects turns out to be much larger.

To compare to the experiment, we use that the pulse duration is $\Delta\tau = 50$ fs generating a field of about 13 mT via the inverse Faraday effect. Using that the oscillation period of the breathing mode is 175 ps, we estimate

$$\Delta\theta \approx \frac{1.1^\circ \cdot 10^{-7}}{N_s \alpha} \ll 1^\circ \cdot 10^{-6}$$

where we assume that $\alpha > 10^{-4}$ and that about hundred skyrmions rotate simultaneously in our sample. Clearly, the pumping induced by the Gilbert damping alone, cannot explain our experiment which shows rotation angles which are about 6 orders of magnitude larger. Therefore, a different mechanism to generate rotational torques is needed to explain the experiment. Above, we showed that the Gilbert damping has two different roles. On one hand, it provides damping (left-hand side of Eq. (S4)), thus counteracting any rotation. But on the other hand, via $T_{\alpha,pump}^R$ the Gilbert damping also transforms the oscillatory breathing-mode into a rotational torques which induces rotations. The same also applies for disorder. First, it is the source of (collective) pinning by disorder, which counteracts any rotation. Second, in the presence of disorder there will be a ratchet-like motion where disorder induces rotations of the skyrmion crystal. A quantitative numerical simulation of this problem is challenging (and beyond the scope of this paper) as the rotational motion and the depinning physics is very complicated (involving defects in the skyrmion crystal [1]) and one must consider very large systems. Particle-base models as in ref. [1] cannot be used as they do not include the physics of the breathing mode. Previous simulations of the motion of single skyrmions [2] in the presence of oscillating magnetic fields show that relatively fast motion can be induced along defect tracks. Thus, we conclude

that defect-assisted rotational torques (perhaps together with surface terms) induced by breathing-mode oscillations are likely to explain our experiment.

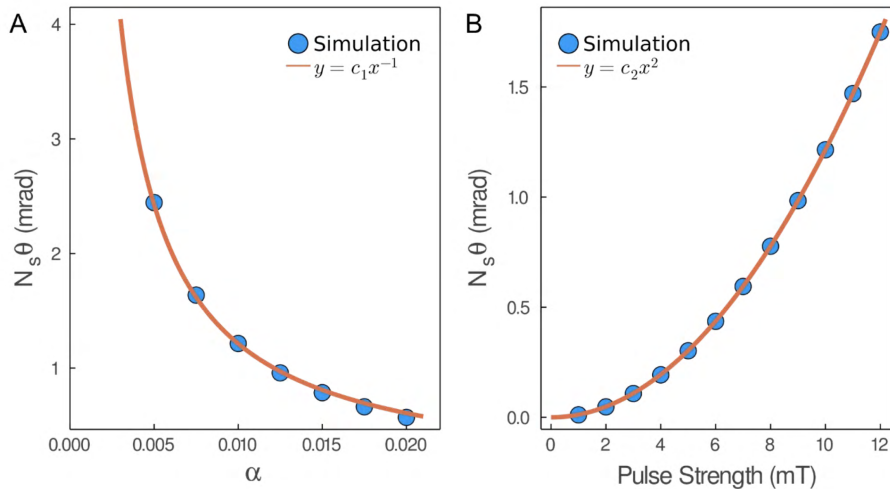


FIG. 3. As predicted by Eq. (S7), the rotation angle is inversely proportional to the Gilbert damping α and quadratic in the pulse strength (parameters: pulse strength of 10 mT for panel (a) and $\alpha = 0.011$ for panel (b), pulse duration 10 ps).

II. ESTIMATION OF INVERSE FARADAY EFFECT BY PUMP BEAM

The formula we use is [3]:

$$M = \frac{\lambda V}{2\pi c} (I_R - I_L), \quad (\text{S9})$$

where I_R (I_L) is the peak intensity of the right (left) hand circularly polarized pulse, λ the wavelength, and V the corresponding Verdet constant. These values are in the cgs system and $V = 3.0 \times 10^{-2} \text{ rad Oe}^{-1} \text{ cm}^{-1}$. The experimental parameters:

$$\lambda = 1.2 \times 10^{-4} \text{ cm}$$

$$E = 0.14 \frac{\mu\text{J}}{\text{pulse}} = 1.4 \frac{\text{erg}}{\text{pulse}}$$

$$\tau = 50 \text{ fs}$$

$$d = 40 \mu\text{m}$$

Hence, we obtain $I_{R,peak} = 4.46 \times 10^{18} \text{ erg s}^{-1} \text{ cm}^{-2}$ and $M = 85 \text{ G} = 8.5 \text{ mT}$. To calculate the effective magnetic field B_{eff} resulting from the pulse, we used M/H values measured in ref. [4]:

$$M(30 \text{ mT}) = 0.1 \mu_B / \text{Cu}^{2+}.$$

Given the concentration of Cu atoms $= \frac{16}{8.911 \text{ A}} = 2.26 \times 10^{28} \text{ m}^{-3}$, we find $H_{\text{eff}} = \frac{8.5 \times 30}{26.3} = 10 \text{ mT}$.

III. PHASE DIAGRAM OF THE SAMPLES MEASURED WITH TEM

We measured the phase diagram of the samples by taking images in the TEM. This information is provided below in Fig. 4. We prepare the sample by first applying the appropriate field at room temperature, and then lowering the temperature to a minimum temperature of 5K. The data points for the transition from paramagnetic to skyrmion phase are shown in blue.

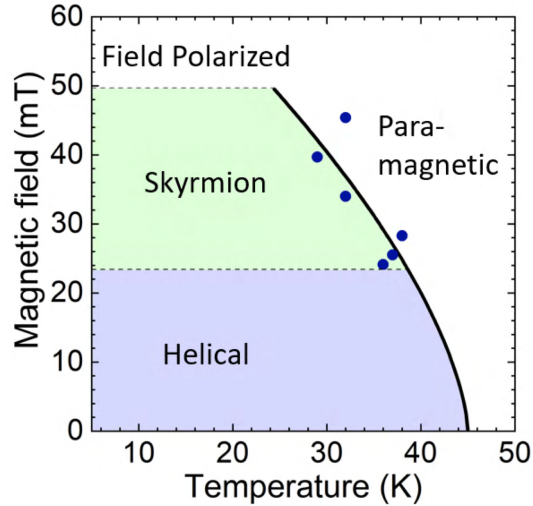


FIG. 4. Phase diagram of the field cooled samples used in this manuscript.

IV. DETAILS ON THE GRIDDED ANALYSIS OF SKYRMION ROTATION IN OUR IMAGE

The full data set used to generate Figure 4 in the main text is shown in Fig. 5. The real space image was divided into regions of 460 nm. From each gridded subsection, the Fourier Transform was taken, and a coordinate transform is made from cartesian to polar coordinates. We then integrate over a certain region in the radial coordinate. Due to symmetry, we average the data from angles 0-180° with data from angles 180-360°. We then plot intensity vs. angle and choose the peak with the highest intensity and plot a region in angle space around this peak. This provides us with intensity maps in the angle coordinate. By fitting these intensity maps with a gaussian function, we extract the central peak and use this to plot the function of angle vs. number of pulses seen in Fig. 1 of the main text, and to calculate the fluence dependence for Fig. 2a of the main text.

V. FINITE ELEMENT MODELLING OF TIMESCALES AND FINAL TEMPERATURE REACHED FOLLOWING LASER PULSE EXCITATION

To understand and rule out all thermal timescales relevant for the rotation process, it is important to identify the evolution of temperature in the sample following the absorption of the laser pulse. We modeled the heating and cooling dynamics of the sample following ultrafast laser excitation using the finite element method. Our model

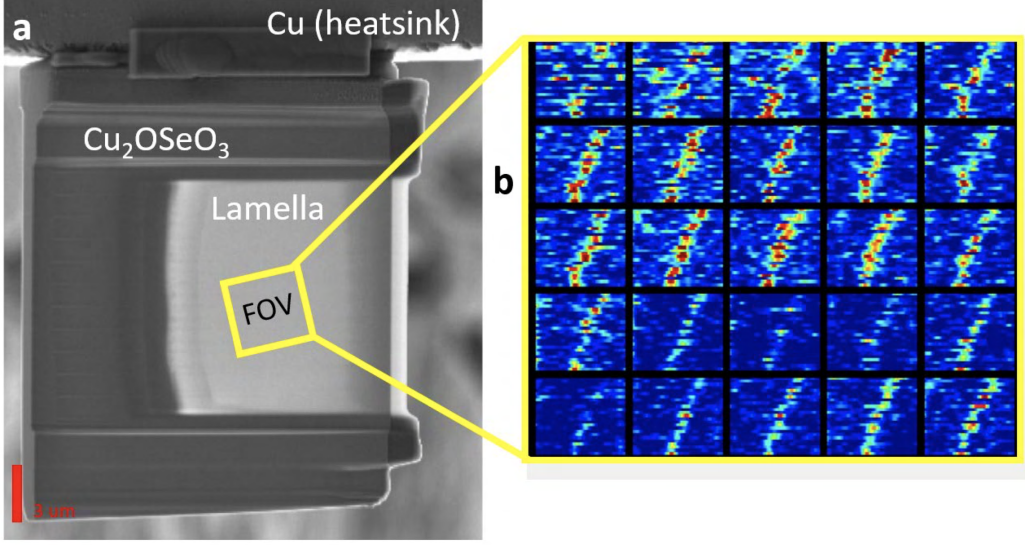


FIG. 5. (a) Scanning electron microscope image of lamella. The scale bar (bottom left) is $3 \mu\text{m}$. The range of interest (ROI) of our L-TEM images is given by the yellow box. (b) Each box maps the angle of a single point in the FT of a subsection of the image following excitation during a train of circularly polarized laser pulses (1 image for each pulse. The number of pulses sent on the y axis was 16 and the x-axis runs from 3.5 to 88 degrees.

uses experimental values for the heat capacity and heat conduction in Cu_2OSeO_3 [5, 6]. At the threshold fluence ($2.2 \text{ mJ}/\text{cm}^2$), our calculations show that the sample reaches a maximum temperature of $\sim 27 \text{ K}$ and remains at that temperature for at least 2-3 ns, followed by cooling via the cold finger on the timescale of 100s of nanoseconds. We then performed the simulation with two laser pulses, separated by a delay of 100 ps (as was done in the experiment and resulted in no rotation, see Fig. 2b). We find that the peak temperature reached does not change significantly despite the separation of the two pulses by 100 ps. This information combined with the fact that the cooling timescale (100s of ns) is much slower than the dynamics that we observe in our time resolved measurements and the coherent nature of the rotations observed, all serve to show that thermal effects are not relevant for the rotation dynamics observed here. The thermodynamic finite element model of the Cu_2OSeO_3 sample, heated by an ultrafast laser pulse, has been implemented using COMSOL. The geometry implemented is shown in Fig. 6. Here, the domain is divided in two regions: the lamella (in red), with a thickness of 100 nm, and the support (green), with a thickness of $1 \mu\text{m}$. The experimental sequence has been described analytically as a two pulse Gaussian beam, having a flux $\phi(x, y, t) = T_{opt} \cdot (1 - R)\phi_{inc} \cdot \exp(-2r_f^2/r_s^2) \cdot (gp(t, \tau_{pulse}, t_1) + gp(t, \tau_{pulse}, t_2))$, with a spot radius of $r_s = 20 \mu\text{m}$ and incident from the top with a power density $\phi_{inc} = 2.2 \times 10^{10} \text{ W cm}^2$ (corresponding to the incident fluence of $1.1 \text{ mJ}/\text{cm}^2$) in each pulse. r_c is the radial distance from the beam axial center and is defined as $r_c^2 = (x-x_c)^2 + (y-y_c)^2$, with x_c and y_c being the planar coordinates of the central axis. $T_{opt} = 0.88$ is the transmission coefficient of the optical system (window and reflective mirror inside the microscope) while $R = 0.11$ is the reflection coefficient of Cu_2OSeO_3 at $= 1.24 \mu\text{m}$ (1 eV). $gp(t, \tau_{pulse})$ is a normalized gaussian pulse with duration $\tau_{pulse} = 50 \text{ fs}$, centered around $t_1 = 0.5 \text{ ps}$ for the first pulse and $t_2 = t_1 + 100 \text{ ps}$ for the second one, to model the first experimentally observed null (no rotation) in the double pulse experiment (see Figure 2b of main text). The heating induced on the sample by the laser pulse has

been introduced through a volumetric heat source, modelled as $Q_0 = \alpha \phi_{inc} \exp(\alpha(z - z_0))$, where $\alpha = 318.66 \text{ cm}^{-1}$. Here, z_0 corresponds to the longitudinal coordinate of the top surfaces for both lamella and support. One of the support's lateral surfaces has been fixed to the temperature of 5 K, emulating the behavior of the heatsink. Initial temperature has been set to 5 K all over the structure.

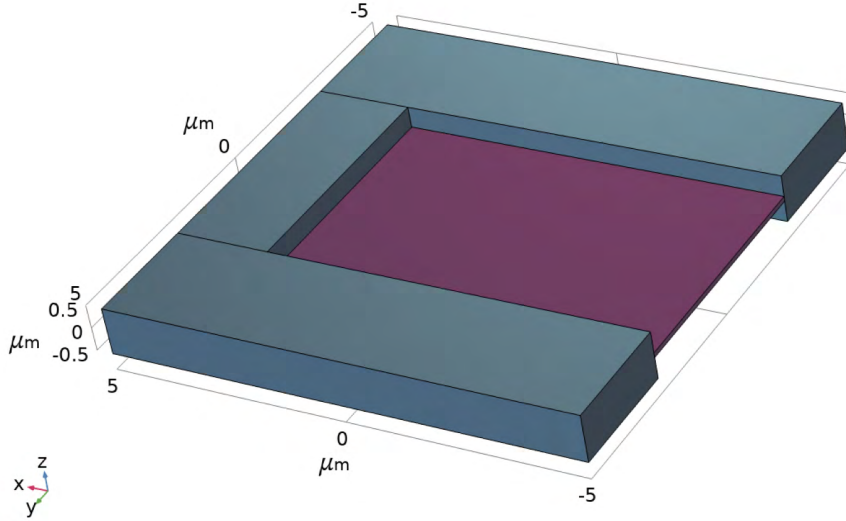


FIG. 6. Geometry of the Cu_2OSeO_3 sample implemented in Comsol Multiphysics. The domain has been divided in two regions: the lamella in purple and the support in grey.

The time dependent simulation is run for a period of $1 \mu\text{s}$, considering the temperature dependent heat capacity $C(T)$ and heat conductivity $k_L(T)$ discussed in Section VI, with non-uniform time steps. The temperature trend resulting from the simulation are shown in Fig. 7 in case two pulses, spaced 100 apart, heat the sample. Here, we show the maximum, minimum and average temperatures reached by the sample as a whole (Fig. 10A) and by the lamella (Fig. 10B) following the laser excitation. Fig. 7A shows that the absolute maximum temperature reached by the support are of 21.68 K after the first laser pulse and 26.54 K after the second laser pulse. The average temperature slowly decays to $\text{avg}(T) \sim 20 \text{ K}$ reached in $t \sim 6.8 \text{ ns}$ and finally to 5 K in a time interval of $0.5 \mu\text{s}$. Maximum temperature in the support is kept almost constant up to $t \sim 60 \text{ ns}$, corresponding to the onset of the cooling of the last part of the support, the farthest from the heatsink. The minimum temperature measured all over the support is always 5K, representative of the heatsink surface. Fig. S7B shows that the absolute maximum temperature reached by the thin lamella is of 21.87 K after the first pulse and of 26.80 after the second. The temperature in the lamella is quite uniform during the heating phase, in fact $\text{max}(T) - \text{min}(T) = 1\text{-}2 \text{ K}$. At $t = 1.5 \mu\text{s}$ the minimum temperature drops from 25.6K to 8K in 25 ns, meaning that the cold region, with the temperature imposed by the heatsink, is entering the lamella's domain.

The entire process of cooling takes approximately $0.5 \mu\text{s}$. Fig. 8, shows the isothermal contours obtained on the top surface at $t = 120 \text{ ps}$, thus 20 ps after the second pulse hit the sample. The gradient imprinted on the surface is circular due to the gaussian shape of the laser beam. Note that within the region of the lamella (where measurements are taken), the heating is nearly uniform (gradient less than 1 K over $10 \mu\text{m}$).

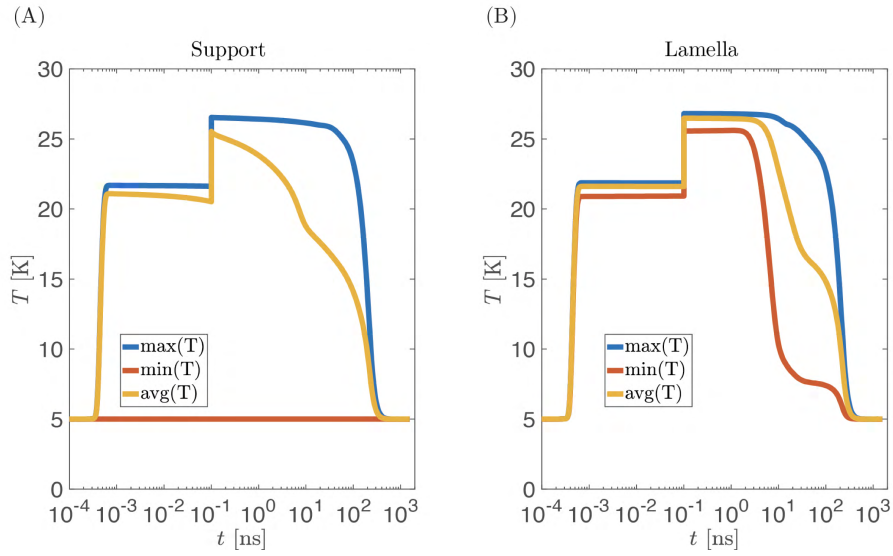


FIG. 7. Maximum (blue), minimum (red) and average (yellow) temperature obtained in the support (A) and in the lamella (B) in case two laser pulses, spaced 100 ps apart, heat the sample.

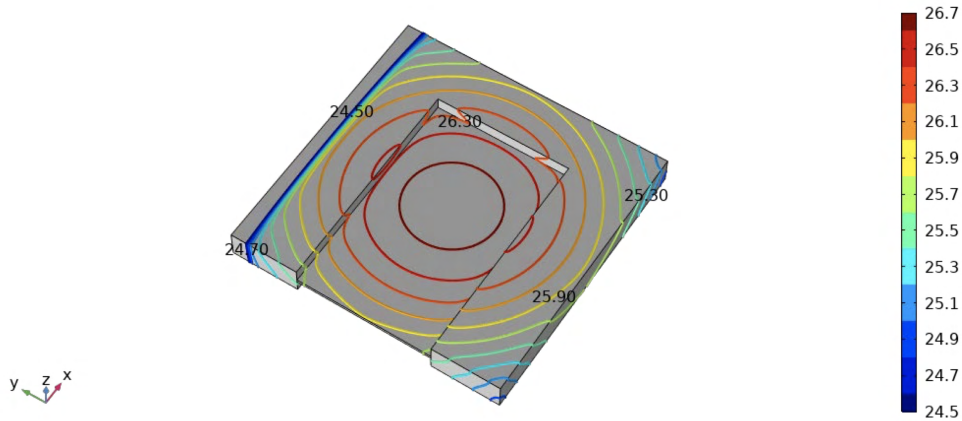


FIG. 8. Isothermal contours after two pulses laser irradiation ($t = 120$ ps) on the top surface. Black labels represent the temperature. Heat sink surface is on the top left.

Next we show the case when the two 1.1 mJ/cm^2 pulses arrive simultaneously, i.e. $t_1 = t_2$. Fig. 9 shows the temperature evolution. In this case, the maximum temperature reached in the lamella is of 25.81 K, while the one in the support is of 26.57 K, which is very similar to the case of Fig. 7.

Fig. S10 shows the temperature map at $t = 30$ ns and at $t = 90$ ns, thus during the cooling process of the lamella. The gradient, during this phase, is imprinted by the heatsink, leading to a linear boundary between the hot and cold domains.

The peak temperature of ~ 27 K reached in the film is below the paramagnetic melting point of the skyrmion crystal, thus the sample can still “remember” the previous skyrmion orientation, which explains well the rotation observed in

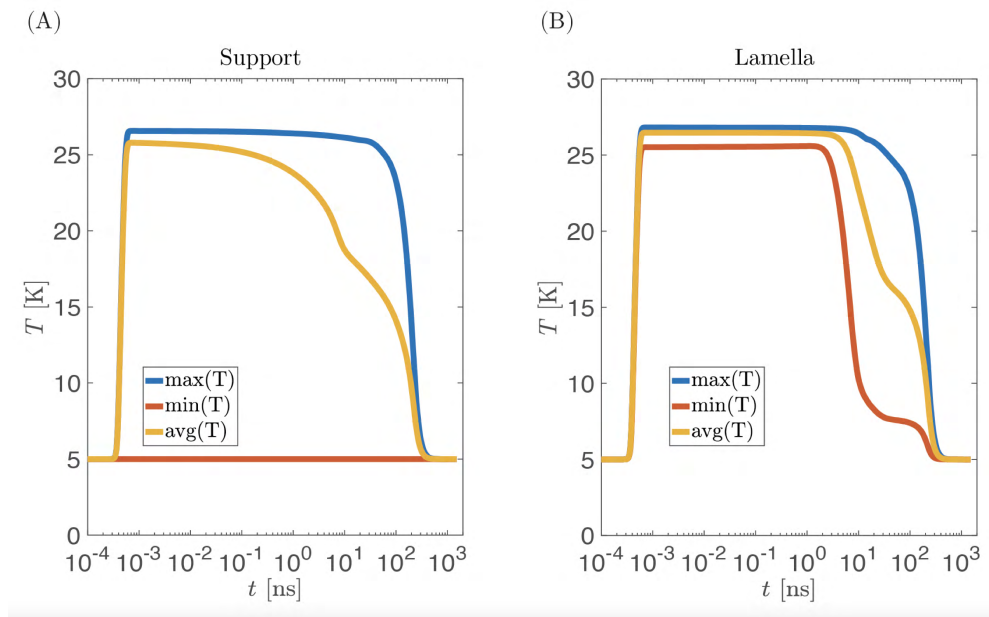


FIG. 9. Maximum (blue), minimum (red) and average (yellow) temperature obtained in the support (A) and in the lamella (B) in case two laser pulses arrive simultaneously.

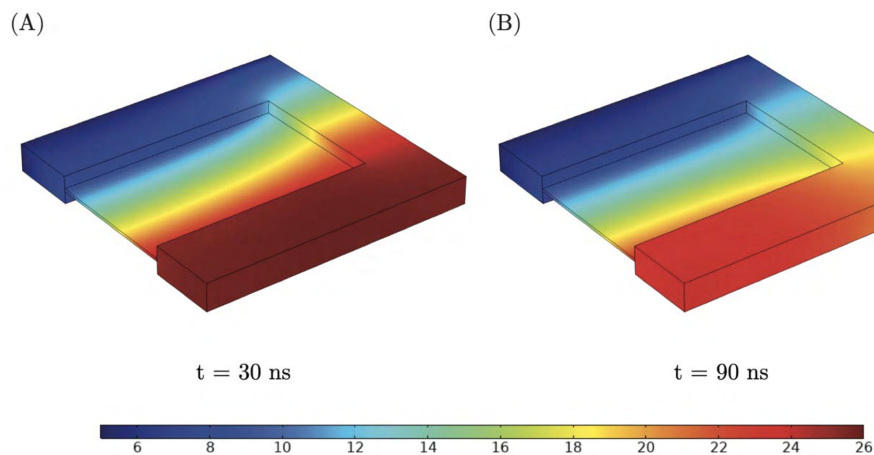


FIG. 10. Temperature map of the Cu_2OSeO_3 sample during the cooling phase in two different time instants: at $t = 30$ ns (A) and $t = 90$ ns (B). Color legend indicates the temperature in Kelvin. The top left surface is representative of the heat sink and it is kept at the constant temperature of 5 K during the simulation.

our images. This is a fundamentally different mechanism than many previous studies of skyrmion or magnetic bubble formation [7, 8].

VI. DETAILS OF THE PHONONIC HEAT CAPACITY AND HEAT CONDUCTIVITY USED IN FINITE ELEMENT METHOD

Experimental data on the temperature dependent heat capacity of Cu_2OSeO_3 has been retrieved from ref. [9]. Fitting these data with a model of 287 K:

$$C_{ph}(T) = A \left(\frac{T}{\theta_D} \right)^3 \int_0^{\theta_D/T} \frac{x^4}{(e^x - 1)(1 - e^{-x})} dx \quad (\text{S10})$$

where A and θ_D are fitting parameters. For the heat conductivity we used the Callaway model [10], together with its update [11], as done in ref. [12]. In particular, the integral expression for the phononic heat conductivity is the

$$\kappa_L = \frac{k_B}{2\pi^2\nu} \left(\frac{k_B}{\hbar} \right)^3 T^3 \left[\int_0^{\theta_D/T} \frac{x^4 e^x}{(e^x - 1)^2} \tau_c(x, T) dx \right] \times \left(1 + \frac{\overline{\tau_c(T)/\tau_N(T)}}{\overline{\tau_c(T)/\tau_R(T)}} \right) \quad (\text{S11})$$

with

$$\frac{\overline{\tau_c(T)/\tau_N(T)}}{\overline{\tau_c(T)/\tau_R(T)}} = \int_0^{\theta_D/T} \frac{x^4 e^x}{(e^x - 1)^2} \frac{\tau_c(x, T)}{\tau_N(x, T)} dx \bigg/ \int_0^{\theta_D/T} \frac{x^4 e^x}{(e^x - 1)^2} \frac{\tau_c(x, T)}{\tau_R(x, T)} dx \quad (\text{S12})$$

where ν is the Debye-averaged sound speed, $x = \hbar\omega/k_B T$ is the reduced phonon energy and $\tau_c^{-1}(x, T) = \tau_N^{-1}(x, T) + \tau_R^{-1}(x, T)$. In the latter equation $\tau_N^{-1}(x, T)$ and $\tau_R^{-1}(x, T)$ are the phonon scattering rates for the normal (that conserve momentum) and resistive processes (that do not conserve the momentum), respectively. Their expressions are given below:

$$\tau_R^{-1}(x, T) = \nu l_{ph} + Ax^2 T^4 \exp\left(-\frac{\theta_D}{bT}\right) + Cx^4 T^4 \quad (\text{S13})$$

$$\tau_N^{-1}(x, T) = \gamma Ax^2 T^4. \quad (\text{S14})$$

$\tau_R^{-1}(x, T)$ includes terms accounting for scattering from boundaries (Umklapp scattering), other phonons and point-like defects. Here A, b, C and γ are fitting parameters. To model our $10 \mu\text{m}$ Cu_2OSeO_3 sample, we used for A, b, C and γ the values reported in ref. [12] for the smallest available $k_L = (l_0 = 0.31 \text{ mm})$, reevaluating k_L assuming $l_{ph} = l_0 = 10 \mu\text{m}$. Fig. 11 reports the heat conductivity obtained following the aforementioned model. More precisely the fitting parameters used are $A = 1.5 \times 10^4 \text{ K}^{-4}$, $b = 6.35$, $C = 110 \text{ K}^{-4}$, and $\gamma = 0$. θ_D has been chosen equal to 287 K to be coherent with the heat capacity model. The condition $\gamma = 0$ is equivalent to set $\frac{\overline{\tau_c(T)/\tau_N(T)}}{\overline{\tau_c(T)/\tau_R(T)}} = 0$.

VII. ADDITIONAL TIME-VARIED DATA TAKEN AT 10K ON DIFFERENT LAMELLA

All data were collected from two independent lamellas which were both cut from the same crystal at different times. Below Fig. 12 shows time varied data taken from the second lamella at 10 K.

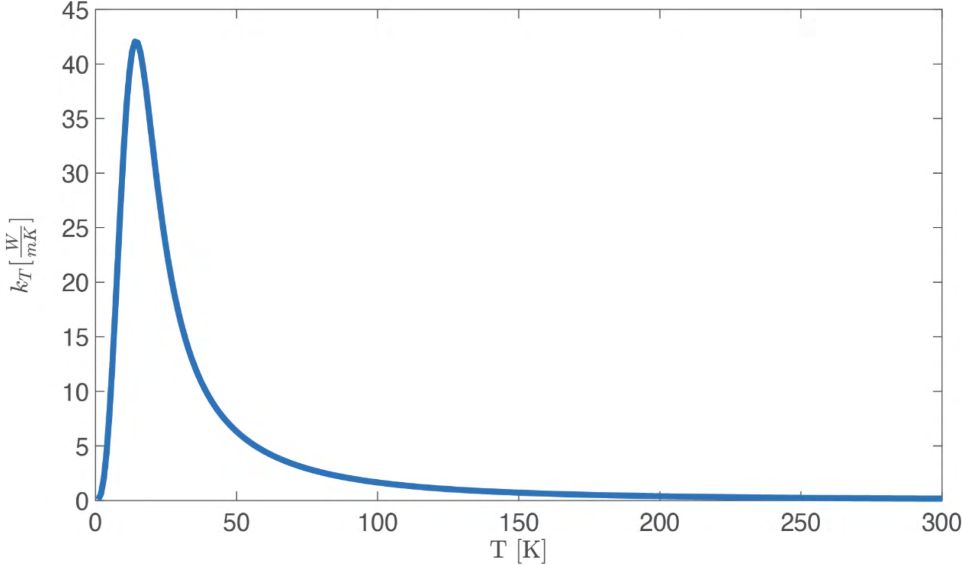


FIG. 11. Analytical heat conductivity obtained with the Callaway model using the fitting parameters of Ref. [13], $\theta_D = 287 K$ and $l_{ph} = l_0 = 10 \mu\text{m}$.

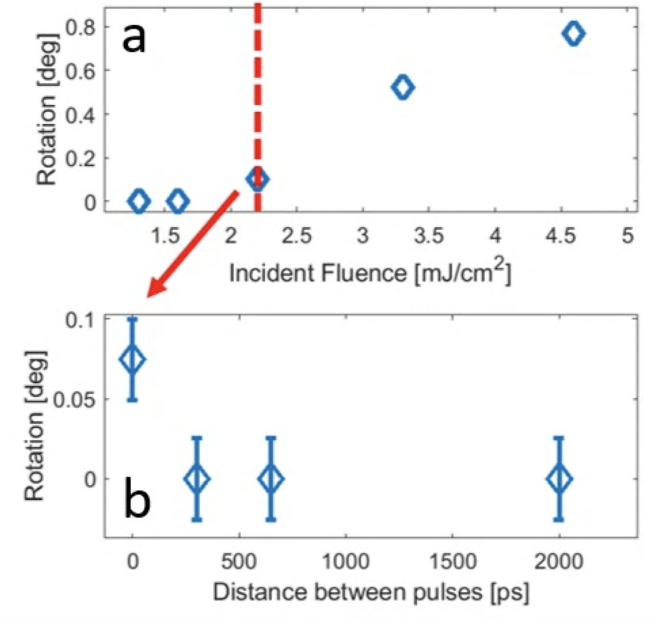


FIG. 12. (a) Fluence threshold at 10 K and (b) Time-varied dynamics at 10 K with a different lamella cut from the same crystal.

-
- [1] S. Pöllath, J. Wild, L. Heinen, T. N. G. Meier, M. Kronseder, L. Tutsch, A. Bauer, H. Berger, C. Pfleiderer, J. Zweck, A. Rosch, and C. H. Back, Dynamical Defects in Rotating Magnetic Skyrmion Lattices, *Physical Review Letters* **118**, 207205 (2017).
- [2] W. Chen, L. Liu, and Y. Zheng, Ultrafast Ratchet Dynamics of Skyrmions by Defect Engineering in Materials with Poor Conductivity Under Gigahertz Magnetic Fields, *Physical Review Applied* **14**, 064014 (2020).
- [3] P. S. Pershan, J. P. van der Ziel, and L. D. Malmstrom, Theoretical Discussion of the Inverse Faraday Effect, Raman Scattering, and Related Phenomena, *Physical Review* **143**, 574 (1966).
- [4] E. Ruff, P. Lunkenheimer, A. Loidl, H. Berger, and S. Krohns, Magnetoelectric effects in the skyrmion host material Cu_2OSeO_3 , *Scientific Reports* **5**, 1 (2015).
- [5] T. Seifert, S. Jaiswal, U. Martens, J. Hannegan, L. Braun, P. Maldonado, F. Freimuth, A. Kronenberg, J. Henrizi, I. Radu, E. Beaupreire, Y. Mokrousov, P. M. Oppeneer, M. Jourdan, G. Jakob, D. Turchinovich, L. M. Hayden, M. Wolf, M. Münzenberg, M. Kläui, and T. Kampfrath, Efficient metallic spintronic emitters of ultrabroadband terahertz radiation, *Nature Photonics* **10**, 483 (2016).
- [6] N. Prasai, A. Akopyan, B. A. Trump, G. G. Marcus, S. X. Huang, T. M. McQueen, and J. L. Cohn, Spin phases of the helimagnetic insulator Cu_2OSeO_3 probed by magnon heat conduction, *Physical Review B* **99**, 020403 (2019).
- [7] M. Finazzi, M. Savoini, A. R. Khorsand, A. Tsukamoto, A. Itoh, L. Duò, A. Kirilyuk, T. Rasing, and M. Ezawa, Laser-Induced Magnetic Nanostructures with Tunable Topological Properties, *Physical Review Letters* **110**, 177205 (2013).
- [8] W. Koshibae and N. Nagaosa, Creation of skyrmions and antiskyrmions by local heating, *Nature Communications* **5**, 5148 (2014).
- [9] T. Adams, A. Chacon, M. Wagner, A. Bauer, G. Brandl, B. Pedersen, H. Berger, P. Lemmens, and C. Pfleiderer, Long-Wavelength Helimagnetic Order and Skyrmion Lattice Phase in Cu_2OSeO_3 , *Physical Review Letters* **108**, 237204 (2012).
- [10] R. Berman and P. G. Klemens, Thermal Conduction in Solids, *Physics Today* **31**, 56 (1978).
- [11] P. B. Allen, Improved Callaway model for lattice thermal conductivity, *Physical Review B* **88**, 144302 (2013).
- [12] N. Prasai, B. A. Trump, G. G. Marcus, A. Akopyan, S. X. Huang, T. M. McQueen, and J. L. Cohn, Ballistic magnon heat conduction and possible Poiseuille flow in the helimagnetic insulator Cu_2OSeO_3 , *Physical Review B* **95**, 224407 (2017).
- [13] J. S. White, I. Levatić, A. A. Omrani, N. Egetenmeyer, K. Prša, I. Živković, J. L. Gavilano, J. Kohlbrecher, M. Bartkowiak, H. Berger, and H. M. Rønnow, Electric field control of the skyrmion lattice in Cu_2OSeO_3 , *Journal of Physics: Condensed Matter* **24**, 432201 (2012).

5.3 Open questions & perspectives

5.3.1 Quantitative simulation and Topological inverse Faraday effect

In the present study, although in good agreement qualitatively reproducing the coherent oscillations observed, our simulation is off by a few orders of magnitude in absolute value. It is expected, as our simulation considers a clean system. In other words, the model neglects disorder, and pinning effects important in the physics of skyrmion [331–333]. Hence, the damping process is anticipated to be much higher, increasing the rotational torque applied. Another intriguing possible explanation resides in the estimated effective field with $H_{\text{eff}} = 10\text{mT}$. First, we note that the Verdet constant and the magnetization calibration used might differ in our sample. Although, it can not account for the orders of magnitude difference alone. A more attractive proposal directly involves light-matter coupling. Indeed, the computed induced field relies on the regular inverse Faraday effect originating from strong spin-orbit coupling interactions. However, in this microscopic theory, a uniform magnetization with trivial topology is considered [334, 335]. Clearly, it is different from our case. Furthermore, an effective magnetic field originating from the complex light interaction with the magnetic texture topology has been recently predicted [145, 147] and might be relevant in our case as the scalar spin chirality that would couple to the laser is $\sim 10^1$ ($\sim 10^{-3}$ in the helical phase). While the topological inverse Faraday effect (TIFE) has not yet been reported experimentally, it remains an appealing lead that we potentially have witnessed in our experiment.

5.3.2 What defines the rotation direction of the skyrmion crystal

Skyrmion polarity changes the sense of rotation

The inverse Faraday effect shows an out-of-phase difference by a π factor in the magnetization response between the two different handedness (see Fig 5.1a). A similar behavior has been measured in Cu_2OSeO_3 inside the conical and the skyrmion phase as shown in Fig 5.1b,c. Hence, we initially supposed that the light helicity would define the sense of skyrmion crystal rotation. However, our data do not show such a dependence. Instead, one direction was reported (see Fig. 1 in ref. [104]). Our model captures this effect caused by the quadratic field dependency eq. (S7). So, if the induced effective field does not play a role in the direction of the rotation, what defines it? Intuitively, we can expect that the external magnetic field imposes such constrain as it breaks time-reversal symmetry and is important in the skyrmion relaxation after photoexcitation (see Chapter 4, section 4.4). Furthermore, a recent study has demonstrated the sign reversal of the SHE when inverting the skyrmion polarity [336] in an individual skyrmion metallic system. To confirm this hypothesis, we inverted the direction of the applied field and illuminated the sample in the same experimental condition. Indeed, the sense of rotation is inverted and changes from clockwise (CW) to counterclockwise (CCW) shown in Fig. 5.2, thus confirming the essential role of the external magnetic field. Nevertheless, spins forming Bloch-type skyrmions can whirl clockwise or counterclockwise,

characterized by its helicity, sometimes named chirality, illustrated in Fig. 5.3. The exact role of the skyrmion helicity in the reported skyrmion rotation mechanism needs to be clarified. Indeed, we have investigated skyrmions with the same helicity due to highly preferred crystal chirality during the single crystal growth process that should define the skyrmion helicity in Cu_2OSeO_3 [337]. Still, the other crystal chirality remains possible to grow, thus keeping the door open for further investigation.

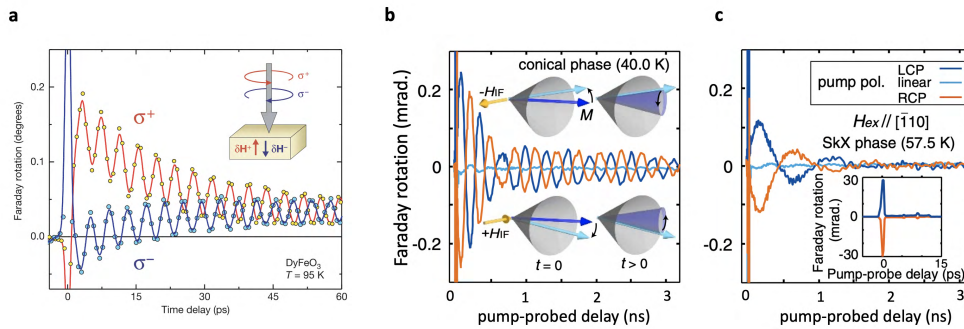


Figure 5.1 – **Driving coherent magnetic modes using inverse Faraday effect.** **a:** First demonstration of the ultrafast photomagnetic ultrafast control via the IFE. Image reproduced from [33]. Ultrafast photoexcitation with 1.0 eV photon energy of Cu_2OSeO_3 showing magnetic collective responses in **(b)** the conical phase and **(c)** the skyrmion phase. Image from [280].

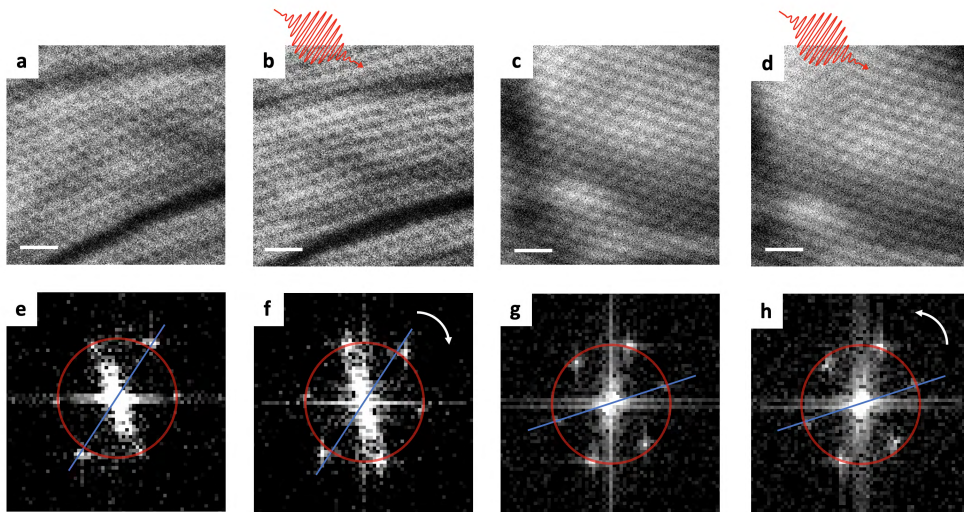


Figure 5.2 – **Skyrmion crystal rotation and skyrmion polarity.** **a:** LTEM image of the initial black skyrmion crystal state. **b:** An second image is taken after a single shot photoexcitation. **e-f:** A CW rotation is observed shown in their corresponding Fourier transform. By inverting the applied field and keeping the same defocus length, the skyrmion polarity is switched denoted by the white skyrmions. Similarly as in the previous series, an image is taken **(c)** before the photoexcitation and **(d)** after showing a CCW rotation. **g-h:** Their corresponding Fourier transforms are shown below each image. The red circle has the same reciprocal length for all Fourier transform. The blue line is a guide for the eye. The white scale bar is 100 nm.

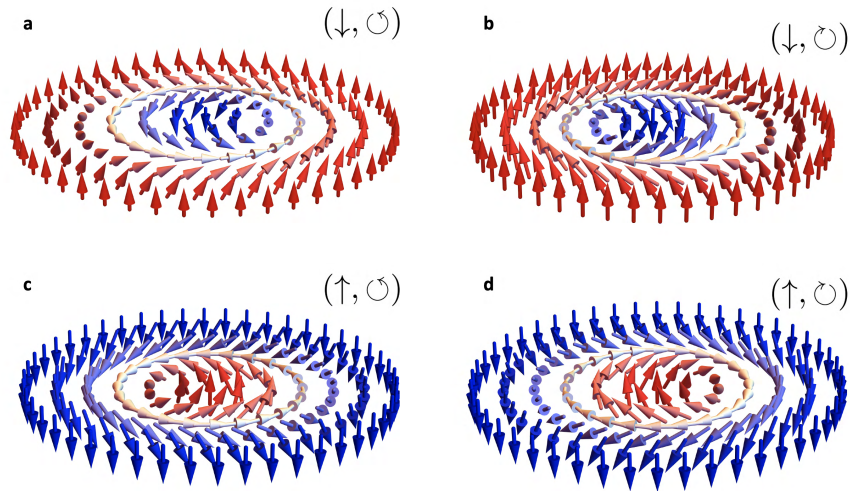


Figure 5.3 – **Illustration of Bloch-type skyrmion.** **a-d:** The four possible Bloch-type skyrmion configurations depending on the helicity and the polarity are presented. The arrow denotes the core spin orientation, while the circle indicates the sense of whirling. Images of courtesy P. Baral.

5.3.3 Breakdown of the skyrmion crystal and skyrmion lattice expansion

In this work, we focused on a single skyrmion domain picture. If we consider skyrmion as a rigid particle, it is evident that the initially large skyrmion single crystal must break down under rotation into smaller clusters, as at a certain point, as the tangential rotation will exceed the speed of light. In the extreme case, neglecting relativistic effects and the increase of the rotation speed predicted to scale linearly with the number of skyrmions, thus considering a rotation speed of $\sim 10^{10}$ deg/sec, the radius of the skyrmion crystal has to be larger than ~ 2 metres to approach such a limit, order of magnitude larger than our sample size. Nonetheless, we observed the breakdown of the initial large single crystal into many smaller crystallites with an approximative size of 460 nm, containing roughly 50 skyrmions that rotate simultaneously (see Fig. 5.4 and Fig. 4 in ref.[104]). Similar effects occur in the other sample investigated. Furthermore, in most cases, the skyrmion lattice expands by $\sim 10\%$, from an average modulation length of 65 nm to 70 nm to rotate, after one single shot photoexcitation shown in Fig. 5.5. Sending additional laser pulses does not change the pitch length, which remains stable for minutes. Actually, we did not observe any recovery toward the initial pitch length. These two observations indicate the presence of an optimal rotation configuration, which is not captured by our simulation, limited to a few skyrmions interactions and periodic boundary conditions. Thus, it suggests the presence of a hidden interaction that prevents the skyrmion crystal from rotating uniformly and must emerge from a long-range ~ 500 nm skyrmion interaction. We proposed a few candidates responsible for the skyrmion crystal breakdown: edge effects, frictions between the skyrmion cluster, and disorder, discussed in

the next part. In addition, the question of what defines the center of rotation is still open. Our observations demonstrate emergent properties of the skyrmion interactions at mesoscale, opening exciting perspectives for investigating the collective skyrmion dynamics at a large scale and might be relevant for unconventional superconductors in which magnetic vortices similar to skyrmion exist at similar length scale.

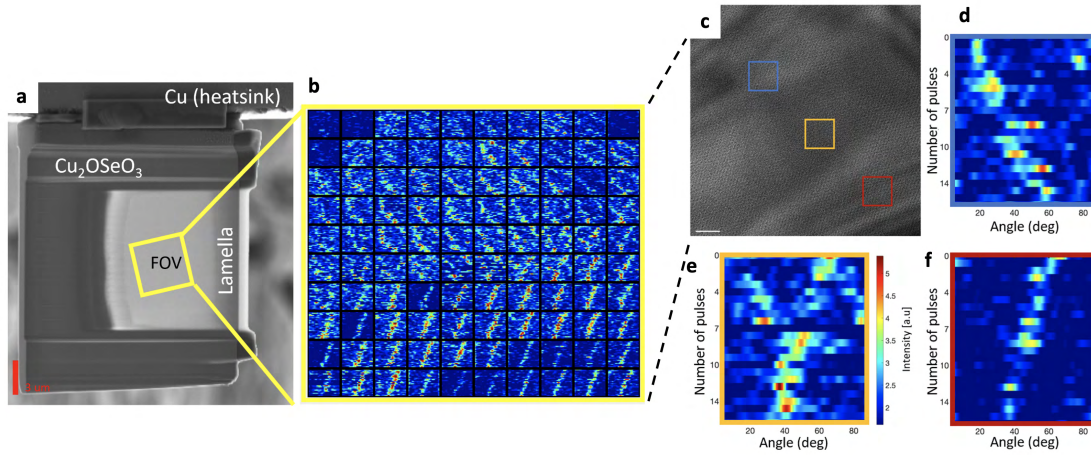


Figure 5.4 – **Spatial dependence on the skyrmion rotation.** **a:** A SEM image of the lamella investigated and the field of view investigated. **b:** After dividing the field of view by a 10×10 sub-images of 460 nm size containing approximately 50 skyrmions, their corresponding Fourier transform have been computed and show the skyrmion profile evolution (see Fig. 4.12 for the method). Two senses of rotation with two different rotation rates are observed. **c:** Real space image of the field of view studied. The white scale is 500 nm. We present three sub-images at different sample regions showing **(d)** CW rotation, **(f)** CCW rotation, and **(e)** an intermediate state.

Coexistence of CW and CCW rotating skyrmion crystal

Previously, we have seen the crucial role of the external magnetic field that can change the sense of rotation. The lamella size is of the order of $\sim 10 \mu\text{m}^2$ immersed in a homogeneous magnetic field. Thus, we should expect the same sense of rotation for all skyrmion crystals. Surprisingly, by inspecting different lamella regions (the same as the one presented above in [104]), we observed clear boundaries between two rotating skyrmion configurations at roughly the center of the sample (see Fig. 5.4b). In the two other samples studied, we did not observe such an effect, excluding stray-field effects as the lamellae have similar geometry, and the effect occurs far from the edges. At the same time, we report anomalies in the magnetic contrast that can be explained by a twinned crystal discussed in Chapter 6, section 6.1.3. We can make two other suppositions regarding this intriguing effect. One invokes the total angular momentum conservation. Our theory of rotational torques relies on such conservation. However, it considers only one single skyrmion crystal and neglect all other crystals rotating. Thus, it

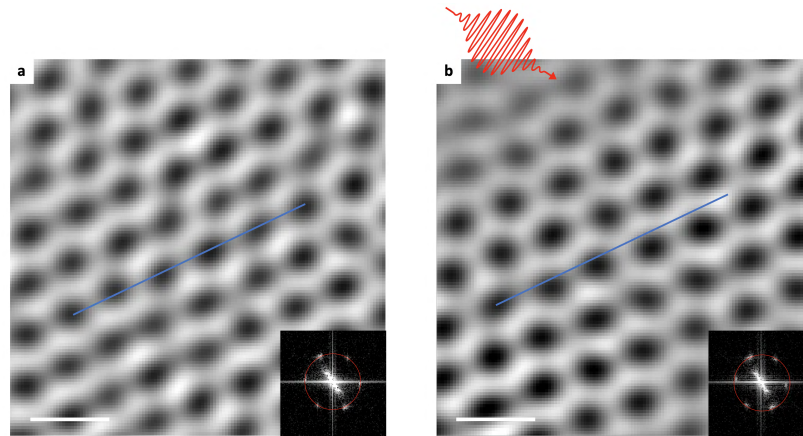


Figure 5.5 – **Variation of the skyrmion pitch length after photoexcitation.** **a:** LTEM image of the initial skyrmion state with a pitch length of 65 nm. **b:** LTEM image after circularly polarized single pulse NIR photoexcitation. A rotation of the lattice is observed concomitant with an increase of the skyrmion lattice modulation length to ~ 70 nm. Insets are the corresponding FFT, and the red circles have the same reciprocal length. Data were taken at 5 K, and at 32 mT. A Fourier filter has been applied to enhance skyrmion contrast. The blue lines give a reference to illustrate the rotation and the increase of the pitch length. The white scale bar is 100 nm.

is possible to conceive that for specific parameters such as the sample size, thickness, and defects along with the field strength, the most efficient way for the skyrmion breathing mode to relax is to induce the rotation in both directions. The second hypothesis also originates from the large amount of rotating skyrmion single crystals (shown in Fig. 5.4b) and invokes viscosity between the different skyrmion clusters inducing frictions and consequently favor both senses of rotation. In that scenario, the fact that we did not observe the phenomenon in the two other lamellae can be easily explained by size and defect effects. Hall viscosity, another type of dissipationless viscosity-inducing asymmetries, has recently been predicted [338, 339] and demonstrated in an electron fluid [340]. For magnetic skyrmions, this effect has been recently theoretically investigated [341, 342]. In our case, no direct current is flowing. Hence no skyrmion hall effect is directly present. Still, we can ask ourselves what would be the emerging magnetic and electric field induced by the rotating breathing skyrmions, and how will it relate to the presence of a charged particle? This question is all the more legitimate since a continuous flow of electrons crosses our sample.

5.3.4 Controlling the rotation direction using ultrafast OAM optical beam

The total angular momentum carried in a light beam is the sum of the spin angular momentum (SAM) and the orbital angular momentum (OAM). Although usually not considered, the latter has recently proven its relevance in the ultrafast demagnetization process [343] and is proposed to contribute to the IFE [344]. Furthermore, OAM beam is anticipated to

control the skyrmion motion whirling around the beam as the topological charge carried by the optical vortex dictates the skyrmion sense of rotation [146, 345]. We investigated this exciting approach using an ultrafast NIR (1200 nm) OAM laser beam obtained by a spatial light modulator (SLM) that applies a phase-mask, thus modifying the phase of the propagating wave (see Fig. 5.6). We observed a change in the rotation direction that depends on the angular orbital momentum (see Fig. 5.7), unlike the pure SAM contribution that triggers always the same sense. The preliminary results are highlighted in Tab. 5.1. Hence, we conclude that OAM beam is able to induce skyrmion rotation at a similar fluence that in ref.5.5, and allow controlling the direction rotation. Although the exact microscopic mechanism remains to be clarified, we anticipate revealing a new type of light-matter coupling with a topological magnetic texture. We should mention that a double pulse experiment type, as done in ref. [104] with an OAM beam, is currently beyond state-of-the-art. Indeed, the technique already involved to obtain such results is extremely challenging, as it requires cryo-LTEM, ultrafast NIR that is obtained through a highly non-linear optical process, an almost perfect transverse electromagnetic mode, and the sample size $\sim 5 \mu\text{m}$ is much smaller than the non-homogeneous OAM beam footprint $\sim 100 \mu\text{m}$. Our preliminary results demonstrate exciting prospects for energy-efficient and all-optical skyrmion control at ultrafast timescales.

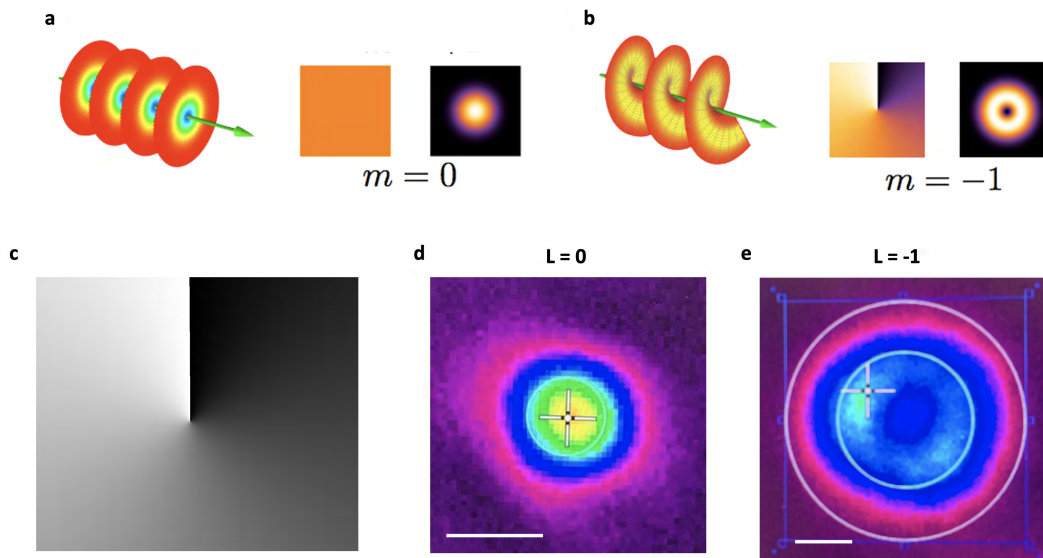


Figure 5.6 – **Generation of an ultrafast OAM beam.** Illustration (from left to right) of the beam wavefront, the phase-mask associated, and its spatial distribution in (a) a trivial beam and (b) in a twisted wavefront forming a helix and characterized by a nonzero topological charge. c: Example of a phase-mask used in our SLM, (d) modifying our initial Gaussian beam to (e) an OAM beam characterized by a different spatial distribution. The cross indicates the sample position. The white scale bar is $50 \mu\text{m}$. Images a and b are from wiki media common.

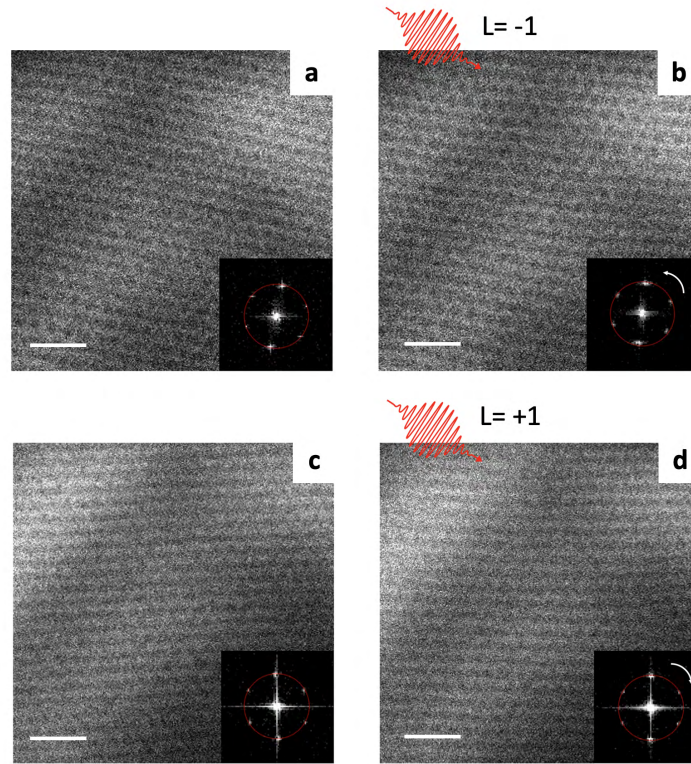


Figure 5.7 – **Skyrmion rotation controlled by ultrafast OAM beam.** LTEM images **a** and **c** are taken before the photo-excitation. LTEM images **b** and **d** show the skyrmion order after ultrafast OAM photo-excitation with linear polarization, for $L = -1$ and $L = +1$, respectively. Data were taken at 5 K, and at 32 mT. The inset shows the corresponding Fourier transform. The white scale bar is 200 nm.

Occurrence	Clockwise \odot	Counterclockwise \ominus
$L = +1, P = \leftarrow\uparrow\rightarrow$	4	1
$L = +1, P = \sigma^+$	1	1
$L = +1, P = \sigma^-$	0	2
$L = -1, P = \leftarrow\uparrow\rightarrow$	1	5
$L = -1, P = \sigma^+$	2	1
$L = -1, P = \sigma^-$	0	2

Table 5.1 – **Controlling skyrmion crystal with an ultrafast OAM beam.** The table presents the result obtained in one lamella acquired in two different sessions. The rotation is spatially dependent. The effect has been reproduced in a second lamella (not shown here). The first column indicates the different beam condition with ± 1 the angular momentum and $\leftarrow\uparrow\rightarrow$, σ^+ , σ^- indicating linear polarization, right-handed and left-handed circular polarization, respectively. The second and third columns correspond to the number of occurrences for CW and CCW rotation, respectively, observed during the preliminary analysis. The data was acquired at 5 K with $\mu_0 H = 32$ mT, using LTEM.

5.4 Conclusion

Light offers appealing prospects in the energy-efficient and ultrafast manipulation of the magnetic order needed for next-generation devices and the development of quantum functionalities. Here, we report a new mechanism that allows us to control a few spins arrangement at the nanometre and sub-ns spatio-temporal scales with low energy absorption, harnessing the insulating character of Cu_2OSeO_3 . To understand the underlying mechanism, we developed a new theory that captures our observation qualitatively. Nonetheless, many exciting open questions and suppositions remain to be challenged. To mention only a few, the exact microscopic light coupling with a topological spin texture is elusive, and the role of defects might be important to describe the experiment quantitatively. In addition, we proposed a long-range interaction emerging from the collective skyrmion motions that must be clarified to catch the entire mesoscale dynamics. Finally, we show enthusiastic preliminary results demonstrating that the skyrmion rotation can be controlled by OAM light, thus paving the way for ultrafast all-optical skyrmion control essential for skyrmion-based devices.

6 Open questions in the skyrmion host material Cu_2OSeO_3

Contribution

I contributed to this project by taking the data, compiling them, and performing the preliminary analysis. Furthermore, I installed with the collaboration of A. A. Sapozhnik the laser beam line allowing NIR in-situ photoexcitation. The dataset for the [001] sample was acquired and compiled by myself and A. A. Sapozhnik, while the other datasets presented were taken by myself, A. A. Sapozhnik and P. Tengdin. The samples were provided by P. Che and T. Schönenberger. Single crystals are grown by A. Magrez and P. Baral. T. LaGrange and I. Madan gave experimental support. F. Carbone supervised this work.

6.1 Real space exploration under various magnetic field conditions

LTEM allows to investigation magnetic orders with nanometric resolution in real space. Therefore, defects in the magnetic texture and spatial-dependent magnetization can be resolved, while for reciprocal bulk techniques, those effects are invisible. Furthermore, only a few seconds of exposure time are needed to acquire an image with a good signal-to-noise ratio. The latter is essential to resolve potential magnetic dynamics that exist on similar or longer timescales. Cu_2OSeO_3 is a fascinating material that is still under current investigation. No less than fifteen scientific articles were published containing the keyword " Cu_2OSeO_3 " in 2022¹. During this thesis, we investigated eighteen Cu_2OSeO_3 TEM lamella using real space LTEM and acquired more than one TB of images. By carefully analyzing the images shot, we found several surprising results. Although we were not able to assign their precise origin, these observation merits being presented, as they could be helpful for the community. To begin with, we found a spiral state. Such states have been recently observed using reciprocal technique and assigned to a surface state [346, 347]. In addition, a skyrmion elongation leading to an anisotropic skyrmion lattice has been identified. We report the coexistence of *white* and *black* skyrmions, which translates into Bloch-type skyrmion with the two possible helicities, and

¹<https://www.webofscience.com/>

suggest twinned crystal as an explanation. Probably, one of the most promising discoveries is a topological fluctuation uncovered in the low-temperature skyrmion phase at high fields. In that phase, skyrmions that have short-range order but have lost long-range interaction appear and disappear on a few-second timescale. This chapter aims to be more descriptive and therefore uses more colloquial language justified by the status of the investigation.

In this section, we present some fresh experimental observations in Cu_2OSeO_3 lamella in and out-of-equilibrium, using cryo-LTEM. The discussion below is mainly based on a descriptive approach. The current literature overviewed in the past Chapters might provide some clarifications. However, further investigations are needed and are left for future work. In particular, we investigated the magnetic orders when the sample is under an external magnetic field along high-symmetry axes, namely $[111]$, $[1\bar{1}0]$, $[001]$. For clarity, we used the notation " $[111]$ ", " $[1\bar{1}0]$ ", and " $[001]$ " to refer as the applied magnetic orientation field that is parallel to the crystallographic axes of the sample. For example, the $[111]$ sample refers to a lamella prepared to expose the $[111]$ direction out-of-plane. Consequently, the magnetic field is parallel to $[111]$ due to the LTEM geometry. The TEM goniometer allows to rock the sample. This is typically done in order to optimize image quality. During the sample preparation, the miscut angle can be a few degrees. The combination of both factors usually is below 5° . Hence, the contribution of the in-plane magnetic field is generally neglected. Our minimal applied magnetic field is around 10-14 mT, which corresponds to the remanent field of the TEM objective lens. Consequently, in our experimental condition, when referring to ZFC, we refer to the fact that no electrical current was injected into the objective lens. The presentation of the results is divided into three distinct subsections. Each section corresponds to one magnetic field configuration. First, the $[1\bar{1}0]$ sample discussed possesses a surface spiral state and elongated skyrmions. The second part focuses on the exploration of low-temperature skyrmion (LT-skyrmion) phase, recently found. We found evidence of a new strongly fluctuating skyrmion phase and anomalies in the skyrmion pitch length. In the last part, we reported the coexistence of two kinds of Bloch-type skyrmion differentiated by their polarity or helicity and possible signature of the TIFE.

6.1.1 Surface spiral state and skyrmion elongation with $\mathbf{H} \parallel [1\bar{1}0]$

Initially, this work was done while investigating the skyrmion photo-creation using an NIR (1200 nm - 1.03 eV) ultrashort laser pulse presented in Chapter 4 and compiled in ref. [219]. Indeed, the skyrmion photo-creation process in Cu_2OSeO_3 is a puzzling problem, as a strong wavelength dependence was observed, inconsistent with a thermal-like mechanism reported lately by our group in FeGe [217]. In particular, we were investigating the possibility of a transient electric field induced by the laser pulse that would have coupled to the electric polarization and favored the skyrmion phase. We performed a similar exploration to study such a hypothesis as in ref. [219] by applying the magnetic field along the direction $[1\bar{1}0]$. One strong piece of evidence would be to identify a substantial fluence threshold difference and a polarization dependence. It turns out that no clear evidence was found supporting this idea.

6.1. Real space exploration under various magnetic field conditions

No notable linear polarization dependence was observed, and the threshold is roughly comparable ($0.18 \text{ mJ}/\text{cm}^2$ absorbed fluence) to the $[111]$ sample ($0.06 \text{ mJ}/\text{cm}^2$ absorbed fluence). However, in the process, we uncovered an unusual helical-type state that emerges at low fields upon field-cooled cooling (FCC) when the magnetic field is parallel to the $[1\bar{1}0]$ direction and coexists with the conical phase. The new helical-like order, which we will refer as a spiral state in the following, is characterized by a longer pitch length $\sim 80 \text{ nm}$ compared to the usual pitch length of approximately 65 nm . Surprisingly, 80 nm corresponds to the modulation length of the LT-skyrmion lattice, while the usual helical pitch length ($\sim 65 \text{ nm}$) matches with the high-temperature skyrmion (HT-skyrmion) modulation length. It exists only along a specific direction, which is tilted by 15° from the $[1\bar{1}0]$ in-plane direction (see Fig. 6.1a) and forms a 60° angle with the normal helical state. Additionally, we did not observe a third helical state propagating along the third axis rotated by 120° , and a change in the pitch length was not reported at thermodynamic equilibrium.

For higher magnetic fields, as in the $[111]$ geometry, a metastable skyrmion phase appears at low temperatures during the field-cooled process. Interestingly, close to the magnetic transition around 23 mT instead of forming a single skyrmion crystal, multidomain crystals are observed coexisting with the conical phase as shown in Fig. 6.1e. For skyrmions generated close to the transition and at higher fields, in both cases, an elongation of the skyrmion is identified along the direction close to the spiral state. This is visible in the FFT of the image, as two spots are closer to the center, corresponding to a shorter q -vector describing the skyrmion lattice. In the equilibrium skyrmion pocket obtained by ZFC/field-increased (FI) the skyrmion phase is also stretched along the same direction. We reconstructed a magnetic phase diagram from our real space investigation presented in Fig. 6.2a. For an extensive and precise phase diagram, further work is needed. Indeed, coexisting phases are usually present, and a skyrmion reorientation and elongation have been observed for fields larger than $\sim 80 \text{ mT}$ (not shown), which are not represented in our phase diagram. Unlike most $[111]$ lamella investigated, the equilibrium magnetic skyrmion phase extends down to 5 K (hatched area), consistent with other study [267]. Our data shows a hysteretic behavior when suppressing the magnetic skyrmion order by increasing the temperature, shown in the red-shaded area, absent in bulk crystal and probably originating from the topological energy barrier of the skyrmion and surface effects.

Recently, a similar expansion in the helical modulation period was reported in a TEM lamella [268]. In this study, the authors shows a field and thickness dependence of the modulation length, that they associated to the interplay of the stray-field and magnetic anisotropy energies. Although, the angle formed between the helical state and the spiral state differs in the two independent experiments, the pitch length of the newly reported extended modulation, as well as its orientation are in extremely good agreement with our observation. As the spiral state arises from surface effect, it should not exist in bulk Cu_2OSeO_3 . This is supported by bulk magnetic susceptibility measurement where no signature of such state was observed [251]. Furthermore, a new REXS experiment was carried out by Baral *et al.*, with a penetration depth of 100 nm in Cu_2OSeO_3 [348]. They observed extra magnetic spots (designated by the

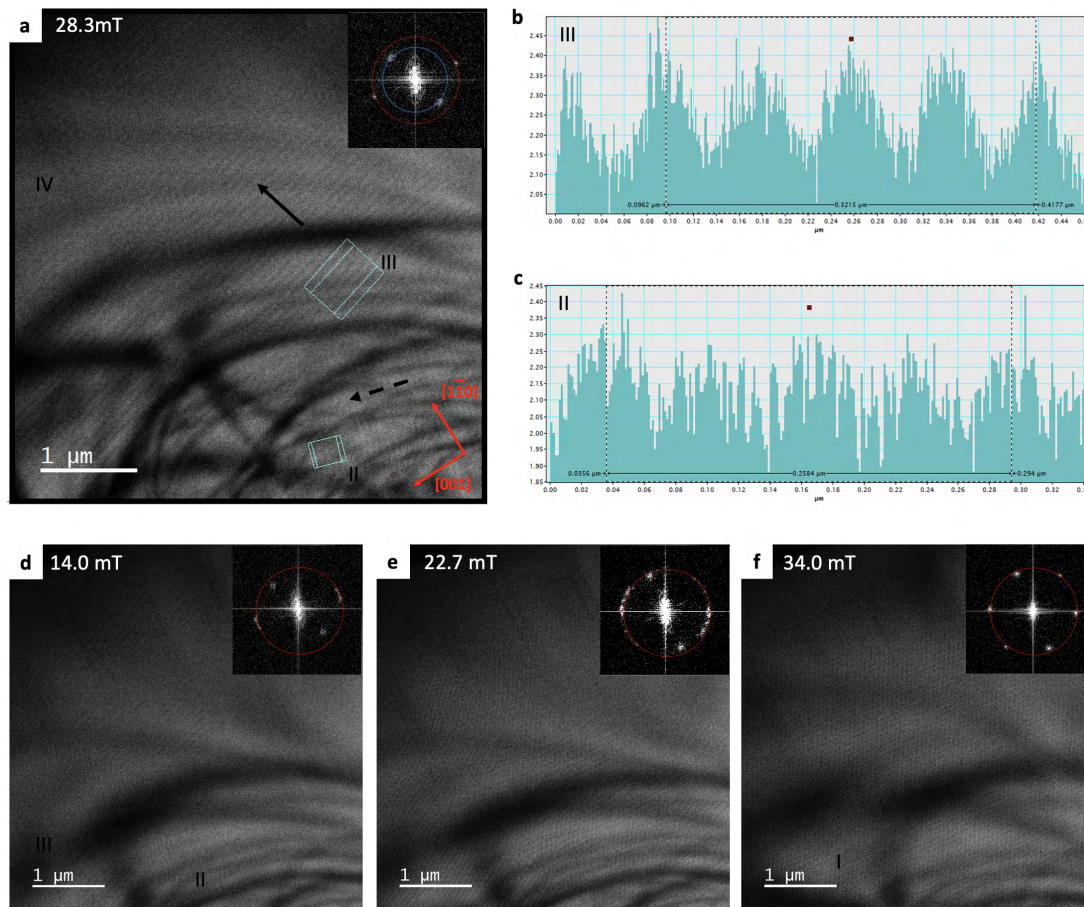


Figure 6.1 – **Observation of a spiral surface state and non-symmetric skyrmion crystals.** **a,d-f:** LTEM images showing the magnetic contrast with 2 mm defocus length. All images were acquired in EFTEM mode with a K2TM camera, at 5 K after FCC protocol. **a:** A field cycling (> 400 mT) was applied to increase the number of helices. The solid black arrow denotes the novel spiral phase propagation. The dashed arrow corresponds to the usual helices propagation. The profile of the spiral and helical state are presented in **b** and **c**, respectively. **d-f** show the final magnetic state upon FCC for different applied magnetic fields. Insets of the images **a,d-f** show their corresponding FFT. The skyrmion, helical, spiral, and conical states are numbered from I to IV, respectively.

red arrows in Fig. 6.2b), which they associated with a surface spiral state, as the blurred spot in the REXS pattern is a signature of a surface state. The extracted pitch length of the surface spiral state from the REXS data is around 120-130 nm longer than what we observed (80 nm). The more intense magnetic spots (shown by the black arrows) correspond to the usual helical phases (~65 nm). For those extra reflections to appear, field cycling is required, i.e., cooling down, ramping the field to saturation, and progressively decreasing the field to the desired value. Although, in our measurement, we observed the spiral order without field cycling (see Fig. 6.1d), by doing so, we remove the helical state in favor of the spiral state shown in

6.1. Real space exploration under various magnetic field conditions

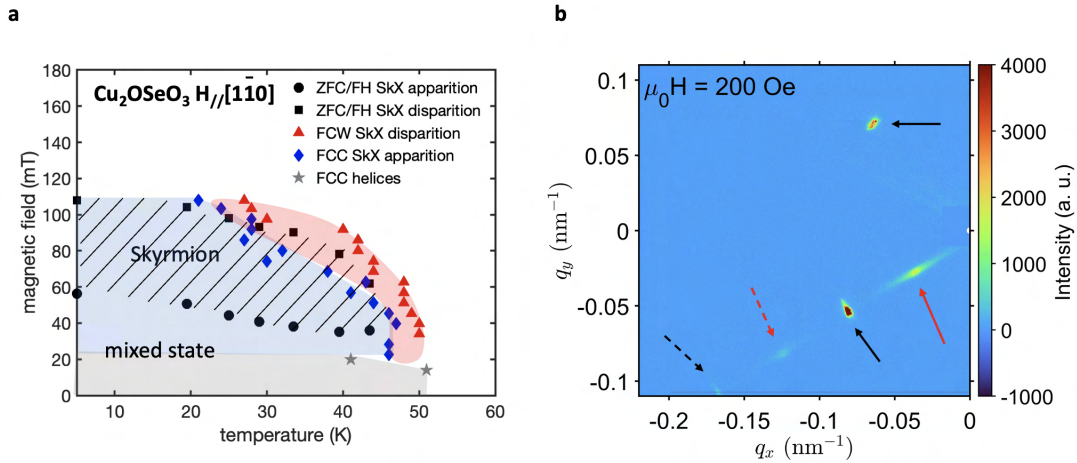


Figure 6.2 – **Magnetic phase diagram and surface spiral spin state.** **a:** Magnetic phase diagram obtained from LTEM measurement, the mixed state corresponds to the coexistence of the conical phase and the two helical spin textures observed. The transition temperature is around 51 K, higher than its bulk counterpart (58 K), the offset is due to surface effect in good agreement with ref.[268]. **b:** resonant elastic x-ray scattering (REXS) pattern showing the helical phase modulated along [010] and [100] (black arrows) and its second harmonic (dashed black arrow). Two blurred spots appear along [010] and are associated with a surface spin chiral. The red arrow shows the fundamental, and the dashed red arrow its third harmonic. The origin corresponds to the structural Bragg reflection (100). The REXS pattern was collected at 20 K. After a zero-field cool down, at 20 K, the field was ramped up to saturation and then reduced to 20 mT for the measurement. The horizontal in-plane magnetic field was off from the [110] zone axis by 9 deg. Data acquisition was made by Baral *et al.* at the BL-29 Boreas at ALBA synchrotron facility (Barcelona). More information can be found in Chapter 7 in ref.[251].

Fig. 6.3a-b.

If they are the same phase, this suggests that the pitch length of the surface spiral state is strongly thickness dependent as REXS has a penetration depth of 100 nm in Cu_2OSeO_3 and our lamella thickness is around 150 nm, consistent with the observation made by Han *et al.* [268]. Furthermore, it does not exist in bulk. We extended the investigation by illuminating the sample with an ultrashort NIR laser pulse, as we are interested in manipulating the magnetic order out-of-equilibrium.

The general (if not mentioned differently) protocol used to investigate the magnetic order upon ultrashort illumination is the following: First, the sample is cooled down to 5 K. Then, we saturated the sample with a field > 400 mT and progressively reduced the field to its nominal value. A NIR (1200 nm - 1.03 eV) linearly polarized single pulse with a duration of approximately 50 fs illuminates the sample homogeneously, as the beam footprint is ten times larger compared to the sample size of a few microns. The image is then acquired a few seconds

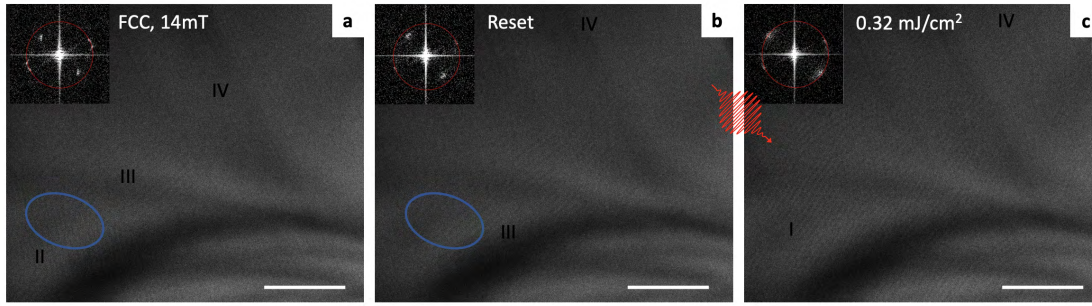


Figure 6.3 – **Magnetic reorientation and skyrmion photo-creation in $[1\bar{1}0]$ sample.** **a:** Magnetic final state reached upon FCC at 5 K. A mixture of three magnetic orders is visible, the conical, helical, and spiral state. **b:** After field cycling, a reorientation of the magnetic orders occurs and transforms the helical order to the spiral order depicted within the blue oval. **c:** Demonstration of the skyrmion photo-creation upon ultrafast excitation. Several domains are formed, and preferential orientations are observed. The inset shows the corresponding FFT. The white scale bar is $1\mu\text{m}$. The skyrmion, helical, spiral, and conical states are numbered from I to IV, respectively.

after the pulse is sent. An additional field cycling is executed to repeat the procedure and reset the magnetic state.

We reported the capability to photo-induce a hidden skyrmion phase, similar to the skyrmion phase reported [219] (discussed in Chapter 4). Indeed, this skyrmion phase exists below the critical field and can not be reached by other means. The lowest incident fluence threshold to generate the skyrmion phase reported is $36\text{ mJ}/\text{cm}^2$, corresponding to an absorbed fluence of $0.18\text{ mJ}/\text{cm}^2$ as the photon pump energy is far beneath the bandgap. The threshold value is three times larger than the value found in [111] samples. Using the heating model used in ref. [104], the estimated temperature rise is approximately 60 K and the initial temperature is recovered on μs time scale. At the lowest field possible allowed by our setup (14 mT), unlike in the [111] field configuration where the skyrmion phase expands and stabilizes after the photoexcitation (ref. [219] and Chapter 4), here the skyrmion phase decays on a few minutes time scale towards the mixed helical, spiral and conical phase (see Fig. 6.4a-d). This indicates a major difference in the magnetic ground state nature between the [111] and $[1\bar{1}0]$ geometries that merits further theoretical and experimental studies. This argument is supported by examining the stability of the metastable skyrmion phase present when the sample is field-cooled at higher fields upon photoexcitation. After illumination, the initial skyrmion single crystal relaxes into a mixture of coexisting magnetic textures; a smaller skyrmion single crystal, the conical, the helical and spiral phases as presented in Fig. 6.4e-f.

We have also investigated the magnetic response upon photoexcitation at 28.3 mT, which is still below the equilibrium skyrmion pocket. Some results are presented in Fig. 6.5. The lowest reported fluence required to create the skyrmion phase is $0.18\text{ mJ}/\text{cm}^2$, equivalent to the value found at 14 mT. Pumping below the threshold value favors the development of the spiral state.

6.1. Real space exploration under various magnetic field conditions

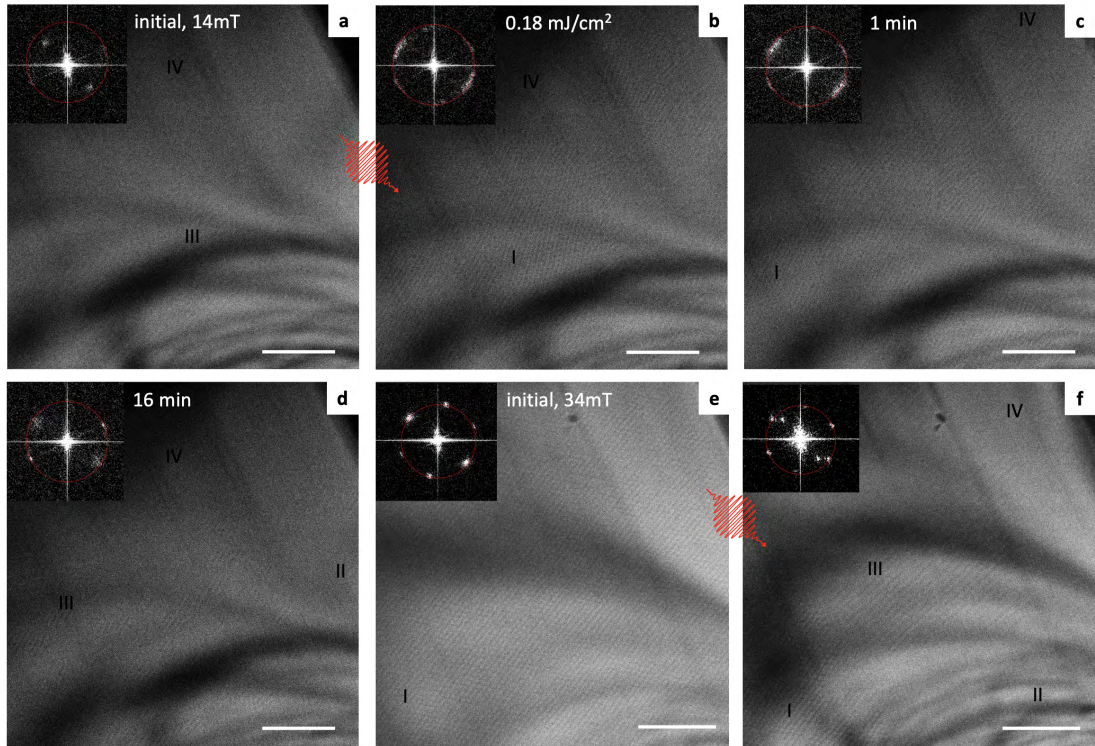


Figure 6.4 – **Instability of the skyrmion state.** **a:** The initial magnetic state is prepared in the mixed state (conical, helical, spiral) at 14 mT. **b:** A single ultrashort laser pulse illuminates the sample and generates skyrmion domains. **c:** Shortly after, the skyrmion domains rearrange to align themselves. **d:** After 16 minutes, almost all skyrmions have decayed into the mixed phase. However, the spiral spin order has not yet reached its equilibrium as a pitch length spans from the initial 65 nm to 80 nm, illustrated by the blurred FFT two spots. **e:** Metastable skyrmion single crystal, obtained after FCC. **f:** A train of 800 pulses separated by 50 ms and an absorbed fluence of 0.35 mJ/cm^2 triggers the relaxation of the skyrmion crystal to a mixture of all reported phases, well distinguished spatially. The white scale bar is $1 \mu\text{m}$. The skyrmion, helical, spiral, and conical states are numbered from I to IV, respectively.

Above the threshold, the skyrmion phase can coexist with all the initial phases (see Fig. 6.5d) or suppress the spiral phase. No trace of skyrmion elongation was observed, in that case.

In conclusion, we observed a magnetic state resembling a helical state with a longer modulation period. It exists only when the magnetic field is applied along $[1\bar{1}0]$ and is characterized by a longer pitch length ($\sim 80 \text{ nm}$) and a strong preferential direction close to the $[1\bar{1}0]$ axis, which we associated to the spiral state found recently by Han *et al.* [268]. From our LTEM investigation, a phase diagram has been constructed showing a magnetic hysteresis and suggests that the nature of the magnetic interaction differs from the $[111]$ case at low temperatures. An elongation of the skyrmion lattice close to $[1\bar{1}0]$ direction obtained by conventional temperature versus field protocol is identified. The skyrmion photo-creation was demonstrated.

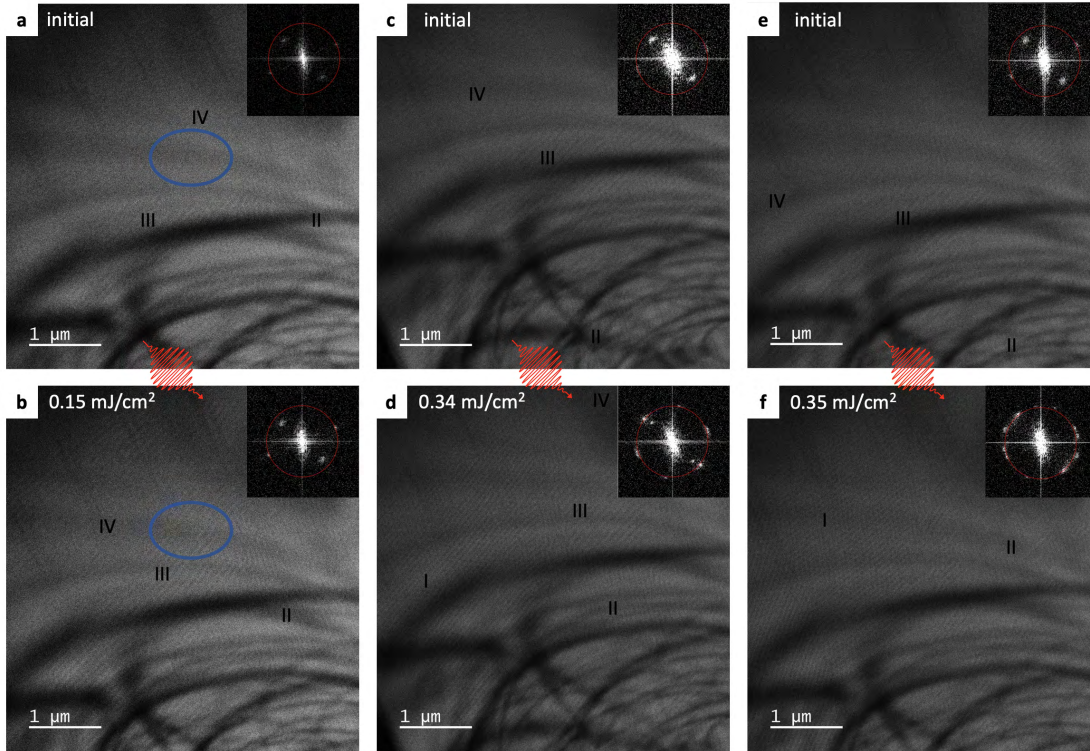


Figure 6.5 – **Light-induced magnetic phase transition.** The same initial magnetic state is prepared with field cycling, and a nominal 28.3 mT magnetic field is applied. **a-f:** A series of three different fluences are presented, one below the fluence threshold and two above. **b:** Although no skyrmions are formed, the spiral state is enhanced. **d:** The photo-induced skyrmion phase coexists with the conical, spiral, and helical phases. **f:** In some cases, the formation of skyrmion multidomains is preferred without the spiral phase. Their corresponding initial state is shown in **a, c, e**, respectively. The skyrmion, helical, spiral, and conical states are numbered from I to IV, respectively.

In that case, no elongation was observed, but instabilities led the skyrmions to decay on a minute time scale at moderated fields. The fluence required is slightly higher than the (111) configuration, and no evident polarization dependence was observed. Thus, indicating that the excitation triggered by the laser pulse is not laser-field driven.

6.1.2 low-temperature skyrmion phase with $\mathbf{H} \parallel [001]$

In this thesis, we investigated essentially the metastable skyrmion (MT-skyrmion) phase stabilized with [111] magnetic field, which originates from the HT-skyrmion phase and exists at low-temperature in a lamella. Although no dramatic change in the shape of the HT-skyrmion pocket was observed in bulk Cu_2OSeO_3 , while applying the magnetic field along other crystallographic directions [251, 349], recently, Chacon *et al.* have reported a new skyrmion phase

6.1. Real space exploration under various magnetic field conditions

using neutron scattering techniques. In particular, this phase is independent of the usual HT-skyrmion phase, as it exists only at low-temperature and requires the presence of high magnetic fields along the specific crystallographic axis [001]. It differentiates by two main aspects; it does not possess a long-range order but keeps its short-range order as the neutron scattering data show a blurred ring in reciprocal space, and no thermal fluctuation is required to stabilize the skyrmion phase. Instead, the authors ascribed its origin from large magnetic anisotropy and strong magnetic fluctuation. In addition, the newly reported skyrmion phase pocket strongly depends on the followed temperature versus field protocols (see Fig. 6.6b-d).

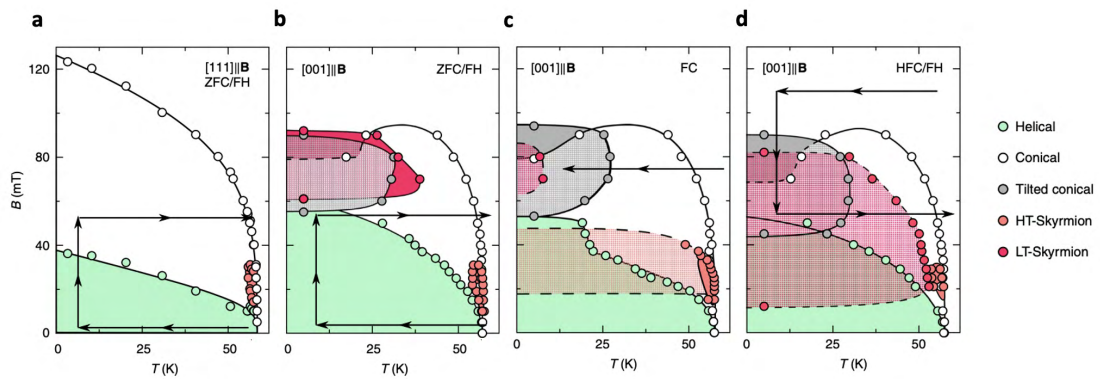


Figure 6.6 – **Observation of an independent skyrmion phase at low-temperature (LT).** a-d: The different magnetic phase diagrams obtained by neutron scattering studies along different crystallographic orientations and with the use of different temperature versus field protocols, with respectively ZFC/field-heated (FH), field-cooled (FC) and high-field-cooled (HFC)/FH. Image reproduced from [171].

To date, no real space images of this so-called LT-skyrmion phase have been published. In addition, the existence of LT-skyrmion in a thin lamella remains to demonstrate. We investigated the presence of this novel phase using cryo-LTEM in our laboratory. Consistent with the neutron experiment, we found an independent skyrmion phase similar to the LT-skyrmion phase described by Chacon *et al.*. Furthermore, we identified several novelties that need to be further analyzed. We observed a second skyrmion phase in three different protocols; ZFC/FI (Fig. 6.9), high-magnetic FCC/field-decreased (FD) (Fig. 6.10), intermediate FCC reaching the MT-skyrmion phase and then increasing the field inducing the transition towards the LT-skyrmion phase (Fig. 6.8). The differences from the MT-skyrmion phase are fourfold; it does not possess a long-range order, its pitch length is larger, it is less robust at lower fields, and it strongly fluctuates at high magnetic fields. This opens intriguing questions of the relation between magnetic anisotropy and the role of quantum fluctuation present in the magnetic building block when the two effects becomes comparable.

Interestingly, the skyrmions do not form a large single crystal but rather small skyrmion islands. While short-range order is preserved as the size of one skyrmion cluster is approximately 250 skyrmions at 98 mT, the long-range order is lost. The skyrmion domains have no strong

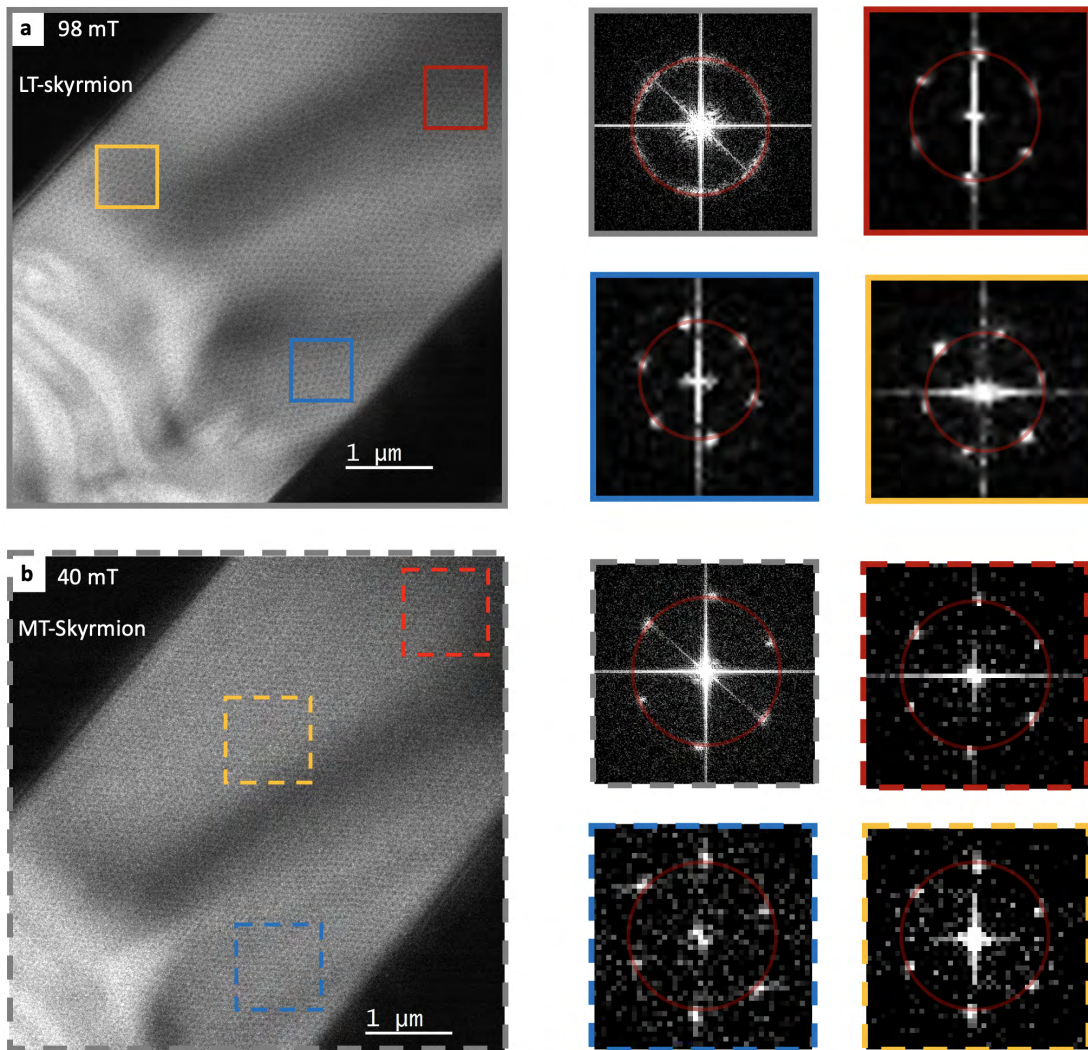


Figure 6.7 – **Comparison of the MT-skyrmion and the LT-skyrmion phases.** **a:** Real space LTEM image of the low-temperature skyrmion phase, obtained by ZFC/FI. The long-range order is lost in this phase, and many coexisting smaller skyrmion crystals with different orientations are observed, similar to a hexatic phase. **b:** Real space LTEM image of the metastable-temperature skyrmion phase obtained by FCC, showing an almost perfect skyrmion single crystal. Both images were taken at 5 K. The magnification factor is $\times 4000$ for image **a** and $\times 3000$ for image **c**. FFT for different regions are shown. Grey panels are the total FFT image, while colored panels are the FFT of specific regions. The red circle denotes the same reciprocal length for their respective associated image. Note that skyrmion anisotropy emerges (blue boxes) in thinner regions (see Fig. 6.8a). Solid (dashed) square box size is 800 nm ($1 \mu\text{m}$).

preferential direction like in the MT-skyrmion phase. Nevertheless, weak polarization is observed along the same preferential direction of the metastable skyrmion phase as shown by the total Fourier transform (solid grey box in Fig. 6.7a), suggesting the presence of a hexatic

6.1. Real space exploration under various magnetic field conditions

skyrmion phase. However, the symmetry of the FFT skyrmion ring depends on the protocol followed and the strength of the applied magnetic field. In addition, the size of the skyrmion cluster also strongly depends on the magnetic field and the sample thickness. In particular, anisotropy in the skyrmion modulation length appears for both skyrmion phases in thinner regions (blue boxes in Fig. 6.7). For thicker areas, we observed a clear difference between the two skyrmion pitch length values. The MT-skyrmion phase has a pitch length of ~ 65 nm, while a longer modulation length of ~ 80 nm is measured for the LT-skyrmion phase. A similar value (~ 77 nm) is found in the neutron experiment [171].

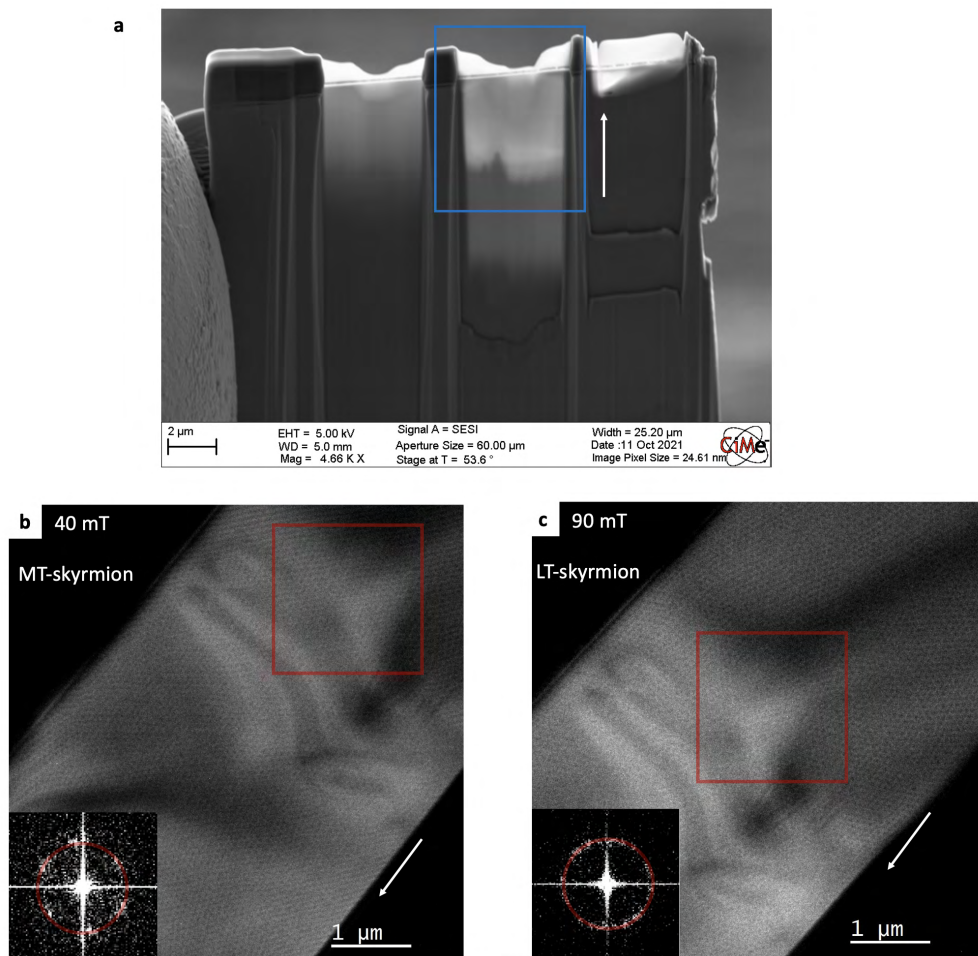


Figure 6.8 – [001] TEM lamella and MT-skyrmion to LT-skyrmion phase transition. **a**: SEM image of the lamella under investigation. The blue rectangle indicates the region studied, and the white arrow indicates the image orientation for all reported LTEM images and is shown explicitly in images **a** and **b**. The transformation from the **(b)** metastable skyrmion obtained by FCC to **(c)** the low-temperature skyrmion phase. Insets present the associated FFT image showing an expansion of the skyrmion lattice modulation length and a loss of the long-range order. The red circle denotes the same reciprocal length for both insets.

The transformation from the MT-skyrmion to the LT-skyrmion phase occurs around 60 mT and is characterized by a smooth magnetic transition. The progressive loss of the long-range order is observed and as well as the change of the pitch length demonstrated in Fig. 6.8. In the ZFC/FI (see Fig. 6.9), the LT-skyrmion first formed around 65 mT at the edge of the lamella. We observed the formation and coexistence of the skyrmion, helical and conical phases in different zones of the lamella, which we attributed to a thickness effect (see Fig. 6.8a). When increasing the field, the skyrmions progress towards the thicker region and fill the entire field of view (FoV) at 86 mT. At higher fields, the conical phase appears and coexists with the LT-skyrmions. Above 130 mT, the LT-skyrmion phase vanishes. Then, we investigated the inverse protocol presented in Fig. 6.10 by cooling the sample from 65 K to 5 K under a magnetic field of 157 mT and progressively reducing the field strength. The LT-skyrmions appear between 135 mT and 121 K and are fully established at 98 mT. However, unlike in the ZFC/FI protocol, reducing the field induces the shrinking and the rearrangement of the LT-skyrmion phase, which transforms into a skyrmion phase similar to the MT-skyrmion and the conical phase appears, to progressively leave the place to the formation of helices. Below 40 mT down to 14 mT, no skyrmion remained, and only helices were observed. This observation is in opposition to the counterpart bulk study where FCC/FD protocol gives a more stable character of the skyrmion. We noticed that the decay is proper to the LT-skyrmion phase as the metastable skyrmions survive at low fields under similar experimental protocols (see Fig. 6.11a-c).

One of the most intriguing observations made during this investigation is the strong fluctuation nature of the LT-skyrmions at high fields (~ 100 mT). Such topological magnetic fluctuation is unique and occurs on the second time scale. Indeed, the exposition time to acquire an image is 1-2 seconds, and we would not be able to resolve the fluctuation if the phenomenon occurs on a faster timescale. Furthermore, this observation required a real space technique, as no signature would appear in reciprocal space. Nonetheless, a new magnetic phase has been recently identified in bulk Cu_2OSeO_3 using magnetic susceptibility and SANS studies that share similar characteristics with our observation [267]. The authors speculated a formation of a superstructure that is a conical spiral composed of tilted spirals. Although the reported phase exists at much lower fields (~ 40 mT), dissipation processes have also been measured at higher fields with the magnetic field along [001] direction in crystals grown by the same crystal grower (see Fig. 5.2 in ref. [251]) and might be a signature of the phase we observe.

In summary, we exploited electron microscopy's capability to visualize the low-temperature skyrmion phase in real space. The LT-skyrmion phase is characterized by a longer modulation length and the loss of long-range order. The skyrmion crystallite size and orientation depend on magnetic fields and shares similarities with a hexatic phase. Compression of the skyrmion crystal along one specific is noticed in the vicinity of the sample edge where the thickness is smaller for both phases. Thus, giving an anisotropic nature of the skyrmion lattice that probably originates from magnetic anisotropic and stray-field effects that become important. By comparing the LT-skyrmion versus the MT-skyrmion, and the ZFC/FI versus FCC/FD

6.1. Real space exploration under various magnetic field conditions

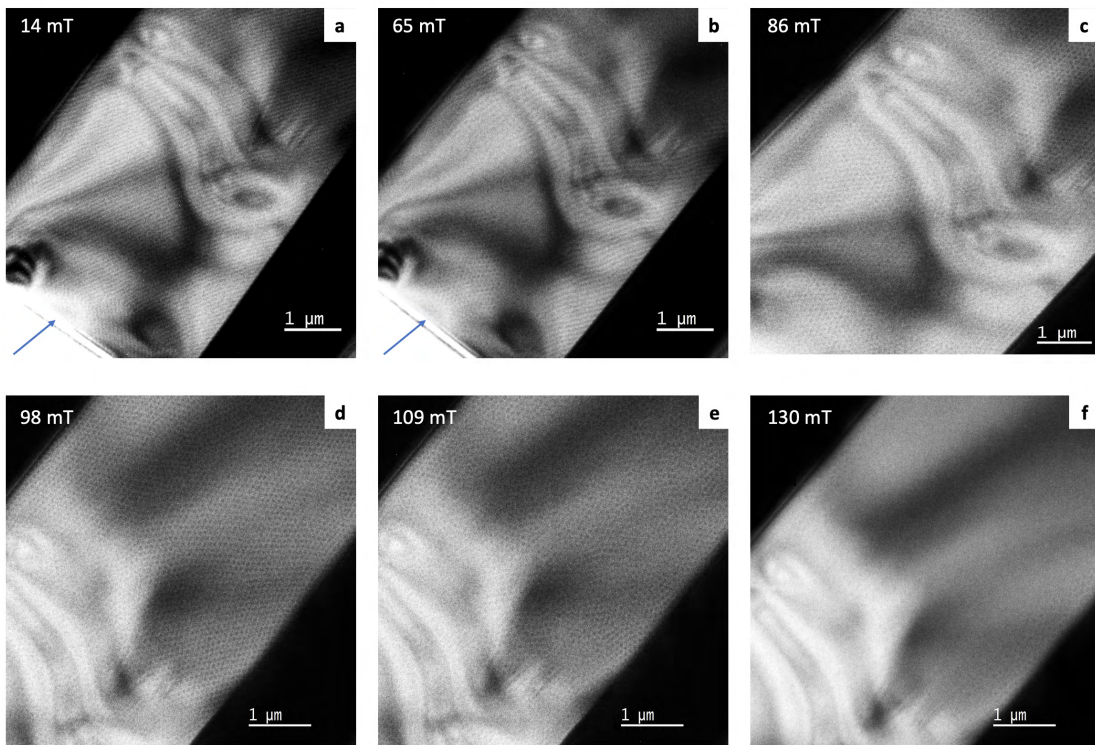


Figure 6.9 – **LT-skyrmion phase from low-fields to high-fields.** a-f: Series of LTEM images while ramping up the magnetic field after ZFC. The apparition of the low-temperature skyrmion phase is around 65 mT from the lamella edge, shown by the blue arrow. They disappear above 130 mT. The images were acquired at 5 K.

protocols, we revealed that ordered metastable skyrmions are more robust against magnetic fields compared to the disordered low-temperature skyrmions, thus, highlighting the importance of the periodic potential order in the total magnetic free energy. Finally, we unveiled a topological magnetic fluctuation in the low-temperature skyrmion phase that occurs on the second timescale. Although the exact nature of the fluctuation remains to be clarified, it is tempting to ascribe their origin to the quantum fluctuation present in the magnetic building block of Cu_2OSeO_3 [264]. Moreover, magnetic quantum fluctuation has been identified in a multiferroic material sharing the same spin-dependent $d-p$ hybridization model [350]. Few questions follow: Can we photo-induce this phase? Will the laser pulse affect and favor one magnetic ordering? In particular will the out-of-equilibrium response stabilize or on the contrary induce more fluctuation? Our work demonstrates that Cu_2OSeO_3 is an ideal playground to study the role of the long-range order in a topological magnetic phase transition and opens exciting perspectives for quasi-2D magnetic crystal melting in a strongly dynamical fluctuating environment.

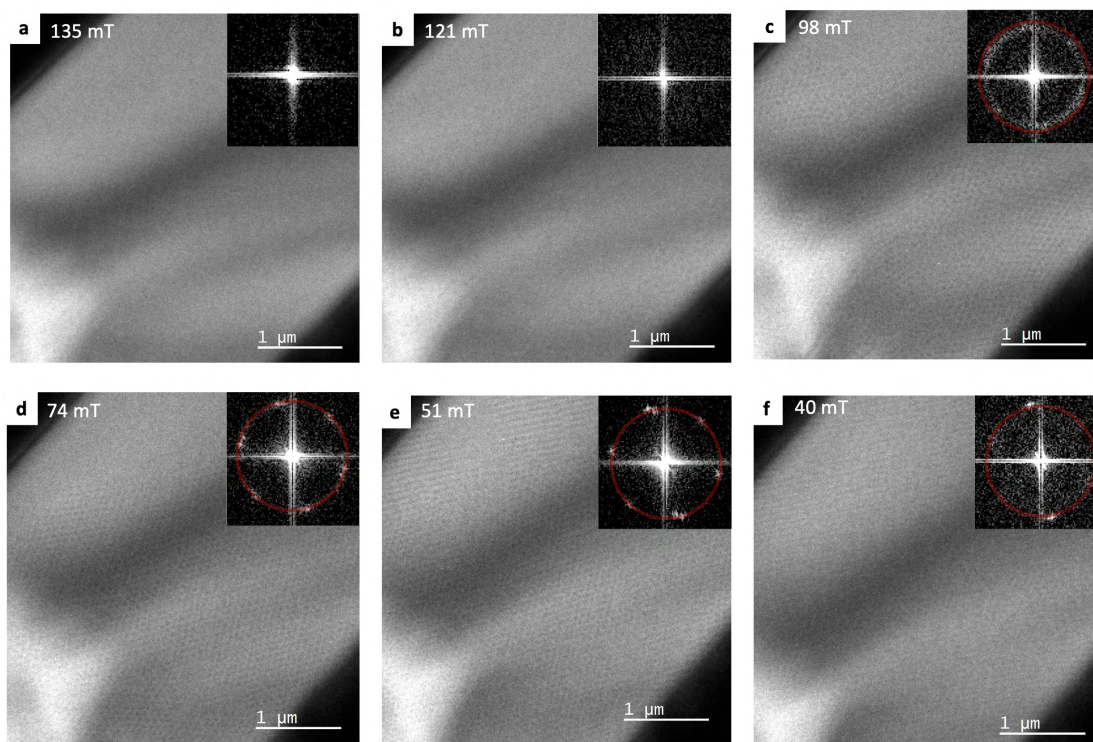


Figure 6.10 – LT-skyrmion phase from high-fields to low-fields. a-f: Series of LTEM images while ramping down the magnetic field after ZFC. The apparition of the low-temperature skyrmion phase is around 121 mT, and they vanish below 40 mT. A large change in the pitch length is observed, as well as skyrmion domain rearrangement. Insets show the associated FFT, red circle denotes the same reciprocal length for all insets. The images were acquired at 5 K.

6.1. Real space exploration under various magnetic field conditions

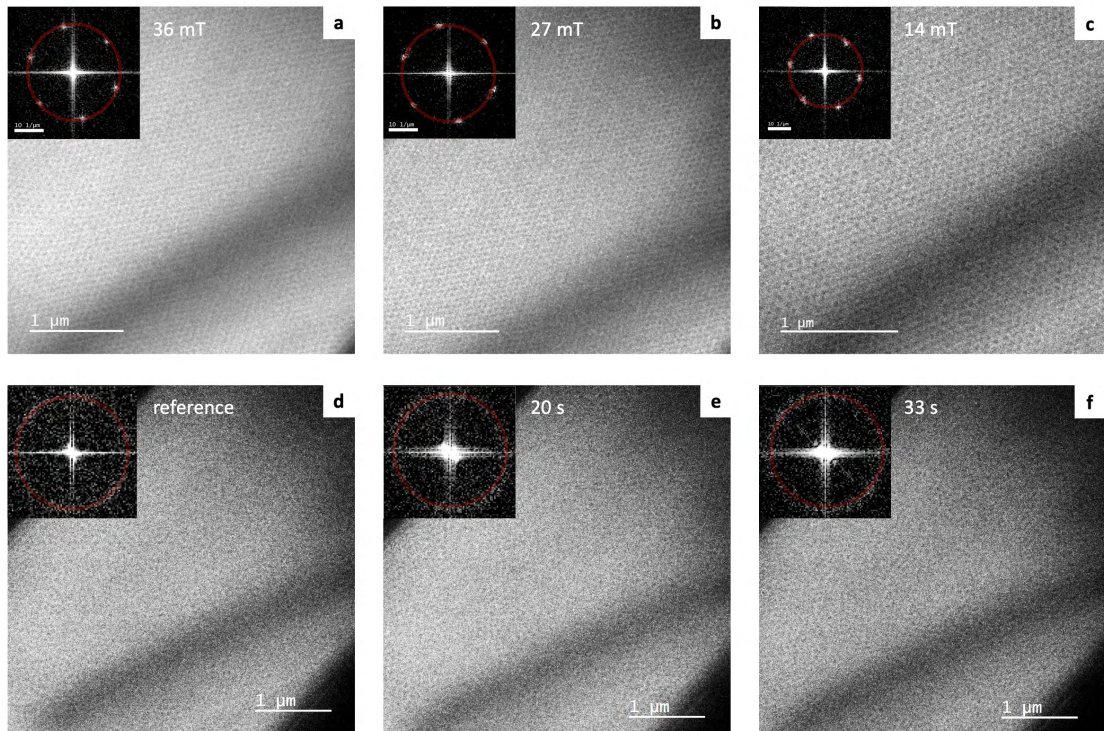


Figure 6.11 – **Stability of the MT-skyrmions and fluctuation of the LT-skyrmion phase.** The robustness of the metastable skyrmion phase is studied. **a**: The skyrmions are generated through FCC with an applied magnetic field of 36 mT. The field is progressively decreased to **(b)** 27 mT to reach our minimum value **(c)** 14 mT where the skyrmion phase still exists. Anisotropy in the skyrmion lattice is visible at 14 mT in the FFT (inset). **d-f**: Series of the images of the LT-skyrmion phase taken at 109 mT, demonstrating a strong fluctuation nature on the second time scale, only visible in real space. All images were acquired at 5 K. Insets show the FFT of each image. The red circle denotes the same reciprocal length for **d-f** and **a-b**.

6.1.3 Black and white skyrmions and shrinking of the skyrmion pocket with $\mathbf{H} \parallel [111]$

White and black skyrmions

In a LTEM image, a change in the magnetic contrast for Bloch-type skyrmion from *white* skyrmion to *black* skyrmion or vice-versa can correspond to several cases. One, the defocus length is changed from under-focus to over-focus, or conversely. Note that there is no direct relation, as a change in the magnetic contrast is also related to the helicity (sometimes named chirality [351]) of the Bloch-skyrmion, directly linked with its structural properties [337]. Moreover, the skyrmion polarity determined by the direction of the applied magnetic field plays an essential role in the magnetic contrast.

Curiously, in one Cu_2OSeO_3 [111] lamella, we observed at thermodynamic equilibrium white and dark skyrmions coexisting shown in Fig. 6.12a. They form two large independent single crystals rotated by precisely 30 degrees. Upon FCC, black skyrmions are usually observed. However, we noticed that the cooling rate seems to influence the final magnetic state. A slow field cooling rate of a few K/min from 60 K down to 5 K favors the apparition of white skyrmions. In contrast, a faster cooling rate fosters black skyrmions. Further work is needed to provide an accurate conclusion as stochastic effects may take place. Unlike in $[1\bar{1}0]$, where the stray-field energy is essential in the spiral state stabilization [268], in that case, such effect is unlikely as it was not observed in other samples with similar geometry. One possibility that could explain the observation is that the lamella is composed by two single crystals with different structural chirality. Consequently, the two skyrmion kinds would coexist and interact. In addition, no evident skyrmion lattice mismatch would appear for small-angle grain boundaries [352]. This hypothesis would also explain the origin of the two different senses of skyrmion rotation observed when photoexcited, discussed in Chapter 5. We tested this supposition by determining the sample chirality using convergent-beam electron diffraction (CBED). Unfortunately, the operation was not conclusive, as the sample was too thin to obtain reliable results.

It is possible to invert the polarity/chirality by sending a circularly polarized NIR ultrafast laser pulse. However, the effect is not fully reproducible. Switching the skyrmion polarity using circularly polarized light has been recently proposed [145, 147] invoking the Topological inverse Faraday effect. In this theory, the TIFE arises when a laser field couples to a non-trivial topological magnetic texture, and acts as an effective magnetic field. This effect does not require spin-orbit coupling and is predicted to have comparable strength. This potential additional contribution could also provide insights for a better quantitative model, in ref. [104], presented in Chapter 5.

6.1. Real space exploration under various magnetic field conditions

Our observation opens a few intriguing questions

1. Where do originate this reversal phenomenon?
2. Do the behavior of the two skyrmion kind differ, and how do they interact?
3. Did we witness the topological inverse Faraday effect?

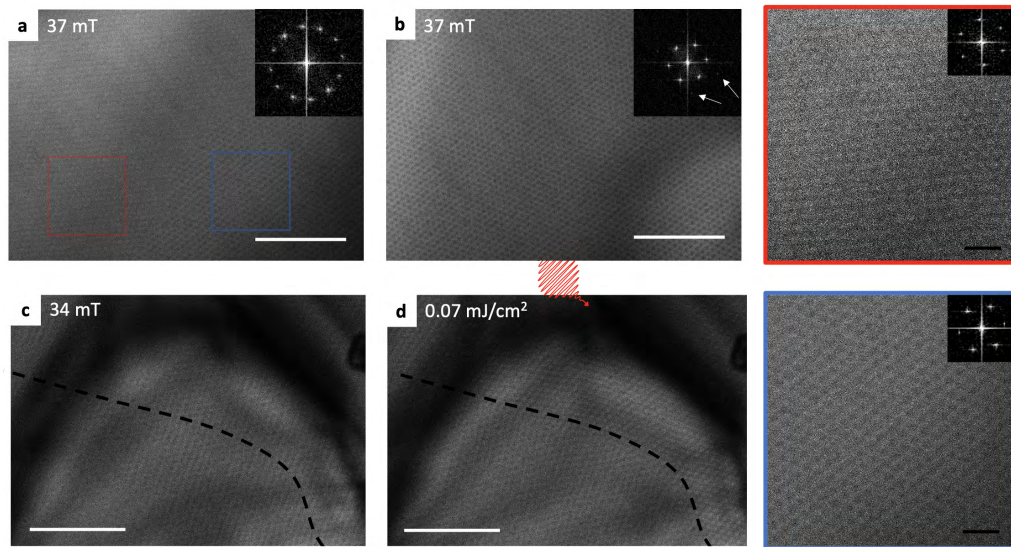


Figure 6.12 – **Skyrmion polarity/chirality reversal.** **a:** Coexistence of two independent white and black skyrmion crystals rotated by 30 degrees. **b:** Black single skyrmion crystal. White arrows in the inset shows second order spots of the reciprocal skyrmion lattice, demonstrating the excellent skyrmion crystallinity. **c** and **d** show the magnetic change after a single circularly polarized laser pulse. Image **c** is acquired before and **d** after the photoexcitation, showing a clear change in the magnetic contrast. The pulse duration of the 1200 nm (1.03 eV) is approximately 50 fs. Red (blue) panel is a zoom in of the image **a** highlighting the white (black) skyrmions. Top right black insets shows the FFT of the corresponding image. The white scale bar is 1 μm .

Few experimental suggestions can be proposed to elucidate those observation. We suggest investigating the cooling rate effect and the initial temperature. Indeed, the temperature starting point before cooling shows to influence the final magnetic phase. We also observed this effect in other lamella where the skyrmion and helical phases compete for the final state. The origin might come from the important fluctuations present in the vicinity of the topological phase transition [277]. Furthermore, verifying the chirality hypothesis is a promising lead and requires the possibility of investigating a sample possessing the opposite structural chirality. Finally, one way to demonstrate the TIFE is by comparing the Faraday rotation when the laser beam is sent perpendicularly or parallelly to the skyrmion tubes.

Reduction of the skyrmion pocket phase with in-plane magnetic field

During our investigation to determine the origin of the photocreation process reported in ref. [219] and Chapter 4 and testing the laser-field mechanism (discussed in Section 6.1.1), we compared the photocreation process when the lamella is off-axis. Indeed, tilting the sample will allow if they exist different electric field coupling. Although we did not find any noticeable change in the fluence threshold, we unveiled a substantial shrinking of the skyrmion phase, shown in Fig. 6.13. We assigned this effect to the presence of an in-plane magnetic field, that becomes non-negligible for higher tilt angles. Indeed for a tilt angle of 16° off the vertical axis where the magnetic field is applied, a 30 mT field along z will induce an in-plane component of 8.3 mT while the out-of-plane component is barely reduced to 28.8 mT. Such observation has two consequences; For large tilt angles, the in-plane magnetic field component can not be neglected. While a clear reduction of the upper critical field is induced, the question remains open for the lower critical bound and merits to be further studied. Recently, the collapse of skyrmions has been investigated with the presence of an in-plane magnetic field [285]. The experimental study supported by atomistic spin simulations shows a collapse rate up to four orders of magnitude faster with the presence of an in-plane magnetic field (see Fig. 6.13c-f). Although the system investigated has a completely different electronic nature compared to Cu_2OSeO_3 , it emphasizes the consequences of applying an in-plane magnetic field in a skyrmion system. Further examinations are needed to fully understand the reported effect. Nevertheless, we demonstrated a novel aspect to control the skyrmion phase in Cu_2OSeO_3 . Although we are not able to determine if the effect originates from interplay of underlying magnetic interaction in the presence of different field components, we suggest that its origin may lie in the topological nature of the skyrmion.

6.1. Real space exploration under various magnetic field conditions

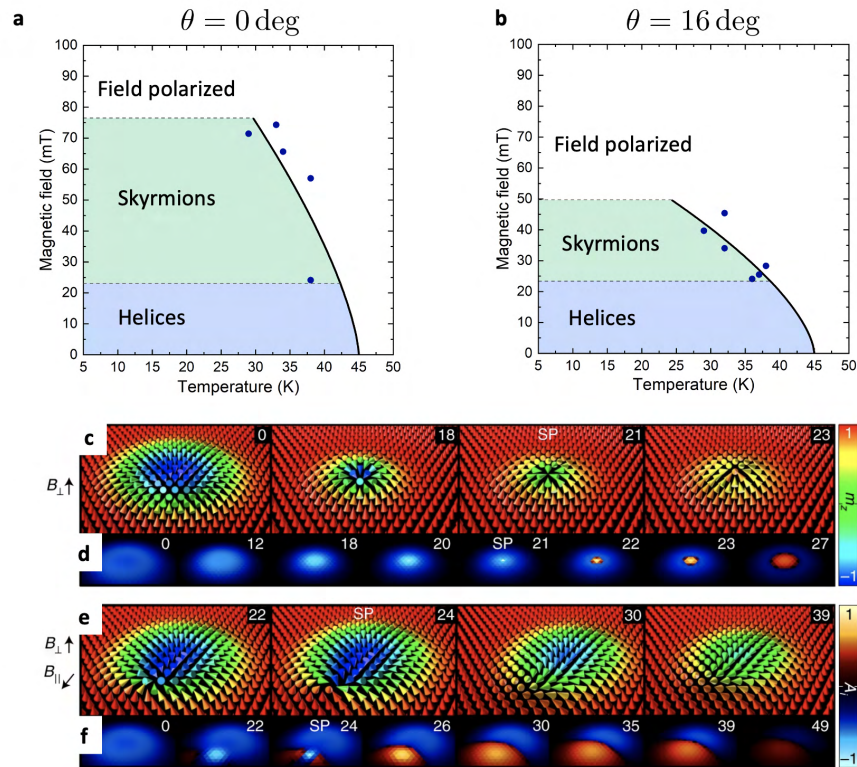


Figure 6.13 – **Shrinking of the skyrmion phase with the presence of an in-plane magnetic field.** Magnetic phase diagrams were obtained upon FCC protocol for the (a) untilted case and (b) for the same lamella with a tilted angle of 16° . c and e show the skyrmion collapse evolution without and with the presence of an in-plane magnetic field, respectively. d and f illustrate the evolution of the topological charge annihilation without and with the presence of an in-plane field, respectively. Image c-f are reproduced from [285].

6.2 Conclusion

In this chapter, we investigated magnetic phases at equilibrium under various magnetic field configuration. We identified curious observations such as the surface spiral state, skyrmion lattice anisotropies and a strongly fluctuating skyrmion phase, to name only a few. In all cases, magnetic anisotropy is proposed to play an essential role. Although existing at different spatial scale, we speculate that quantum fluctuation is reflected in the strong fluctuating topological order and can be investigated in a multiferroic compound in and out-of-equilibrium. Furthermore, we investigated out-of-equilibrium responses of the magnetic system upon ultrafast NIR radiation and show the manipulation of magnetic state by both creating and destroying the skyrmion phase. In summary, Cu_2OSeO_3 provide a fascinating platform to study real space topology and magnetic interactions and still hides many secrets that wait to be discovered.

Ultrafast generation of hidden phases **Part III**

7 Magnetite Fe_3O_4 as the prototypical MIT system

Metal-insulator transitions (MIT) in strongly correlated systems captive the interest of various research communities for their tremendous physical prominence for fundamental research and technological applications [353]. Due to an atypical MIT known as the Verwey transition, Magnetite (Fe_3O_4) is probably one of the most investigated strongly correlated systems. This peculiar transition originates from the complex interplay of degrees of freedom (charge ordering, orbital ordering, and trimeron formation). Ultrafast photon pulses have demonstrated the capability to manipulate such degrees of freedom and their respective coupling giving rise to the emergences of metastable (hidden) states inaccessible adiabatically through conventional stimuli such as temperature, pressure, or chemical doping [29]. Such new states are not only of interest for fundamental research in strongly correlated systems but also bear potential for ultrafast technological application. In that respect, Magnetite has been the subject of recent extensive research [38, 73, 354–358]. DeJong et al. has shown that near-infrared light (800 nm) drives the crystal structure transiently from monoclinic to cubic [38] in a thermal-like transition by melting the charge ordering below the Verwey temperature. Further investigations [354] have revealed that this structural transient transition is more subtle and consists of a mixture of coexisting monoclinic regions (insulators) and cubic regions (metallic states). These structural and electronic changes have been attributed to the microscopic arrangement of the trimerons following a disorder-order transition [355]. Trimeron quasiparticle consists of a specific electronic arrangement that is destroyed upon 800 nm optical excitation. However, previous ultrafast experiments have not considered other electronic excitations that can be triggered by tuning the photon energy pulse. Such fine details are instead significant for external manipulations of the intertwined degrees of freedom, leaving an essential question about the MIT mechanism evolving non-adiabatically following different energy photoexcitation.

This chapter addresses this question and investigates the out-of-equilibrium MIT processes with two distinct photon energy, 800 nm (1.55 eV) and 400 nm (3.10 eV). Our data reveal opposite behaviors when photoexciting the system with 800 nm or 400 nm, associated with triggering two distinct electronic excitations. The 800 nm light activates d-d electronic transitions that lead to the destruction of the long-range zigzag network of the trimerons and generate a metastable

phase separation between cubic-metallic and monoclinic-insulating in a multistep process. The 400 nm light promotes the long-range order of the trimeron network, enhancing its connectivity which leads to a metastable intermediate structural phase. This new hidden phase is characterized by a stronger monoclinic distortion unattainable in the equilibrium process. Furthermore, we extend the structural dynamics investigation to a temporal range of 1.3 ns previously limited to 10 ps after 800 nm photoexcitation, unveiling a multiple structural stage process different from the equilibrium first-order single stage transition [359]. Although the exact origin remains unknown, a complex and long relaxation mechanism is also observed, demonstrating the strong coupling between electron-phonon and phonon-phonon. In addition, our results are consistent with former studies and show a transient transition from the monoclinic structure to the phase separation phase leading to the cubic phase.

Our findings demonstrate the importance of the different electronic excitations on the trimeron arrangement in Magnetite and, thus, the generation of metastable intermediate states. These results show the ability to establish novel hidden phases in quantum materials via specific electronic excitations in a strongly correlated environment. Therefore, we are confident that our work will profoundly impact multiple fields, such as light-induced phenomena in strongly correlated systems, Magnetite, and metal-insulator transitions.

The content of this Chapter is adapted from the preprint "Ultrafast generation of hidden phases via energy-tuned electronic photoexcitation in magnetite" by B. Truc, P. Usai, F. Pennacchio, G. Berruto, R. Claude, I. Madan, V. Sala, T. LaGrange, G. M. Vanacore, S. Benhabib, and F. Carbone, arXiv:2210.00070 [360].

Contribution

Initiated in 2015 by former members, I contributed to this project by compiling, analyzing, and interpreting data acquired over the years. In addition, I took additional measurements at equilibrium data and upon 800 nm photoexcitation, in particular, the extended time delay data and the high-fluence regime with the help of P. Usai and R. Claude. Diffraction simulations were performed by P. Usai, and the remaining data presented (400 nm photoexcitation and second 800 nm data set) were data taken by F. Pennacchio, G. Berutto, I. Madan, V. Sala, G. M. Vanacore, S. Benhabib, and F. Carbone supervised this work.

7.1 History of the oldest magnetic material

Discovered 2500 years ago by Thales of Miletus (625-547 BCE), Fe_3O_4 Magnetite is the first magnetic material known. Due to its 'magic' magnetic properties, this compound has fascinated Humans for centuries. It has led to numerous inventions, such as the magnetic compass (see Fig. 7.1b) and discoveries in magnetism. For instance, Magnetite was used to validate Néel's ferrimagnetism model [361]. Most of the present knowledge of magnetism roots in Magnetite studies.

7.1. History of the oldest magnetic material

Nowadays, Magnetite is present in various fields. In biomagnetism, it is found that some animals use the Earth's magnetic field to orient themselves and possess Magnetite in their organism [362]. Magnetite is biocompatible and offers opportunities for biomedical application [363]. The human brain also contains Magnetite and is still under investigation [364]. From catalysis reactions treating toxic environments to paleomagnetism [365] aiming to understand the Earth's magnetic field history, Magnetite has gathered a wide interest over the years. In total, more than 11.000 scientific papers have been published¹. In all previous fields, Magnetite is studied at room or higher temperatures. For physicists, it is around 120 K that Magnetite takes a special place in transition metal oxide compounds as it exhibits an atypical and complex phase transition, named the Verwey transition, and has remained debated for more than a century since its discovery.

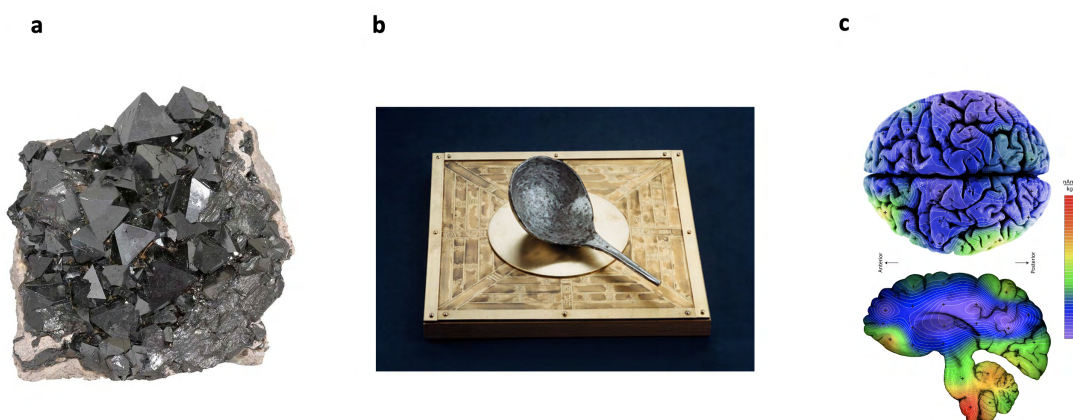


Figure 7.1 – Fe_3O_4 Magnetite is everywhere in magnetism. **a:** Ore of natural Magnetite found in Bolivia. Image taken from Rob Lavinsky (www.mindat.org). **b:** Magnetic compass dated 220 BCE from the Chinese empire. Image taken from Susan Silverman AC (www.smith.edu). **c:** Illustration of the Magnetite distribution in Human brain [364].

7.1.1 The Verwey transition and trimerons

In modern physics, Magnetite is probably one of the most famous strongly correlated electronic systems [359]. It offers a unique playground where electronic, orbital, and structural degrees of freedom compete, giving rise to peculiar and complex phase transitions (see Fig. 7.2). The precise origin of those phase transitions have remained elusive for more than a century. In 1913, the first anomalies in the magnetic responses were measured around 120 K by Renger during his thesis at ETHZ (Switzerland) under the supervision of Pierre Weiss and Albert Einstein. A few years later, other anomalies were reported in the specific heat, thermal expansion, and electric resistivity. In the latter, Verwey observed two orders of magnitude jump in the resistivity. In particular, he found that the temperature transition and amplitude strongly

¹statistics from Web of Science Core Collection.

Chapter 7. Magnetite Fe_3O_4 as the prototypical MIT system

depend on the stoichiometry of the sintered crystals [366, 367]. Bragg *et al.* determined that Magnetite possesses a spinel structure with the form AB_2O_4 , where A and B are usually two non-equivalent metal cations embedded in a cubic face-centered structure of O^{2-} anions. This assignment puzzled Verwey, who realized that the conductivity of Magnetite is surprisingly high ($\sim 10^4 \Omega^{-1}\text{m}^{-1}$) compared to other known spinel structures such as Co_3O_4 or Mn_3O_4 ($\sim 10^{-5} \Omega^{-1}\text{m}^{-1}$).

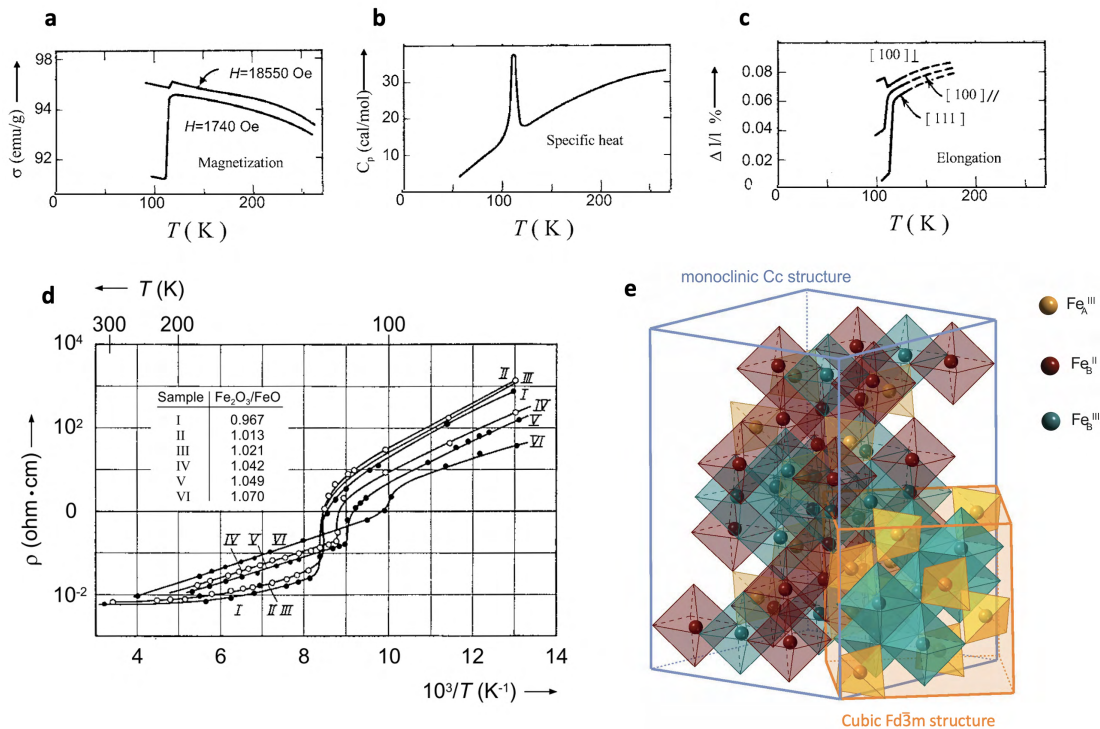


Figure 7.2 – **Manifestation of the Verwey transition** (a) in the spontaneous magnetization [368], (b) heat capacity measurements [369], (c) and thermal lattice expansion along specific directions [370]. **d**: Verwey’s original specific resistivity depending on the $\text{Fe}_2\text{O}_3:\text{FeO}$ ratios during the sample preparation [367]. **e**: Representation of HT cubic phase and the $\sqrt{2}a \times \sqrt{2}a \times 2a$ acentric monoclinic supercell with a $-\pi/4$ rotation around the c axis of the cubic unit cell.

In 1947, Verwey enunciated the first consistent model explaining the conductivity behavior and proposed that Magnetite has actually an inverse spinel structure formally written $\text{Fe}^{3+}[\text{Fe}^{2+}\text{Fe}^{3+}]\text{O}_4$ where the first Fe^{3+} occupy the tetrahedral sites (A-type), whereas $[\text{Fe}^{2+}\text{Fe}^{3+}]$ (B-type), construct the octahedra structure. Supported by x-ray and conductivity investigations, the resistivity jump would naturally originate from a spontaneous charge localization in that scenario. This model was further supported by saturation magnetization experiments which measured 4.07 Bohr magnetons (μ_B) per formula unit, close to the expected $4 \mu_B$ value predicted within Néel’s ferrimagnetism framework developed at the same period. Although withstanding for years, the Verwey model fails to explain the structural symmetry reduction in

the low-temperature phase reported lately. Refined three-dimensional neutron diffraction shows that the system transforms from the cubic $Fd\bar{3}m$ space group in the high-temperature (HT) phase to the monoclinic Cc space group in the low-temperature (LT) phase, with a small monoclinic tilt angle of 90.20° [371]. For decades, the precise mechanism of the Verwey has been debated. Indeed, sample preparation and quality have been neglected and turned out to be essential. In addition, the formation of domains appearing in the low-temperature phase with sub-micrometer size [372] and the complexity of the acentric monoclinic structure hampered crystallographic studies that require the development of microcrystal synchrotron radiation technique. Although progress in theoretical calculation has been made, dealing with a high number of atoms in the low-symmetry unit cell and electronic correlations remains a significant challenge, even today. Since then, intense effort has been undertaken to solve this atypical metal-insulator transition.

In 2012, almost a century after the first measurement done by Renger, high-accuracy x-ray experiment provided direct evidence of $\text{Fe}^{2+}/\text{Fe}^{3+}$ charge ordering predicted by Verwey and orbital ordering. Furthermore, Senn *et al.* unveiled a novel structural distortion. They found a bond shortening of fourteen out of the sixteen inequivalent Fe_B in the inverse spinel structure. This was attributed to a new type of bond-dimerized state [373] boosted by Jahn-Teller effect and charge ordering, named trimeron. The trimeron quasiparticle consists of linear arrangement of three Fe_B cations with a central Fe^{2+} and two Fe^{3+} . The minority spin electron from the central Fe^{2+} site is delocalized into the nearest neighbors Fe^{3+} and forms the bound state. The discovery of the trimerons has provided new insights and has revitalized one of the oldest problems in solid-state physics. Nowadays, thanks to temperature dependence inelastic neutron scattering experiments carried out in our laboratory [355, 374, 375] the equilibrium (quasi-adiabatic) Verwey transition (VT) is seen as a disorder-order transition where critical fluctuation of the trimerons comes into play, even above the Verwey transition (see Fig. 7.3) [73, 355, 376, 377]. In addition, the emergent trimeron structure is expected to play an essential role as structural anomalies have been detected along the [110] crystallographic orientation attributed to the specific trimeron arrangement [378] and site-selective doping effect has been demonstrated [379, 380]. Within the rise of ultrafast science, the out-of-equilibrium version of the Verwey transition has been investigated, establishing the speed limit of the MIT and revealing a hidden phase separation [38, 354, 357, 358]. The strongly-correlated system Magnetite offers an ideal playground for the search for exotic and novel ultrafast phenomena. Recently, the generation of forbidden phonons and coherent soft electronic modes have been demonstrated [381, 382]. Moreover, a dual-stage process has been revealed in the structural dynamics illustrating the strong trimeron-phonon interplay [356].

In that spirit, this work aims to harness the strongly-correlated nature of Magnetite to generate (hidden) phases inaccessible thermodynamically, along with collecting new insights that will provide a deeper understanding of the Verwey transition. We will investigate the structural response in equilibrium and out-of-equilibrium along the [110] direction by triggering different electronic excitations using energy-tuned ultrafast photons.

Chapter 7. Magnetite Fe_3O_4 as the prototypical MIT system

More details about the fascinating history of Magnetite and the Verwey transition can be found in [359, 375, 383, 384].

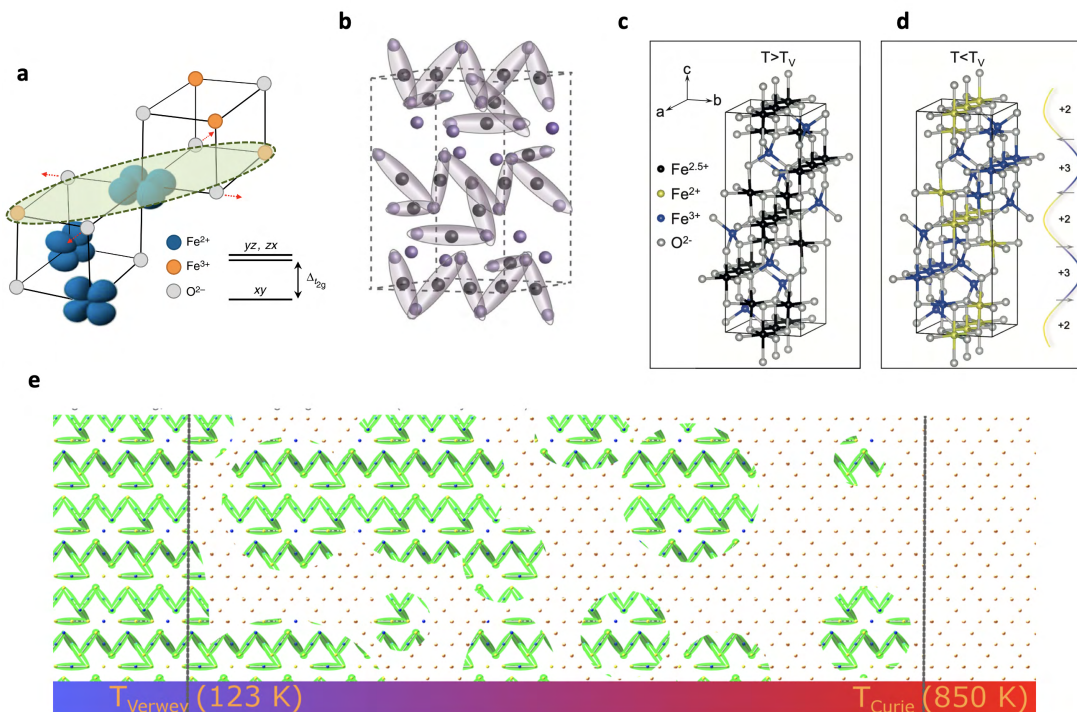


Figure 7.3 – **Trimeron structure and its emergent network.** **a:** In the trimeron scenario, the formation of the quasiparticle emerges from a collective effect induced by charge localization of minority spin t_{2g} and the Jahn-Teller effect [385]. **b:** Sketch of the trimeron arrangement taken from [382]. Fe^{2+} atoms are represented in grey, and Fe^{3+} ions are in light purple. Note that some Fe^{3+} ions are involved in the construction of up to three trimers while others do not participate. **c** and **d** show respectively the charge distribution above and below the critical temperature enunciated by Verwey, images from [375]. **e:** Sketch of the different electronic and structural fluctuation regimes [376]. The Verwey transition can be seen as trimeron Wigner liquid that emerges below the Curie Temperature enabling magnetic ordering that crystallizes in an order-disorder fashion below T_V .

7.2 Tracking the Verwey transition with electron diffraction

Due to the nature of the electron, the scattering cross-section is about six to seven orders larger than its x-ray analog. Therefore, Ultrafast Electron Diffraction (UED) technique provides a tabletop approach to investigate structural dynamics with pm and sub-ps spatio-temporal resolution [111?]. The reflection geometry named RHEED is the method of choice as it overcomes the need for a thin lamella. In this work the grazing angle varies from 0.5° to 5° . Further details on the experimental setup can be found in Chapter 2. As Magnetite possesses a

7.2. Tracking the Verwey transition with electron diffraction

complex electronic and structural interplay, URHEED is an ideal tool to investigate the Verwey transition at equilibrium and study the out-of-equilibrium response in this strongly-correlated system.

The sample investigated is a synthetic high-quality single crystal of Fe_3O_4 showing a first-order Verwey transition around $T_V \approx 117\text{ K}$ characterized by transport measurement (see Fig. 7.4a). The surface is polished to get optical flatness. The out-of-plane axis corresponds to the $[110]$ direction as confirmed by x-ray diffraction presented in Fig. 7.4b, giving a lattice parameter $a = 8.385\text{ \AA}$, at ambient conditions.

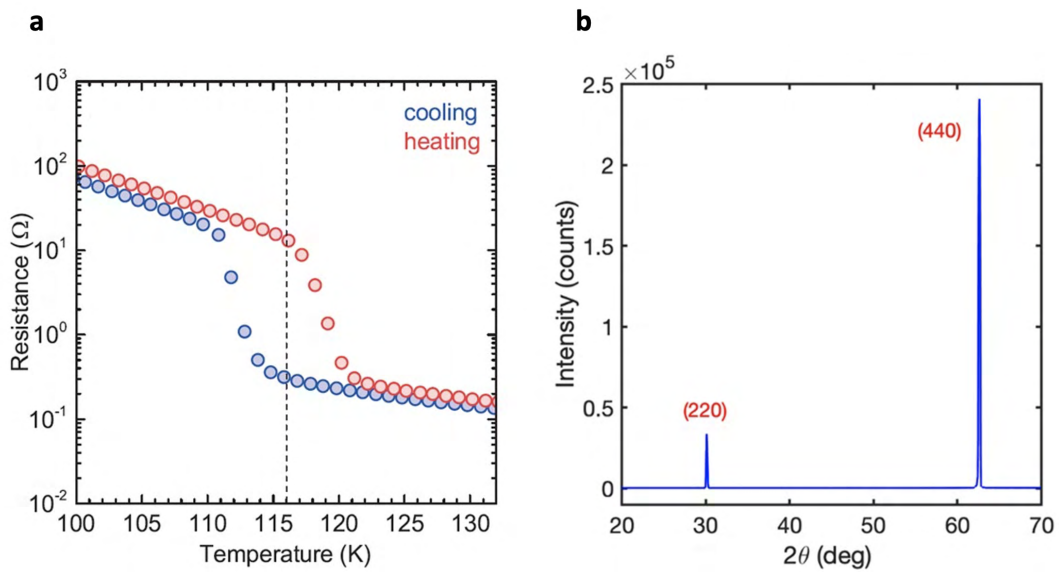


Figure 7.4 – Fe_3O_4 sample characterization. **a**: The first-order metal-to-insulator Verwey transition shows a transition temperature $T_V \approx 117\text{ K}$ confirming the high-quality of the crystal. An hysteresis behaviour originates from irreversible twinning effects. **b**: The $[110]$ out-of-plane direction was characterized by x-ray diffraction using k_{α_1} and k_{α_2} copper radiations at ambient conditions giving a lattice spacing $a = 8.385\text{ \AA}$.

Fig. 7.5a presents the available Bragg reflection within our experimental limitation at room temperature. At low-temperature (below T_V), the $(660)_c$ Bragg peak remains the only reflection intense enough, with a well-defined shape visible (see Fig. 7.6). Hence, we monitored the evolution of the $(660)_c$ Bragg peak upon cooling with a temperature range from 300 K to 38 K, crossing the Verwey transition presented in Fig. 7.5b. In the following the c and m indices denote cubic or monoclinic coordinates axes, respectively.

By fitting the $(660)_c$ Bragg peak with a Voigt profile, we extracted its different physical parameters, such as the intensity (integrated area), full-width-at-half-maximum (FWHM), and its center position. At $T_V = 117\text{ K}$, the intensity decreases abruptly (see Fig. 7.7b). This originates from multiple scattering effects caused by the multiple domains present in the

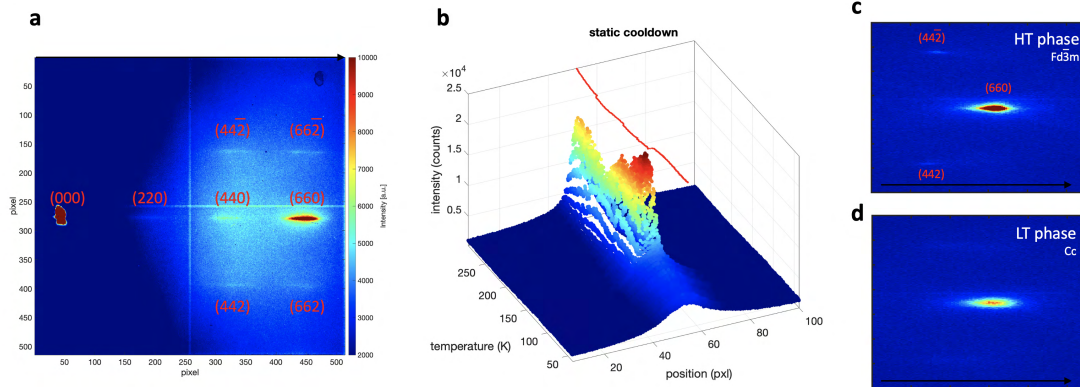


Figure 7.5 – **Magnetite and the Verwey transition probed by RHEED.** **a:** Stack of all images acquired during the rocking curve in the cubic high-temperature phase at room temperature, enabling the peak assignment. The zone axis is along $[1\bar{1}0]$. **b:** Evolution of the $(660)_c$ reflection upon cooling. At T_V , the peak broadens and shows a drop in intensity. The red line indicates the peak center position showing a jump at T_V , around 117 K. Evolution of the $(660)_c$ Bragg reflection (c) above T_V and (d) below T_V .

low-temperature phase (see section 7.6.1). This reflects in the broadening of the Bragg peak as the coherence length is reduced and strain appears, translated in the increase of the FWHM shown in Fig. 7.7c. In addition, a shift in the peak position is observed, from which we retrieve the atomic interplanar lattice displacement (expansion/compression) presented in Fig. 7.7a. Taking 150 K as the reference temperature, during the transition, a substantial lattice expansion of 1% (~ 1 pm) occurs along the $[110]$ direction corresponding to the shear strain ϵ_{xy} , specific of the cubic to monoclinic structural transition.

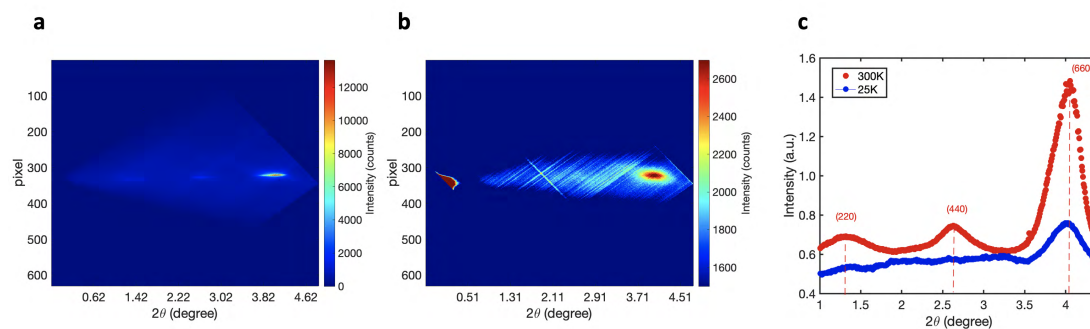


Figure 7.6 – **Rocking curve of Fe_3O_4 in RHEED** (a) in the high-temperature cubic phase and (b) in the low-temperature monoclinic phase. **c:** Peaks profile extracted from the vertical binning. Only the $(660)_c$ remains resolvable in the LT phase.

The abrupt changes in all the different physical parameters characteristic of a first-order phase transition demonstrate that RHEED along the $[110]$ crystallographic direction is sensitive to

7.2. Tracking the Verwey transition with electron diffraction

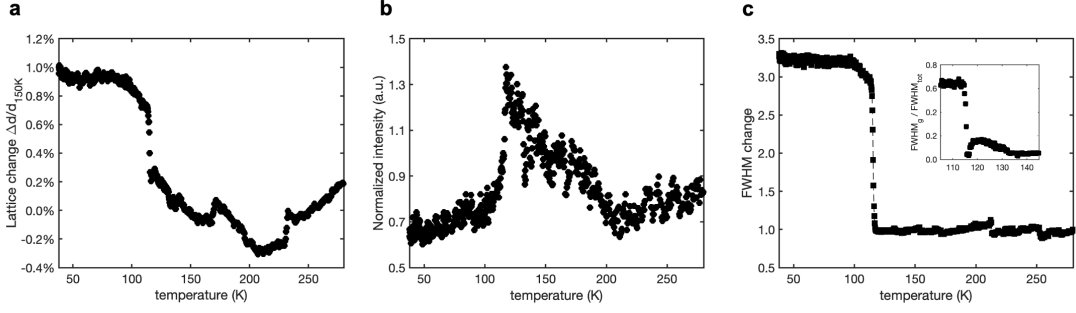


Figure 7.7 – **Signature of the Verwey transition in RHEED** at ~ 117 K, in the evolution of (a) the atomic lattice change along [110], (b) the integrated area and (c) the FWHM change across the Verwey transition. The reference temperature for the normalization is 150 K. The inset shows the ratio of the Gaussian FWHM contribution over the total FWHM showing the presence of fluctuation 20 K above the transition. All physical parameters show a first-order transition and anomalies around 210 K. The spikes around 170 K and 230 K in the lattice change are experimental artifacts.

the Verwey transition and can provide new insights both in and out-of-equilibrium. One consequence appears in the Ginzburg-Landau framework, a theory for phase transition from which the symmetry of the order parameter can be retrieved. Before diving into this exercise, it is useful to apply conventional elastic theory to the magnetite system and convince ourselves that the mode probed corresponds to a particular shear mode that is an appropriate measure of the Verwey transition.

In the following analysis, the system will be considered as a 3D bulk structure. Although URHEED is a moderate surface technique with a penetration depth of a few nm, the concomitant jump in the shear elastic constant c_{44} at the Verwey transition probed by ultrasound [386], which is a bulk technique demonstrates that our observation is representative of the bulk dynamics and justify this simplification.

7.2.1 Elastic theory and the shear mode

In the theory of elasticity for small deformation, the strain tensor ε_{ij} is defined by [387]:

$$\varepsilon_{ij} = \frac{1}{2} \left(\frac{\partial u_i}{\partial x_j} + \frac{\partial u_j}{\partial x_i} \right) \quad (7.1)$$

where, u is the atomic displacement and x the atomic position. The indices i and j denote the coordinate axes x , y and z . The presence of strain (ε) is a consequence of applied stress (σ). These two quantities are related by the elastic tensor c_{ijkl} through Hooke's law:

$$\sigma_{ij} = \sum_{kl} c_{ijkl} \varepsilon_{kl}. \quad (7.2)$$

Chapter 7. Magnetite Fe₃O₄ as the prototypical MIT system

The most general form of the elastic tensor has 81 components. By symmetry, this simplifies to 36 independent components and takes the form:

$$c_{ijkl} = \left(\begin{array}{c|c} C_1 & C_2 \\ \hline C_3 & C_4 \end{array} \right) = \left(\begin{array}{ccc|ccc} c_{11} & c_{12} & c_{13} & c_{14} & c_{15} & c_{16} \\ c_{21} & c_{22} & c_{23} & c_{24} & c_{25} & c_{26} \\ c_{31} & c_{32} & c_{33} & c_{34} & c_{35} & c_{36} \\ \hline c_{41} & c_{42} & c_{43} & c_{44} & c_{45} & c_{46} \\ c_{51} & c_{52} & c_{53} & c_{54} & c_{55} & c_{56} \\ c_{61} & c_{62} & c_{63} & c_{64} & c_{65} & c_{66} \end{array} \right), \quad (7.3)$$

where by convention the m, n indices of C_{mn} are defined as $1 = xx, 2 = yy, 3 = zz$ for the compression modes and $4 = yz, 5 = zx, 6 = xy$ for the shear modes. In particular, the elastic tensor can be divided into four sub-parts, each corresponding to specific modes. The C_1 part corresponds to pure compression modes, C_4 to pure shear modes, and the diagonal terms C_2 and C_3 to coupled mixed modes.

In the high-temperature phase of Magnetite, the system possesses a cubic symmetry. Hence, the elastic tensor c_{ijkl} simplifies and contains only three non-equivalent component c_{11} (longitudinal mode), c_{12} (transverse mode), and c_{44} (shear mode). This is expressed as:

$$\begin{pmatrix} \sigma_{xx} \\ \sigma_{yy} \\ \sigma_{zz} \\ \sigma_{yz} \\ \sigma_{xz} \\ \sigma_{xy} \end{pmatrix} = \begin{pmatrix} c_{11} & c_{12} & c_{12} & 0 & 0 & 0 \\ c_{12} & c_{12} & c_{12} & 0 & 0 & 0 \\ c_{12} & c_{12} & c_{11} & 0 & 0 & 0 \\ 0 & 0 & 0 & c_{44} & 0 & 0 \\ 0 & 0 & 0 & 0 & c_{44} & 0 \\ 0 & 0 & 0 & 0 & 0 & c_{44} \end{pmatrix} \times \begin{pmatrix} \varepsilon_{xx} \\ \varepsilon_{yy} \\ \varepsilon_{zz} \\ 2\varepsilon_{yz} \\ 2\varepsilon_{xz} \\ 2\varepsilon_{xy} \end{pmatrix}.$$

In this work, the interplanar atomic expansion/compression probed are along the [110] direction, corresponding to the shear mode ε_{xy} depicted in Fig. 7.8a. The relation of the associated stress σ_{xy} is given by

$$\sigma_{xy} = 2c_{44}\varepsilon_{xy}. \quad (7.4)$$

For the monoclinic structure in the low-temperature phase, the elastic tensor c_{ijkl} becomes:

$$\begin{pmatrix} \sigma_{xx} \\ \sigma_{yy} \\ \sigma_{zz} \\ \sigma_{yz} \\ \sigma_{xz} \\ \sigma_{xy} \end{pmatrix} = \begin{pmatrix} c_{11} & c_{12} & c_{13} & 0 & c_{15} & 0 \\ c_{12} & c_{22} & c_{23} & 0 & c_{25} & 0 \\ c_{13} & c_{23} & c_{33} & 0 & c_{35} & 0 \\ 0 & 0 & 0 & c_{44} & 0 & c_{46} \\ c_{15} & c_{25} & c_{35} & 0 & c_{55} & 0 \\ 0 & 0 & 0 & c_{46} & 0 & c_{66} \end{pmatrix} \times \begin{pmatrix} \varepsilon_{xx} \\ \varepsilon_{yy} \\ \varepsilon_{zz} \\ 2\varepsilon_{yz} \\ 2\varepsilon_{xz} \\ 2\varepsilon_{xy} \end{pmatrix}.$$

7.2. Tracking the Verwey transition with electron diffraction

In the monoclinic structure the shear strain ε_{xy} couples to two stresses σ_{yz} and σ_{xy} through the c_{46} and c_{66} elastic constants, respectively. The exact values of the elastic tensor in the low-temperature phase remain unknown. Determining quantitatively such elastic constants typically required bulk methods such as ultrasound measurement [386]. However, in the low-temperature, the appearance of structural domains (twinning) dramatically reduces the acoustic wave propagation, which prevents a proper measure.

Thus, to compute the strain energy associated with the structural deformation, we consider the cubic symmetry, which is expected to give acceptable results, as the monoclinic tilt angle is small 90.236° [373] $\approx 90^\circ$, the lattice parameters a and b remain constant and the reported elastic shear component c_{44} is sensitive to the Verwey transition. For linear and small deformations, the elastic potential energy per unit volume W_{el} is:

$$W_{el} = \frac{1}{2} \sum_{i=1}^3 \sum_{j=1}^3 \sigma_{ij} \varepsilon_{ij}. \quad (7.5)$$

Therefore, we can compute the strain energy density associated to the shear strain w_{xy} induced during the transition. Combining eq. (7.5) and eq.(7.4), we find

$$w_{xy} = c_{44} \varepsilon_{xy}^2. \quad (7.6)$$

Using the reported value in c_{44} [386] and our experimental data, we computed the elastic energy density depending on the temperature presented in Fig. 7.8b. As expected, a strong first-order transition appears, characteristic of the structural transformation in the Verwey transition.

In this part, we have demonstrated that the shear strain detected with our experimental setup (RHEED) is highly sensitive to the Verwey transition. Ginzburg-Landau (GL) theory invokes the existence of an order parameter (OP) to describe first-order phase transition [388]. Hence, in this framework, we can ascribe the measured shear strain being strongly coupled with the order parameter. Consequently, the symmetry of the OP Δ can be retrieved using fundamental group theory analysis. The detailed analysis is presented in the following section.

7.2.2 Ginzburg-Landau & group theory analysis

Researchers have tried to uncover the genuine order parameter for many years using different theoretical approaches. Although symmetry arguments can not directly retrieve the order parameter, they restrict the possible candidates list. Eventually, the constraint is strong enough to deduce the veritable order parameter in some cases.

Here, we apply group theory and Ginzburg-Landau's theory on the newly discovered anomalies in the shear strain to find the symmetry of the order parameter (OP).

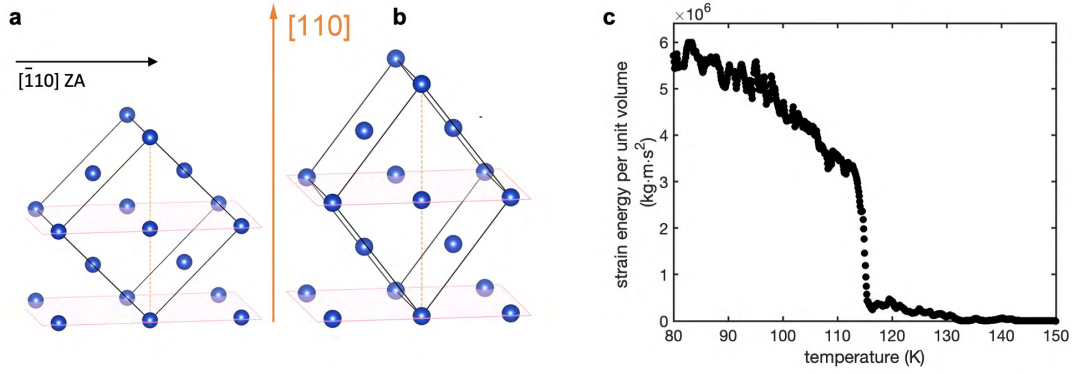


Figure 7.8 – **Shear deformation and its associated elastic energy.** Sketch of the structural distortion probed along [110] from (a) the initial cubic phase which transform (b) to the monoclinic phase below T_V . c: Interpolated elastic energy associated to the shear deformation. Elastic constant values are taken from [386] and have been shifted by 10 K to match the transition temperature. The reference temperature is 150 K.

O_h group	E	$8C_3$	$6C_2$	$6C_4$	$3C_2$	i	$6S_4$	$8S_6$	$3\sigma_h$	$6\sigma_d$	linear functions, rotations	quadratic functions
A_{1g}	+1	+1	+1	+1	+1	+1	+1	+1	+1	+1	-	$x^2 + y^2 + z^2$
A_{2g}	+1	+1	-1	-1	+1	+1	-1	+1	+1	-1	-	-
E_g	+2	-1	0	0	+2	+2	0	-1	+2	0	-	$(2z^2 - x^2 - y^2, x^2 - y^2)$
T_{1g}	+3	0	-1	+1	-1	+3	-1	0	-1	-1	(R_x, R_y, R_z)	-
T_{2g}	+3	0	+1	-1	-1	+3	-1	0	-1	+1	-	(xz, yz, xy)
A_{1u}	+1	+1	+1	+1	+1	-1	-1	-1	-1	-1	-	-
A_{2u}	+1	+1	-1	-1	+1	-1	+1	-1	-1	+1	-	-
E_u	+2	-1	0	0	+2	-2	0	+1	-2	0	-	-
T_{1u}	+3	0	-1	+1	-1	-3	-1	0	+1	+1	-	-
T_{2u}	+3	0	+1	-1	-1	-3	+1	0	+1	-1	-	-

Table 7.1 – Characters table for O_h point group.

The total Free energy F is defined as follows:

$$F = F_0 + \alpha\Delta^2 + \frac{\beta}{2}\Delta^4 + \underbrace{g\varepsilon\Delta}_{\text{coupling term}} + \underbrace{\dots}_{\text{higher orders}} \quad (7.7)$$

where α and β are coefficient and Δ is the order parameter. For small deformations, the dominating free energy coupling term $F_{coupling}$ is the linear order and couples the strain ε and the OP as follows:

$$F_{coupling} = g\varepsilon\Delta, \quad (7.8)$$

where g is the coupling constant. The free energy coupling term is part of the total free energy, which is a real number. Therefore, the coupling term must remain invariant under all symmetry operations.

7.2. Tracking the Verwey transition with electron diffraction

	A_{1g}	A_{2g}	E_g	T_{1g}	T_{2g}	A_{1u}	A_{2u}	E_u	T_{1u}	T_{2u}
A_{1g}	A _{1g}	A _{2g}	E _g	T _{1g}	T _{2g}	A _{1u}	A _{2u}	E _u	T _{1u}	T _{2u}
A_{2g}	A _{2g}	A _{1g}	E _g	T _{1g}	T _{2g}	A _{2u}	A _{1u}	E _u	T _{1u}	T _{2u}
E_g	E _g	E _g	A _{1g} +A _{2g} +E _g	T _{1g} +T _{2g}	T _{1g} +T _{2g}	E _u	E _u	A _{1u} +A _{2u} +E _u	T _{1u} +T _{2u}	T _{1u} +T _{2u}
T_{1g}	T _{1g}	T _{2g}	T _{1g} +T _{2g}	A _{1g} +E _g +T _{1g} +T _{2g}	A _{2g} +E _g +T _{1g} +T _{2g}	T _{1u}	T _{2u}	T _{1u} +T _{2u}	A _{1u} +E _u +T _{1u} +T _{2u}	A _{2u} +E _u +T _{1u} +T _{2u}
T_{2g}	T _{2g}	T _{1g}	T _{1g} +T _{2g}	A _{2g} +E _g +T _{1g} +T _{2g}	A _{1g} +E _g +T _{1g} +T _{2g}	T _{2u}	T _{1u}	T _{1u} +T _{2u}	A _{2u} +E _u +T _{1u} +T _{2u}	A _{1u} +E _u +T _{1u} +T _{2u}
A_{1u}	A _{1u}	A _{2u}	E _u	T _{1u}	T _{2u}	A _{1g}	A _{2g}	E _g	T _{1g}	T _{2g}
A_{2u}	A _{2u}	A _{1u}	E _u	T _{2u}	T _{1u}	A _{2g}	A _{1g}	E _g	T _{2g}	T _{1g}
E_u	E _u	E _u	A _{1u} +A _{2u} +E _u	T _{1u} +T _{2u}	T _{1u} +T _{2u}	E _g	E _g	A _{1g} +A _{2g} +E _g	T _{1g} +T _{2g}	T _{1g} +T _{2g}
T_{1u}	T _{1u}	T _{2u}	T _{1u} +T _{2u}	A _{1u} +E _u +T _{1u} +T _{2u}	A _{2u} +E _u +T _{1u} +T _{2u}	T _{1g}	T _{2g}	T _{1g} +T _{2g}	A _{1g} +E _g +T _{1g} +T _{2g}	A _{2g} +E _g +T _{1g} +T _{2g}
T_{2u}	T _{2u}	T _{1u}	T _{1u} +T _{2u}	A _{2u} +E _u +T _{1u} +T _{2u}	A _{1u} +E _u +T _{1u} +T _{2u}	T _{2g}	T _{1g}	T _{1g} +T _{2g}	A _{2g} +E _g +T _{1g} +T _{2g}	A _{1g} +E _g +T _{1g} +T _{2g}

Table 7.2 – Product table of the O_h point group.

In the high-temperature phase, the point group of Magnetite is O_h . The corresponding character table is shown in Table 7.1. The A_{1g} representation is the only invariant representation. Consequently, the symmetry product between the symmetry representation of ε_{xy} and Δ must belong to the A_{1g} representation. Since the shear strain ε_{xy} has a T_{2g} representation, the only symmetry product that contains A_{1g} representation is as well T_{2g} (see Table 7.2). That means the order parameter Δ must belong to the T_{2g} representation.

Hence, the order parameter is an object containing three components as it has the T_{2g} representation and takes the form:

$$\Delta = (\Delta_{xy}, \Delta_{yz}, \Delta_{xz}). \quad (7.9)$$

Thus, we can rewrite the coupling free energy (eq. (7.8)) term as:

$$F_{coupling} = \underbrace{g_1 \varepsilon_{xy} \Delta_{xy}}_{\alpha_1} + \underbrace{g_2 \varepsilon_{yz} \Delta_{yz}}_{\alpha_2} + \underbrace{g_3 \varepsilon_{xz} \Delta_{xz}}_{\alpha_3} \quad (7.10)$$

Three possible scenarios arise, each giving a different structural distortion leading to a different symmetry change from the initial cubic symmetry illustrated in Fig. 7.9. Note that α_1 , α_2 , and α_3 are equivalent in the cubic case.

1. $\alpha_1, \alpha_2, \alpha_3 \neq 0$

In this case, the three shear strains are finite, and applying the structural deformation leads to a deviation of all the angles from 90° , keeping the lattice parameters, a , b , and c constant, giving a trigonal distortion (case **a** in Fig. 7.9).

2. $\alpha_1, \alpha_2 \neq 0$ and $\alpha_3 = 0$

By simultaneously applying two shear strains ε_{xy} and ε_{yz} induces three tilt angles different from 90° accompanied by non-equivalent lattice parameters $a \neq b \neq c$ generating a triclinic distortion (case **b** in Fig. 7.9).

3. $\alpha_1 \neq 0$, $\alpha_2, \alpha_3 = 0$

The presence of only one shear strain ε_{xy} modifies the lattice parameter c and keeps a

and b unchanged, and one angle is different from 90° , leading to a monoclinic distortion (case **c** in Fig.7.9).

The latter case agrees with the low-temperature structure of Magnetite Cc [371, 373, 389]. Hence, we found that the OP responsible for the structural change has a T_{2g} representation with one nonzero component, i.e., $\Delta = (\Delta_{xy}, 0, 0)$. In that respect, the trimeron network topology along the $[110]$ crystallographic axis fulfills the symmetry criterion and is a valid OP candidate.

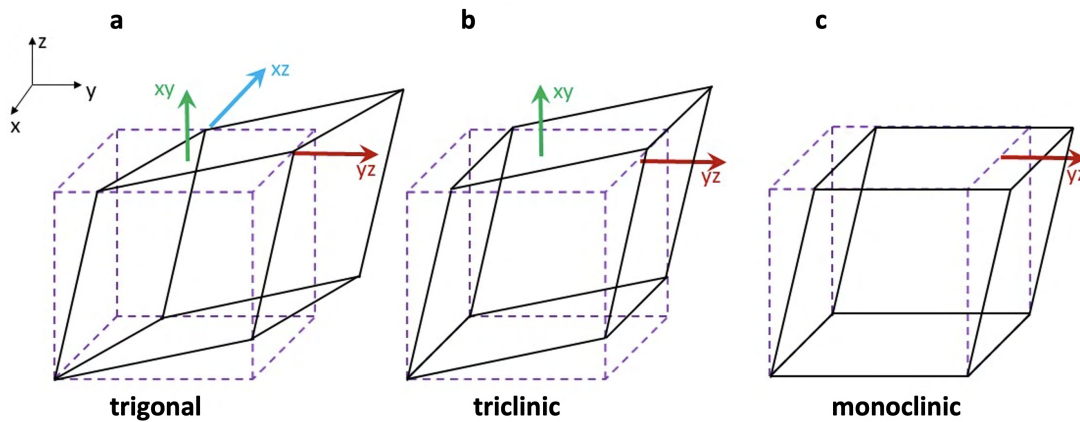


Figure 7.9 – **Possible structural transformation from the initial cubic phase.** Representation of the (a) trigonal, (b) triclinic and (c) monoclinic structural transformations from the initial cubic structure (dashed purple lines) corresponding to the three possible cases allowed by the T_{2g} symmetry constrain. The arrows represent the strain directions.

7.2.3 Further analysis and open questions

The zone axis used in our experimental condition is $[\bar{1}10]_c$. Consequently the $(660)_c$ reflection in the HT phase is expected to become $(\bar{1}200)_m$ in the monoclinic structure and is consistent to the simulation shown in Fig. 7.17b. Indeed, the supercell Cc is acentric and rotated by $-\pi/4$ around the c -axis of the cubic unit cell. The computed intensity ratio between the $(\bar{1}200)_m / (660)_c$ is 0.68, close to the experimental value found to be 0.65 ± 0.2 corresponding to the intensity ratio of $(660)_{40\text{K}} / (660)_{150\text{K}}$. Nevertheless, it is not possible to claim a clear assignment of the $(660)_c$ reflection below T_V as more Bragg peaks are required. The c and m indices denote the cubic and monoclinic axes, respectively.

In the previous part, we focused on the Verwey transition around ~ 117 K. Extending our investigation to higher temperatures, we notice two intriguing features.

7.3. Hidden phases on demand using selective electronic excitations

1. In our analysis, we used a Voigt profile that best captures the evolution of the Bragg peak. This allows us to extract the FWHM Gaussian and Lorentz contributions which physically represent the inhomogeneous and homogeneous broadening effects, respectively. Above the transition, starting around 135 K, fluctuation appears and then collapses at the transition as presented in the inset of Fig. 7.7c. This temperature is close to the spin-reorientation transition, which suggests a direct coupling of the magnetic and structural fluctuations.
2. Around 210 K a transition occurs and is noticeable in all physical parameters. Specifically, in the structural response, the lattice experienced a conventional thermal contraction upon cooling. However, between 210 K and 117 K, we observed a substantial lattice expansion of almost 0.6%. As the [110] direction is sensitive to the trimeron arrangement, this suggests that trimeron start to condensate below this critical temperature, forming an intermediate state between the Wigner crystal and Wigner liquid. In a recent preprint the authors uncovered an electronic nematic phase coupled to the lattice order through thermal fluctuation above the Verwey temperature using electron diffraction [73]. The temperature onset value of the nematic phase matches our observed transition temperature, reinforcing the trimeron network topology along the [110] as the order parameter hypothesis.

7.3 Hidden phases on demand using selective electronic excitations

Magnetite is insulating at low-temperature with an electronic bandgap of approximately a few hundred of meV and becomes metallic above the critical Verwey temperature, although recent calculations have shown that the electronic gap does not entirely collapse [390]. Using light to trigger MIT is particularly interesting for ultrafast optoelectronics and understanding fundamental interactions in strongly-correlated systems. In particular, researchers have wondered how fast this transition can occur and how microscopically the transition takes place. Recently, de Jong *et al.* used a free electron laser at the National Accelerator Laboratory (Stanford) to perform ultrafast resonant x-ray diffraction [38]. They used 800 nm ultrashort laser pulse to excite the system across the transition and probed the structural and electronic responses. Their experiment revealed a two step process characterized by first the destruction of the trimers, followed by a change in the structure recovering to the high-temperature cubic phase through a phase separation with a characteristic time scale of 300 fs and 1.5 ps, respectively. This novel out-of-equilibrium phase consists of forming cubic islands embedded in the insulating monoclinic background. Lately, ultrafast optical measurement has revealed different fluence regimes upon 800 nm optical excitation [354]. This surprisingly coincides with the equilibrium thermodynamics version of the Verwey transition accounting for latent heat required to cross the transition. The authors conclude that the 800 nm photon pulses depose energy in the system, acting like a sudden heating. In addition, experimental evidence found direct relations between the magnetic responses and anisotropy behaviors and the 800 nm photo-induced state [357, 358].

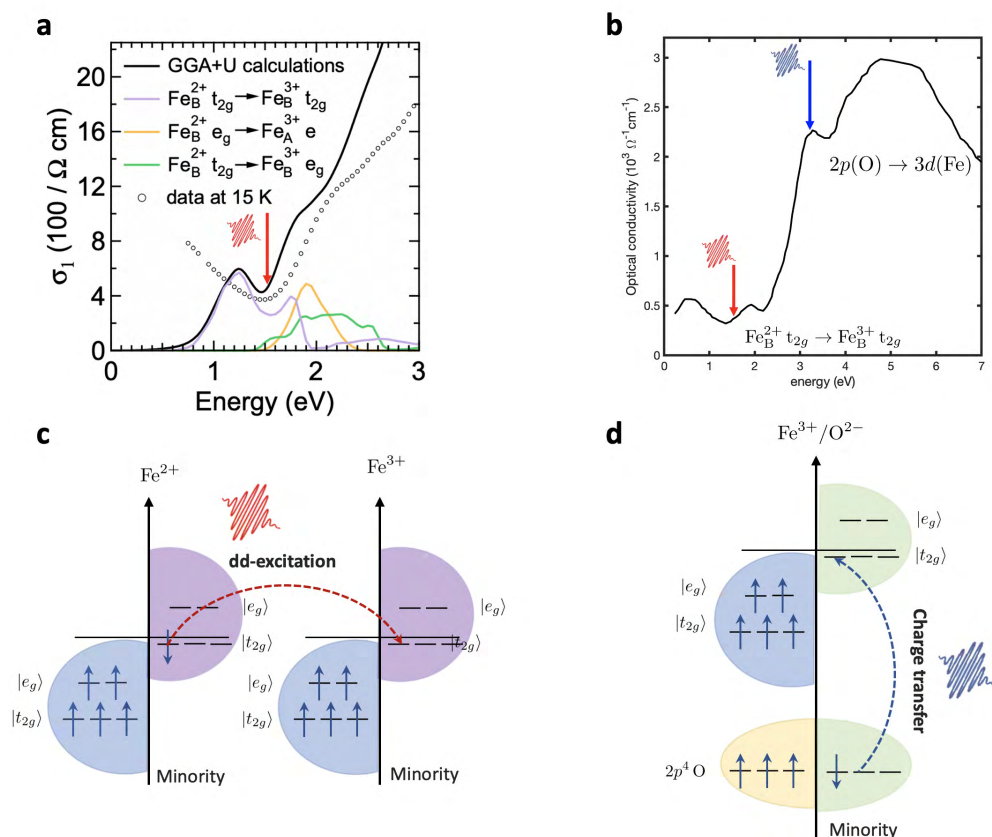


Figure 7.10 – **Optical electronic excitations in Fe_3O_4 .** **a:** The different d-d electronic transitions present around 1.55 eV (800 nm) obtained using GGA+U calculation [381]. The red arrow shows the photon-excitation used, which mainly triggers the $\text{Fe}_B^{2+} t_{2g} \rightarrow \text{Fe}_B^{3+} t_{2g}$. **b:** Optical response of magnetite from [391]. Charge transfer electronic excitations start above 3 eV. Below this energy, d-d inter-site electronic transitions take place. The two photon energies used in that work are represented with the red and blue arrows. Sketch of the triggered electronic excitation **(c)** upon 1.55 eV (800 nm) and **(d)** 3.10 eV (400 nm) photoexcitation.

All previous ultrafast studies used 800 nm - 1.55 eV as the photon energy. This triggers d-d electronic excitations, with $\text{Fe}_B^{2+} t_{2g} \rightarrow \text{Fe}_B^{3+} t_{2g}$ as the main optical transition contribution according to GGA+U calculations [381]. To date, other electronic excitations present in Magnetite have not been considered and can be triggered by tuning the photon energy pulse. Such fine details are instead significant for external manipulations of the intertwined degrees of freedom, leaving an essential question about the MIT mechanism evolving non-adiabatically following different energy photoexcitation.

In this part, we address this fundamental question by probing the structural dynamics along the [110] direction with time-resolved electron diffraction followed by ultrashort photon pulses with two distinct energies triggering specific electronic excitation (see Fig. 7.10). Practically, we investigated in the first place the lattice dynamics upon 800 nm (1.55 eV) photoexcitation

and compared our results to the recent literature. In addition, we extended the time range investigated up to 1.3 ns previously limited to the first 10 ps [38, 73, 354]. We unveiled a new multistage compression and a complex recovery process, which we attributed to the strong electron-phonon and phonon-phonon interactions. Furthermore, we explored the structural response after 400 nm (3.10 eV) photoexcitation inducing charge transfer, another type of electronic excitation. We observed an opposite behavior as the 800 nm case and showed the emergence of new hidden phases characterized by an additional monoclinic distortion inaccessible adiabatically. Therefore, we demonstrated for the first time the generation of hidden phases through manipulating their different degrees of freedom and their respective coupling using selective electronic photoexcitation.

7.4 Results

To get insight into the non-equilibrium response of Magnetite, we tracked the response of the $(660)_c$ Bragg reflection by using a Voigt fit following the laser illumination. We used the equilibrium (static) results discussed in the previous section as a benchmark and compared our observation with recent time-resolved ultrafast diffraction studies. If not mentioned, the experiments were performed at a nominal temperature of 80 K, below the T_V . Firstly, the dynamical response upon 800 nm photoexcitation is studied using two different fluence regimes, classify to the *intermediate* and *high* fluence regimes, accordingly to [354]. In the second part, higher photon energy (400 nm - 3.10 eV) corresponding to the frequency doubling of the laser fundamental wavelength is used to pump the system. As a technical note, the 400 nm data and the second *intermediate* fluence 800 nm data (3.9 mJ/cm^2) sets presented were taken with the old experimental setup (see Chapter 2). Whereas the first data set extending the time range investigated for 800 nm photoexcitation (2.7 mJ/cm^2), the *high* fluence regime data, the equilibrium data set discussed previously were recorded with the upgraded experimental setup. The results are consistent and demonstrate the robustness of this study taken over seven years.

7.4.1 800 nm / 1.55 eV photon energy

In the first place, the lattice undergoes a compression, following the 800 nm (1.55 eV) photoexcitation. Based on our static data, in the LT phase, a compression along the [110] direction denotes a recovery towards a cubic structure (see Fig. 7.11a). This is consistent with recent studies [38, 354], previously limited to ~ 10 ps. Investigating longer time delays reveals a multistep compression process. Qualitatively, within the first 20 ps (phase 1) a compression of about -0.03% is observed. Then a stabilization plateau appears in which the strain remains almost constant and survives for approximately 8 ps (phase 2). A maximum compression of -0.06% is reached in the third phase at 50 ps. This multistep process is a signature of different involved dynamics, such as strong electron-phonon and phonon-phonon interactions. Note that our temporal resolution of few ps in these experiments does not allow us to resolve the

electron-electron interaction expected to happen on a faster time scale < 300 fs [38]. After 50 ps a complex relaxation process towards the initial monoclinic phase initiates. The first recovery stage (phase 4) reaches a compressed state close to -0.03% , which interestingly corresponds to the plateau value (phase 2). Then, a second long process takes place toward the initial equilibrium state, which is still not fully recovered after 1.3 ns. The whole time trace is presented in Fig. 7.12. A second data set confirms the multiple compression mechanism set (see Fig. 7.11d). Comparing the two data sets quantitatively is a delicate task as they were not taken in the exact same experimental conditions. Nevertheless, some observations can be made. A different stage's duration and amplitude are observed, which suggests that a higher compression with a longer time scale is achieved when increasing the fluence. Curiously, the ratio in the compression values reached between the first and third stages is close to 1 for both data sets. Other similarities are found in the correlation analysis discussed below. In the *high* fluence regime, only one compression stage is observed and occurs on a longer time scale.

In Fig. 7.11b, a significant intensity reduction of about 20% is observed. Considering only the recovery towards the HT cubic phase, which has a higher symmetry and less twinning effect, an increase in the intensity is expected, which is not observed. This suggests other non-adiabatic effects might occur as the formation of the phase separation, which does not exist at equilibrium, consistent with the small fraction ($\sim 6\%$) of the compression achieved as compared to the equilibrium transition. In addition, structural disorder induced by the increase of the lattice temperature contributes to the intensity reduction and is known as the Debye-Waller effect. More details can be found in [360]. As in the lattice response, the initial intensity value is not recovered after 1.3 ns (see Fig. 7.12b), demonstrating the complexity of the thermalization mechanism characterized by the metastability of the observed phase. Increasing the fluence to the *high* fluence regime shows the opposite behavior with a 10% increase in intensity. This is expected from a thermal-like transition proposed in [354]. However, using the calorimetric equation, the estimated temperature increase by the energy deposited by the laser pulse is about 120 K giving a maximum temperature of 200 K far above the Verwey transition [360]. In that case, we would expect a complete recovery to the high-temperature cubic phase. By comparing the structural photo-induced response and the equilibrium structural transition, we noticed that the *high* fluence photo-induced state had accomplished only $\sim 5\%$ towards the full HT phase recovery. In the calorimetric calculation, the heat dissipation with the insulating LT phase environment is not included and can explain the discrepancy. Further experimental investigations are required to council this observation and are left for future work.

The FWHM expresses the coherence length of the structure. Despite initially having a similar response as the lattice strain, the FWHM crosses its initial value and gets broader after 200 ps (see Fig. 7.12c). After 1.3 ns, the broadening is still increasing, and there is no sign of trend inversion towards the initial value. Such anomalous behavior supported by a long lifetime is a signature of a potential novel out-of-equilibrium (hidden) phase that might differ structurally and electronically from the previously reported phase separation state. At equilibrium, peak broadening is a direct consequence of the presence of strain and is described through the

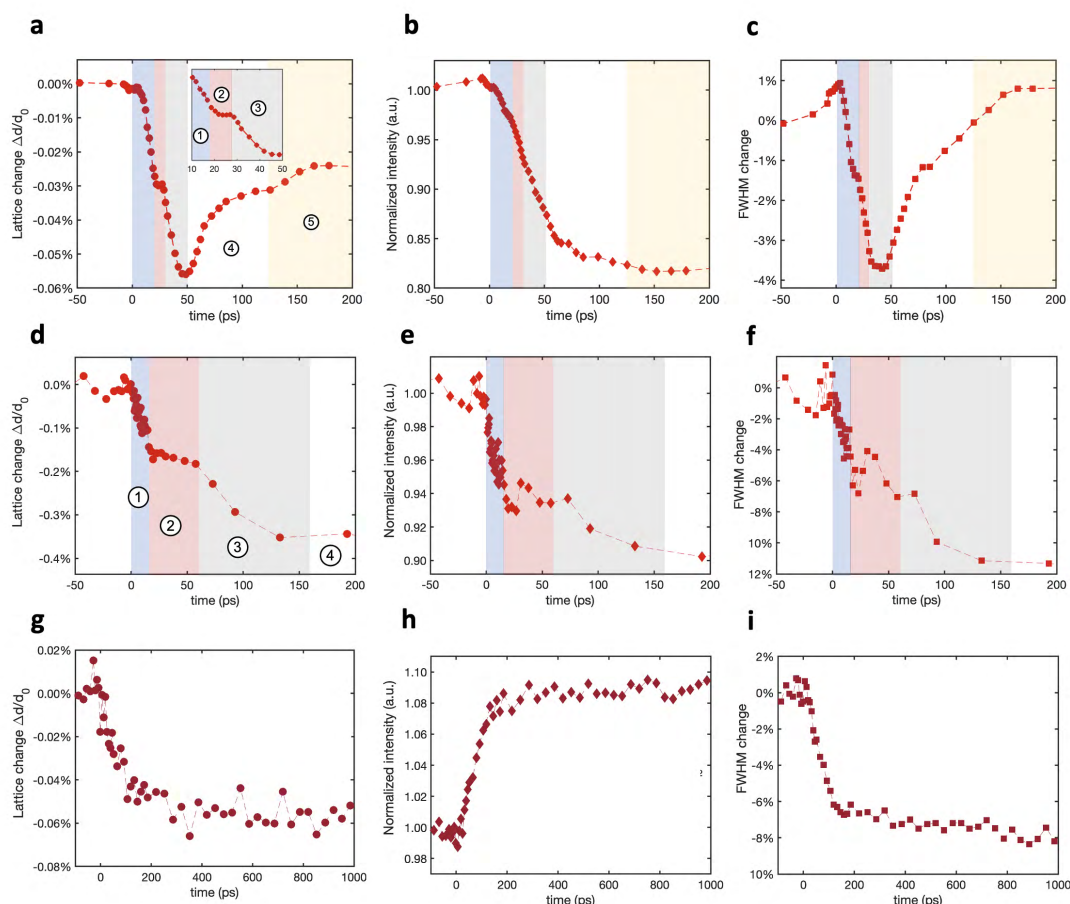


Figure 7.11 – **Ultrafast structural dynamics in Fe_3O_4 upon 800 nm - 1.55 eV photoexcitation.** Lattice (**a, d, g**), intensity (**b, e, h**) and FWHM (**c, f, i**) responses extracted from the $(660)_c$ Bragg reflection upon 800 nm ultrashort (50 fs) photoexcitation. The first (**a-c**) and second (**d-e**) data sets were taken in the *intermediate* fluence regime with a fluence of 2.7 mJ/cm^2 and 3.9 mJ/cm^2 , respectively. The third data set (**g-i**) shows the structural response using a fluence of 9.0 mJ/cm^2 corresponding to the *high* fluence regime. The first and third data sets were recorded with the same upgraded setup as in equilibrium case (Fig.7.7). All data were taken at 80 K in the low-temperature monoclinic phase. The shaded areas indicate the different phases.

Williamson-Hall relation. Such potential correlation is investigated by getting rid of the temporal axis to plot the different parameters (strain, FWHM, and intensity) in function of the remaining parameters. For example, strain versus FWHM or strain versus intensity. Such correlation plots are presented in the Fig. 7.13. Several regimes can be clearly identified and illustrated the different electron-phonon and phonon-phonon dynamics. While one regime is observed for the *high* fluence case, different correlation relations appears in the *intermediate* regime. All stages except the plateau phase (phase 2) show strong correlation with each other as shown in Tab.7.3. Interestingly, in that phase both the intensity and FWHM are not

Chapter 7. Magnetite Fe_3O_4 as the prototypical MIT system

correlated with the lattice change. This indicates during that phase electronic effects directly contributing in the intensity and FWHM are independent of the structural dynamics. The second *intermediate* data set presents a similar behavior.

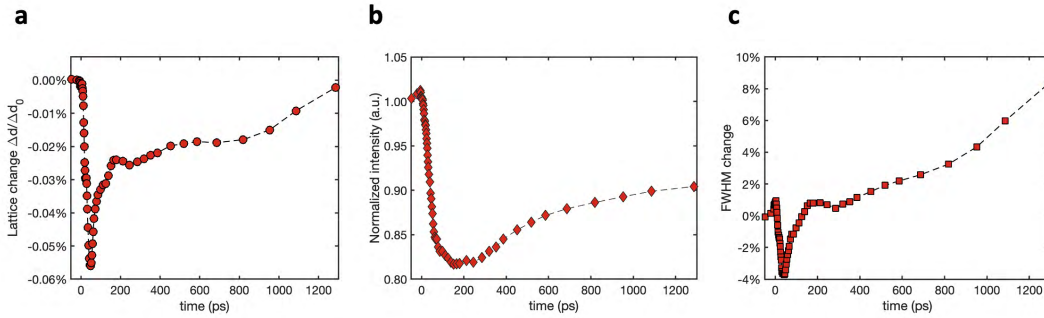


Figure 7.12 – **Metastability a signature of hidden phases.** Extending to 1.3 ns the investigation of (a) the lattice, (b) intensity and (c) FWHM dynamics extracted from the $(660)_c$ Bragg reflection change following 800 nm photoexcitation at 2.9 mJ/cm^2 reveals a long and a complex recovery towards a cubic phase.

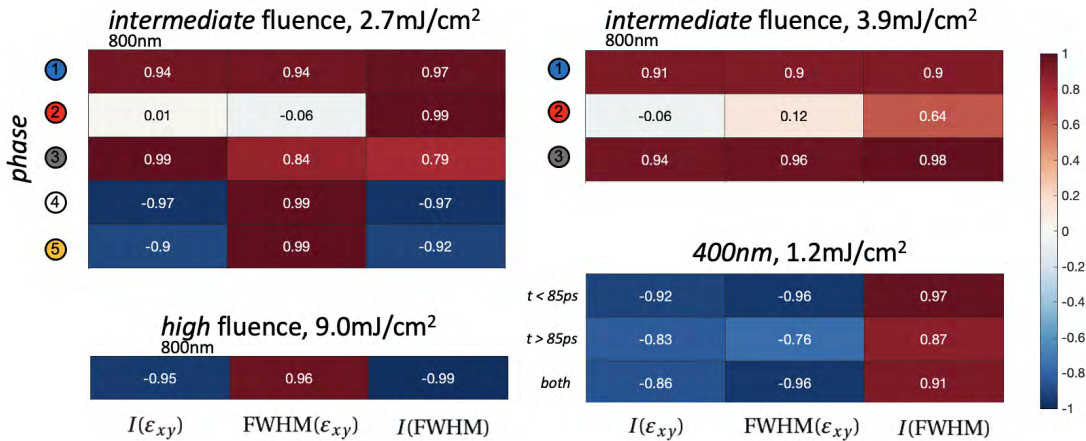


Table 7.3 – **Correlation coefficients depending on the different compression and relaxation phases and photon energy.** All phases show strong correlations except in the second phase upon 800 nm photoexcitation, where both correlation plots depending on the lattice strain ϵ_{xy} show no linear dependence.

7.4.2 400 nm / 3.10 eV photon energy

We extended our investigation in Magnetite by tuning the photon energy to 3.1 eV (400 nm), which has sufficient energy to initiate charge transfer electronic excitation [391]. A striking result is an opposite behavior in lattice evolution that undergoes a 0.4% expansion along [110],

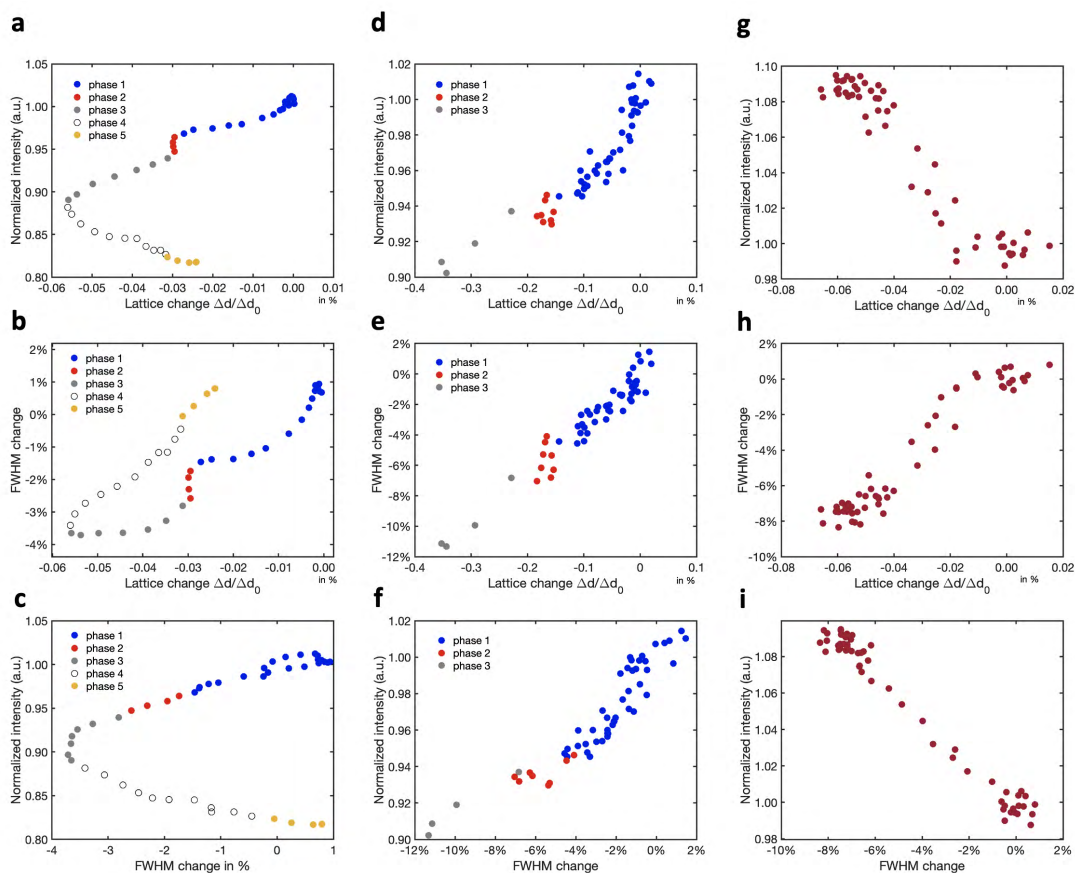


Figure 7.13 – Correlation plots upon 800 nm photoexcitation in the LT phase. **a-c**: intermediate fluence 2.7 mJ/cm^2 , **d-f**: intermediate fluence 3.9 mJ/cm^2 , **g-i**: high fluence 9.0 mJ/cm^2 . The corresponding correlation coefficients are presented in Tab.7.3.

instead of a contraction present in both the 800 nm photo-induced state, and the equilibrium quasi-adiabatic phase transition towards the HT cubic phase. This additional expansion along [110] is not accessible thermally as the expansion induced by the structural transition during the quasi-adiabatic cooling stabilizes after 90 K down to 40 K (see Fig. 7.7a). Therefore, we associate this photo-induced structural phase with a novel emergent hidden phase.

At equilibrium, during the structural transition, the tilt angle initially at $\beta = 90^\circ$ in the HT cubic phase 1 changes to $\beta_M = 90.236^\circ$ at 90 K in the monoclinic phase [373]. For a monoclinic structure and at equilibrium, the relation between the different lattice parameters a , b , c and the monoclinic tilt angle β_M is given by:

$$\frac{1}{d^2} = \frac{1}{a^2} \frac{h^2}{\sin^2 \beta_M} + \frac{1}{b^2} k^2 + \frac{1}{c^2} \frac{l^2}{\sin^2 \beta_M} - \frac{2hl \cos \beta_M}{ac \sin^2 \beta_M} \quad (7.11)$$

with h, k, l the Miller indices. In our case, the Bragg peak probed is the $(660)_c$, the (7.11) simplifies to:

$$\frac{1}{d_{660}^2} = 36 \left(\frac{1}{a^2 \sin^2 \beta_M} + \frac{1}{b^2} \right) \quad (7.12)$$

In Magnetite, the lattice constants a and b are equivalent at equilibrium. Hence, an expansion of the interplanar distance along (660) leads to three possible structural configurations:

1. A change of the monoclinic tilt angle β_M , preserving the symmetry, as a and b remain constant and equivalent.
2. A change in the lattice parameter a or/and b , inducing a symmetry breaking, and thus a reduced point symmetry.
3. A combination of both.

Recent, ultrafast optical measurement using the same photon energy has revealed the generation of a forbidden coherent oscillation attributed to a T_{2g} phonon mode directly linked to the monoclinic angle [381]. This strongly suggests that the novel structural photo-induced phase is characterized by a larger monoclinic angle i.e., $\beta_{M,400\text{ nm}} > \beta_M$. To disentangle and provide a quantitative estimate of each contribution, one would need to monitor the behavior of multiple Bragg peaks along different zone axes.

Nevertheless, our data clearly show that 400 nm optical excitation induces a lattice change, previously unknown and only accessible through ultrashort illumination, as no T_{2g} phonon mode is detected upon a continuous 400 nm laser excitation [381]. The novel emergent structural phase takes around 50 ps to establish and remains stable with no sign of recovery for at least 300 ps, characteristic of a metastable hidden state. One direct expansion dynamics occurs, which we relate mainly to strong electron-phonon coupling.

Following the 400 nm photoexcitation, a significant drop in the intensity response is observed in Fig. 7.14b. In addition, a second consequent drop appears around 80 ps, which is concomitant to the point where the lattice spacing and the FWHM stabilize. This suggests that the emergence of the hidden phase is fully established after 80 ps. For the 800 nm case, thermal effects and multiple scatterings from the mixed phase are the origins of the intensity drop. Here, we can attribute the reduction in intensity to the expected reduction of the structure factor inherent to a stronger monoclinic distortion. Moreover, as the atomic d_{660} spacing evolves, the Bragg condition changes and might not be fulfilled anymore, contributing to the drop in intensity. The presence of structural domains can account for the intensity reduction through multiple scattering processes. However, this is not consistent with the observed shrinking of the FWHM (Fig. 7.14c), indicating a higher homogeneity, which suggests that the new hidden structural state possesses a larger structural long-range order. The correlation plots and coefficients are presented in Fig. 7.14d-f and Tab. 7.3, respectively.

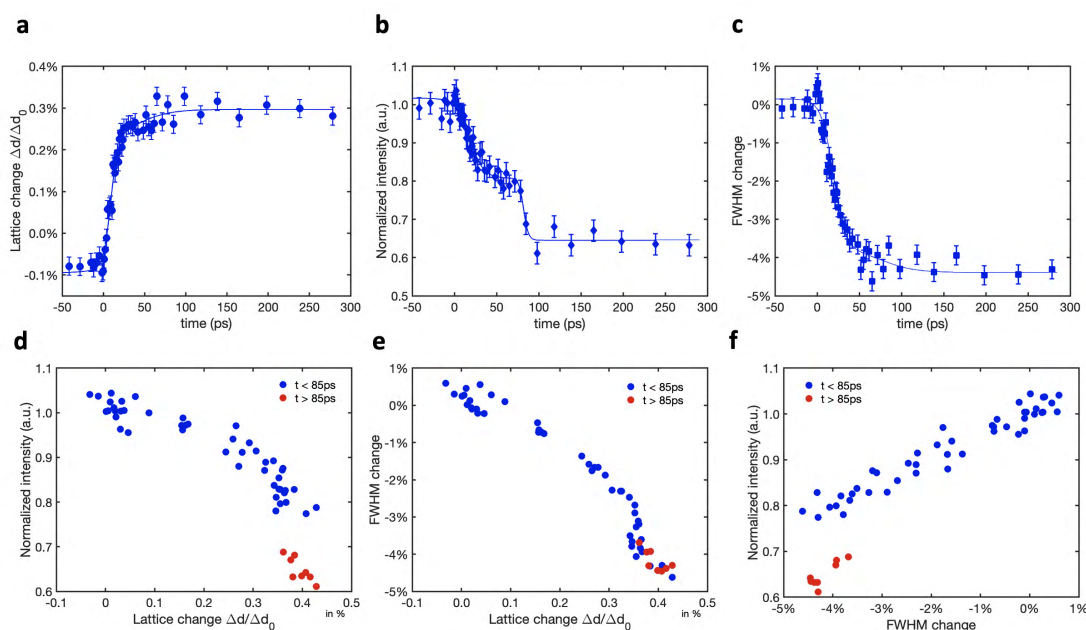


Figure 7.14 – **Ultrafast structural dynamics in Fe_3O_4 upon 400 nm - 3.10 eV photoexcitation.** Evolution of (a) the lattice, (b) intensity and (c) FWHM extracted from the $(660)_c$ Bragg reflection change following 400 nm photoexcitation at $1.2 \text{ mJ}/\text{cm}^2$. The solid lines are guide for the eye. Error bars correspond to the standard deviation before $t = 0$. **d-f**: Correlation plots between the different extracted parameters.

7.5 Discussion

7.5.1 Inter-site d-d electronic transitions

Pumping Fe_3O_4 Magnetite with 800 nm (1.55 eV) photon pulses triggers inter-site electronic d-d transition expressed as $3d_i^6 3d_j^5 \rightarrow 3d_i^5 3d_j^6$. The d-d excitations encompass three electronic transitions supported by both theoretical LSDA+U and GGA+U calculation [381, 392] and experimental observation probing the optical conductivity [354, 391]. The dominant electronic transition at 1.55 eV corresponds to the hopping of a localized electron from an occupied t_{2g} of Fe_B^{+2} to an unoccupied t_{2g} orbital of Fe_B^{+3} . The two other possibilities occur at higher energy around 2 eV, (see Fig. 7.10a) and are less likely to happen. However, both would give the same consequence [360]. Initially frozen, the restoration of the minority spin t_{2g} electrons mobility induces the valency to change for both sites Fe_B^{+2} and Fe_B^{+3} melting the charge order (CO). In addition, the delocalization of the minority spin t_{2g} electrons induces the Fe_B^{+2} and Fe_B^{+3} sites to alternate within the trimeron. Consequently, the long-range order of the trimeron is suppressed. The destruction of the trimeron occurs at an ultrashort time scale 300-600 fs [38, 73, 358]. Following the trimeron destruction the $\text{Fe}_B - \text{Fe}_B$ distance recovers to its initial value. Hence, the structure relaxes, and a phase separation appears with the emergence of

cubic islands embedded in the insulating monoclinic background (phase 1). The relaxation process of excited electrons has been well studied [393–397]. In a nutshell, once excited electrons relax through the interaction with high-energy optical phonons. Then, the excited phonons decay into lower energy acoustic phonon mode anharmonically via a three-phonon scattering process.

For Magnetite, the multistage compression observed can be explained by a similar mechanism. After the illumination, the induced delocalized electrons destroy the trimeron as well as the CO through electron-electron scattering. Due to the strong trimeron-phonon coupling [377], X₃ (TO) phonons are driven, which then decay to Δ₅ (TA) phonon modes. This is supported by a recent time-resolved electron diffraction study where the authors show using the same photon energy (800 nm) that the X₃ (TO) mode is preferably triggered via the electron-phonon coupling [73]. Interestingly, in a second study, the same group extended their investigation to 20 ps and reported the observation of a dual-stage process [356]. However, in our case, a three-step process occurs, with the presence of a plateau (phase 2). The origin of this plateau remains unclear, and at least two suggestions can be proposed:

1. In this scenario, a fully microscopic picture is discussed. First, the X₃ phonon modes are initially triggered and lead to the first compression stage (phase 1). Then it couples to Δ₅ phonons, giving an additional compression. However, few possibilities arise since we observed two compression stages (phase 2 and phase 3)
 - (a) The coupling to Δ₅ phonons occurs during phase 2, which induces a weak additional compression. The extra compression (phase 3) is created through the coupling with other phonon modes, which is unlikely since Δ₅ phonon modes have the lowest energy.
 - (b) The transition between X₃ and Δ₅ phonons involves a latent heat-like behavior, leading to a plateau (phase 2).
 - (c) Δ₅ phonons are triggered incoherently, then a synchronization process appears (phase 2) and leads to the emergence of a collective structural vibration mode which provides an extra compression contribution (phase 3).
2. The second scenario relies on a mesoscale approach. After the illumination, the trimerons and CO are suppressed, leading to the relaxation of the crystal structure (phase 1) and inducing a phase separation characterized by the coexistence of trimeron islands and melted trimeron domains. Then, through thermal fluctuation, the electronic charges rearrange, restoring some form of homogeneity (phase 2). After reaching a critical distribution, the residual stress (trimeron islands) of the system percolates, relaxing towards the cubic phase expressed as an additional compression (phase 3).

The second scenario can easily explain the three fluence regimes. In the *low* fluence regime, the number of trimerons remains too large to induce the percolation, and the system behaves as a warmer charge-ordered lattice. The *intermediate* regime corresponds to the discussed

case 2 and is sketched in Fig. 7.15. In the last *high* fluence regime, the trimeron order is completely melted, and no phase separation appears. The correlation analysis supports this proposition as in phase 2, the electronic and structural degrees of freedom are decoupled.

7.5.2 Ligand-Metal charge transfer

Tuning the photon energy allows for triggering higher energy electronic transition. At equilibrium, in the low-temperature phase, high-accuracy synchrotron x-ray structure refinements have revealed the presence of a high connectivity trimeron network instead of a homogeneous randomized distribution [373, 379]. At 90 K, Fe_B^{3+} sites can be involved within the formation of up to three trimerons, leaving four of the eight non-equivalent Fe_B^{3+} sites inactive [373]. Our equilibrium data shows no additional lattice expansion along the [110] between 90 K down to 40 K, which indicates that the equilibrium maximum connectivity state is reached a few kelvins below T_V .

Using 3.1 eV (400 nm) as photon energy, multiple electronic excitations are driven. The dominant excitation is the charge transfer from 2p oxygen orbitals to 3d bands of Fe_B [391]. Upon photoexcitation, the ligand-metal charge transfer is activated, and oxygens of the octahedron FeO_6 supply electrons to the Fe_B^{3+} . Recently, Pachoud *et al.* have shown that chemically doped Magnetite introduces B site-selective Fe^{2+} vacancies (which become Fe^{3+}) and weakens the trimeron long-range order [379]. Lately, core x-ray spectroscopy unveiled a selective self-doping effect temperature-driven [380]. In our case, the photoexcitation provides extra charges to Fe_B^{3+} ions acting as a photo-doping effect which we speculate to be site-selective and is consistent with the increase of the coherence length (Fig. 7.14c). Consequently, Fe_B^{3+} ions transform to Fe_B^{2+} , thus increasing the proportion of Fe_B^{2+} at the inactive B-sites. This creates additional trimerons and strengthens the t_{2g} orbital ordering. The newly formed photo-induced state is characterized by higher connectivity of the trimeron network. The cooperative effect of the $\text{Fe}_B - \text{Fe}_B$ distance shortening induced by the charge localization within the extended trimeron network (charge ordering) [373, 398] and the stronger Jahn-Teller distortion boosted by the t_{2g} orbital ordering provokes additional stress. This translates to a larger monoclinic distortion beyond the thermodynamic limit that we assigned to a hidden structural phase. In this scenario sketched in Fig. 7.15, the process can be seen as follows: the trimeron network forms an imperfect Wigner crystal in which vacancies are present (inactive Fe^{3+} B-sites). The 400 nm photon pulse triggers the charge transfer excitations, acting as a photo-doping effect. Microscopically, the oxygen ligands selectively supply additional electrons to non-participating Fe^{3+} B-sites, creating new trimerons. These additional trimeron units enhance the trimeron network connectivity and complete the Wigner crystal, which ultimately reinforces the monoclinic distortion through the strong electron-phonon coupling.

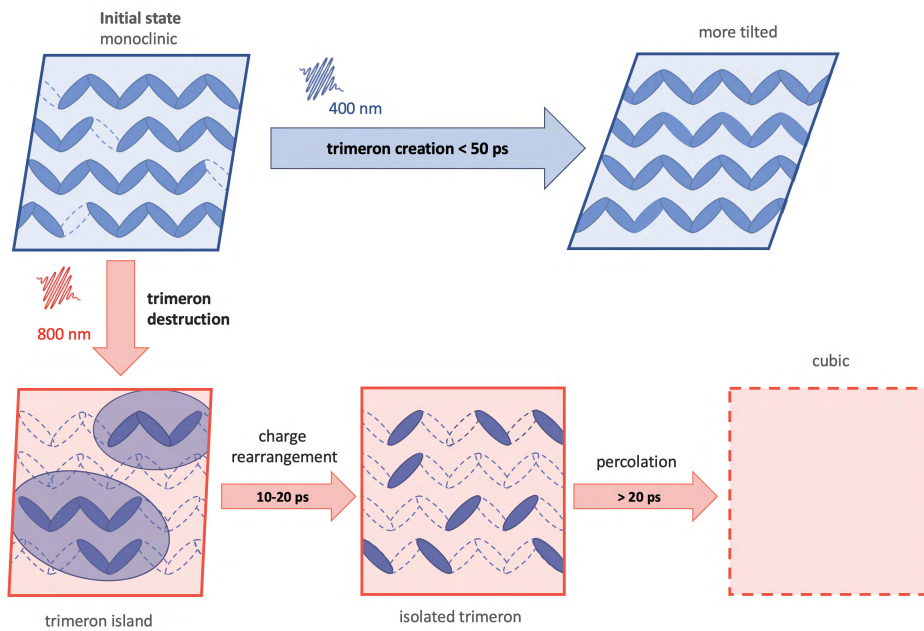


Figure 7.15 – **Sketch of the different photo-induced structural dynamics pathway.** Top: The 400 nm photoexcitation acts as a photo-doping effect creating additional trimerons, which leads to a stronger monoclinic distortion. Bottom: In scenario 2, the 800 nm photoexcitation induces a phase separation which rearranges until reaching a critical homogeneity giving rise to percolation.

7.6 Limitation and perspectives

7.6.1 Twinning and domain morphology considerations

Before discussing the twinning effects, let us emphasize that additional reflections are expected to appear due to the symmetry reduction from $Fd\bar{3}m$ to Cc as shown in the diffraction simulations in Fig. 7.17, which we do not observe (Fig. 7.6). We explained this for three main reasons:

1. The intensities of the additional peaks are expected to be much weaker due to their inherent structure factor. For example, the intensity ratio between the $(660)_c$ in the HT phase is 215x as compared to the $(\bar{1}20\bar{2})_m$ and 39x for the $(\bar{1}00\bar{4})_m$ reflections (See Fig. 7.17).
2. The presence of micro-sized domains (twins) at the low-temperature phase leads to multiple scatterings (Fig. 7.16a), drastically reducing the intensity and hindering the appearance of those additional peaks in our data. We explain schematically the multiple scattering processes induced by the domain in Fig. 7.16b.

3. The inherent strain leads to a strong broadening of the peak that could hide the presence of extra peaks.

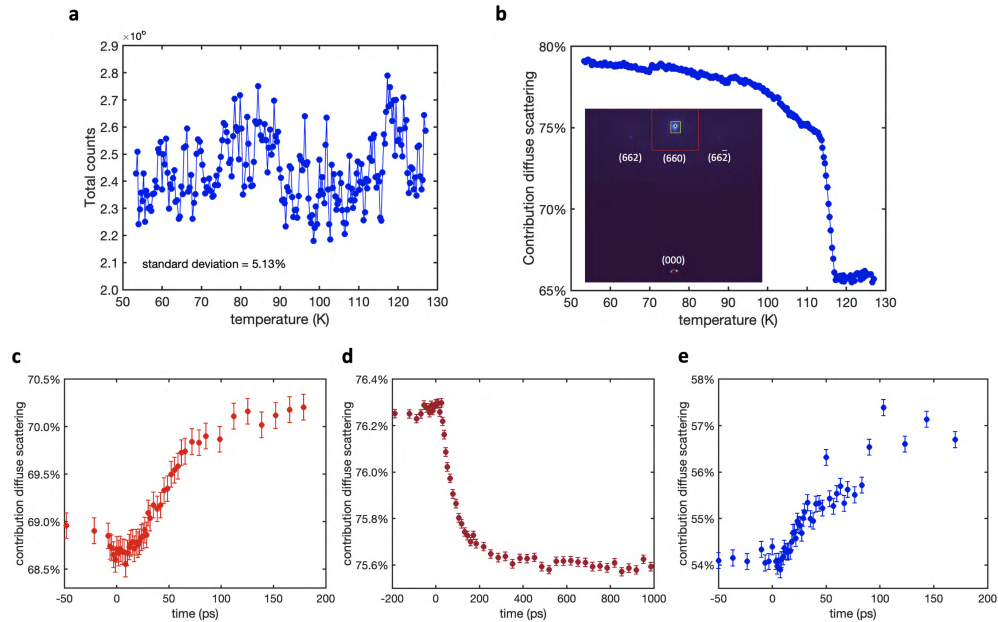


Figure 7.16 – **Beam stability and diffuse scattering.** **a:** Conservation of the total number of electrons across the Verwey transition. The direct beam is not considered due to the saturation of pixels. **b:** Evolution of the diffuse scattering contribution computed from the total count's difference near the (660) reflection (red area) by subtracting the elastic Bragg contribution (yellow area) depending on the temperature. **c-d:** Using a similar approach as done as in **b**, evolution of the diffuse scattering ration upon 800 nm optical pumping in the *intermediate* and *high* fluence regime, and upon 400 nm photoexcitation, respectively.

Another limitation arises as we can investigate a single Bragg peak only with a probe footprint larger than the domain size. In this work, our discussion relies on the single domain description. However, it is well known that twinning effects are present in the LT phase. It is natural to question if our data measured the average contribution of the domain morphology instead of being an accurate microscopic probe. In other words, if the diffraction signal is a mixture of domains with different orientations, would it not be possible to get apparent contraction/expansion depending on the domain morphology? For instance, if the lattice contract/expands along $[110]$, the opposite behavior is expected along $[1\bar{1}0]$.

Indeed, due to the electron beam size, at LT, it is likely that we simultaneously probe several domains that are present along various directions in the crystal. Nonetheless, the UED is a surface technique with a penetration depth of ~ 5 nm, and, therefore, some considerations must be taken.

1. To the best of our knowledge, x-ray diffraction experiments probing micron-length thicknesses show the presence of only two peaks for each reflection. The same experiments have shown that the c-direction (where the doubling of the cubic unit cell takes place) is uniquely defined in the near-surface region.
2. The surface of Magnetite is very labile. The effect of stress created by polishing or even the strains at the surface imposes a certain preferred domain orientation in the near-surface region [399]. The good reproducibility of our data demonstrates this effect and is consistent with the clear strain changes at LT induced by the different laser excitations (1.55 eV and 3.10 eV). In addition, the two 800 nm data sets in the *intermediate* fluence regime were taken at different regions in the sample and different years, showing similar behaviors.
3. Furthermore, the displacement of domain walls is a highly non-reproducible phenomenon and is incompatible with pump-probe experiments. The excellent reversibility of the observed effect suggests that either the region probed is a single domain or that the morphology of the domains relaxes exactly in its initial configuration.
4. In addition, our 800 nm out-of-equilibrium data agree with previous x-rays experiments where the probed regions ranged from 200 to 500 microns [38]. The 800 nm *high* fluence data set is also consistent with the literature [354, 357].

Although the electron beam footprint is larger than the domain size and the electron beam divergence leads to a very poor lateral resolution, our measured $(6\ 6\ 0)_c$ reflection includes potential contributions from other domains of the same type like the $(0\ 12\ 0)_m$ and $(12\ 0\ 0)_m$ (see Fig. 7.17). Combining the arguments above, we are confident that those reflections resulting from the monoclinic distortion and ensuing domains should behave in the same way upon illumination.

As our probe is a surface technique, and the excited volume is embedded in the unperturbed insulating background crystal structure. One would expect some bulge or depression formation and acoustic wave propagation at the surface. One could argue that the measured effects originate from the surface deformation effect instead of the discussed microscopic mechanism. However, in that case, the depression would form at the interface between the unperturbed background and the excited volume or near it. Since the penetration depth of the electron beam is smaller (~ 5 nm) than the laser penetration depth (~ 34 nm for 400 nm and ~ 108 nm for 800 nm [360]), the background crystal is not appearing in the experiments. Furthermore, the presence of the domains gives rise to a strong attenuation (hundreds of Angstroms to few micrometers) and, thus, prevent the propagation of any acoustic wave along the different directions [387].

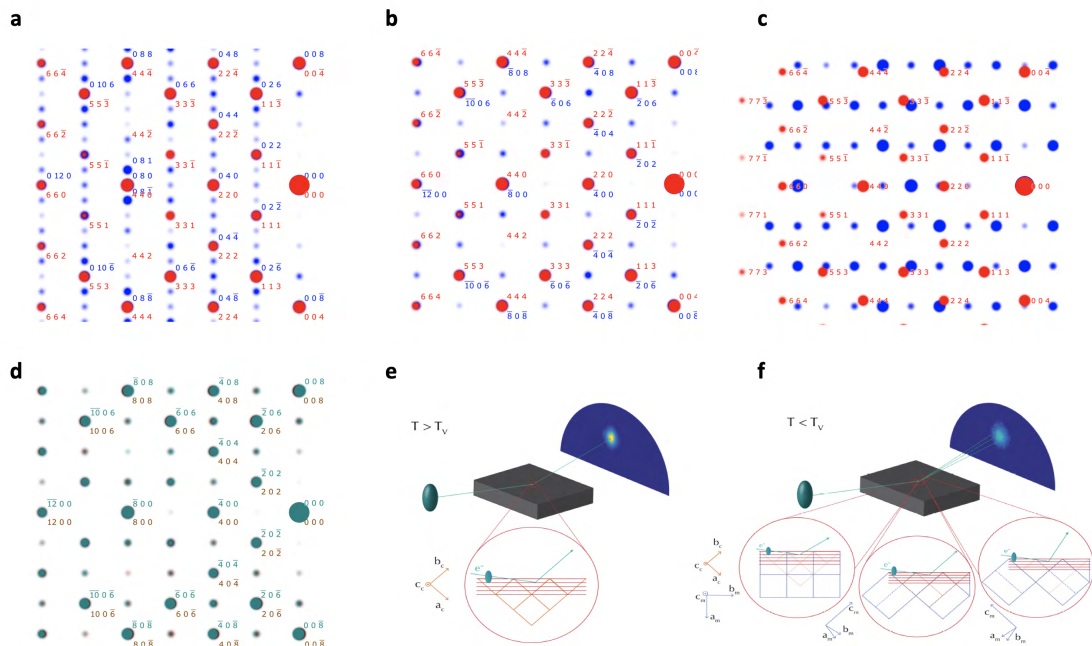


Figure 7.17 – **Transmission electron diffraction simulations and the broadening twinning effect.** Overlap of expected Bragg reflections. The red spots indicate the $Fd\bar{3}m$ cubic phase diffraction pattern obtained with the $[\bar{1}10]_c$ zone axis (ZA) used in our experiment. The blue spots show the expected Cc monoclinic reflections in the LT phase for different ZA. **a:** $[100]_m$. **b:** $[010]_m$. **c:** Stack of the diffraction patterns with $[\bar{1}11]_m$, $[1\bar{1}1]_m$, $[11\bar{1}]_m$, and $[111]_m$ as zone axes. For those ZA all the reflections are far from the initial $(660)_c$. **d:** Comparison of the $[010]_m$ ZA pattern (green spots) and $[0\bar{1}0]_m$ ZA pattern (brown spots). **e,f:** Sketch of the diffraction patterns in the HT and LT phase, respectively. The **(e)** cubic and **(f)** monoclinic unit cells are illustrated. In the LT phase, the monoclinic structure leads to the appearance of domains. The qualitative effect of the three main twin orientations on the diffraction pattern is shown.

7.6.2 Open questions and further investigation

Demonstrating the use of triggering different electronic excitations to generate inaccessible (hidden) thermodynamically phases is one of the significant results of this work, which goes along with the detection of a complex multistage process. This opens further questions, such as the genuine nature of the multistage process or the photo-induced phase's structural, electronic, and magnetic properties. Here, we discuss a few aspects to go beyond the current experimental and investigation limitations.

1. The electron probe footprint is larger ($\sim 500 \mu\text{m}$) than the expected sub-micrometer domain sizes in the low-temperature phase. Although some considerations must be made (see subsection 7.6.1), a second limitation arises from the probe size. The coherence

length of the trimeron network (insulating phase) shrinks to a few hundred nanometres during the phase separation induced upon 800 nm illumination [38]. Hence, our probe averages out the total phase separation dynamics and can not assign the origin of the observed multistep compression. Two scenarios have been proposed, a microscopic single-domain picture or an emergent phenomenon from the mesoscopic interplay of the phase separation. Nano-probes as ultrafast convergent beam electron diffraction (UCBED) would provide further insights.

2. In addition, RHEED is a moderate surface technique, and our discussion is based on a bulk crystal approximation motivated by the concomitant anomalies along the specific [110] crystallographic direction [378, 386]. State-of-the-art time-resolved transmission electron diffraction with nanometres probe size should be able to address both limitations; finding the true origin of the complex multistage processes and validating the bulk-like dynamics.
3. During this study, only one Bragg peak was investigated, which limits our observation. In particular, investigating additional Bragg reflections along different zone axis will provide insight into the hidden structural phase induced by 3.10 eV (400 nm) photoexcitation and answer if an additional symmetry breaking emerges.
4. Many studies have reported the fluctuation of charge density waves far above the Verwey transition temperature. Recently, Borroni et al. have demonstrated the stabilization of such critical fluctuation by triggering the charge transfer 3.10 eV (400 nm) photoexcitation [381]. It would be interesting to perform a temperature-dependent experiment and shows that the hidden phase can also be generated above T_V
5. Qualitatively, all physical parameters investigated confirm the thermal-like Verwey transition for the *high* fluence regime. However, quantitatively only a fraction of a cubic structure has been recovered, the estimated temperature rise is far above the transition, and a longer time scale is observed. The first two aspects can be explained by the pump spot size, which is comparable to the probe beam leading to inhomogeneous illumination and simplification in the heating model where thermal conduction has been neglected. The time dynamics is not explained by the optical study [354] where no time dependence has been measured. A proper fluence dependence experiment must be done to elucidate these few discrepancies.
6. Upon cooling, between 300 K and 210 K a compression of the lattice spacing along [110] is observed and can be assigned to the conventional thermal contraction. However, around 210 K far above T_V , the lattice changes its behaviors and starts to expand substantially. Charge-ordering fluctuation and spin-reorientation are known to occur above the Verwey temperature [73, 370, 400]. Spin-reorientation transition is expected to occur around 130 K, much cooler than the observed 210 K. In a recent preprint, an electronic nematic phase coupled to the structural order has been discovered, Its transition temperature matches reasonably our observation and reinforces our order parameter

hypothesis to be the trimeron network topology along the [110]. The origin of this transition remains unclear and further work is needed. Conventional synchrotron x-ray and electron microscopy should provide useful information.

7.7 Conclusion

Our static equilibrium measurement shows a first-order transition in the lattice spacing at the Verwey transition temperature. From this observation, we derived, using Ginzburg-Landau theory and fundamental group theory, the symmetry of the order parameter proposed to be the trimeron arrangement along the [110] crystallographic direction. Intriguingly, our data reveals a second transition far above the Verwey transition corresponding to the onset of charge-ordering, suggesting the condensation of the trimeron liquid. Furthermore, we exploit the strongly correlated nature of Magnetite to demonstrate the ability to generate metastable structural hidden phases using energy-tuned photoexcitation. In detail, we reveal two distinct emergent structural behaviors by driven specific electronic excitations. The 800 nm light triggers d-d excitations, which melt the trimeron charge order. This results in the relaxation of the structure towards a cubic phase. The relaxation pathway depends on the fluence used, and a complex multistage process is unveiled, which originates either from a microscopic mechanism or an emergent interplay in the phase separation at the mesoscale. The 400 nm light activate ligand-metal charge transfer, which creates additional trimers and promotes t_{2g} orbital ordering. Hence, the connectivity of the trimeron network is enhanced, which fosters a larger monoclinic distortion inaccessible adiabatically. This work demonstrates the crucial role of the trimeron structural network in Magnetite and shows the ability to establish novel hidden phases in quantum materials via specific electronic excitations in a strongly correlated environment.

List of acronyms

CBED convergent-beam electron diffraction	126
CDW charge-density wave	12
CW clockwise	103
CCW counterclockwise	103
DMI Dzyaloshinskii-Moriya interaction	27
DFT density functional theory	48
EELS electron energy loss spectroscopy	13
EFTEM energy-filtered transmission electron microscopy	12
EM electron microscopy	7
FC field-cooled	119
FCC field-cooled cooling	113
FD field-decreased	119
FFT Fast Fourier Transform	48

Chapter 7. Magnetite Fe_3O_4 as the prototypical MIT system

FH field-heated	119
FI field-increased	113
FoV field of view	122
GGA+U Generalized gradient approximation + U	50
HFC high-field-cooled	119
HT-skyrmion high-temperature skyrmion	113
HRTEM high-resolution transmission electron microscopy	48
IFE inverse Faraday effect	54
LT low-temperature	119
LT-skyrmion low-temperature skyrmion	112
LTEM Lorentz transmission electron microscopy	15
MOKE Magneto-Optical Kerr effect	41
MT-skyrmion metastable skyrmion	118
NIR near-infrared radiation	7
OAM orbital angular momentum	107
OPA optical parametric amplifier	20

QI Quantum interferometry	42
REXS resonant elastic x-ray scattering	115
RHEED Reflective High-Energy Electron Diffraction	7
RKKY Runderman-Kittel-Kasuya-Yosida	32
SAED selected area electron diffraction	48
SAM spin angular momentum	107
SANS small-angle neutron scattering	49
SEM scanning electron microscope	11
SHE skyrmion Hall effect	33
SkL skyrmion lattice	27
SkX skyrmion crystal	27
SLM spatial light modulator	108
SOC spin-orbit coupling	49
STEM scanning transmission electron microscope	10
TEM transmission electron microscope	10
THE Topological Hall effect	33

Chapter 7. Magnetite Fe_3O_4 as the prototypical MIT system

TPT Topological phase transition	28
TIE transport-of-intensity equation	15
TIFE topological inverse Faraday effect	103
URHEED Ultrafast Reflective High-Energy Electron Diffraction	21
UV ultraviolet	20
ZFC zero-field-cooled	58

A Crystal growth and characterization

Before and along with my thesis, I had the opportunity to work at the EPFL crystal growth facility headed by Dr. A. Magrez. My main focus was synthesizing new potential skyrmion host materials and developing the growth process for Cu_2OSeO_3 . Notably, I found a protocol for growth size-controlled nanoparticles that has led to the work [274]. A specific article discussing the growth method is in preparation. The growth method I used the most was hydrothermal synthesis, as it allows to synthesize reasonably large crystalline samples that are unstable close to the melting point. Consequently can not be grown by solid-state methods or floating zone techniques. Once synthesized, the sample is characterized with powder x-ray diffractometry, and their magnetic properties are measured using a vibrating-sample magnetometer. In the process, I synthesized two novel compounds, $(\text{H}_3\text{O})\text{Fe}_3(\text{SeO}_4)_2(\text{OH})_6$ and $\text{Fe}[\text{SeO}_4]\text{OH}$. One article presenting the last compound is presented below and has been recently accepted in *CrysEngComm*. Other publications are in preparation.

A.1 $\text{Fe}[\text{SeO}_4]\text{OH}$

I contributed to this work by first synthesized and characterized the newly reported crystal with N. Maamouri, a master student that I was supervising, and gave insights for the manuscript.

A. Arakcheeva, N. Maamouri, W. H. Bi, **B. Truc**, A. Magrez, Synthesis, Crystal Structure of $\text{Fe}[\text{SeO}_4]\text{OH}$ and Prediction of Polytypes in the extended $R[\text{MO}_4]\text{Z}$ Family, *CrysEngComm*, **25**, 1608, Feb 2023.

Cite this: *CrystEngComm*, 2023, 25, 1608

Synthesis and crystal structure of Fe[SeO₄]OH and prediction of polytypes in the extended R[MO₄]Z family†

Alla Arakcheeva,^a Noémie Maamouri,^a Wen Hua Bi,^a Benoît Truc^c and Arnaud Magrez^a

Single crystals of Fe[SeO₄]OH have been synthesized by hydrothermal treatment. The Fe[SeO₄]OH structure was investigated using the superspace approach. It is shown that the structure belongs to a family of compounds including kieserite-like and paufferite-like structure types. All these structures consist of topologically identical layers interconnected either by a mirror plane (*m*) or by an inversion centre ($\bar{1}$). The sequence of these local elements of symmetry, *m* and $\bar{1}$, determines each member of the family. We used the (3 + 1)-dimension superspace group *Pnam*(00 γ)000 applied to an average structure to be able to reproduce known polytypes and predict new ordered and partially or completely disordered structures in the R[MO₄]Z structural family.

Received 11th November 2022,
Accepted 9th February 2023

DOI: 10.1039/d2ce01533a

rsc.li/crystengcomm

Introduction

The intensive investigation of the crystal growth, structure and properties of transition metal hydro, hydroxo, oxo and halogeno selenates and sulfates has already been very successful. New materials have been discovered and exciting physical and chemical properties could be studied. Many of these materials are being applied in Li-ion batteries, solar cells, catalysis, and spintronic devices to name but a few. The interest in Fe[SO₄](H₂O/OH) originates from the perspective of tuning the physical properties by the oxidation state of the iron, which can be controlled, *via* the H₂O/OH content. Basic iron hydroxyl sulphate, Fe^{III}[SO₄]OH, is used in the processing of refractory gold concentrates by pressure oxidation,¹ in preparation of novel electrode materials² among other applications.^{3–5} If OH is replaced by H₂O, iron in Fe[SO₄]H₂O has a 2+ oxidation state. The material exhibits a strong reducing potential which is used for the desulfurization and

neutralization of wastewater. Fe[SO₄]H₂O also has application in the construction industry as well as in agriculture.^{6,7}

The crystal structure of Fe^{II}[SO₄]H₂O (ref. 8) belongs to the kieserite type,^{9,10} which is well known for many related synthetic compounds and many minerals^{11,12} including some rocks collected on Mars.¹³ It crystallises in the monoclinic space group *C2/c* with unit cell parameters $a \approx c \approx 7.5 \pm 0.3$ Å, $b \approx 7.2 \pm 0.2$ Å, and $\beta \approx 120.0^\circ$. Natural Fe^{III}[SO₄]OH also crystallizes in the kieserite-like monoclinic modification,¹⁴ but being synthesised by hydrothermal treatment,¹⁵ it exhibits the β -V[SO₄]O structure type which is also known as paufferite.¹⁶ It is characterized by the orthorhombic space group *Pnma* (equal to *Pnam*) with unit cell parameters $a \approx 7.5 \pm 0.3$ Å, $b = 0.5a\sqrt{3} \approx 6.5 \pm 0.3$ Å, and $c \approx 7.2 \pm 0.2$ Å.

Both the monoclinic and orthorhombic Fe^{III}[SO₄]OH structures can be seen as built from identical structural layers and have therefore been presented as polytypes.^{14,17} The order–disorder (OD) approach is actually very effective for understanding the origin of any polytype family.¹⁸ Using OD, an infinite number of ordered or disordered members of Fe^{III}[SO₄]OH was predicted by alternating specific local symmetry operators between the layers.¹⁷ An ordered member is defined by a periodic alternating sequence, while an aperiodic sequence corresponds to a disordered member. Using the OD approach, the monoclinic and orthorhombic structures were found as two maxima of the degree of order for Fe^{III}[SO₄]OH.¹⁷ However, the prediction of the exact symmetry and the corresponding atomic sites was proved to be difficult. The incorrect space group *P2₁/c* assigned to the monoclinic structure was later corrected to *C2/c* based on experimental diffraction data.¹⁴

^a SB, IPHYS, Crystal Growth Facility, Ecole Polytechnique Fédérale de Lausanne, Lausanne 1015, Switzerland. E-mail: alla.arakcheeva@epfl.ch, arnaud.magrez@epfl.ch

^b Phase Solutions Co Ltd, ch. des Mésanges 7, Lausanne 1012, Switzerland

^c SB, IPHYS, Laboratory for Ultrafast Microscopy and Electron Scattering, Ecole Polytechnique Fédérale de Lausanne, Lausanne 1015, Switzerland

† Electronic supplementary information (ESI) available: Practical details for generating polytypes using the JANA2006 software; sketches of structures formed by topologically identical *L*_{ss}-layers similar to Fe[MO₄]OH (M = S, Se); comparison of predicted and experimental data for 1M and 1O polytypes. See DOI: <https://doi.org/10.1039/d2ce01533a>

Herein, we first report on the synthesis and structure determination of iron hydroxyl selenate $\text{Fe}^{\text{III}}[\text{SeO}_4]\text{OH}$ isostructural to the monoclinic $\text{Fe}^{\text{III}}[\text{SO}_4]\text{OH}$.

Second, we used the superspace approach to describe a family of related structure types,¹⁹ and we demonstrate that both the orthorhombic (pauflerite-like, space group $Pnma$ or its equivalent $Pnam$) and monoclinic (kieserite-like, space group $C2/c$) polytypes as well as the newly predicted polytypes can be derived from a single $(3 + 1)$ -dimension, $(3 + 1)\text{D}$, structure. Unlike the OD approach, the superspace approach can not only reproduce the topology of the structures, but also predict their 3D symmetry, the unit cell as well as the atomic sites. We show that the proposed approach can be applied not only to $\text{Fe}[\text{MO}_4]\text{OH}$ ($M = \text{S}, \text{Se}$) but also for many known compounds with the general composition $\text{R}[\text{MO}_4]\text{Z}$ ($R = \text{Mg}, \text{Fe}, \text{Ni}, \text{Co}, \text{Zn}, \text{Mn}, \text{Al}, \text{V}, \text{Sb}, \text{and Y}$; $M = \text{S}, \text{Se}, \text{P}, \text{and As}$; $Z = \text{OH}, \text{H}_2\text{O}, \text{F}, \text{and O}$) when their structures are built from topologically similar layers. The monoclinic kieserite-like polytype can also be assigned to $\text{Al}[\text{SO}_4]\text{OH}$,²⁰ $\text{Fe}[\text{SO}_4]\text{F}$,^{21,22} $\text{Sb}[\text{PO}_4]\text{O}$,²³ and CaCrF_5 (ref. 24) structure types. On the other hand, $\text{Y}[\text{SO}_4]\text{F}$,²⁵ $\text{Cd}[\text{SO}_4]\text{F}$,²⁶ $\text{Np}[\text{PO}_4]\text{F}$,²⁷ $\text{Ce}[\text{AsO}_4]\text{F}$,²⁸ $\text{U}[\text{PO}_4]\text{F}$ (ref. 29) and $\text{V}[\text{HPO}_4]\text{O}$ (ref. 30) belong to the pauflerite-like polytype. In addition, the superspace approach also predicts new ordered members and shows that partially or completely disordered and aperiodic polytypes can be formed. Consequently, the proposed $(3 + 1)\text{D}$ structure can be used as the aristotype, from which several (known and possible) 3D structures can be deduced.

Experimental

Growth of $\text{Fe}[\text{SeO}_4]\text{OH}$ crystals

Single crystals of $\text{Fe}[\text{SeO}_4]\text{OH}$ were prepared using the hydrothermal method. A 125 ml Teflon vessel was filled with $\text{Fe}(\text{NO}_3)_3 \cdot 9\text{H}_2\text{O}$ (26.174 g, $\geq 98\%$ Sigma-Aldrich reagent grade) and selenic acid H_2SeO_4 (10 ml, 40% Alfa Aesar reagent grade) in a molar ratio of $\text{Fe}:\text{Se} = 3.33:2$. The autoclave was heated and kept at 200 °C for 5 days. The resulting product was then washed with distilled water. Dark green single crystals of $\text{Fe}[\text{SeO}_4]\text{OH}$ were collected to perform single-crystal XRD. It has to be noted that two other phases were identified, Fe_2O_3 and $(\text{H}_3\text{O})\text{Fe}_3(\text{SeO}_4)_2(\text{OH})_6$ hydronium jarosite selenate, using conventional powder XRD (Empyrean Diffractometer from PANalytical with $\text{Cu-K}\alpha_1$ and $\text{Cu-K}\alpha_2$ radiation).

XRD experiments

A crystal of $\text{Fe}[\text{SeO}_4]\text{OH}$ with a suitable size was selected and mounted on a goniometer head with cryo-loops. The data collection was performed at 100 K on a Rigaku Synergy-I XtaLAB X-ray diffractometer, equipped with a Mo micro-focusing source ($\lambda_{\text{K}\alpha} = 0.71073 \text{ \AA}$) and HyPix-3000 Hybrid Pixel Array detector. The temperature was controlled by a Cryostream 800 from Oxford Cryosystems Ltd. CrysAlisPro³¹ and JANA2006 software³² were used for the raw experimental data processing and structural refinements, respectively.

Structure solutions were obtained from the Superflip program.³³ DIAMOND from Crystal Impact was used to represent the crystal structures.³⁴

Results and discussion

Details of the structure solution for $\text{Fe}[\text{SeO}_4]\text{OH}$

The XRD experimental data are shown in Fig. 1. The b unit cell parameter can be unambiguously determined with $b = 7.26 \text{ \AA}$ (Fig. 1c). However, the pseudo-hexagonal symmetry of both the $h0l$ (Fig. 1a) and $h2l$ (Fig. 1b) cross sections is ambiguous. It can be interpreted in two different ways. First, an orthorhombic unit cell with parameters $a_{\text{ort}} = 7.57 \text{ \AA}$ and $c_{\text{ort}} = a_{\text{ort}}\sqrt{3} = 13.11 \text{ \AA}$ can be chosen. The obtained systematic extinction of the reflections ($hkl: h + l = 2n$) indicates an orthorhombic B -centered lattice. Second, to index the pseudo-

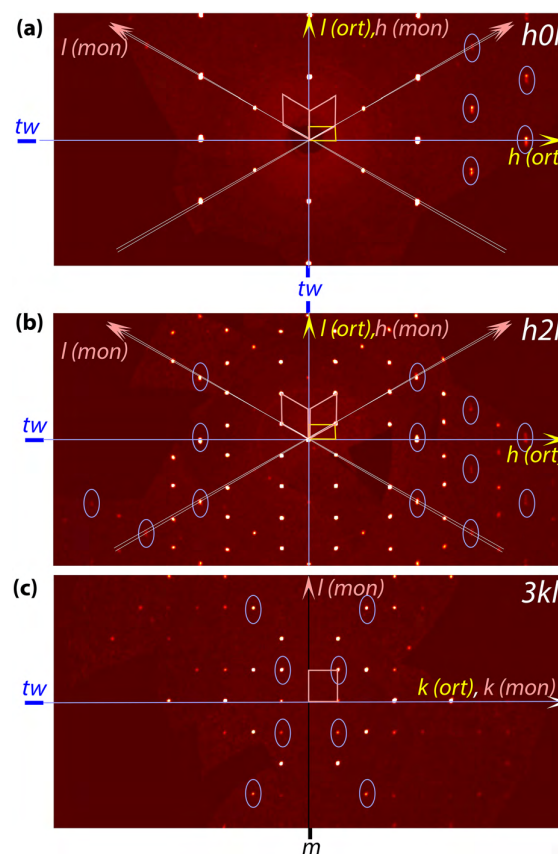


Fig. 1 Representative cross sections (a) $h0l$, (b) $h2l$ and (c) $3kl$ of the reciprocal space reconstruction for the $\text{Fe}[\text{SeO}_4]\text{OH}$ crystal. The axes $h_{\text{ort}}, k_{\text{ort}}$ and l_{ort} (yellow colour) correspond to the orthorhombic unit cell with the parameters $a_{\text{ort}} = 7.57 \text{ \AA}$, $b = 7.26 \text{ \AA}$ and $a_{\text{ort}} = a_{\text{ort}}\sqrt{3} = 13.11 \text{ \AA}$. The axes $h_{\text{mon}}, k_{\text{mon}}$ and l_{mon} (pink colour) correspond to the monoclinic unit cell with the parameters $a_{\text{mon}} = 7.57 \text{ \AA}$, $b_{\text{mon}} = 7.26 \text{ \AA}$ and $c_{\text{mon}} = 7.58 \text{ \AA}$ and angle $\beta = 120.05(3)^\circ$. The reflections with blue ellipsoids indicate twinning by the m -planes (tw) either by splitting or by difference in their intensity. The mirror symmetry of the m -plane (m) normal to the k -direction is well defined. The reciprocal unit cell is marked in pink and yellow for the monoclinic and orthorhombic unit cells, respectively.

hexagonal planes $h0l$ and $h2l$, one can use either a monoclinic cell with $\beta = 120.05(3)^\circ$ refined according to the set of experimental data, or an orthorhombic cell. The relation between two bases normal to the common b -direction is shown in Fig. 1a and b. A careful inspection of the reciprocal cross sections reveals splitting of the reflections outlined by the blue ellipses. It looks like the monoclinic domains are linked by a twinning plane (tw), which should be a mirror plane in an orthorhombic structure. These observations indicate that our crystal rather corresponds to the $C2/c$ monoclinic cell, including twinning, *i.e.* it has a structure similar to the monoclinic $\text{Fe}[\text{SO}_4]\text{OH}$ (**1M** in Fig. 2a).

The twinned monoclinic and the untwinned orthorhombic models for $\text{Fe}[\text{SeO}_4]\text{OH}$ were refined in the space groups $C2/c$ and $Bm\bar{m}$, respectively. The results of the refinement are listed in Table 1. As discussed later, the orthorhombic structure is partially disordered (Fig. 2b). Comparing the experimental (Fig. 1b, right) and simulated (Fig. 2b, right) $h2l$ sections of the reciprocal space, some contribution of the orthorhombic partially disordered polytype can be assumed.

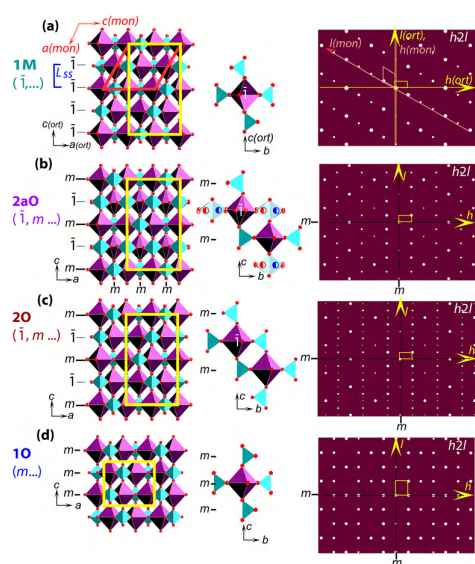


Fig. 2 Representative characteristics of the simplest possible polytypes for $\text{Fe}[\text{MO}_4]\text{OH}$ with $M = \text{S}$ and Se . The projection of the structure along the b -axis (left column), the surrounding of the FeO_6 octahedra by the MO_4 tetrahedra (centre column) and the $h2l$ simulated section of the reciprocal space (right column) are shown. Polytypes are distinguished by different alternation of local symmetry operations (inversion centre, $\bar{1}$, and mirror m -plane) along the c -axis. The half-filled circles indicate half-occupancy of the O and M atomic positions. The polytype identifiers: “O” and “M” denote orthorhombic and monoclinic symmetry, respectively; index “1” or “2” is related to the number of minimal translation along the c -axis; “a” indicates a partially disordered structure. The unit cell is shown in yellow and red colour for the monoclinic and the orthorhombic cells, respectively. (a) Polytype **1M** ($\bar{1}, \dots$) is characteristic of the monoclinic kieselite-like structure type. (b) Predicted partially disordered polytype **2aO** ($\bar{1}, m, \dots$). (c) Predicted fully ordered polytype **2O** ($\bar{1}, m, \dots$). (d) Fully ordered polytype **1O** (m, \dots) characteristic of the orthorhombic paufferite structure type.

Experimental details corresponding to the preferred model of $\text{Fe}[\text{SeO}_4]\text{OH}$ as a monoclinic and twinned structure are available as a CIF file under CSD number 2216126.

Generation of polytypes using the superspace approach

General remarks and description of the methodology. As mentioned in the introduction, the monoclinic (kieselite-like) and orthorhombic (paufferite-like) structures are polytypes and, consequently, formed by an identical layer. Using the OD approach, the L_{OD} layer (Fig. 3) was chosen to describe both polytypes.^{14,17} Here, we propose a different choice of the layer, L_{SS} in Fig. 3. In both cases, adjacent layers are interconnected by one of two translation vectors, $t_{1,2} = \pm a/4 + b/2 + c/2$, indicated in Fig. 3. Despite the fact that these vectors are the same, it turns out that two adjacent L_{SS} -layers are interconnected along the c -axis either by a mirror m -plane (Fig. 3a), as in the paufferite-like orthorhombic polytype (**1O** in Fig. 2d), or by the inversion centre $\bar{1}$ (Fig. 3b), as in the monoclinic kieselite-like polytype (**1M** in Fig. 2a). It can be assumed that different alternating sequences of m and $\bar{1}$ along the c -axis can be chosen to predict additional structures that form a family of polytypes. We apply here the superspace approach,¹⁹ and generate the $\text{R}[\text{MO}_4]\text{Z}$ polytype family. Previously, the same method was successfully applied to characterize the $\text{K}_5\text{-Yb}(\text{MoO}_4)_4$ polytypes and the family of scheelite-like compounds.^{35,36} In this method, 3-dimensional (3D) structures are deduced from a single $(3 + 1)$ -dimensional, $(3 + 1)\text{D}$, structure using rational values of the q -vector, an attribute of the corresponding superspace group (SSG).

The theoretical basis of the method was published by I. Orlov *et al.*³⁷ The corresponding database used here is available from the Superspace Group Finder in the International Tables of Crystallography Online.³⁸

Average structure and disordered (1aO)-polytype. The first step of the method is to establish the average structure, from which it is possible to derive or predict kieselite-like (**1M** in Fig. 2a) and paufferite-like (**1O** in Fig. 2d) structures and other polytypes using the superspace approach with the $(3 + 1)\text{D}$ SSG. To this end, the atomic positions of the orthorhombic $\text{Fe}[\text{SO}_4]\text{OH}$ paufferite-like structure¹⁵ are modified. While keeping the space group $Pnam$ and lattice parameters, a splitting of $M = \text{S}$, O_2 and O_3 atoms is applied (Table 2). The site occupancy of the separated atoms, defined as $0 \leq \tau \leq 1$, is complementary. The absence of these atoms ($\tau = 0$ or 1) corresponds to the **1O** polytype (paufferite-like structure). The separated atoms with half occupancy ($\tau = 1/2$) reproduce the completely disordered polytype **1aO**, which contains both the m and $\bar{1}$ local symmetry operations connecting the L_{SS} -layers along the c axis (Fig. 4, left).

Any $0 < \tau < 1$ indicates the presence of two alternative tetrahedra, $[\text{MO}_4]$ and $[\text{M}(\text{a})\text{O}_4]$, with occupancy τ and $(1 - \tau)$, respectively. Both $[\text{MO}_4]$ and $[\text{M}(\text{a})\text{O}_4]$ type tetrahedra form the $[\text{FeO}_6]$ octahedron in two corresponding alternative orientations rotated around the c axis (Fig. 4, right).

Table 1 Experimental details for Fe[SeO₄]OH structure determination and refinement

	Unit cell without twinning (2aO polytype)	Unit cell assuming crystal twinning (1M polytype)
Chemical formula	Fe[SeO ₄]OH	Fe[SeO ₄]OH
Space group	<i>Bmcm</i> (no. 67)	<i>C12/c1</i> (no. 15)
<i>a</i> , <i>b</i> , <i>c</i> , (Å); β (°)	7.589(2), 7.259(4), 13.124(2)	7.577(3), 7.2594(4), 7.589(4); 120.05(3)
Twin matrix, mass fraction	—	(100/010/001), 0.479(3); (-100/0-10/-101), 0.521(3)
<i>R</i> _{int}	0.057	0.047
<i>R</i> [<i>F</i> ² > 2σ(<i>F</i> ²)], <i>wR</i> [<i>F</i> ²]; <i>S</i>	0.0533, 0.1194; 2.06	0.0428, 0.0879; 1.59
No. of reflections	427	524
No. of parameters	53	37
ρ _{max} , ρ _{min} (e Å ⁻³)	2.40, -6.25	1.23, -1.22

Modulated structures. Using atomic sites of the average structure in the *Pnam*(00γ)000 (3 + 1)D SSG (No. 62.1.9.3³⁹) with the modulation vector $\mathbf{q} = \gamma\mathbf{c}^*$ ($\gamma \leq 1$), the occupancies of the atomic positions are considered as the magnitude of τ for [MO₄] and of (1 - τ) for [M(a)O₄] tetrahedral domains elongated in the fourth, *x*₄, axis, with a period equal to the complete filling of the tetrahedra position. In other words, *x*₄ is the axis onto which the occupancy modulation is projected. Using the JANA2006 software,³² the crenel-

function⁴⁰ was applied to establish the occupancy modulation of the atomic positions. The relevant input files used are available in the ESI† (Fig. S1).

In the modulation vector $\mathbf{q} = \gamma\mathbf{c}^*$, any irrational value of γ corresponds to a (3 + 1)D periodic (incommensurately modulated) structure along the *c*-direction. In this case, the local symmetry operations *m* and $\bar{1}$ are not periodically alternating along the *c* axis. Any rational value of $\gamma = n/m$ determines 3D structure models with a supercell characterized by an *m*-fold increase in the *c*-parameter compared to the average structure. Specific sections *t*₀ along the *x*₄ axis define the structure models and their symmetry for a certain rational γ . Fig. 5 illustrates this for $\gamma = 1/2$. This figure shows: (i) the (*x*₃*x*₄) section of a (3 + 1)D-crystal, the unit cell of which is indicated by black lines; (ii) M (red) and M(a) (blue) domains stretched along the *x*₄ axis; (iii) different *t*₀-sections of the (3 + 1)D-space, perpendicular to *x*₄, defining 3D structures with different periodic sequences of [MO₄] and [M(a)O₄] tetrahedra along the *c*-axis.

To summarize, the rational parameters γ , τ and *t*₀ are variables to derive 3D structures using the *Pnam*(00γ)000 superspace group (see Fig. S1† for details).

Paufferite-like (1O) and kieserite-like (1M) polytypes. As can be seen in the previous paragraphs, the paufferite-like structure, polytype 1O (Fig. 2d), is reproduced with $\tau = 0$ or 1 from the average structure or from the superspace model with $\gamma = 1$. Details are given in Table 3, row 1O.

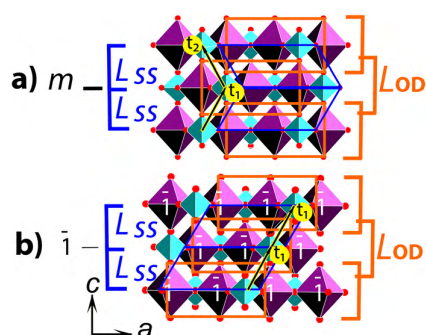


Fig. 3 Choice of a layer to represent (a) paufferite-like and (b) kieserite-like structures as polytypes. *L*_{OD} has been chosen for such representation using the OD approach,^{14,17} and *L*_{SS} for the representation using the superspace approach in the present work. The blue and orange quadrilaterals denote the translational building blocks in the *L*_{SS} and *L*_{OD} layers, respectively. Along the *c*-direction, these blocks are interconnected by one of two vectors, $\mathbf{t}_1 = +\mathbf{a}/4 + \mathbf{b}/2 + \mathbf{c}/2$ and $\mathbf{t}_2 = -\mathbf{a}/4 + \mathbf{b}/2 + \mathbf{c}/2$, which are the same despite the different layer selection.

Table 2 Atomic parameters in the average structure Fe[MO₄]OH (M = S, Se). The space group is *Pnam*; the unit cell parameters: *a* ≈ 7.6 Å, *b* ≈ 7.2 Å, and *c* ≈ 6.6 Å. Atoms M, O1, O2, and O3 and atoms M(a), O1, O2(a), and O3(a) define two alternative tetrahedra, [MO₄] and [M(a)O₄], respectively

Atom	Wyckoff site symmetry	Occupancy	<i>x</i>	<i>y</i>	<i>z</i>
Fe	4 <i>c</i>	1	0.127	-0.25	3/4
O1	8 <i>d</i>	1	0.125	-0.253	0.433
O2	4 <i>c</i>	τ	0.288	-0.017	1/4
O2(a)	4 <i>c</i>	1 - τ	0.288	0.517	1/4
O3	4 <i>c</i>	τ	-0.042	-0.018	1/4
O3(a)	4 <i>c</i>	1 - τ	-0.042	0.518	1/4
M	4 <i>c</i>	τ	0.124	-0.133	1/4
M(a)	4 <i>c</i>	1 - τ	0.124	0.633	1/4
OH	4 <i>c</i>	τ	-0.126	-0.341	3/4
OH(a)	4 <i>c</i>	1 - τ	-0.126	0.841	3/4

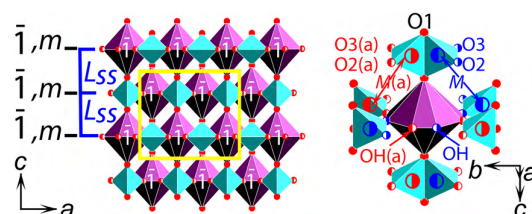


Fig. 4 Average structure of Fe[MO₄]OH with M = S and Se. The projection of the structure along the *b*-axis (left) and the environment of the Fe atom (right) are shown. Local symmetry operations, inversion centres, $\bar{1}$, and mirror *m*-planes interconnecting adjacent *L*_{SS} layers, are indicated. The unit cell is highlighted in yellow. The half-filled circles indicate half-occupancy of the O and M atoms, which is a characteristic of completely disordered polytype 1aO. The identification of the atoms corresponds to Table 2.

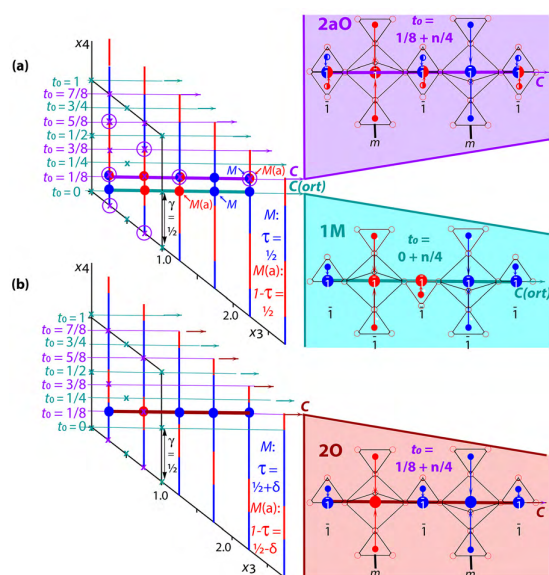


Fig. 5 Illustration of the generation of the simplest polytypes for $\text{Fe}[\text{MO}_4]\text{OH}$ ($M = \text{S}, \text{Se}$) using the superspace group $Pn\bar{a}m(00g)000$ with $\gamma = 1/2$. The (x_3x_4) projections (left) shown for the atomic domains M (vertical blue lines) and M(a) (vertical red lines): (a) the lengths of both M and M(a) domains are $\tau = 1/2$; (b) $\tau = 1/2 + \delta$ and $\tau = 1/2 - \delta$ for M and M(a), respectively. A unit cell is shown as black lines in the x_3x_4 section. Inversion centres (violet and green crosses) are indicated in the unit cell. These symmetry elements are intersected by two types (cyan and violet lines) of t_0 -sections perpendicular to x_4 . The intersection of each t_0 -section with the atomic domains M and M(a) or their superposition defines the projection of the corresponding atoms onto the structure c -axis. The cyan, violet and brown bold horizontal lines indicate the period of the projection, which characterize the **1M**, **2aO** and **2O** polytypes, respectively. The local symmetry operations $\bar{1}$ and m are indicated in the structure fragment (right). The vertical arrows are shown in the fragment to explain the formation of the atomic projections on the structural c -axis for polytypes **1M**, **2O**, and **2aO**.

The kieserite-like structure, polytype **1M** (Fig. 2a), is deduced following the methodology with $\gamma = 1/2$, $\tau = 1/2$ and sections $t_0 = 0 + n/4$ with n being an integer. In Fig. 5a, each of these t_0 -sections (green lines) intersects the M (red) and M(a) (blue) domains, defining a periodic sequence of the corresponding tetrahedra as $2[\text{MO}_4]-2[\text{M(a)O}_4]$ along the c -axis. The derived 3D supercell model is described in the monoclinic space group $P2_1/a$ with $\beta \approx 90^\circ$. The reciprocal space reconstructions made for this model (Fig. 2a, right) indicate the reflection condition $hkl: h + l = 2n$.

This condition forces the reduction of this B -centered monoclinic unit cell by the matrix $(1/2 \ 0 \ 1/2)/(0 \ 1 \ 0)/(-1 \ 0 \ 0)$ to the standard (optimized) monoclinic unit cell with β close to 120° (Fig. 2a, left). The cell volume is reduced by 2. The simulated reciprocal space reconstruction after the reduction indicates the reflection condition $hkl: h + k = 2n$ (Fig. 2a, right), which points to C centering of the monoclinic cell and, consequently, to the $C2/c$ space group, as expected for kieserite-like structures. The results are summarized in row **1M** in Table 3. The close agreement between the derived

(after optimization) and experimental atomic coordinates for $\text{Fe}[\text{SeO}_4]\text{OH}$ (Table 4) confirms the capacity of the applied method and validates the selected $(3 + 1)\text{D}$ structure to predict 3D polytypes.

Prediction of new polytypes. As previously mentioned, 3D structures can be obtained using the superspace group $Pn\bar{a}m(00\gamma)000$ when γ is rational. Consequently, the number of predicted 3D structures is unlimited. We restricted the search for the simplest structures with $\gamma = 1/2$, *i.e.* with the unit cell parameter $c = 2c_{\text{avr}}$ (Table 3). In addition to **1O** (paufferite-like), **1M** (kieserite-like) and **1aO** (completely disordered) polytypes, two other polytypes can be predicted with $\gamma = 1/2$ (Fig. 5).

First, $[\text{MO}_4]$ and $[\text{M(a)O}_4]$ tetrahedra can be equivalently present in the structure. In this situation, corresponding to $\tau = 1/2$, additional inversion centers are induced between the domains M and M(a) at their points of contact (violet circles in Fig. 5a, left). The sections $t_0 = 1/8 + n/4$ (violet horizontal lines in Fig. 5a) containing these points define a structure, which contains statistically both the tetrahedra, each occupying half of the sites. Each of these t_0 -sections intersects the M (red), M(a) (blue) and mixed domains. The corresponding periodic sequence of the tetrahedra distribution is therefore: $[\text{MO}_4] - (1/2[\text{MO}_4] + 1/2[\text{M(a)O}_4]) - [\text{M(a)O}_4] - (1/2[\text{MO}_4] + 1/2[\text{M(a)O}_4])$ along the c -axis. Two links in this sequence consist of M- and M(a)-tetrahedra, represented with an equal probability of 50%. The corresponding space group of this partially disordered structure (**2aO** polytype) is $P2_1am$ (Table 3). The simulated reciprocal space reconstructions of this predicted model (Fig. 2b, right) reveal extra reflection conditions: $h + l = 2n$ for hkl ; $h = 2n$ and $l = 2n$ for $h0l$. These conditions lead to the space group $Bm\bar{m}$ (row **2aO** in Table 3). The resulting **2aO** model corresponds to the partially disordered polytype as seen in Fig. 2b, left. This model is considered as a possible untwinned orthorhombic structure for $\text{Fe}[\text{SeO}_4]\text{OH}$ (Table 1, left). The predicted and experimental atomic coordinates are in close agreement as can be seen in Table 5.

Second, $[\text{MO}_4]$ and $[\text{M(a)O}_4]$ tetrahedra can be inequivalently present, *i.e.* $\tau = 1/2 + \delta$ (Fig. 5b). In this case, section $t_0 = 1/8 + n/4$ does not contain inversion centres between the M and M(a) domains. Each of these t_0 -sections (brown horizontal lines in Fig. 5b) intersects the domains M (red) and M(a) (blue) defining a periodic sequence of the corresponding tetrahedra as $[\text{MO}_4]-3[\text{M(a)O}_4]$ along the c -axis. The corresponding **2O** polytype (Fig. 2c) is predicted in the space group $P2_1am$. Since no additional reflection conditions are observed (Fig. 2c, left), there is no need for additional lattice transformations (row **2O** in Table 3). The corresponding approximate atomic parameters of the predicted **2O** polytype are listed in Table 6. In this polytype, local symmetry operations alternate as $(\bar{1}, m, \bar{1}, m, \dots)$ along the c -axis (Fig. 2c).

Powder X-ray diffraction patterns. The powder X-ray diffraction (XRD) patterns were calculated for both the disordered and ordered polytypes of $\text{Fe}[\text{SeO}_4]\text{OH}$.

Table 3 Predictions of the simplest polytypes for $\text{Fe}[\text{MO}_4]\text{OH}$ ($M = \text{S}, \text{Se}$) using the superspace group $Pn\bar{m}(00\gamma)000$, the vector $\mathbf{q} = 1/2\mathbf{c}^*$ and the average structure parameters

Polytype	Variables		Derived supercell model		Matrix for the transformation	Optimized supercell model		Known similar structure types
	t_0	τ	SG; unit cell parameters	Extra reflection conditions		Extra reflection conditions	SG; unit cell parameters	
10	0	0 (or 1)	$Pn\bar{m}$; $a = a_{\text{avr}}$ $b = b_{\text{avr}}$ $c = c_{\text{avr}}$	None	$(1\ 0\ 0/0\ 1\ 0/0\ 0\ 1)$	None	$Pn\bar{a}m$; $a = a_{\text{avr}}$ $b = b_{\text{avr}}$ $c = c_{\text{avr}}$	$\beta\text{-V}[\text{SO}_4]\text{O}$, ¹⁶ $\text{Y}[\text{SO}_4]\text{F}$, ²⁵ $\text{V}[\text{HPO}_4]\text{O}$ (ref. 30)
1M ($\bar{1}, \dots$)	0	1/2	$P2_1/a$; $a = a_{\text{avr}}$ $b = b_{\text{avr}}$ $c = 2c_{\text{avr}}$ $\beta = 90^\circ$	hkl : $h + l = 2n$	$((1/2\ 0\ 1/2)/0\ 1\ 0/-1\ 0\ 0)$	hkl : $h + k = 2n$	$C2/c$; $a \approx c_{\text{avr}}\sqrt{3}$, $b = b_{\text{avr}}$ $c = a_{\text{avr}}$ $\beta \approx 120^\circ$	$\text{Mg}[\text{SO}_4]\text{H}_2\text{O}$, ⁹⁻¹³ $\text{Al}[\text{SO}_4]\text{OH}$, ²⁰ $\text{Fe}[\text{SO}_4]\text{F}$, ^{21,22} $\text{Sb}[\text{PO}_4]\text{O}$ (ref. 23) $\text{Ca}[\text{CrF}_4]\text{F}$ (ref. 24)
20 ($\bar{1}, m \dots$)	1/8	$1/2 + \delta$	$P2_1am$; $a = a_{\text{avr}}$ $b = b_{\text{avr}}$ $c = 2c_{\text{avr}}$	None	$(1\ 0\ 0/0\ 1\ 0/0\ 0\ 1)$	None	$P2_1am$; $a = a_{\text{avr}}$ $b = b_{\text{avr}}$ $c = 2c_{\text{avr}}$	None
2a0 ($\bar{1}, m \dots$)	1/8	1/2	$P2_1am$; $a = a_{\text{avr}}$ $b = b_{\text{avr}}$ $c = 2c_{\text{avr}}$	hkl : $h + l = 2n$ $h0l$: $h = 2n$, $l = 2n$	$(1\ 0\ 0/0\ 1\ 0/0\ 0\ 1)$	hkl : $h + l = 2n$ $h0l$: $h = 2n$, $l = 2n$	Bnm ; $a = a_{\text{avr}}$ $b = b_{\text{avr}}$ $c = 2c_{\text{avr}}$	$\text{Ge}[\text{PO}_4]\text{OH}$ (ref. 41)

Table 4 Atomic coordinates for Fe[SeO₄]OH in the space group *C2/c*. Experimental values corresponding to the structure refinement (Table 1, right column) are given with standard deviations; values derived from the superspace model for the **1M** polytype are in italics

Atom; occupancy	Wyckoff site symmetry	x	y	z
Fe; 1	4a	0	0	0
Se; 1	4e	0	0.61253(9)	1/4
			<i>0.616</i>	
O1; 1	4e	0	-0.0893(7)	3/4
			<i>-0.095</i>	
O2; 1	8f	-0.0147(7)	0.7362(6)	0.0653(8)
		<i>0.0</i>	<i>0.733</i>	<i>0.0840</i>
O3; 1	8f	0.6944(6)	0.0257(5)	0.8385(17)
		<i>0.683</i>	<i>0.0</i>	<i>0.8415</i>

The patterns of the **1M** and **2aO** polytypes simulated from the experimental single crystal X-ray data (Tables 1, 4 and 5) are very similar (Fig. 6), confirming these two structures being indistinguishable by powder XRD. On the other hand, the newly predicted **2O** polytype can be distinguished from the paufferite-like structure, **1O**, as well as from the disordered average structure **1aO** as shown in Fig. 6.

Extended R[MO₄]Z polytype family and its aristotype. The described method to derive/predict possible polytypes for Fe[MO₄]OH (M = S, Se) can be extended to additional compounds. There are several 3D structure types that belong either to the space group *Pnam* (equal to *Pnma*) or to the space group *C2/c* and can be considered as formed by an *L_{ss}*-layer. Fig. 7 and, in more detail, Fig. S2† illustrates these structure types. Thus, the **1M** polytype can be considered as a characteristic of many compounds belonging to kieserites,^{9–13} and to Al[SO₄]OH,²⁰ Fe[SO₄]F,^{21,22} Sb[PO₄]O (ref. 23) and CaCrF₅ (ref. 24) structure types (Table 3, row **1M**; Table S1†). The fully ordered polytype **1O** (*m*, ...) is characteristic of the

Table 5 Atomic coordinates for Fe[SeO₄]OH in space group *Bmcm*. Experimental values corresponding to the structure refinement (Table 1, left column) are given with standard deviations; values derived from the superspace model for the **2aO** polytype are in italics

Atom; occupancy	Wyckoff site symmetry	x	y	z
Fe1; 1	4c	0	0	0
Fe2; 1	4f	1/4	1/2	3/4
Se1; 1	4g	1/4	0.38890(14)	0
			<i>0.384</i>	
Se2; 0.5	8l	0	0.1119(3)	3/4
			<i>0.116</i>	
O1; 1	4g	1/4	0.0878(9)	1/2
			<i>0.095</i>	
O2; 0.5	8l	0	0.5886(16)	1/4
			<i>0.595</i>	
O3; 1	8h	0	0	0.8485(5)
			<i>0.8415</i>	
O4; 0.5	16o	0.1772(12)	0.2372(11)	0.7584(6)
		<i>0.166</i>	<i>0.233</i>	<i>0.750</i>
O5; 1	8m	0.0715(7)	0.2633(7)	0
		<i>0.084</i>	<i>0.233</i>	
O6; 1	8n	1/4	0.5303(8)	-0.0965(4)
			<i>0.50</i>	<i>-0.0915</i>

Table 6 Atomic coordinates for the predicted, **2O**, polytype of Fe[MO₄]OH (M = S, Se) in the space group *P2₁am*. The unit cell parameters: *a* ≈ 7.6 Å, *b* ≈ 7.2 Å, *c* ≈ 2 × 6.6 = 13.2 Å

Atom; occupancy	Wyckoff site symmetry	x	y	z
Fe1; 1	2b	0.00	0.00	1/2
Fe2; 1	2a	0.00	0.00	0
Fe3; 1	4c	0.750	0.50	0.750
Se1; 1	4c	0.00	0.116	0.250
Se2; 1	2a	0.750	0.384	0
Se3; 1	2b	0.750	0.616	1/2
O11; 1	4c	0.00	0.00	0.3415
O12; 1	4c	0.000	0.000	0.8415
O13; 1	4c	0.750	0.500	0.5915
O14; 1	4c	0.750	0.500	0.0915
O21; 1	4c	0.166	0.233	0.250
O22; 1	2a	0.584	0.267	0
O23; 1	2b	0.584	0.733	1/2
O31; 1	4c	0.834	0.233	0.250
O32; 1	2a	-0.084	0.267	0
O33; 1	2b	-0.084	0.733	1/2
O41; 1	4c	0.00	0.595	0.750
O42; 1	2a	0.750	0.905	0
O43; 1	2b	0.750	0.095	1/2

orthorhombic structure not only of Fe[MO₄]OH but also of β-V[SO₄]O,¹⁶ Y[SO₄]F,²⁵ V[HPO₄]O,³⁰ Cd[SO₄]F,²⁶ Np[PO₄]F,²⁷ Ce[AsO₄]F,²⁸ and U[PO₄]F,²⁹ which belong to three structure types (Table 3, row **1O**; Table S2†). The predicted partially ordered **2aO** polytype was reported for Ge[PO₄]OH.⁴¹ These facts suggest that the (3 + 1)D structure type can be used as an aristotype encompassing the previously mentioned 3D structure types having the general formula R[MO₄]Z, with R = Mg, Fe, Ni, Co, Zn, Mn, Cd, Al, V, Sb, Y, Ge, Ce, U, and Np; M = S, Se, P, and As; Z = OH, H₂O, F, and O. This aristotype is characterised by: (i) the (3 + 1)D superspace group *Pnam*(00γ)000; (ii) the average unit cell with *a* ≈ 7.5 ± 0.3 Å, *b* ≈ 7.2 ± 0.2 Å, and *c* = 0.5*a*√3 ≈ 6.5 ± 0.3 Å; (iii) a set of atomic sites (Table 2) and (iv) specific characteristics of the atomic parameters for each site in the *Pnam*(00γ)000 (3 + 1)D superspace group. Rational values of γ in the modulation vector **q** = γ*c*^{*}, specific sections *x*₄ = *t*₀, and the occupancy parameter *τ* are variables for reproducing known structures and for predicting possible polytypes. Practical details for the structure prediction/derivation are presented in Fig. S1†

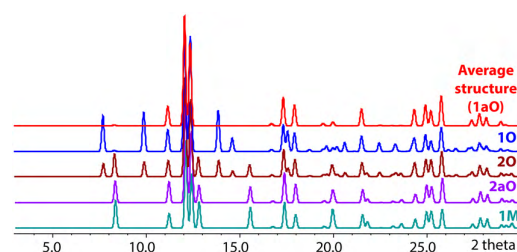


Fig. 6 Powder XRD patterns of the simplest Fe[MO₄]OH (M = S, Se) polytypes. Experimental data were used for **1M** and **2aO**. For others, data predicted from the superspace approach were used. The patterns are calculated for Mo Kα radiation.

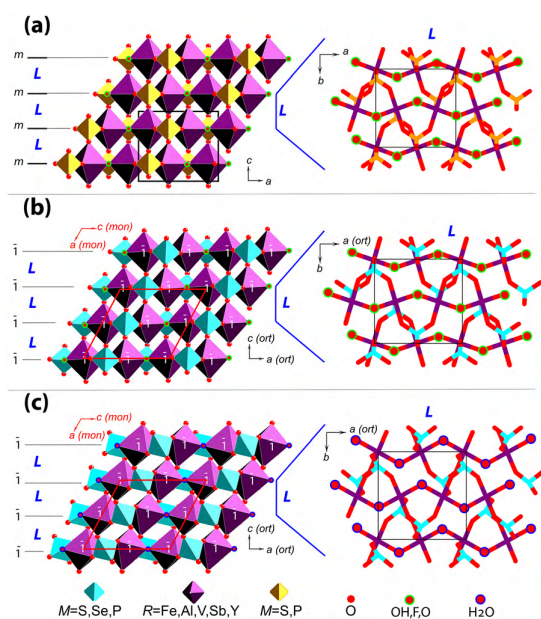


Fig. 7 Sketches of structures formed by L_{ss} -layers, similar to $\text{Fe}[\text{MO}_4]\text{OH}$ ($M = \text{S}, \text{Se}$). Panel (a): $\beta\text{-V}(\text{SO}_4)\text{O}$, $\text{Y}(\text{SO}_4)\text{F}$ and $\text{V}(\text{HPO}_4)\text{O}$ structure types with space group $Pnam$ can be attributed to the 1O (m, \dots) polytype. Panel (b): Structure types $\text{Fe}(\text{SO}_4)\text{F}$, CaCrF_5 ($=\text{Ca}(\text{CrF}_4)\text{F}$), and $\text{Al}[\text{SO}_4]\text{OH}$ with space group $C2/c$ can be identified with the 1M (i, \dots) polytype. Panel (c): The kieserite structure type with the general formula $\text{R}[\text{MO}_4]\text{H}_2\text{O}$ ($\text{R} = \text{Mg}, \text{Fe}, \text{Ni}, \text{Co}, \text{Mn}, \text{Zn}$; $M = \text{S}, \text{Se}$) can also be assigned to the 1M polytype, since H_2O molecules deform the structure, but do not change the space group and atomic sites of this polytype.

Conclusions

We report on the growth and detailed investigation of the crystal structure of the new kieserite-like compound $\text{Fe}[\text{SeO}_4]\text{OH}$. Using the superspace approach, we show that both paufferite-like and kieserite-like structures, as well as other ordered, partially disordered, completely disordered and aperiodic structures, form a family of polytypes. All members of this family can be derived from one single $(3 + 1)\text{D}$ -structure. We consider this structure as an aristotype.

Author contributions

B. T. and A. M. initiated the study. A. A. performed the crystal structural investigations and prepared the early version of the manuscript. W. H. B. performed the XRD experiments. B. T., N. M. and A. M. prepared the crystals. All the authors read, commented and revised the manuscript.

Conflicts of interest

The authors declare no conflict of interest.

Acknowledgements

The funding of this research was provided by the Swiss National Science Foundation (SNSF) Sinergia network NanoSkymionics (Grant No. CRSII5-171003).

Notes and references

- C. A. Fleming, *Miner. Metall. Process.*, 2010, **27**(2), 81.
- M. A. Reddy, V. Pralong, V. Caignaert, U. V. Varadaraju and B. J. Raveau, *Electrochem. Commun.*, 2009, **11**, 1807.
- G. Ventruti, G. Della-Ventura, M. A. Gomez, G. Capitani, M. Sbroscia and A. Sodo, *Phys. Chem. Miner.*, 2020, **47**, 42.
- T. C. Cheng and G. P. Demopoulos, *Ind. Eng. Chem. Res.*, 2004, **43**, 6299.
- J. Xu, N. Gao, Y. Tang, Y. Deng and M. Sui, *J. Environ. Sci.*, 2010, **22**, 1807.
- M. J. Gazquez, M. Contreras, S. M. Perez-Moreno, J. L. Guerrero, M. Casas-Ruiz and J. P. Bolivar, *Minerals*, 2021, **11**, 575.
- C. B. Godsey, J. P. Schmidt, A. J. Schlegel, R. K. Taylor, C. R. Thompson and R. J. Gehl, *Agron. J.*, 2003, **95**, 160.
- M. Wildner and G. Giester, *Neues Jahrb. Mineral., Monatsh.*, 1991, **7**, 296.
- J. Leonardt and R. Weiss, *Naturwissenschaften*, 1957, **44**, 338.
- J. Brégeault, P. Herpin, J. Manoli and G. Pannetier, *Bull. Soc. Chim. Fr.*, 1970, **12**, 4243.
- S. Aleksovska, V. M. Petrusovski and B. Soptrajanov, *Acta Crystallogr., Sect. B: Struct. Sci.*, 1998, **54**, 564.
- L. D. Iskhakova and N. P. Kozlova, *Kristallografiya*, 1995, **40**, 635.
- M. Wildner, B. A. Zakharov, N. E. Bogdanov, D. Talla, E. V. Boldyreva and R. Miletich, *IUCrJ*, 2022, **9**, 194.
- G. Ventruti, G. D. Ventura, M. A. Gomez, G. Capitani, M. Sbroscia and A. Sodo, *Phys. Chem. Miner.*, 2020, **47**, 43.
- G. Johansson, *Acta Chem. Scand.*, 1962, **16**, 1234.
- S. V. Krivovichev, L. P. Vergasova, S. N. Britvin, S. K. Filatov, V. Kahlenberg and V. V. Ananiev, *Can. Mineral.*, 2007, **45**, 921.
- G. Ventruti, F. Scordari, E. Schingaro, A. F. Gualtieri and C. Meneghini, *Am. Mineral.*, 2005, **90**(4), 679.
- K. Dornberger-Schiff and K. Fichtner, *Krist. Tech.*, 1972, **7**, 1035.
- T. Janssen, G. Chapuis and M. de Boissieu, *Aperiodic Crystals: From Modulated Phases to Quasicrystals*, Oxford University Press, 2007.
- A. J. Anderson, H. Yang and R. T. Downs, *Am. Mineral.*, 2015, **100**, 330.
- B. C. Melot, G. Rouse, J. N. Chotard, M. Ati, J. Rodriguez Carvajal, M. C. Kemei and J. M. Tarascon, *Chem. Mater.*, 2011, **23**, 2922.
- B. L. Ellis, T. N. Ramesh, L. J. M. Davis, G. R. Goward and L. F. Nazar, *Chem. Mater.*, 2011, **23**, 5138.
- Y. Piffard, S. Oyetola, A. Verbaere and M. Tournoux, *J. Solid State Chem.*, 1986, **63**, 81.
- K. K. Wu and I. D. Brown, *Mater. Res. Bull.*, 1973, **5**, 593.
- X. Wang, L. Liu, K. Ross and A. J. Jacobson, *Solid State Sci.*, 2000, **2**, 109.
- M. S. Wickleder, *Z. Anorg. Allg. Chem.*, 1999, **625**, 725.
- T. H. Bray, T. A. Sullens, T. Y. Shvareva, R. E. Sykora, R. G. Haire and T. E. A. Schmitt, *J. Solid State Chem.*, 2007, **180**(1), 70.
- J. Rouse and M. T. Weller, *Dalton Trans.*, 2009, 10330.
- J. B. Felder, S. Calder and H.-C. Zur Loye, *Inorg. Chem.*, 2018, **57**(15), 9286.
- L. Wilde, J. Trommer, U. Steinike, H. Worzala and G. U. Wolf, *Mater. Sci. Forum*, 1998, **278**, 704.

- 31 Oxford Diffraction, CrysAlisPRO. Agilent Technologies, Version 1.171.37.35 (release 13-08-2014 CrysAlis171.NET) (compiled Aug 13 2014,18:06:01), 2014.
- 32 V. Petříček, M. Dusek and L. Palatinus, *Z. Kristallogr.*, 2014, **229**, 345.
- 33 L. Palatinus and G. Chapuis, *J. Appl. Crystallogr.*, 2007, **40**, 786.
- 34 Diamond – Crystal and Molecular Structure Visualization, Crystal Impact – Dr. H. Putz and Dr. K. Brandenburg GbR, Kreuzherrenstr. 102, 53227 Bonn, Germany, (See: <https://www.crystalimpact.com/diamond/references.htm>).
- 35 A. Arakcheeva and G. Chapuis, *Acta Crystallogr., Sect. B: Struct. Sci.*, 2008, **64**, 12.
- 36 A. Arakcheeva and G. Chapuis, *Acta Crystallogr., Sect. B: Struct. Sci.*, 2006, **62**, 52.
- 37 I. Orlov, L. Palatinus and G. Chapuis, *J. Appl. Crystallogr.*, 2008, **41**, 1182.
- 38 Superspace Group Finder – International Table of Crystallography Online, See: <https://it.iucr.org/resources/finder/>.
- 39 T. H. Stokes, B. J. Campbell and S. van Smaalen, *Acta Crystallogr., Sect. A: Found. Crystallogr.*, 2011, **67**, 45.
- 40 V. Petříček, V. Eigner, M. Dusek and A. Cejchan, *Z. Kristallogr.*, 2016, **231**(5), 301.
- 41 V. H. Mayer and H. Völlenkle, *Z. Kristallogr., Kristallgeom., Kristallphys., Kristallchem.*, 1972, **136**, 387.

Bibliography

- [1] D. N. Basov, R. D. Averitt, and D. Hsieh. Towards properties on demand in quantum materials. *Nature Materials*, 16(11):1077–1088, 2017.
- [2] B. Keimer and J. E. Moore. The physics of quantum materials. *Nature Physics*, 13(11):1045–1055, nov 2017.
- [3] Jacqueline Bloch, Andrea Cavalleri, Victor Galitski, Mohammad Hafezi, and Angel Rubio. Strongly correlated electron–photon systems. *Nature*, 606(7912):41–48, jun 2022.
- [4] G. Grüner. The dynamics of charge-density waves. *Reviews of Modern Physics*, 60(4):1129–1181, oct 1988.
- [5] Xuetao Zhu, Yanwei Cao, Jiandi Zhang, E. W. Plummer, and Jiandong Guo. Classification of charge density waves based on their nature. *Proceedings of the National Academy of Sciences*, 112(8):2367–2371, feb 2015.
- [6] Anshul Kogar, Alfred Zong, Pavel E. Dolgirev, Xiaozhe Shen, Joshua Straquadine, Ya-Qing Bie, Xirui Wang, Timm Rohwer, I-Cheng Tung, Yafang Yang, Renkai Li, Jie Yang, Stephen Weathersby, Suji Park, Michael E. Kozina, Edbert J. Sie, Haidan Wen, Pablo Jarillo-Herrero, Ian R. Fisher, Xijie Wang, and Nuh Gedik. Light-induced charge density wave in LaTe_3 . *Nature Physics*, 16(2):159–163, 2020.
- [7] Hailan Luo, Qiang Gao, Hongxiong Liu, Yuhao Gu, Dingsong Wu, Changjiang Yi, Junjie Jia, Shilong Wu, Xiangyu Luo, Yu Xu, Lin Zhao, Qingyan Wang, Hanqing Mao, Guodong Liu, Zhihai Zhu, Youguo Shi, Kun Jiang, Jiangping Hu, Zuyan Xu, and X. J. Zhou. Electronic nature of charge density wave and electron-phonon coupling in kagome superconductor KV_3Sb_5 . *Nature Communications*, 13(1):273, jan 2022.
- [8] J. Bardeen, L. N. Cooper, and J. R. Schrieffer. Theory of Superconductivity. *Physical Review*, 108(5):1175–1204, dec 1957.
- [9] Masayuki Suda, Reizo Kato, and Hiroshi M. Yamamoto. Light-induced superconductivity using a photoactive electric double layer. *Science*, 347(6223):743–746, feb 2015.
- [10] M. Mitrano, A. Cantaluppi, D. Nicoletti, S. Kaiser, A. Perucchi, S. Lupi, P. Di Pietro, D. Pontiroli, M. Riccò, S. R. Clark, D. Jaksch, and A. Cavalleri. Possible light-induced superconductivity in K_3C_{60} at high temperature. *Nature*, 530(7591):461–464, 2016.
- [11] Masatoshi Sato and Yoichi Ando. Topological superconductors: a review. *Reports on Progress in Physics*, 80(7):076501, jul 2017.
- [12] Cyril Proust and Louis Taillefer. The Remarkable Underlying Ground States of Cuprate Superconductors. *Annual Review of Condensed Matter Physics*, 10(1):409–429, mar 2019.

Bibliography

- [13] Albert Fert, Nicolas Reyren, and Vincent Cros. Magnetic skyrmions: advances in physics and potential applications. *Nature Reviews Materials*, 2(7):17031, jun 2017.
- [14] Yoshinori Tokura and Naoya Kanazawa. Magnetic Skyrmion Materials. *Chemical Reviews*, 121(5):2857–2897, mar 2021.
- [15] H. M. Rønnow, R. Parthasarathy, J. Jensen, G. Aeppli, T. F. Rosenbaum, and D. F. McMorrow. Quantum Phase Transition of a Magnet in a Spin Bath. *Science*, 308(5720):389–392, apr 2005.
- [16] Subir Sachdev. Quantum magnetism and criticality. *Nature Physics*, 4(3):173–185, mar 2008.
- [17] S. Haravifard, A. Banerjee, J. C. Lang, G. Srajer, D. M. Silevitch, B. D. Gaulin, H. A. Dabkowska, and T. F. Rosenbaum. Continuous and discontinuous quantum phase transitions in a model two-dimensional magnet. *Proceedings of the National Academy of Sciences*, 109(7):2286–2289, feb 2012.
- [18] Markus Heyl. Dynamical quantum phase transitions: a review. *Reports on Progress in Physics*, 81(5):054001, may 2018.
- [19] Kristian Mæland and Asle Sudbø. Quantum topological phase transitions in skyrmion crystals. *Physical Review Research*, 4(3):L032025, aug 2022.
- [20] Yuan Cao, Valla Fatemi, Shiang Fang, Kenji Watanabe, Takashi Taniguchi, Efthimios Kaxiras, and Pablo Jarillo-Herrero. Unconventional superconductivity in magic-angle graphene superlattices. *Nature*, 556(7699):43–50, 2018.
- [21] Zachariah Hennighausen and Swastik Kar. Twistronics: a turning point in 2D quantum materials. *Electronic Structure*, 3(1):014004, mar 2021.
- [22] Maciej Lewenstein, Anna Sanpera, Veronica Ahufinger, Bogdan Damski, Aditi Sen(De), and Ujjwal Sen. Ultracold atomic gases in optical lattices: mimicking condensed matter physics and beyond. *Advances in Physics*, 56(2):243–379, mar 2007.
- [23] Anton Frisk Kockum, Adam Miranowicz, Simone De Liberato, Salvatore Savasta, and Franco Nori. Ultrastrong coupling between light and matter. *Nature Reviews Physics*, 1(1):19–40, jan 2019.
- [24] James A. Hutchison, Tal Schwartz, Cyriaque Genet, Eloïse Devaux, and Thomas W. Ebbesen. Modifying Chemical Landscapes by Coupling to Vacuum Fields. *Angewandte Chemie International Edition*, 51(7):1592–1596, feb 2012.
- [25] F. Schlawin, D. M. Kennes, and M. A. Sentef. Cavity quantum materials. *Applied Physics Reviews*, 9(1):011312, mar 2022.
- [26] Herschel Rabitz, Regina de Vivie-Riedle, Marcus Motzkus, and Karl Kompa. Whither the future of controlling quantum phenomena? *Science*, 288(5467):824–828, 2000.
- [27] J. W. McIver, B. Schulte, F.-U. Stein, T. Matsuyama, G. Jotzu, G. Meier, and A. Cavalleri. Light-induced anomalous hall effect in graphene. *Nature Physics*, 16(1):38–41, 2020.
- [28] Changhua Bao, Peizhe Tang, Dong Sun, and Shuyun Zhou. Light-induced emergent phenomena in 2D materials and topological materials. *Nature Reviews Physics*, 4(1):33–48, nov 2021.

- [29] D Fausti, R I Tobey, N Dean, S Kaiser, A Dienst, M C Hoffmann, S Pyon, T Takayama, H Takagi, and A Cavalleri. Light-Induced Superconductivity in a Stripe-Ordered Cuprate. *Science*, 331(6014):189–191, jan 2011.
- [30] Alberto de la Torre, Dante M. Kennes, Martin Claassen, Simon Gerber, James W. McIver, and Michael A. Sentef. Colloquium: Nonthermal pathways to ultrafast control in quantum materials. *Reviews of Modern Physics*, 93(4):041002, oct 2021.
- [31] E. Beaurepaire, J.-C. Merle, A. Daunois, and J.-Y. Bigot. Ultrafast spin dynamics in ferromagnetic nickel. *Phys. Rev. Lett.*, 76:4250–4253, May 1996.
- [32] P. Beaud, S. L. Johnson, E. Vorobeva, U. Staub, R. A. De Souza, C. J. Milne, Q. X. Jia, and G. Ingold. Ultrafast structural phase transition driven by photoinduced melting of charge and orbital order. *Phys. Rev. Lett.*, 103:155702, Oct 2009.
- [33] A. V. Kimel, A. Kirilyuk, P. A. Usachev, R. V. Pisarev, A. M. Balbashov, and Th Rasing. Ultrafast non-thermal control of magnetization by instantaneous photomagnetic pulses. *Nature*, 435(7042):655–657, 2005.
- [34] Andrei Kirilyuk, Alexey V. Kimel, and Theo Rasing. Ultrafast optical manipulation of magnetic order. *Rev. Mod. Phys.*, 82:2731–2784, Sep 2010.
- [35] Kenji Yonemitsu and Keiichiro Nasu. Theory of Photoinduced Phase Transitions. *Journal of the Physical Society of Japan*, 75(1):011008, jan 2006.
- [36] L. Stojchevska, I. Vaskivskiy, T. Mertelj, P. Kusar, D. Svetin, S. Brazovskii, and D. Mihailovic. Ultrafast switching to a stable hidden quantum state in an electronic crystal. *Science*, 344(6180):177–180, 2014.
- [37] P. Beaud, A. Caviezel, S. O. Mariager, L. Rettig, G. Ingold, C. Dornes, S-W. Huang, J. A. Johnson, M. Radovic, T. Huber, T. Kubacka, A. Ferrer, H. T. Lemke, M. Chollet, D. Zhu, J. M. Glowia, M. Sikorski, A. Robert, H. Wadati, M. Nakamura, M. Kawasaki, Y. Tokura, S. L. Johnson, and U. Staub. A time-dependent order parameter for ultrafast photoinduced phase transitions. *Nature Materials*, 13(10):923–927, oct 2014.
- [38] S. de Jong, R. Kukreja, C. Trabant, N. Pontius, C. F Chang, T. Kachel, M. Beye, F Sorgenfrei, C. H. Back, B. Bräuer, W. F. Schlotter, J. J. Turner, O. Krupin, M. Doehler, D. Zhu, M. A. Hossain, A. O. Scherz, D. Fausti, F. Novelli, M. Esposito, W. S. Lee, Y. D. Chuang, D. H. Lu, R. G. Moore, M. Yi, M. Trigo, P. Kirchmann, L. Pathey, M. S. Golden, M. Buchholz, P. Metcalf, F. Parmigiani, W. Wurth, A. Föhlisch, C. Schüßler-Langeheine, and H. A. Dürr. Speed limit of the insulator–metal transition in magnetite. *Nature Materials*, 12(10):882–886, oct 2013.
- [39] M. Först, R. Mankowsky, and A. Cavalleri. Mode-selective control of the crystal lattice. *Accounts of Chemical Research*, 48(2):380–387, Feb 2015.
- [40] A. von Hoegen, R. Mankowsky, M. Fechner, M. Först, and A. Cavalleri. Probing the interatomic potential of solids with strong-field nonlinear phononics. *Nature*, 555(7694):79–82, 2018.
- [41] Daniele Nicoletti and Andrea Cavalleri. Nonlinear light–matter interaction at terahertz frequencies. *Adv. Opt. Photon.*, 8(3):401–464, Sep 2016.

Bibliography

- [42] Tobias Kampfrath, Koichiro Tanaka, and Keith A. Nelson. Resonant and nonresonant control over matter and light by intense terahertz transients. *Nature Photonics*, 7(9):680–690, 2013.
- [43] Matteo Rini, Ra’anan Tobey, Nicky Dean, Jiro Itatani, Yasuhide Tomioka, Yoshinori Tokura, Robert W. Schoenlein, and Andrea Cavalleri. Control of the electronic phase of a manganite by mode-selective vibrational excitation. *Nature*, 449(7158):72–74, 2007.
- [44] R. Mankowsky, A. Subedi, M. Först, S. O. Mariager, M. Chollet, H. T. Lemke, J. S. Robinson, J. M. Glowia, M. P. Minitti, A. Frano, M. Fechner, N. A. Spaldin, T. Loew, B. Keimer, A. Georges, and A. Cavalleri. Nonlinear lattice dynamics as a basis for enhanced superconductivity in $\text{YBa}_2\text{Cu}_3\text{O}_{6.5}$. *Nature*, 516(7529):71–73, 2014.
- [45] T. F. Nova, A. S. Disa, M. Fechner, and A. Cavalleri. Metastable ferroelectricity in optically strained SrTiO_3 . *Science*, 364(6445):1075–1079, 2019.
- [46] T. F. Nova, A. Cartella, A. Cantaluppi, M. Först, D. Bossini, R. V. Mikhaylovskiy, A. V. Kimel, R. Merlin, and A. Cavalleri. An effective magnetic field from optically driven phonons. *Nature Physics*, 13(2):132–136, 2017.
- [47] M. Först, C. Manzoni, S. Kaiser, Y. Tomioka, Y. Tokura, R. Merlin, and A. Cavalleri. Nonlinear phononics as an ultrafast route to lattice control. *Nature Physics*, 7(11):854–856, 2011.
- [48] G. Gavrila, K. Godehusen, C. Weniger, E. T. J. Nibbering, T. Elsaesser, W. Eberhardt, and P. Wernet. Time-resolved X-ray absorption spectroscopy of infrared-laser-induced temperature jumps in liquid water. *Applied Physics A*, 96(1):11–18, jul 2009.
- [49] Yaniv Kurman, Raphael Dahan, Hanan Herzig Sheinfux, Kangpeng Wang, Michael Yannai, Yuval Adiv, Ori Reinhardt, Luiz H. G. Tizei, Steffi Y. Woo, Jiahua Li, James H. Edgar, Mathieu Kociak, Frank H. L. Koppens, and Ido Kaminer. Spatiotemporal imaging of 2D polariton wave packet dynamics using free electrons. *Science*, 372(6547):1181–1186, jun 2021.
- [50] Nara Rubiano da Silva, Marcel Möller, Armin Feist, Henning Ulrichs, Claus Ropers, and Sascha Schäfer. Nanoscale mapping of ultrafast magnetization dynamics with femtosecond lorentz microscopy. *Phys. Rev. X*, 8:031052, Aug 2018.
- [51] Hyun Soon Park, J. Spencer Baskin, and Ahmed H. Zewail. 4D lorentz electron microscopy imaging: Magnetic domain wall nucleation, reversal, and wave velocity. *Nano Letters*, 10(9):3796–3803, Sep 2010.
- [52] Xuewen Fu, Shawn D. Pollard, Bin Chen, Byung-Kuk Yoo, Hyunsoo Yang, and Yimei Zhu. Optical manipulation of magnetic vortices visualized in situ by lorentz electron microscopy. *Science Advances*, 4(7), 2018.
- [53] Bo Huang, Mark Bates, and Xiaowei Zhuang. Super-Resolution Fluorescence Microscopy. *Annual Review of Biochemistry*, 78(1):993–1016, jun 2009.
- [54] Lothar Schermelleh, Rainer Heintzmann, and Heinrich Leonhardt. A guide to super-resolution fluorescence microscopy. *Journal of Cell Biology*, 190(2):165–175, jul 2010.
- [55] Leonhard Möckl, Don C. Lamb, and Christoph Bräuchle. Super-resolved Fluorescence Microscopy: Nobel Prize in Chemistry 2014 for Eric Betzig, Stefan Hell, and William E. Moerner. *Angewandte Chemie International Edition*, 53(51):13972–13977, dec 2014.

- [56] Silvia Pujals, Natalia Feiner-Gracia, Pietro Delcanale, Ilja Voets, and Lorenzo Albertazzi. Super-resolution microscopy as a powerful tool to study complex synthetic materials. *Nature Reviews Chemistry*, 3(2):68–84, jan 2019.
- [57] D.W. POHL. Scanning Near-field Optical Microscopy (SNOM). pages 243–312. 1991.
- [58] Paul Bazylewski, Sabastine Ezugwu, and Giovanni Fanchini. A Review of Three-Dimensional Scanning Near-Field Optical Microscopy (3D-SNOM) and Its Applications in Nanoscale Light Management. *Applied Sciences*, 7(10):973, sep 2017.
- [59] Xinzhong Chen, Debo Hu, Ryan Mescall, Guanjun You, D. N. Basov, Qing Dai, and Mengkun Liu. Modern Scattering-Type Scanning Near-Field Optical Microscopy for Advanced Material Research. *Advanced Materials*, 31(24):1804774, jun 2019.
- [60] Brent Fultz and James Howe. *Transmission Electron Microscopy and Diffractometry of Materials*. Graduate Texts in Physics. Springer Berlin Heidelberg, Berlin, Heidelberg, 2013.
- [61] Weishi Wan, Fu-Rong Chen, and Yimei Zhu. Design of compact ultrafast microscopes for single- and multi-shot imaging with MeV electrons. *Ultramicroscopy*, 194:143–153, nov 2018.
- [62] Jiong Zhao, Qingming Deng, Alicja Bachmatiuk, Gorantla Sandeep, Alexey Popov, Jürgen Eckert, and Mark H. Rummeli. Free-standing single-atom-thick iron membranes suspended in graphene pores. *Science*, 343(6176):1228–1232, 2014.
- [63] Yi Jiang, Zhen Chen, Yimo Han, Pratiti Deb, Hui Gao, Saien Xie, Prafull Purohit, Mark W. Tate, Jiwoong Park, Sol M. Gruner, Veit Elser, and David A. Muller. Electron ptychography of 2D materials to deep sub-ångström resolution. *Nature*, 559(7714):343–349, jul 2018.
- [64] Zhen Chen, Yi Jiang, Yu-Tsun Shao, Megan E. Holtz, Michal Odstrčil, Manuel Guizar-Sicairos, Isabelle Hanke, Steffen Ganschow, Darrell G. Schlom, and David A. Muller. Electron ptychography achieves atomic-resolution limits set by lattice vibrations. *Science*, 372(6544):826–831, may 2021.
- [65] Naoya Shibata, Takehito Seki, Gabriel Sánchez-Santolino, Scott D. Findlay, Yuji Kohno, Takao Matsumoto, Ryo Ishikawa, and Yuichi Ikuhara. Electric field imaging of single atoms. *Nature Communications*, 8(1):15631, may 2017.
- [66] L J Allen, A J D’Alfonso, S D Findlay, J M LeBeau, N R Lugg, and S Stemmer. Elemental mapping in scanning transmission electron microscopy. *Journal of Physics: Conference Series*, 241:012061, jul 2010.
- [67] Dale E. Newbury and Nicholas W. M. Ritchie. Elemental mapping of microstructures by scanning electron microscopy-energy dispersive X-ray spectrometry (SEM-EDS): extraordinary advances with the silicon drift detector (SDD). *Journal of Analytical Atomic Spectrometry*, 28(7):973, 2013.
- [68] M. Kociak and L.F. Zagonel. Cathodoluminescence in the scanning transmission electron microscope. *Ultramicroscopy*, 176:112–131, may 2017.
- [69] Harvey Guthrey and John Moseley. A Review and Perspective on Cathodoluminescence Analysis of Halide Perovskites. *Advanced Energy Materials*, 10(26):1903840, jul 2020.

Bibliography

- [70] L.A. Bendersky and F.W. Gayle. Electron diffraction using transmission electron microscopy. *Journal of Research of the National Institute of Standards and Technology*, 106(6):997, nov 2001.
- [71] Kai Sun, Shuaishuai Sun, Chunhui Zhu, Huanfang Tian, Huaixin Yang, and Jianqi Li. Hidden cdw states and insulator-to-metal transition after a pulsed femtosecond laser excitation in layered chalcogenide 1T-TaS_{2-x}Se_x. *Science Advances*, 4(7), jul 2018.
- [72] Thomas Danz, Till Domröse, and Claus Ropers. Ultrafast nanoimaging of the order parameter in a structural phase transition. *Science*, 371(6527):371–374, jan 2021.
- [73] Wei Wang, Jun Li, Zhixiu Liang, Lijun Wu, Pedro M. Lozano, Alexander C. Komarek, Xiaozhe Shen, Alex H. Reid, Xijie Wang, Qiang Li, Weiguo Yin, Kai Sun, Yimei Zhu, Ian K. Robinson, Mark P. M. Dean, and Jing Tao. Verwey transition as evolution from electronic nematicity to trimerons via electron-phonon coupling. *arxiv.org2202.08744*, feb 2022.
- [74] Naoya Shibata, Scott D. Findlay, Takao Matsumoto, Yuji Kohno, Takehito Seki, Gabriel Sánchez-Santolino, and Yuichi Ikuhara. Direct Visualization of Local Electromagnetic Field Structures by Scanning Transmission Electron Microscopy. *Accounts of Chemical Research*, 50(7):1502–1512, jul 2017.
- [75] Xuewen Fu, Erdong Wang, Yubin Zhao, Ao Liu, Eric Montgomery, Vikrant J. Gokhale, Jason J. Gorman, Chunguang Jing, June W. Lau, and Yimei Zhu. Direct visualization of electromagnetic wave dynamics by laser-free ultrafast electron microscopy. *Science Advances*, 6(40), oct 2020.
- [76] W. X. Xia, Y. S. Chun, S. Aizawa, K. Yanagisawa, Kannan M. Krishnan, D. Shindo, and A. Tonomura. Investigation of magnetic structure and magnetization process of yttrium iron garnet film by Lorentz microscopy and electron holography. *Journal of Applied Physics*, 108(12):123919, dec 2010.
- [77] Hyun Soon Park, J. Spencer Baskin, and Ahmed H. Zewail. 4D Lorentz Electron Microscopy Imaging: Magnetic Domain Wall Nucleation, Reversal, and Wave Velocity. *Nano Letters*, 10(9):3796–3803, sep 2010.
- [78] M. J. G. Cottet, M. Cantoni, B. Mansart, D. T. L. Alexander, C. Hébert, N. D. Zhigadlo, J. Karpinski, and F. Carbone. Quantitative imaging of flux vortices in the type-II superconductor MgB₂ using cryo-Lorentz transmission electron microscopy. *Physical Review B*, 88(1):014505, jul 2013.
- [79] C. Phatak, A.K. Petford-Long, and M. De Graef. Recent advances in Lorentz microscopy. *Current Opinion in Solid State and Materials Science*, 20(2):107–114, apr 2016.
- [80] Li-cong Peng, Ying Zhang, Shu-lan Zuo, Min He, Jian-wang Cai, Shou-guo Wang, Hong-xiang Wei, Jian-qi Li, Tong-yun Zhao, and Bao-gen Shen. Lorentz transmission electron microscopy studies on topological magnetic domains. *Chinese Physics B*, 27(6):066802, jun 2018.
- [81] Gabriele Berruto. *Fast and Ultrafast electron microscopies for skyrmions and plasmonics*. PhD thesis, EPFL, 2019.
- [82] Ryosuke Senga, Kazu Suenaga, Paolo Barone, Shigeyuki Morishita, Francesco Mauri, and Thomas Pichler. Position and momentum mapping of vibrations in graphene nanostructures. *Nature*, 573(7773):247–250, 2019.

- [83] M. E. Hale, H. W. Fuller, and H. Rubinstein. Magnetic domain observations by electron microscopy. *Journal of Applied Physics*, 30(5):789–791, 1959.
- [84] Luis Alfredo Rodriguez Gonzalez. *In situ Lorentz microscopy and electron holography in magnetic nanostructures*. PhD thesis, Universite de Toulouse, 2014.
- [85] R. Jagannathan. Quantum theory of electron lenses based on the Dirac equation. *Physical Review A*, 42(11):6674–6689, dec 1990.
- [86] Chapman J. Petford-Long A. *Magnetic Microscopy of Nanostructures*. Springer, Berlin, Heidelberg, 2005.
- [87] Peter Baum, Ding-Shyue Yang, and Ahmed H. Zewail. 4D Visualization of Transitional Structures in Phase Transformations by Electron Diffraction. *Science*, 318(5851):788–792, nov 2007.
- [88] David J. Flannigan and Ahmed H. Zewail. 4D Electron Microscopy: Principles and Applications. *Accounts of Chemical Research*, 45(10):1828–1839, oct 2012.
- [89] Dmitry Shorokhov and Ahmed H. Zewail. Perspective: 4D ultrafast electron microscopy—Evolutions and revolutions. *The Journal of Chemical Physics*, 144(8):080901, feb 2016.
- [90] L. Piazza, D.J. Masiel, T. LaGrange, B.W. Reed, B. Barwick, and Fabrizio Carbone. Design and implementation of a fs-resolved transmission electron microscope based on thermionic gun technology. *Chemical Physics*, 423:79–84, sep 2013.
- [91] Sandhya Susarla, Mit H. Naik, Daria D. Blach, Jonas Zipfel, Takashi Taniguchi, Kenji Watanabe, Libai Huang, Ramamoorthy Ramesh, Felipe H. da Jornada, Steven G. Louie, Peter Ercius, and Archana Raja. Hyperspectral imaging of exciton confinement within a moiré unit cell with a subnanometer electron probe. *Science*, 378(6625):1235–1239, dec 2022.
- [92] Brett Barwick, David J. Flannigan, and Ahmed H. Zewail. Photon-induced near-field electron microscopy. *Nature*, 462(7275):902–906, 2009.
- [93] Xuewen Fu, Francesco Barantani, Simone Gargiulo, Ivan Madan, Gabriele Berruto, Thomas LaGrange, Lei Jin, Junqiao Wu, Giovanni Maria Vanacore, Fabrizio Carbone, and Yimei Zhu. Nanoscale-femtosecond dielectric response of Mott insulators captured by two-color near-field ultrafast electron microscopy. *Nature Communications*, 11(1):5770, nov 2020.
- [94] Ahmed H. Zewail. Four-dimensional electron microscopy. *Science*, 328(5975):187–193, 2010.
- [95] Nara Rubiano da Silva, Marcel Möller, Armin Feist, Henning Ulrichs, Claus Ropers, and Sascha Schäfer. Nanoscale Mapping of Ultrafast Magnetization Dynamics with Femtosecond Lorentz Microscopy. *Physical Review X*, 8(3):031052, aug 2018.
- [96] Katharina E. Priebe, Christopher Rathje, Sergey V. Yalunin, Thorsten Hohage, Armin Feist, Sascha Schäfer, and Claus Ropers. Attosecond electron pulse trains and quantum state reconstruction in ultrafast transmission electron microscopy. *Nature Photonics*, 11(12):793–797, 2017.
- [97] G. M. Vanacore, I. Madan, G. Berruto, K. Wang, E. Pomarico, R. J. Lamb, D. McGrouther, I. Kaminer, B. Barwick, F. Javier García de Abajo, and F. Carbone. Attosecond coher-

Bibliography

- ent control of free-electron wave functions using semi-infinite light fields. *Nature Communications*, 9(1):2694, jul 2018.
- [98] A. Ryabov, J. W. Thurner, D. Nabben, M. V. Tsarev, and P. Baum. Attosecond metrology in a continuous-beam transmission electron microscope. *Science Advances*, 6(46), nov 2020.
- [99] Wyatt A. Curtis and David J. Flannigan. Toward Å–fs–meV resolution in electron microscopy: systematic simulation of the temporal spread of single-electron packets. *Physical Chemistry Chemical Physics*, 23(41):23544–23553, 2021.
- [100] T. LaGrange, M. R. Armstrong, K. Boyden, C. G. Brown, G. H. Campbell, J. D. Colvin, W. J. DeHope, A. M. Frank, D. J. Gibson, F. V. Hartemann, J. S. Kim, W. E. King, B. J. Pyke, B. W. Reed, M. D. Shirk, R. M. Shuttlesworth, B. C. Stuart, B. R. Torralva, and N. D. Browning. Single-shot dynamic transmission electron microscopy. *Applied Physics Letters*, 89(4):044105, jul 2006.
- [101] Chao Lu, Tao Jiang, Shengguang Liu, Rui Wang, Lingrong Zhao, Pengfei Zhu, Yaqi Liu, Jun Xu, Dapeng Yu, Weishi Wan, Yimei Zhu, Dao Xiang, and Jie Zhang. Imaging nanoscale spatial modulation of a relativistic electron beam with a mev ultrafast electron microscope. *Applied Physics Letters*, 112(11):113102, 2018.
- [102] Matthieu Picher, Kerstin Bücker, Thomas LaGrange, and Florian Banhart. Imaging and electron energy-loss spectroscopy using single nanosecond electron pulses. *Ultramicroscopy*, 188:41–47, may 2018.
- [103] Shyam K. Sinha, Amir Khammari, Matthieu Picher, Francois Roulland, Nathalie Viart, Thomas LaGrange, and Florian Banhart. Nanosecond electron pulses in the analytical electron microscopy of a fast irreversible chemical reaction. *Nature Communications*, 10(1):3648, 2019.
- [104] Phoebe Tengdin, Benoit Truc, Alexey Sapozhnik, Lingyao Kong, Nina del Ser, Simone Gargiulo, Ivan Madan, Thomas Schönenberger, Priya R. Baral, Ping Che, Arnaud Magrez, Dirk Grundler, Henrik M. Rønnow, Thomas Lagrange, Jiadong Zang, Achim Rosch, and Fabrizio Carbone. Imaging the Ultrafast Coherent Control of a Skyrmion Crystal. *Physical Review X*, 12(4):041030, dec 2022.
- [105] Sajedeh Manzeli, Dmitry Ovchinnikov, Diego Pasquier, Oleg V. Yazyev, and Andras Kis. 2D transition metal dichalcogenides. *Nature Reviews Materials*, 2, 2017.
- [106] Hiroki Ikegami and Kimitoshi Kono. Review: Observation of Majorana Bound States at a Free Surface of $^3\text{He-B}$. *Journal of Low Temperature Physics*, 195(3-4):343–357, may 2019.
- [107] Xiaoming Zhang and Feng Liu. Prediction of Majorana edge states from magnetized topological surface states. *Physical Review B*, 103(2):024405, jan 2021.
- [108] Wenbin Li, Xiaofeng Qian, and Ju Li. Phase transitions in 2D materials. *Nature Reviews Materials*, 6(9):829–846, apr 2021.
- [109] Laëtitia Baringthon, Thi Huong Dang, Henri Jaffrès, Nicolas Reyren, Jean-Marie George, Martina Morassi, Gilles Patriarche, Aristide Lemaitre, François Bertran, and Patrick

- Le Fèvre. Topological surface states in ultrathin $\text{Bi}_{1-x}\text{Sb}_x$. *Physical Review Materials*, 6(7):074204, jul 2022.
- [110] Giulia Fulvia Mancini, Barbara Mansart, Saverio Pagano, Bas van der Geer, Marieke de Loos, and Fabrizio Carbone. Design and implementation of a flexible beamline for fs electron diffraction experiments. *Nuclear Instruments and Methods in Physics Research Section A: Accelerators, Spectrometers, Detectors and Associated Equipment*, 691:113–122, nov 2012.
- [111] Francesco Pennacchio, Giovanni M. Vanacore, Giulia F. Mancini, Malte Oppermann, Rajeswari Jayaraman, Pietro Musumeci, Peter Baum, and Fabrizio Carbone. Design and implementation of an optimal laser pulse front tilting scheme for ultrafast electron diffraction in reflection geometry with high temporal resolution. *Structural Dynamics*, 4(4):044032, jul 2017.
- [112] J. Williams, F. Zhou, T. Sun, Z. Tao, K. Chang, K. Makino, M. Berz, P. M. Duxbury, and C. Y. Ruan. Active control of bright electron beams with RF optics for femtosecond microscopy. *Structural Dynamics*, 4(4), jul 2017.
- [113] J. G.H. Franssen and O. J. Luiten. Improving temporal resolution of ultrafast electron diffraction by eliminating arrival time jitter induced by radiofrequency bunch compression cavities. *Structural Dynamics*, 4(4), jul 2017.
- [114] Fabrizio Carbone, Peter Baum, Petra Rudolf, and Ahmed H. Zewail. Structural preablation dynamics of graphite observed by ultrafast electron crystallography. *Physical Review Letters*, 100(3):4–7, 2008.
- [115] Fabrizio Carbone, Ding-Shyue Yang, Enrico Giannini, and Ahmed H Zewail. Direct role of structural dynamics in electron-lattice coupling of superconducting cuprates. *Proceedings of the National Academy of Sciences*, 105(51):20161–20166, dec 2008.
- [116] Shuji Hasegawa. Reflection High-Energy Electron Diffraction. In *Characterization of Materials*. John Wiley & Sons, Inc., Hoboken, NJ, USA, oct 2012.
- [117] I. Madan, G. M. Vanacore, S. Gargiulo, T. LaGrange, and F. Carbone. The quantum future of microscopy: Wave function engineering of electrons, ions, and nuclei. *Applied Physics Letters*, 116(23):230502, jun 2020.
- [118] Benjamin J. McMorran, Amit Agrawal, Ian M. Anderson, Andrew A. Herzing, Henri J. Lezec, Jabez J. McClelland, and John Unguris. Electron Vortex Beams with High Quanta of Orbital Angular Momentum. *Science*, 331(6014):192–195, jan 2011.
- [119] K.Y. Bliokh, I.P. Ivanov, G. Guzzinati, L. Clark, R. Van Boxem, A. Béch e, R. Juchtmans, M.A. Alonso, P. Schattschneider, F. Nori, and J. Verbeeck. Theory and applications of free-electron vortex states. *Physics Reports*, 690:1–70, may 2017.
- [120] Hugo Lourenço-Martins, Davy Gérard, and Mathieu Kociak. Optical polarization analogue in free electron beams. *Nature Physics*, 17(5):598–603, may 2021.
- [121] Martin Kozák. Electron Vortex Beam Generation via Chiral Light-Induced Inelastic Ponderomotive Scattering. *ACS Photonics*, 8(2):431–435, feb 2021.
- [122] Jan-Wilke Henke, Arslan Sajid Raja, Armin Feist, Guan hao Huang, Germaine Arend, Yujia Yang, F. Jasmin Kappert, Rui Ning Wang, Marcel M oller, Jiahe Pan, Junqiu Liu, Ofer Kfir,

Bibliography

- Claus Ropers, and Tobias J. Kippenberg. Integrated photonics enables continuous-beam electron phase modulation. *Nature*, 600(7890):653–658, dec 2021.
- [123] M Yan, D Manor, G Weng, H Chao, L Rothberg, T M Jedju, R R Alfano, and R H Callender. Ultrafast spectroscopy of the visual pigment rhodopsin. *Proceedings of the National Academy of Sciences*, 88(21):9809–9812, nov 1991.
- [124] Igor Schapiro, Mikhail Nikolaevich Ryazantsev, Luis Manuel Frutos, Nicolas Ferré, Roland Lindh, and Massimo Olivucci. The Ultrafast Photoisomerizations of Rhodopsin and Bathorhodopsin Are Modulated by Bond Length Alternation and HOOP Driven Electronic Effects. *Journal of the American Chemical Society*, 133(10):3354–3364, mar 2011.
- [125] H. Eugene Stanley. Scaling, universality, and renormalization: Three pillars of modern critical phenomena. *Reviews of Modern Physics*, 71(2):S358–S366, mar 1999.
- [126] Jean Zinn-Justin. Mean Field Theory For Ferromagnetic Systems. In *Quantum Field Theory and Critical Phenomena*, pages 592–615. Oxford University Press, jun 2002.
- [127] Joao Paulo Casquilho and Paulo Ivo Cortez Teixeira. Phase transitions and critical phenomena. In *Introduction to Statistical Physics and to Computer Simulations*, pages 269–297. Cambridge University Press, Cambridge.
- [128] Ralph V. Chamberlin. Mean-field cluster model for the critical behaviour of ferromagnets. *Nature*, 408(6810):337–339, nov 2000.
- [129] Conradin Kraemer, Neda Nikseresht, Julian O. Piatek, Nikolay Tsyruhin, Bastien Dalla Piazza, Klaus Kiefer, Bastian Klemke, Thomas F. Rosenbaum, Gabriel Aeppli, Ché Gannarelli, Karel Prokes, Andrey Podlesnyak, Thierry Strässle, Lukas Keller, Oksana Zaharko, Karl W. Krämer, and Henrik M. Rønnow. Dipolar Antiferromagnetism and Quantum Criticality in LiErF_4 . *Science*, 336(6087):1416–1419, jun 2012.
- [130] D.S. Inosov. Quantum magnetism in minerals. *Advances in Physics*, 67(3):149–252, jul 2018.
- [131] E Y Vedmedenko, R K Kawakami, D D Sheka, P Gambardella, A Kirilyuk, A Hirohata, C Binek, O Chubykalo-Fesenko, S Sanvito, B J Kirby, J Grollier, K Everschor-Sitte, T Kampfrath, C-Y You, and A Berger. The 2020 magnetism roadmap. *Journal of Physics D: Applied Physics*, 53(45):453001, nov 2020.
- [132] Lucile Savary and Leon Balents. Quantum spin liquids: a review. *Reports on Progress in Physics*, 80(1):016502, jan 2017.
- [133] Yi Zhou, Kazushi Kanoda, and Tai-Kai Ng. Quantum spin liquid states. *Reviews of Modern Physics*, 89(2):025003, apr 2017.
- [134] Hidenori Takagi, Tomohiro Takayama, George Jackeli, Giniyat Khaliullin, and Stephen E. Nagler. Concept and realization of Kitaev quantum spin liquids. *Nature Reviews Physics*, 1(4):264–280, mar 2019.
- [135] C. Broholm, R. J. Cava, S. A. Kivelson, D. G. Nocera, M. R. Norman, and T. Senthil. Quantum spin liquids. *Science*, 367(6475), jan 2020.
- [136] T. H. R. Skyrme. A non-linear field theory. *Proceedings of the Royal Society of London. Series A. Mathematical and Physical Sciences*, 260(1300):127–138, feb 1961.

-
- [137] T.H.R. Skyrme. A unified field theory of mesons and baryons. *Nuclear Physics*, 31:556–569, mar 1962.
- [138] S. Mühlbauer, B. Binz, F. Jonietz, C. Pfleiderer, A. Rosch, A. Neubauer, R. Georgii, and P. Böni. Skyrmion Lattice in a Chiral Magnet. *Science*, 323(5916):915–919, sep 2009.
- [139] X. Z. Yu, Y. Onose, N. Kanazawa, J. H. Park, J. H. Han, Y. Matsui, N. Nagaosa, and Y. Tokura. Real-space observation of a two-dimensional skyrmion crystal. *Nature*, 465(7300):901–904, jun 2010.
- [140] Shi-Zeng Lin. Edge instability in a chiral stripe domain under an electric current and skyrmion generation. *Physical Review B*, 94(2):020402, jul 2016.
- [141] P. Milde, D. Köhler, J. Seidel, L. M. Eng, A. Bauer, A. Chacon, J. Kindervater, S. Mühlbauer, C. Pfleiderer, S. Buhrandt, C. Schütte, and A. Rosch. Unwinding of a skyrmion lattice by magnetic monopoles. *Science*, 340(6136):1076–1080, 2013.
- [142] Christoph Schütte. *Skyrmions and Monopoles in Chiral Magnets & Correlated Heterostructures*. PhD thesis, Universität zu Köln, 2014.
- [143] N. Kanazawa, Y. Nii, X. X. Zhang, A. S. Mishchenko, G. De Filippis, F. Kagawa, Y. Iwasa, N. Nagaosa, and Y. Tokura. Critical phenomena of emergent magnetic monopoles in a chiral magnet. *Nature Communications*, 7(1):11622, may 2016.
- [144] Y. Fujishiro, N. Kanazawa, and Y. Tokura. Engineering skyrmions and emergent monopoles in topological spin crystals. *Applied Physics Letters*, 116(9):090501, mar 2020.
- [145] Katsuhisa Taguchi, Jun-ichiro Ohe, and Gen Tatara. Ultrafast Magnetic Vortex Core Switching Driven by the Topological Inverse Faraday Effect. *Physical Review Letters*, 109(12):127204, sep 2012.
- [146] Wenrui Yang, Huanhuan Yang, Yunshan Cao, and Peng Yan. Photonic orbital angular momentum transfer and magnetic skyrmion rotation. *Optics Express*, 26(7):8778, apr 2018.
- [147] Mana Miyata, Jun-ichiro Ohe, and Gen Tatara. Topological Charge Control of Skyrmion Structure in Frustrated Magnets by Circularly Polarized Light. *Physical Review Applied*, 18(1):014075, jul 2022.
- [148] A. Knigavko and B. Rosenstein. Magnetic Skyrmion Lattices in Heavy Fermion Superconductor UPt_3 . *Physical Review Letters*, 82(6):1261–1264, feb 1999.
- [149] Qi Li, John Toner, and D. Belitz. Skyrmion versus vortex flux lattices in p-wave superconductors. *Physical Review B*, 79(1):014517, jan 2009.
- [150] C. Back, V. Cros, H. Ebert, K. Everschor-Sitte, A. Fert, M. Garst, Tianping Ma, S. Mankovsky, T. L. Monchesky, M. Mostovoy, N. Nagaosa, S S P Parkin, C. Pfleiderer, N. Reyren, A. Rosch, Y. Taguchi, Y. Tokura, K von Bergmann, and Jiadong Zang. The 2020 skyrmionics roadmap. *Journal of Physics D: Applied Physics*, 53(36):363001, sep 2020.
- [151] M. Z. Hasan and C. L. Kane. Colloquium : Topological insulators. *Reviews of Modern Physics*, 82(4):3045–3067, nov 2010.
- [152] Yoshinori Tokura, Kenji Yasuda, and Atsushi Tsukazaki. Magnetic topological insulators. *Nature Reviews Physics*, 1(2):126–143, jan 2019.

Bibliography

- [153] Di Xiao, Ming-Che Chang, and Qian Niu. Berry phase effects on electronic properties. *Reviews of Modern Physics*, 82(3):1959–2007, jul 2010.
- [154] T. Schulz, R. Ritz, A. Bauer, M. Halder, M. Wagner, C. Franz, C. Pfleiderer, K. Everschor, M. Garst, and A. Rosch. Emergent electrodynamics of skyrmions in a chiral magnet. *Nature Physics*, 8(4):301–304, 2012.
- [155] Ping Huang, Thomas Schönenberger, Marco Cantoni, Lukas Heinen, Arnaud Magrez, Achim Rosch, Fabrizio Carbone, and Henrik M. Rønnow. Melting of a skyrmion lattice to a skyrmion liquid via a hexatic phase. *Nature Nanotechnology*, 15(9):761–767, sep 2020.
- [156] Kyohei Takae and Takeshi Kawasaki. Emergent elastic fields induced by topological phase transitions: Impact of molecular chirality and steric anisotropy. *Proceedings of the National Academy of Sciences*, 119(14), apr 2022.
- [157] Soong-Geun Je, Hee-Sung Han, Se Kwon Kim, Sergio A. Montoya, Weilun Chao, Ik-Sun Hong, Eric E. Fullerton, Ki-Suk Lee, Kyung-Jin Lee, Mi-Young Im, and Jung-Il Hong. Direct Demonstration of Topological Stability of Magnetic Skyrmions via Topology Manipulation. *ACS Nano*, 14(3):3251–3258, mar 2020.
- [158] Kang Wang, Vineetha Bheemarasetty, Junhang Duan, Shiyu Zhou, and Gang Xiao. Fundamental physics and applications of skyrmions: A review. *Journal of Magnetism and Magnetic Materials*, 563:169905, dec 2022.
- [159] Kyung Mee Song, Jae-Seung Jeong, Biao Pan, Xichao Zhang, Jing Xia, Sunkyung Cha, Tae-Eon Park, Kwangsu Kim, Simone Finizio, Jörg Raabe, Joonyeon Chang, Yan Zhou, Weisheng Zhao, Wang Kang, Hyunsu Ju, and Seonghoon Woo. Skyrmion-based artificial synapses for neuromorphic computing. *Nature Electronics*, 3(3):148–155, mar 2020.
- [160] Ziyang Yu, Maokang Shen, Zhongming Zeng, Shiheng Liang, Yong Liu, Ming Chen, Zhenhua Zhang, Zhihong Lu, Long You, Xiaofei Yang, Yue Zhang, and Rui Xiong. Voltage-controlled skyrmion-based nanodevices for neuromorphic computing using a synthetic antiferromagnet. *Nanoscale Advances*, 2(3):1309–1317, 2020.
- [161] Tomoyuki Yokouchi, Satoshi Sugimoto, Bivas Rana, Shinichiro Seki, Naoki Ogawa, Yuki Shiomi, Shinya Kasai, and Yoshichika Otani. Pattern recognition with neuromorphic computing using magnetic field-induced dynamics of skyrmions. *Science Advances*, 8(39), sep 2022.
- [162] Sven Bjarke Gudnason, Muneto Nitta, and Nobuyuki Sawado. Black hole Skyrmion in a generalized Skyrme model. *Journal of High Energy Physics*, 2016(9):55, sep 2016.
- [163] Yakov Shnir. Black holes with Skyrmion-anti-Skyrmion hairs. *Physics Letters B*, 810:135847, nov 2020.
- [164] Shao-Wen Wei and Yu-Xiao Liu. Topology of black hole thermodynamics. *Physical Review D*, 105(10):104003, may 2022.
- [165] Hitoshi Murayama and Jing Shu. Topological dark matter. *Physics Letters B*, 686(2-3):162–165, mar 2010.
- [166] S. Tseses, E. Ostrovsky, K. Cohen, B. Gjonaj, N. H. Lindner, and G. Bartal. Optical skyrmion lattice in evanescent electromagnetic fields. *Science*, 361(6406):993–996, sep 2018.

- [167] Zi-Lan Deng, Tan Shi, Alex Krasnok, Xiangping Li, and Andrea Alù. Observation of localized magnetic plasmon skyrmions. *Nature Communications*, 13(1):8, jan 2022.
- [168] Yijie Shen, Eduardo Casas Martínez, and Carmelo Rosales-Guzmán. Generation of Optical Skyrmions with Tunable Topological Textures. *ACS Photonics*, 9(1):296–303, jan 2022.
- [169] Naoto Nagaosa and Yoshinori Tokura. Topological properties and dynamics of magnetic skyrmions. *Nature Nanotechnology*, 8(12):899–911, 2013.
- [170] Pietro Gambardella and Stefan Blügel. Magnetic Surfaces, Thin Films and Nanostructures. pages 625–698. 2020.
- [171] A. Chacon, L. Heinen, M. Halder, A. Bauer, W. Simeth, S. Mühlbauer, H. Berger, M. Garst, A. Rosch, and C. Pfleiderer. Observation of two independent skyrmion phases in a chiral magnetic material. *Nature Physics*, 14(9):936–941, sep 2018.
- [172] S. Seki, X. Z. Yu, S. Ishiwata, and Y. Tokura. Observation of Skyrmions in a Multiferroic Material. *Science*, 336(6078):198–201, apr 2012.
- [173] V. Ukleev, K. Karube, P. M. Derlet, C. N. Wang, H. Luetkens, D. Morikawa, A. Kikkawa, L. Mangin-Thro, A. R. Wildes, Y. Yamasaki, Y. Yokoyama, L. Yu, C. Piamonteze, N. Jaouen, Y. Tokunaga, H. M. Rønnow, T. Arima, Y. Tokura, Y. Taguchi, and J. S. White. Frustration-driven magnetic fluctuations as the origin of the low-temperature skyrmion phase in $\text{Co}_7\text{Zn}_7\text{Mn}_6$. *npj Quantum Materials*, 6(1):40, apr 2021.
- [174] Max Hirschberger, Taro Nakajima, Shang Gao, Licong Peng, Akiko Kikkawa, Takashi Kurumaji, Markus Kriener, Yuichi Yamasaki, Hajime Sagayama, Hironori Nakao, Kazuki Ohishi, Kazuhisa Kakurai, Yasujiro Taguchi, Xiuzhen Yu, Taka-hisa Arima, and Yoshinori Tokura. Skyrmion phase and competing magnetic orders on a breathing kagomé lattice. *Nature Communications*, 10(1):5831, dec 2019.
- [175] Takashi Kurumaji, Taro Nakajima, Max Hirschberger, Akiko Kikkawa, Yuichi Yamasaki, Hajime Sagayama, Hironori Nakao, Yasujiro Taguchi, Taka-hisa Arima, and Yoshinori Tokura. Skyrmion lattice with a giant topological Hall effect in a frustrated triangular-lattice magnet. *Science*, 365(6456):914–918, aug 2019.
- [176] Börge Göbel, Ingrid Mertig, and Oleg A. Tretiakov. Beyond skyrmions: Review and perspectives of alternative magnetic quasiparticles. *Physics Reports*, 895:1–28, feb 2021.
- [177] Shou-Cheng Zhang. A Unified Theory Based on $\text{SO}(5)$ Symmetry of Superconductivity and Antiferromagnetism. *Science*, 275(5303):1089–1096, feb 1997.
- [178] Naoto Nagaosa. Superconductivity and Antiferromagnetism in High- T_c Cuprates. *Science*, 275(5303):1078–1079, feb 1997.
- [179] N. D. Mathur, F. M. Grosche, S. R. Julian, I. R. Walker, D. M. Freye, R. K. W. Haselwimmer, and G. G. Lonzarich. Magnetically mediated superconductivity in heavy fermion compounds. *Nature*, 394(6688):39–43, jul 1998.
- [180] A. Neubauer, C. Pfleiderer, B. Binz, A. Rosch, R. Ritz, P. G. Niklowitz, and P. Böni. Topological Hall Effect in the A Phase of MnSi . *Physical Review Letters*, 102(18):186602, may 2009.

Bibliography

- [181] F. Jonietz, S. Mühlbauer, C. Pfleiderer, A. Neubauer, W. Münzer, A. Bauer, T. Adams, R. Georgii, P. Böni, R. A. Duine, K. Everschor, M. Garst, and A. Rosch. Spin Transfer Torques in MnSi at Ultralow Current Densities. *Science*, 330(6011):1648–1651, dec 2010.
- [182] Wanjun Jiang, Xichao Zhang, Guoqiang Yu, Wei Zhang, Xiao Wang, M. Benjamin Jungfleisch, John E. Pearson, Xuemei Cheng, Olle Heinonen, Kang L. Wang, Yan Zhou, Axel Hoffmann, and Suzanne G. E. te Velthuis. Direct observation of the skyrmion Hall effect. *Nature Physics*, 13(2):162–169, feb 2017.
- [183] P. Bruno, V. K. Dugaev, and M. Taillefumier. Topological Hall Effect and Berry Phase in Magnetic Nanostructures. *Physical Review Letters*, 93(9):096806, aug 2004.
- [184] V. Fock. Über die Beziehung zwischen den Integralen der quantenmechanischen Bewegungsgleichungen und der Schrödingerschen Wellengleichung. *Zeitschrift für Physik*, 49(5-6):323–338, may 1928.
- [185] Michael Victor Berry. Quantal phase factors accompanying adiabatic changes. *Proceedings of the Royal Society of London. A. Mathematical and Physical Sciences*, 392(1802):45–57, mar 1984.
- [186] Robert Bamler. *Phase-Space Berry Phases in Chiral Magnets, Skyrmion Charge, Hall Effect, and Dynamics of Magnetic Skyrmions*. PhD thesis, Universität zu Köln, 2016.
- [187] Yuki Shiomi. *Introduction*, pages 1–23. Springer Japan, Tokyo, 2013.
- [188] Hai-Zhou Lu and Shun-Qing Shen. Quantum transport in topological semimetals under magnetic fields. *Frontiers of Physics*, 12(3):127201, jun 2017.
- [189] Binghai Yan and Claudia Felser. Topological Materials: Weyl Semimetals. *Annual Review of Condensed Matter Physics*, 8(1):337–354, mar 2017.
- [190] M. Ünzelmann, H. Bentmann, T. Figgemeier, P. Eck, J. N. Neu, B. Geldiyev, F. Diekmann, S. Rohlf, J. Buck, M. Hoesch, M. Kalläne, K. Rossnagel, R. Thomale, T. Siegrist, G. Sangiovanni, D. Di Sante, and F. Reinert. Momentum-space signatures of Berry flux monopoles in the Weyl semimetal TaAs. *Nature Communications*, 12(1):3650, jun 2021.
- [191] C. Castelnovo, R. Moessner, and S. L. Sondhi. Magnetic monopoles in spin ice. *Nature*, 451(7174):42–45, jan 2008.
- [192] Alan Farhan, Michael Saccone, Charlotte F. Petersen, Scott Dhuey, Rajesh V. Chopdekar, Yen-Lin Huang, Noah Kent, Zuhuang Chen, Mikko J. Alava, Thomas Lippert, Andreas Scholl, and Sebastiaan van Dijken. Emergent magnetic monopole dynamics in macroscopically degenerate artificial spin ice. *Science Advances*, 5(2), feb 2019.
- [193] Hans-Benjamin Braun. *Solitons in Real Space: Domain Walls, Vortices, Hedgehogs, and Skyrmions*, pages 1–40. Springer International Publishing, Cham, 2018.
- [194] Y. Fujishiro, N. Kanazawa, T. Nakajima, X. Z. Yu, K. Ohishi, Y. Kawamura, K. Kakurai, T. Arima, H. Mitamura, A. Miyake, K. Akiba, M. Tokunaga, A. Matsuo, K. Kindo, T. Koretsune, R. Arita, and Y. Tokura. Topological transitions among skyrmion- and hedgehog-lattice states in cubic chiral magnets. *Nature Communications*, 10(1):1059, mar 2019.
- [195] Predrag Nikolić. Topological orders of monopoles and hedgehogs: From electronic and magnetic spin-orbit coupling to quarks. *Physical Review B*, 101(11):115144, mar 2020.

- [196] Yasuyuki Kato and Yukitoshi Motome. Hidden Topological Transitions in Emergent Magnetic Monopole Lattices. oct 2022.
- [197] Jiadong Zang, Maxim Mostovoy, Jung Hoon Han, and Naoto Nagaosa. Dynamics of Skyrmion Crystals in Metallic Thin Films. *Physical Review Letters*, 107(13):136804, sep 2011.
- [198] N. Kanazawa, Y. Onose, T. Arima, D. Okuyama, K. Ohoyama, S. Wakimoto, K. Kakurai, S. Ishiwata, and Y. Tokura. Large Topological Hall Effect in a Short-Period Helimagnet MnGe. *Physical Review Letters*, 106(15):156603, apr 2011.
- [199] Bom Soo Kim. Skyrmions and Hall transport. *Journal of Physics: Condensed Matter*, 31(38):383001, sep 2019.
- [200] Christian Pfleiderer and Achim Rosch. Single skyrmions spotted. *Nature*, 465(7300):880–881, jun 2010.
- [201] Stephan Sponar, René I. P. Sedmik, Mario Pitschmann, Hartmut Abele, and Yuji Hasegawa. Tests of fundamental quantum mechanics and dark interactions with low-energy neutrons. *Nature Reviews Physics*, 3(5):309–327, apr 2021.
- [202] S. A. Werner, R. Colella, A. W. Overhauser, and C. F. Eagen. Observation of the Phase Shift of a Neutron Due to Precession in a Magnetic Field. *Physical Review Letters*, 35(16):1053–1055, oct 1975.
- [203] H. Rauch, A. Zeilinger, G. Badurek, A. Wilfing, W. Bauspiess, and U. Bonse. Verification of coherent spinor rotation of fermions. *Physics Letters A*, 54(6):425–427, oct 1975.
- [204] R. Colella, A. W. Overhauser, and S. A. Werner. Observation of Gravitationally Induced Quantum Interference. *Physical Review Letters*, 34(23):1472–1474, jun 1975.
- [205] P. Fischer, A. Ioffe, D.L. Jacobson, M. Arif, and F. Mezei. 4π -Periodicity of the spinor wave function under space rotation. *Nuclear Instruments and Methods in Physics Research Section A: Accelerators, Spectrometers, Detectors and Associated Equipment*, 440(3):575–578, feb 2000.
- [206] Massimiliano Sassoli de Bianchi. Theoretical and Conceptual Analysis of the Celebrated 4π -Symmetry Neutron Interferometry Experiments. *Foundations of Science*, 22(3):627–653, sep 2017.
- [207] Armin Danner, Bülent Demirel, Wenzel Kersten, Hartmut Lemmel, Richard Wagner, Stephan Sponar, and Yuji Hasegawa. Spin-rotation coupling observed in neutron interferometry. *npj Quantum Information*, 6(1):23, feb 2020.
- [208] L. Duca, T. Li, M. Reitter, I. Bloch, M. Schleier-Smith, and U. Schneider. An Aharonov-Bohm interferometer for determining Bloch band topology. *Science*, 347(6219):288–292, jan 2015.
- [209] Yuval Ronen, Thomas Werkmeister, Danial Haie Najafabadi, Andrew T. Pierce, Laurel E. Anderson, Young Jae Shin, Si Young Lee, Young Hee Lee, Bobae Johnson, Kenji Watanabe, Takashi Taniguchi, Amir Yacoby, and Philip Kim. Aharonov–Bohm effect in graphene-based Fabry–Pérot quantum Hall interferometers. *Nature Nanotechnology*, 16(5):563–569, may 2021.
- [210] R. C. Liu, B. Odom, Y. Yamamoto, and S. Tarucha. Quantum interference in electron collision. *Nature*, 391(6664):263–265, jan 1998.

Bibliography

- [211] C. J. Lambert. Basic concepts of quantum interference and electron transport in single-molecule electronics. *Chemical Society Reviews*, 44(4):875–888, 2015.
- [212] V. V. Belykh, A. Yu. Kuntsevich, M. M. Glazov, K. V. Kavokin, D. R. Yakovlev, and M. Bayer. Quantum Interference Controls the Electron Spin Dynamics in *n*-GaAs. *Physical Review X*, 8(3):031021, jul 2018.
- [213] M. Mochizuki, X. Z. Yu, S. Seki, N. Kanazawa, W. Koshibae, J. Zang, M. Mostovoy, Y. Tokura, and N. Nagaosa. Thermally driven ratchet motion of a skyrmion microcrystal and topological magnon Hall effect. *Nature Materials*, 13(3):241–246, mar 2014.
- [214] Xiuzhen Yu, Fumitaka Kagawa, Shinichiro Seki, Masashi Kubota, Jan Masell, Fehmi S. Yasin, Kiyomi Nakajima, Masao Nakamura, Masashi Kawasaki, Naoto Nagaosa, and Yoshinori Tokura. Real-space observations of 60-nm skyrmion dynamics in an insulating magnet under low heat flow. *Nature Communications*, 12(1):5079, aug 2021.
- [215] Masatoshi Akazawa, Hyun-Yong Lee, Hikaru Takeda, Yuri Fujima, Yusuke Tokunaga, Taka-hisa Arima, Jung Hoon Han, and Minoru Yamashita. Topological thermal Hall effect of magnons in magnetic skyrmion lattice. *Physical Review Research*, 4(4):043085, nov 2022.
- [216] Seungmo Yang, Kyoung-Woong Moon, Tae-Seong Ju, Changsoo Kim, Hyun-Joong Kim, Juran Kim, Bao Xuan Tran, Jung-Il Hong, and Chanyong Hwang. Electrical Generation and Deletion of Magnetic Skyrmion-Bubbles via Vertical Current Injection. *Advanced Materials*, 33(45):2104406, nov 2021.
- [217] G. Berruto, I. Madan, Y. Murooka, G. M. Vanacore, E. Pomarico, J. Rajeswari, R. Lamb, P. Huang, A. J. Kruchkov, Y. Togawa, T. LaGrange, D. McGrouther, H. M. Rønnow, and F. Carbone. Laser-Induced Skyrmion Writing and Erasing in an Ultrafast Cryo-Lorentz Transmission Electron Microscope. *Physical Review Letters*, 120(11):117201, mar 2018.
- [218] Felix Büttner, Bastian Pfau, Marie Böttcher, Michael Schneider, Giuseppe Mercurio, Christian M. Günther, Piet Helsing, Christopher Klose, Angela Wittmann, Kathinka Gerlinger, Lisa Marie Kern, Christian Strüber, Clemens von Korff Schmising, Josefin Fuchs, Dieter Engel, Alexandra Churikova, Siying Huang, Daniel Suzuki, Ivan Lemesh, Mantao Huang, Lucas Caretta, David Weder, John H. Gaida, Marcel Möller, Tyler R. Harvey, Sergey Zayko, Kai Bagschik, Robert Carley, Laurent Mercadier, Justine Schlappa, Alexander Yaroslavtsev, Loïc Le Guyarder, Natalia Gerasimova, Andreas Scherz, Carsten Deiter, Rafael Gort, David Hickin, Jun Zhu, Monica Turcato, David Lomidze, Florian Erdinger, Andrea Castoldi, Stefano Maffessanti, Matteo Porro, Andrey Samartsev, Jairo Sinova, Claus Ropers, Johan H. Mentink, Bertrand Dupé, Geoffrey S.D. Beach, and Stefan Eisebitt. Observation of fluctuation-mediated picosecond nucleation of a topological phase. *Nature Materials*, 20(1):30–37, 2021.
- [219] Alexey A. Sapozhnik, Benoît Truc, Phoebe Tengdin, Emil Viñas Boström, Thomas Schönenberger, Simone Gargiulo, Ivan Madan, Thomas LaGrange, Arnaud Magrez, Claudio Verdozzi, Angel Rubio, Henrik M. Rønnow, and Fabrizio Carbone. Observation of a new light-induced skyrmion phase in the Mott insulator Cu_2OSeO_3 . *arXiv.2212.07878*, dec 2022.

- [220] Manish Kumar, S. Shankar, Arvind Kumar, Avneesh Anshul, M. Jayasimhadri, and O. P. Thakur. Progress in multiferroic and magnetoelectric materials: applications, opportunities and challenges. *Journal of Materials Science: Materials in Electronics*, 31(22):19487–19510, nov 2020.
- [221] Ganghua Zhang, Hui Wu, Guobao Li, Qingzhen Huang, Chongyin Yang, Fuqiang Huang, Fuhui Liao, and Jianhua Lin. New high T_c multiferroics KBiFe₂O₅ with narrow band gap and promising photovoltaic effect. *Scientific Reports*, 3(1):1265, feb 2013.
- [222] Hanghui Chen and Andrew Millis. Design of new Mott multiferroics via complete charge transfer: promising candidates for bulk photovoltaics. *Scientific Reports*, 7(1):6142, jul 2017.
- [223] Shashank Priya, Hyun-Cheol Song, Yuan Zhou, Ronnie Varghese, Anuj Chopra, Sang-Gook Kim, Isaku Kanno, Liao Wu, Dong Sam Ha, Jungho Ryu, and Ronald G. Polcawich. A Review on Piezoelectric Energy Harvesting: Materials, Methods, and Circuits. *Energy Harvesting and Systems*, 4(1):3–39, aug 2019.
- [224] Nurettin Sezer and Muammer Koç. A comprehensive review on the state-of-the-art of piezoelectric energy harvesting. *Nano Energy*, 80:105567, feb 2021.
- [225] Xiang-Zhong Chen, Marcus Hoop, Naveen Shamsudhin, Tianyun Huang, Berna Özkale, Qian Li, Erdem Siringil, Fajer Mushtaq, Luca Di Tizio, Bradley J. Nelson, and Salvador Pané. Hybrid Magnetoelectric Nanowires for Nanorobotic Applications: Fabrication, Magnetoelectric Coupling, and Magnetically Assisted In Vitro Targeted Drug Delivery. *Advanced Materials*, 29(8):1605458, feb 2017.
- [226] N. A. Spaldin and R. Ramesh. Advances in magnetoelectric multiferroics. *Nature Materials*, 18(3):203–212, mar 2019.
- [227] Nicola A. Spaldin. Multiferroics beyond electric-field control of magnetism. *Proceedings of the Royal Society A: Mathematical, Physical and Engineering Sciences*, 476(2233):20190542, jan 2020.
- [228] Henrik S. Røising, Benjo Fraser, Sinéad M. Griffin, Sumanta Bandyopadhyay, Aditi Mahabir, Sang-Wook Cheong, and Alexander V. Balatsky. Axion-matter coupling in multiferroics. *Physical Review Research*, 3(3):033236, sep 2021.
- [229] Nicola A. Spaldin. Multiferroics: from the cosmically large to the subatomically small. *Nature Reviews Materials*, 2(5):17017, apr 2017.
- [230] T. Kimura, T. Goto, H. Shintani, K. Ishizaka, T. Arima, and Y. Tokura. Magnetic control of ferroelectric polarization. *Nature*, 426(6962):55–58, nov 2003.
- [231] Manfred Fiebig. Revival of the magnetoelectric effect. *Journal of Physics D: Applied Physics*, 38(8):R123–R152, apr 2005.
- [232] W. Eerenstein, N. D. Mathur, and J. F. Scott. Multiferroic and magnetoelectric materials. *Nature*, 442(7104):759–765, aug 2006.
- [233] Sang-Wook Cheong and Maxim Mostovoy. Multiferroics: a magnetic twist for ferroelectricity. *Nature Materials*, 6(1):13–20, jan 2007.
- [234] Yao Wang, Jiamian Hu, Yuanhua Lin, and Ce-Wen Nan. Multiferroic magnetoelectric composite nanostructures. *NPG Asia Materials*, 2(2):61–68, apr 2010.

Bibliography

- [235] Yen-Lin Huang, Dmitri Nikonov, Christopher Addiego, Rajesh V. Chopdekar, Bhagwati Prasad, Lei Zhang, Jyotirmoy Chatterjee, Heng-Jui Liu, Alan Farhan, Ying-Hao Chu, Mengmeng Yang, Maya Ramesh, Zi Qiang Qiu, Bryan D. Huey, Chia-Ching Lin, Tanay Gosavi, Jorge Íñiguez, Jeffrey Bokor, Xiaoqing Pan, Ian Young, Lane W. Martin, and Ramamoorthy Ramesh. Manipulating magnetoelectric energy landscape in multiferroics. *Nature Communications*, 11(1):2836, jun 2020.
- [236] Louis Ponet, S. Artyukhin, Th. Kain, J. Wettstein, Anna Pimenov, A. Shuvaev, X. Wang, S.-W. Cheong, Maxim Mostovoy, and Andrei Pimenov. Topologically protected magnetoelectric switching in a multiferroic. *Nature*, 607(7917):81–85, jul 2022.
- [237] Masahiro Sato, Shintaro Takayoshi, and Takashi Oka. Laser-Driven Multiferroics and Ultrafast Spin Current Generation. *Physical Review Letters*, 117(14):147202, sep 2016.
- [238] A.V. Kimel, A.M. Kalashnikova, A. Pogrebna, and A.K. Zvezdin. Fundamentals and perspectives of ultrafast photoferroic recording. *Physics Reports*, 852:1–46, apr 2020.
- [239] Nicola A. Spaldin and Manfred Fiebig. The Renaissance of Magnetoelectric Multiferroics. *Science*, 309(5733):391–392, jul 2005.
- [240] G. Meunier and M. Bertaud. Constantes cristallographiques de CuSe_2O_5 , CuSeO_3 et Cu_2SeO_4 . *Journal of Applied Crystallography*, 9(4):364–366, aug 1976.
- [241] Kay Kohn. A New Ferrimagnet Cu_2SeO_4 . *Journal of the Physical Society of Japan*, 42(6):2065–2066, jun 1977.
- [242] Jan-Willem G. Bos, Claire V. Colin, and Thomas T. M. Palstra. Magnetoelectric coupling in the cubic ferrimagnet Cu_2OSeO_3 . *Physical Review B*, 78(9):094416, sep 2008.
- [243] M. Belesi, I. Rousochatzakis, H. C. Wu, H. Berger, I. V. Shvets, F. Mila, and J. P. Ansermet. Ferrimagnetism of the magnetoelectric compound Cu_2OSeO_3 probed by ^{77}Se NMR. *Physical Review B*, 82(9):094422, sep 2010.
- [244] A. Maisuradze, Z. Guguchia, B. Graneli, H. M. Rønnow, H. Berger, and H. Keller. μSR investigation of magnetism and magnetoelectric coupling in Cu_2OSeO_3 . *Physical Review B*, 84(6):064433, aug 2011.
- [245] A. Maisuradze, A. Shengelaya, H. Berger, D. M. Djokić, and H. Keller. Magnetoelectric Coupling in Single Crystal Cu_2OSeO_3 Studied by a Novel Electron Spin Resonance Technique. *Physical Review Letters*, 108(24):247211, jun 2012.
- [246] M. Ozerov, J. Romhányi, M. Belesi, H. Berger, J.-Ph. Ansermet, Jeroen van den Brink, J. Wosnitza, S. A. Zvyagin, and I. Rousochatzakis. Establishing the Fundamental Magnetic Interactions in the Chiral Skyrmionic Mott Insulator Cu_2OSeO_3 . *Physical Review Letters*, 113(15):157205, oct 2014.
- [247] K. H. Miller, X. S. Xu., H. Berger, E. S. Knowles, D. J. Arenas, M. W. Meisel, and D. B. Tanner. Magnetodielectric coupling of infrared phonons in single-crystal Cu_2OSeO_3 . *Physical Review B*, 82(14):144107, oct 2010.
- [248] V. P. Gnezdilov, K. V. Lamonova, Yu. G. Pashkevich, P. Lemmens, H. Berger, F. Bussy, and S. L. Gnatchenko. Magnetoelectricity in the ferrimagnetic Cu_2OSeO_3 : symmetry analysis and Raman scattering study. *Low Temperature Physics*, 36(6):550–557, jun 2010.
- [249] T. Nomura, X.-X. Zhang, S. Zherlitsyn, J. Wosnitza, Y. Tokura, N. Nagaosa, and S. Seki. Phonon Magnetochiral Effect. *Physical Review Letters*, 122(14):145901, apr 2019.

- [250] Herta Effenberger and Franz Pertlik. Die Kristallstrukturen der Kupfer(II)-oxo-selenite $\text{Cu}_2\text{O}(\text{SeO}_3)$ (kubisch und monoklin) und $\text{Cu}_4\text{O}(\text{SeO}_3)_3$ (monoklin und triklin). *Monatshefte für Chemie Chemical Monthly*, 117(8-9):887–896, 1986.
- [251] Priya Ranjan Baral. *Topological aspects of non-centrosymmetric magnets*. PhD thesis, EPFL, 2022.
- [252] K. J. A. Franke, P. R. Dean, M. Ciomaga Hatnean, M. T. Birch, D. D. Khalyavin, P. Manuel, T. Lancaster, G. Balakrishnan, and P. D. Hatton. Investigating the magnetic ground state of the skyrmion host material Cu_2OSeO_3 using long-wavelength neutron diffraction. *AIP Advances*, 9(12):125228, dec 2019.
- [253] S. Seki, J.-H. Kim, D. S. Inosov, R. Georgii, B. Keimer, S. Ishiwata, and Y. Tokura. Formation and rotation of skyrmion crystal in the chiral-lattice insulator Cu_2OSeO_3 . *Physical Review B*, 85(22):220406, jun 2012.
- [254] E. Ruff, P. Lunkenheimer, A. Loidl, H. Berger, and S. Krohns. Magnetoelectric effects in the skyrmion host material Cu_2OSeO_3 . *Scientific Reports*, 5:1–9, 2015.
- [255] J. H. Yang, Z. L. Li, X. Z. Lu, M. H. Whangbo, Su Huai Wei, X. G. Gong, and H. J. Xiang. Strong Dzyaloshinskii-Moriya interaction and origin of ferroelectricity in Cu_2OSeO_3 . *Physical Review Letters*, 109(10):1–5, 2012.
- [256] R. B. Versteeg, I. Vergara, S. D. Schäfer, D. Bischoff, A. Aqeel, T. T.M. Palstra, M. Grüninger, and P. H.M. Van Loosdrecht. Optically probed symmetry breaking in the chiral magnet Cu_2OSeO_3 . *Physical Review B*, 94(9):1–9, 2016.
- [257] J S White, I Levatić, A A Omrani, N Egetenmeyer, K Prša, I Živković, J L Gavilano, J Kohlbrecher, M Bartkowiak, H Berger, and H M Rønnow. Electric field control of the skyrmion lattice in Cu_2OSeO_3 . *Journal of Physics: Condensed Matter*, 24(43):432201, oct 2012.
- [258] Ping Huang, Marco Cantoni, Alex Kruchkov, Jayaraman Rajeswari, Arnaud Magrez, Fabrizio Carbone, and Henrik M. Rønnow. In Situ Electric Field Skyrmion Creation in Magnetoelectric Cu_2OSeO_3 . *Nano Letters*, 18(8):5167–5171, aug 2018.
- [259] Ping Huang, Marco Cantoni, Arnaud Magrez, Fabrizio Carbone, and Henrik M. Rønnow. Electric field writing and erasing of skyrmions in magnetoelectric Cu_2OSeO_3 with an ultralow energy barrier. *Nanoscale*, 14(44):16655–16660, 2022.
- [260] Sayantika Bhowal and Nicola A. Spaldin. Magnetoelectric Classification of Skyrmions. *Physical Review Letters*, 128(22):227204, jun 2022.
- [261] R. B. Versteeg, J. Zhu, C. Boguschewski, F. Sekiguchi, A. Sahasrabudhe, K. Budzinauskas, P. Padmanabhan, P. Becker, D. I. Khomskii, and P. H.M. Van Loosdrecht. Coupled dynamics of long-range and cluster-internal spin order in the cluster Mott insulator Cu_2OSeO_3 . *Physical Review B*, 100(6):1–6, 2019.
- [262] Judit Romhányi, Jeroen van den Brink, and Ioannis Rousochatzakis. Entangled tetrahedron ground state and excitations of the magnetoelectric skyrmion material Cu_2OSeO_3 . *Physical Review B*, 90(14):140404, oct 2014.
- [263] Tôru Moriya. Anisotropic Superexchange Interaction and Weak Ferromagnetism. *Physical Review*, 120(1):91–98, oct 1960.

Bibliography

- [264] Oleg Janson, Ioannis Rousochatzakis, Alexander A. Tsirlin, Marilena Belesi, Andrei A. Leonov, Ulrich K. Rößler, Jeroen van den Brink, and Helge Rosner. The quantum nature of skyrmions and half-skyrmions in Cu_2OSeO_3 . *Nature Communications*, 5(1):5376, nov 2014.
- [265] H. Murakawa, Y. Onose, S. Miyahara, N. Furukawa, and Y. Tokura. Comprehensive study of the ferroelectricity induced by the spin-dependent $d - p$ in $\text{Ba}_2X\text{Ge}_2\text{O}_7$ ($X = \text{Mn}, \text{Co}$, and Cu). *Physical Review B*, 85(17):174106, may 2012.
- [266] S. Seki, S. Ishiwata, and Y. Tokura. Magnetoelectric nature of skyrmions in a chiral magnetic insulator Cu_2OSeO_3 . *Physical Review B*, 86(6):060403, aug 2012.
- [267] Fengjiao Qian, Lars J. Bannenberg, Heribert Wilhelm, Grégory Chaboussant, Lisa M. Debeer-Schmitt, Marcus P. Schmidt, Aisha Aqeel, Thomas T. M. Palstra, Ekkes Brück, Anton J. E. Lefering, Catherine Pappas, Maxim Mostovoy, and Andrey O. Leonov. New magnetic phase of the chiral skyrmion material Cu_2OSeO_3 . *Science Advances*, 4, 9 2018.
- [268]
- [269] H. C. Wu, T. Y. Wei, K. D. Chandrasekhar, T. Y. Chen, H. Berger, and H. D. Yang. Unexpected observation of splitting of skyrmion phase in Zn doped Cu_2OSeO_3 . *Scientific Reports*, 5(1):13579, sep 2015.
- [270] H C Wu, K D Chandrasekhar, T Y Wei, K J Hsieh, T Y Chen, H Berger, and H D Yang. Physical pressure and chemical expansion effects on the skyrmion phase in Cu_2OSeO_3 . *Journal of Physics D: Applied Physics*, 48(47):475001, dec 2015.
- [271] I. Levatić, P. Popčević, V. Šurija, A. Kruchkov, H. Berger, A. Magrez, J. S. White, H. M. Rønnow, and I. Živković. Dramatic pressure-driven enhancement of bulk skyrmion stability. *Scientific Reports*, 6(1):21347, feb 2016.
- [272] Liangzi Deng, Hung-Cheng Wu, Alexander P. Litvinchuk, Noah F. Q. Yuan, Jey-Jau Lee, Rabin Dahal, Helmuth Berger, Hung-Duen Yang, and Ching-Wu Chu. Room-temperature skyrmion phase in bulk Cu_2OSeO_3 under high pressures. *Proceedings of the National Academy of Sciences*, 117(16):8783–8787, apr 2020.
- [273] Y. Okamura, F. Kagawa, S. Seki, and Y. Tokura. Transition to and from the skyrmion lattice phase by electric fields in a magnetoelectric compound. *Nature Communications*, 7(1):12669, sep 2016.
- [274] Priya R. Baral, Victor Ukleev, Thomas LaGrange, Robert Cubitt, Ivica Živković, Henrik M. Rønnow, Jonathan S. White, and Arnaud Magrez. Tuning Topological Spin Textures in Size-Tailored Chiral Magnet Insulator Particles. *The Journal of Physical Chemistry C*, 126(28):11855–11866, jul 2022.
- [275] Shilei Zhang, Gerrit van der Laan, Jan Müller, Lukas Heinen, Markus Garst, Andreas Bauer, Helmuth Berger, Christian Pfleiderer, and Thorsten Hesjedal. Reciprocal space tomography of 3D skyrmion lattice order in a chiral magnet. *Proceedings of the National Academy of Sciences*, 115(25):6386–6391, jun 2018.
- [276] Lars J. Bannenberg, Heribert Wilhelm, Robert Cubitt, Ankit Labh, Marcus P. Schmidt, Eddy Lelièvre-Berna, Catherine Pappas, Maxim Mostovoy, and Andrey O. Leonov. Multiple low-temperature skyrmionic states in a bulk chiral magnet. *npj Quantum Materials*, 4(1):11, apr 2019.

- [277] I. Levatić, V. Šurija, H. Berger, and I. Živković. Dissipation processes in the insulating skyrmion compound Cu_2OSeO_3 . *Physical Review B*, 90(22):224412, dec 2014.
- [278] Thomas Schönenberger. *Skyrmion Control and Phase Transitions in Cu_2OSeO_3* . PhD thesis, EPFL, 2022.
- [279] Andrei Kirilyuk, Alexey V. Kimel, and Theo Rasing. Ultrafast optical manipulation of magnetic order. *Reviews of Modern Physics*, 82(3):2731–2784, sep 2010.
- [280] N. Ogawa, S. Seki, and Y. Tokura. Ultrafast optical excitation of magnetic skyrmions. *Scientific Reports*, 5(1):9552, apr 2015.
- [281] M. C. Langner, S. Roy, S. W. Huang, J. D. Koralek, Y.-D. Chuang, G. L. Dakovski, J. J. Turner, J. S. Robinson, R. N. Coffee, M. P. Miniti, S. Seki, Y. Tokura, and R. W. Schoenlein. Nonlinear Ultrafast Spin Scattering in the Skyrmion Phase of Cu_2OSeO_3 . *Physical Review Letters*, 119(10):107204, sep 2017.
- [282] Chuang Ma, Xichao Zhang, Jing Xia, Motohiko Ezawa, Wanjun Jiang, Teruo Ono, S. N. Piramanayagam, Akimitsu Morisako, Yan Zhou, and Xiaoxi Liu. Electric Field-Induced Creation and Directional Motion of Domain Walls and Skyrmion Bubbles. *Nano Letters*, 19(1):353–361, jan 2019.
- [283] Manuel Blanco, Ferran Cambroner, M. Teresa Flores-Arias, Enrique Conejero Jarque, Luis Plaja, and Carlos Hernández-García. Ultraintense Femtosecond Magnetic Nanoprobes Induced by Azimuthally Polarized Laser Beams. *ACS Photonics*, 6(1):38–42, jan 2019.
- [284] S. L. Zhang, W. W. Wang, D. M. Burn, H. Peng, H. Berger, A. Bauer, C. Pfeleiderer, G. van der Laan, and T. Hesjedal. Manipulation of skyrmion motion by magnetic field gradients. *Nature Communications*, 9(1):2115, may 2018.
- [285] Florian Muckel, Stephan von Malotki, Christian Holl, Benjamin Pestka, Marco Pratzer, Pavel F. Bessarab, Stefan Heinze, and Markus Morgenstern. Experimental identification of two distinct skyrmion collapse mechanisms. *Nature Physics*, 17(3):395–402, mar 2021.
- [286] Shubo Zhang. Review of Modern Field Effect Transistor Technologies for Scaling. *Journal of Physics: Conference Series*, 1617(1):012054, aug 2020.
- [287] G. E. Moore. Cramming more components onto integrated circuits. *Electronics*, 16:114–177, 1965.
- [288] M. Mitchell Waldrop. The chips are down for Moore’s law. *Nature*, 530(7589):144–147, feb 2016.
- [289] B. Radisavljevic, A. Radenovic, J. Brivio, V. Giacometti, and A. Kis. Single-layer MoS_2 transistors. *Nature Nanotechnology*, 6(3):147–150, mar 2011.
- [290] Deep Jariwala, Vinod K. Sangwan, Lincoln J. Lauhon, Tobin J. Marks, and Mark C. Hersam. Emerging Device Applications for Semiconducting Two-Dimensional Transition Metal Dichalcogenides. *ACS Nano*, 8(2):1102–1120, feb 2014.
- [291] Elizabeth Gibney. The super materials that could trump graphene. *Nature*, 522(7556):274–276, jun 2015.
- [292] Manish Chhowalla, Debdeep Jena, and Hua Zhang. Two-dimensional semiconductors for transistors. *Nature Reviews Materials*, 1(11):16052, aug 2016.

Bibliography

- [293] Wei Han, YoshiChika Otani, and Sadamichi Maekawa. Quantum materials for spin and charge conversion. *npj Quantum Materials*, 3(1):27, may 2018.
- [294] Ethan C. Ahn. 2D materials for spintronic devices. *npj 2D Materials and Applications*, 4(1):17, jun 2020.
- [295] Christoph Kloeffel and Daniel Loss. Prospects for Spin-Based Quantum Computing in Quantum Dots. *Annual Review of Condensed Matter Physics*, 4(1):51–81, apr 2013.
- [296] Optical Constants.
- [297] Boris M. Chernobrod and Gennady P. Berman. Spin microscope based on optically detected magnetic resonance. *Journal of Applied Physics*, 97(1):014903, jan 2005.
- [298] C. L. Degen, F. Reinhard, and P. Cappellaro. Quantum sensing. *Reviews of Modern Physics*, 89(3):035002, jul 2017.
- [299] Dieter Suter and Fedor Jelezko. Single-spin magnetic resonance in the nitrogen-vacancy center of diamond. *Progress in Nuclear Magnetic Resonance Spectroscopy*, 98-99:50–62, feb 2017.
- [300] David Hopper, Henry Shulevitz, and Lee Bassett. Spin Readout Techniques of the Nitrogen-Vacancy Center in Diamond. *Micromachines*, 9(9):437, aug 2018.
- [301] Santiago Hernández-Gómez and Nicole Fabbri. Quantum Control for Nanoscale Spectroscopy With Diamond Nitrogen-Vacancy Centers: A Short Review. *Frontiers in Physics*, 8, feb 2021.
- [302] Géza Tóth and Iagoba Apellaniz. Quantum metrology from a quantum information science perspective. *Journal of Physics A: Mathematical and Theoretical*, 47(42):424006, oct 2014.
- [303] Hengyun Zhou, Joonhee Choi, Soonwon Choi, Renate Landig, Alexander M. Douglas, Junichi Isoya, Fedor Jelezko, Shinobu Onoda, Hitoshi Sumiya, Paola Cappellaro, Helena S. Knowles, Hongkun Park, and Mikhail D. Lukin. Quantum Metrology with Strongly Interacting Spin Systems. *Physical Review X*, 10(3):031003, jul 2020.
- [304] E.Y. Tsybal and D.G. Pettifor. Perspectives of giant magnetoresistance. pages 113–237. 2001.
- [305] Damhuji Rifai, Ahmed Abdalla, Kharudin Ali, and Ramdan Razali. Giant Magnetoresistance Sensors: A Review on Structures and Non-Destructive Eddy Current Testing Applications. *Sensors*, 16(3):298, feb 2016.
- [306] Sabpreet Bhatti, Rachid Sbiaa, Atsufumi Hirohata, Hideo Ohno, Shunsuke Fukami, and S.N. Piramanayagam. Spintronics based random access memory: a review. *Materials Today*, 20(9):530–548, nov 2017.
- [307] M. N. Baibich, J. M. Broto, A. Fert, F. Nguyen Van Dau, F. Petroff, P. Etienne, G. Creuzet, A. Friederich, and J. Chazelas. Giant Magnetoresistance of (001)Fe/(001)Cr Magnetic Superlattices. *Physical Review Letters*, 61(21):2472–2475, nov 1988.
- [308] G. Binasch, P. Grünberg, F. Saurenbach, and W. Zinn. Enhanced magnetoresistance in layered magnetic structures with antiferromagnetic interlayer exchange. *Physical Review B*, 39(7):4828–4830, mar 1989.
- [309] Claude Chappert, Albert Fert, and Frédéric Nguyen Van Dau. The emergence of spin electronics in data storage. *Nature Materials*, 6(11):813–823, nov 2007.

- [310] Jorge Puebla, Junyeon Kim, Kouta Kondou, and Yoshichika Otani. Spintronic devices for energy-efficient data storage and energy harvesting. *Communications Materials*, 1(1):24, may 2020.
- [311] Will Gilbert, Tuomo Tantt, Wee Han Lim, MengKe Feng, Jonathan Y. Huang, Jesus D. Cifuentes, Santiago Serrano, Philip Y. Mai, Ross C. C. Leon, Christopher C. Escott, Kohei M. Itoh, Nikolay V. Abrosimov, Hans-Joachim Pohl, Michael L. W. Thewalt, Fay E. Hudson, Andrea Morello, Arne Laucht, Chih Hwan Yang, Andre Saraiva, and Andrew S. Dzurak. On-demand electrical control of spin qubits. *Nature Nanotechnology*, jan 2023.
- [312] Atsufumi Hirohata, Keisuke Yamada, Yoshinobu Nakatani, Ioan-Lucian Prejbeanu, Bernard Diény, Philipp Pirro, and Burkard Hillebrands. Review on spintronics: Principles and device applications. *Journal of Magnetism and Magnetic Materials*, 509:166711, sep 2020.
- [313] Priti J. Rajput, Sheetal U. Bhandari, and Girish Wadhwa. A Review on—Spintronics an Emerging Technology. *Silicon*, 14(15):9195–9210, oct 2022.
- [314] Imara Lima Fernandes, Juba Bouaziz, Stefan Blügel, and Samir Lounis. Universality of defect-skyrmion interaction profiles. *Nature Communications*, 9(1):4395, oct 2018.
- [315] Igor Žutić, Jaroslav Fabian, and S. Das Sarma. Spintronics: Fundamentals and applications. *Reviews of Modern Physics*, 76(2):323–410, apr 2004.
- [316] A. V. Chumak, V. I. Vasyuchka, A. A. Serga, and B. Hillebrands. Magnon spintronics. *Nature Physics*, 11(6):453–461, jun 2015.
- [317] Utkalika P. Sahoo, Spandan Anupam, Bidyadhar Das, Mrinal K. Sikdar, Laxmipriya Nanda, and Pratap K. Sahoo. Au-Implanted TiSe₂ Nanocrystals with Defect-Controlled Ferromagnetic Ordering: Implications for Spintronic Devices. *ACS Applied Nano Materials*, 5(3):4072–4081, mar 2022.
- [318] R. Hanson, L. P. Kouwenhoven, J. R. Petta, S. Tarucha, and L. M. K. Vandersypen. Spins in few-electron quantum dots. *Reviews of Modern Physics*, 79(4):1217–1265, oct 2007.
- [319] Sebastian Loth, Kirsten von Bergmann, Markus Ternes, Alexander F. Otte, Christopher P. Lutz, and Andreas J. Heinrich. Controlling the state of quantum spins with electric currents. *Nature Physics*, 6(5):340–344, may 2010.
- [320] K. C. Nowack, F. H. L. Koppens, Yu. V. Nazarov, and L. M. K. Vandersypen. Coherent Control of a Single Electron Spin with Electric Fields. *Science*, 318(5855):1430–1433, nov 2007.
- [321] Junjie Liu, Jakub Mrozek, William K. Myers, Grigore A. Timco, Richard E. P. Winpenny, Benjamin Kintzel, Winfried Plass, and Arzhang Ardavan. Electric Field Control of Spins in Molecular Magnets. *Physical Review Letters*, 122(3):037202, jan 2019.
- [322] Eric Parsonnet, Lucas Caretta, Vikram Nagarajan, Hongrui Zhang, Hossein Taghinejad, Piush Behera, Xiaoxi Huang, Pravin Kavle, Abel Fernandez, Dmitri Nikonov, Hai Li, Ian Young, James Analytis, and Ramamoorthy Ramesh. Nonvolatile Electric Field Control of Thermal Magnons in the Absence of an Applied Magnetic Field. *Physical Review Letters*, 129(8):087601, aug 2022.
- [323] F. Jelezko, T. Gaebel, I. Popa, A. Gruber, and J. Wrachtrup. Observation of Coherent Oscillations in a Single Electron Spin. *Physical Review Letters*, 92(7):076401, feb 2004.

Bibliography

- [324] H. Morishita, L. S. Vlasenko, H. Tanaka, K. Semba, K. Sawano, Y. Shiraki, M. Eto, and K. M. Itoh. Electrical detection and magnetic-field control of spin states in phosphorus-doped silicon. *Physical Review B*, 80(20):205206, nov 2009.
- [325] P. Rabl, S. J. Kolkowitz, F. H. L. Koppens, J. G. E. Harris, P. Zoller, and M. D. Lukin. A quantum spin transducer based on nanoelectromechanical resonator arrays. *Nature Physics*, 6(8):602–608, aug 2010.
- [326] Sungkun Hong, Michael S. Grinolds, Patrick Maletinsky, Ronald L. Walsworth, Mikhail D. Lukin, and Amir Yacoby. Coherent, Mechanical Control of a Single Electronic Spin. *Nano Letters*, 12(8):3920–3924, aug 2012.
- [327] David Press, Thaddeus D. Ladd, Bingyang Zhang, and Yoshihisa Yamamoto. Complete quantum control of a single quantum dot spin using ultrafast optical pulses. *Nature*, 456(7219):218–221, nov 2008.
- [328] Kristiaan De Greve, David Press, Peter L McMahon, and Yoshihisa Yamamoto. Ultrafast optical control of individual quantum dot spin qubits. *Reports on Progress in Physics*, 76(9):092501, sep 2013.
- [329] Ke Wang, Gang Xu, Fei Gao, He Liu, Rong-Long Ma, Xin Zhang, Zhanning Wang, Gang Cao, Ting Wang, Jian-Jun Zhang, Dimitrie Culcer, Xuedong Hu, Hong-Wen Jiang, Hai-Ou Li, Guang-Can Guo, and Guo-Ping Guo. Ultrafast coherent control of a hole spin qubit in a germanium quantum dot. *Nature Communications*, 13(1):206, jan 2022.
- [330] Soong-Geun Je, Pierre Vallobra, Titiksha Srivastava, Juan-Carlos Rojas-Sánchez, Thai Ha Pham, Michel Hehn, Gregory Malinowski, Claire Baraduc, Stéphane Auffret, Gilles Gaudin, Stéphane Mangin, Hélène Béa, and Olivier Boulle. Creation of Magnetic Skyrmion Bubble Lattices by Ultrafast Laser in Ultrathin Films. *Nano Letters*, 18(11):7362–7371, nov 2018.
- [331] Christian Hanneken, André Kubetzka, Kirsten von Bergmann, and Roland Wiesendanger. Pinning and movement of individual nanoscale magnetic skyrmions via defects. *New Journal of Physics*, 18(5):055009, may 2016.
- [332] D. Toscano, S.A. Leonel, P.Z. Coura, and F. Sato. Building traps for skyrmions by the incorporation of magnetic defects into nanomagnets: Pinning and scattering traps by magnetic properties engineering. *Journal of Magnetism and Magnetic Materials*, 480:171–185, jun 2019.
- [333] Raphael Gruber, Jakub Zázvorka, Maarten A. Brems, Davi R. Rodrigues, Takaaki Dohi, Nico Kerber, Boris Seng, Mehran Vafaei, Karin Everschor-Sitte, Peter Virnau, and Mathias Kläui. Skyrmion pinning energetics in thin film systems. *Nature Communications*, 13(1):3144, jun 2022.
- [334] M. Battiato, G. Barbalinardo, and P. M. Oppeneer. Quantum theory of the inverse Faraday effect. *Physical Review B*, 89(1):014413, jan 2014.
- [335] Saikat Banerjee, Umesh Kumar, and Shi-Zeng Lin. Inverse Faraday effect in Mott insulators. *Physical Review B*, 105(18):L180414, may 2022.
- [336] Chengkun Song, Le Zhao, Jiahao Liu, and Wanjun Jiang. Experimental Realization of a Skyrmion Circulator. *Nano Letters*, 22(23):9638–9644, dec 2022.

- [337] D. Morikawa, K. Shibata, N. Kanazawa, X. Z. Yu, and Y. Tokura. Crystal chirality and skyrmion helicity in MnSi and (Fe, Co)Si as determined by transmission electron microscopy. *Physical Review B*, 88(2):024408, jul 2013.
- [338] Carlos Hoyos and Dam Thanh Son. Hall Viscosity and Electromagnetic Response. *Physical Review Letters*, 108(6):066805, feb 2012.
- [339] Carlos Hoyos. Hall viscosity, topological states and effective theories. *International Journal of Modern Physics B*, 28(15):1430007, jun 2014.
- [340] A. I. Berdyugin, S. G. Xu, F. M. D. Pellegrino, R. Krishna Kumar, A. Principi, I. Torre, M. Ben Shalom, T. Taniguchi, K. Watanabe, I. V. Grigorieva, M. Polini, A. K. Geim, and D. A. Bandurin. Measuring Hall viscosity of graphene’s electron fluid. *Science*, 364(6436):162–165, apr 2019.
- [341] Bom Soo Kim. Skyrmions and Hall viscosity. *AIP Advances*, 8(5):055601, may 2018.
- [342] Bom Soo Kim. Modeling Hall viscosity in magnetic-skyrmion systems. *Physical Review Research*, 2(1):013268, mar 2020.
- [343] Eva Prinz, Benjamin Stadtmüller, and Martin Aeschlimann. Twisted light affects ultrafast demagnetization. *arXiv.2206.07502*, jun 2022.
- [344] Vage Karakhanyan, Clément Eustache, Yannick Lefier, and Thierry Grosjean. Inverse Faraday effect from the orbital angular momentum of light. *Physical Review B*, 105(4):045406, jan 2022.
- [345] S. H. Guan, Y. Liu, Z. P. Hou, D. Y. Chen, Z. Fan, M. Zeng, X. B. Lu, X. S. Gao, M. H. Qin, and J. M. Liu. Optical-controlled ultrafast dynamics of skyrmion in antiferromagnets. *arXiv.2301.05577*, jan 2023.
- [346] V. Ukleev, C. Luo, R. Abrudan, A. Aqeel, C. H. Back, and F. Radu. Chiral surface spin textures in Cu₂OSeO₃ unveiled by soft X-ray scattering in specular reflection geometry. *Science and Technology of Advanced Materials*, 23(1):682–690, dec 2022.
- [347] Xiaodong Xie, Kejing Ran, Yizhou Liu, Raymond Fan, Wancong Tan, Haonan Jin, Manuel Valvidares, Nicolas Jaouen, Haifeng Du, Gerrit van der Laan, Thorsten Hesjedal, and Shilei Zhang. Observation of the skyrmion side-face state in a chiral magnet. *Physical Review B*, 107(6):L060405, feb 2023.
- [348] G. van der Laan, S. L. Zhang, and T. Hesjedal. Depth profiling of 3D skyrmion lattices in a chiral magnet—A story with a twist. *AIP Advances*, 11(1):015108, jan 2021.
- [349] T. Adams, A. Chacon, M. Wagner, A. Bauer, G. Brandl, B. Pedersen, H. Berger, P. Lemmens, and C. Pfleiderer. Long-Wavelength Helimagnetic Order and Skyrmion Lattice Phase in Cu₂OSeO₃. *Physical Review Letters*, 108(23):237204, jun 2012.
- [350] Jae Wook Kim, Seunghyun Khim, Sae Hwan Chun, Y. Jo, L. Balicas, H. T. Yi, S.-W. Cheong, N. Harrison, C. D. Batista, Jung Hoon Han, and Kee Hoon Kim. Manifestation of magnetic quantum fluctuations in the dielectric properties of a multiferroic. *Nature Communications*, 5(1):4419, jul 2014.
- [351] Yu. Tikhonov, S. Kondovych, J. Mangeri, M. Pavlenko, L. Baudry, A. Sené, A. Galda, S. Nakhmanson, O. Heinonen, A. Razumnaya, I. Luk’yanchuk, and V. M. Vinokur. Controllable skyrmion chirality in ferroelectrics. *Scientific Reports*, 10(1):8657, may 2020.

Bibliography

- [352] Takao Matsumoto, Yeong-Gi So, Yuji Kohno, Hidetaka Sawada, Ryo Ishikawa, Yuichi Ikuhara, and Naoya Shibata. Jointed magnetic skyrmion lattices at a small-angle grain boundary directly visualized by advanced electron microscopy. *Scientific Reports*, 6(1):35880, oct 2016.
- [353] Masatoshi Imada, Atsushi Fujimori, and Yoshinori Tokura. Metal-insulator transitions. *Reviews of Modern Physics*, 70(4):1039–1263, oct 1998.
- [354] F. Randi, I. Vergara, F. Novelli, M. Esposito, M. Dell’Angela, V. A. M. Brabers, P. Metcalf, R. Kukreja, H. A. Dürr, Daniele Fausti, M. Grüninger, and F. Parmigiani. Phase separation in the nonequilibrium Verwey transition in magnetite. *Physical Review B*, 93(5):054305, feb 2016.
- [355] S. Borroni, G. S. Tucker, F. Pennacchio, J. Rajeswari, U. Stuhr, A. Pisoni, J. Lorenzana, H M Rønnow, and F. Carbone. Mapping the lattice dynamical anomaly of the order parameters across the Verwey transition in magnetite. *New Journal of Physics*, 19(10):103013, oct 2017.
- [356] Wei Wang, Junjie Li, Lijun Wu, Jennifer Sears, Fuhao Ji, Xiaozhe Shen, Alex H Reid, Jing Tao, Ian K Robinson, Yimei Zhu, and Mark P M Dean. Dual-stage structural response to quenching charge order in magnetite. *Physical Review B*, 106(19):195131, nov 2022.
- [357] A. V. Kuzikova, L. A. Shelukhin, F. M. Maksimov, A. I. Chernov, R. V. Pisarev, and A. M. Kalashnikova. Laser-driven 1st order spin reorientation and Verwey phase transitions in the magnetite Fe_3O_4 beyond the range of thermodynamic equilibrium. pages 1–9, nov 2022.
- [358] Xianyang Lu, Guanqi Li, Yuting Gong, Xuezhong Ruan, Yu Yan, Yao Li, Liang He, Jun Du, Vlado K. Lazarov, Jing Wu, Rong Zhang, and Yongbing Xu. Sub-100 femtosecond time scale spin dynamics in epitaxial Fe_3O_4 thin film. *Applied Surface Science*, 572(July 2021):151456, jan 2022.
- [359] Friedrich Walz. The Verwey transition - a topical review. *Journal of Physics: Condensed Matter*, 14(12):R285–R340, apr 2002.
- [360] B. Truc, P. Usai, F. Pennacchio, G. Berruto, R. Claude, I. Madan, V. Sala, T. LaGrange, G. M. Vanacore, S. Benhabib, and F. Carbone. Ultrafast generation of hidden phases via energy-tuned electronic photoexcitation in magnetite. *arxiv.org/2210.00070*, sep 2022.
- [361] M. Louis Néel. Propriétés magnétiques des ferrites ; ferrimagnétisme et antiferromagnétisme. *Annales de Physique*, 12(3):137–198, apr 1948.
- [362] Sönke Johnsen and Kenneth J. Lohmann. Magnetoreception in animals. *Physics Today*, 61(3):29–35, mar 2008.
- [363] Lokesh Srinath Ganapathe, Mohd Ambri Mohamed, Rozan Mohamad Yunus, and Dilla Duryha Berhanuddin. Magnetite (Fe_3O_4) nanoparticles in biomedical application: From synthesis to surface functionalisation. *Magnetochemistry*, 6(4):1–35, 2020.
- [364] Stuart A. Gilder, Michael Wack, Leon Kaub, Sophie C. Roud, Nikolai Petersen, Helmut Heinsen, Peter Hillenbrand, Stefan Milz, and Christoph Schmitz. Distribution of magnetic remanence carriers in the human brain. *Scientific Reports*, 8(1):11363, jul 2018.
- [365] John A. Tarduno, Rory D. Cottrell, Richard K. Bono, Hirokuni Oda, William J. Davis, Mostafa Fayek, Olaf van ’t Erve, Francis Nimmo, Wentao Huang, Eric R. Thern, Sebastian

- Fearn, Gautam Mitra, Aleksey V. Smirnov, and Eric G. Blackman. Paleomagnetism indicates that primary magnetite in zircon records a strong Hadean geodynamo. *Proceedings of the National Academy of Sciences*, 117(5):2309–2318, feb 2020.
- [366] E. J. W. Verwey. Electronic Conduction of Magnetite (Fe_3O_4) and its Transition Point at Low Temperatures. *Nature*, 144(3642):327–328, aug 1939.
- [367] E.J.W. Verwey and P.W. Haayman. Electronic conductivity and transition point of magnetite (“ Fe_3O_4 ”). *Physica*, 8(9):979–987, nov 1941.
- [368] Pierre Weiss and R. Forrer. La saturation absolue des ferromagnétiques et les lois d’approche en fonction du champ et de la température. *Annales de Physique*, 10(12):279–372, apr 1929.
- [369] Russell W. Millar. THE HEAT CAPACITIES AT LOW TEMPERATURES OF “FERROUS OXIDE,” MAGNETITE AND CUPROUS AND CUPRIC OXIDES 1. *Journal of the American Chemical Society*, 51(1):215–222, jan 1929.
- [370] L. R. Bickford. The Low Temperature Transformation in Ferrites. *Reviews of Modern Physics*, 25(1):75–79, jan 1953.
- [371] M. Iizumi, T. F. Koetzle, G. Shirane, S. Chikazumi, M. Matsui, and S. Todo. Structure of magnetite (Fe_3O_4) below the Verwey transition temperature. *Acta Crystallographica Section B Structural Crystallography and Crystal Chemistry*, 38(8):2121–2133, aug 1982.
- [372] Takeshi Kasama, Nathan S. Church, Joshua M. Feinberg, Rafal E. Dunin-Borkowski, and Richard J. Harrison. Direct observation of ferrimagnetic/ferroelastic domain interactions in magnetite below the Verwey transition. *Earth and Planetary Science Letters*, 297(1-2):10–17, aug 2010.
- [373] Mark S. Senn, Jon P. Wright, and J. Paul Attfield. Charge order and three-site distortions in the Verwey structure of magnetite. *Nature*, 481(7380):173–176, jan 2012.
- [374] S. Borroni, G. S. Tucker, U. Stuhr, J. Lorenzana, H. M. Rønnow, and F. Carbone. Energy domain versus time domain precursor fluctuations above the Verwey transition in magnetite. *Physical Review B*, 101(5):054303, feb 2020.
- [375] Simone Borroni. *New Insights into the Verwey Transition in Magnetite*. PhD thesis, Ecole Polytechnique Federale de Lausanne, 2018.
- [376] Giuditta Perversi, Elise Pachoud, James Cumby, Jessica M. Hudspeth, Jon P. Wright, Simon A. J. Kimber, and J. Paul Attfield. Co-emergence of magnetic order and structural fluctuations in magnetite. *Nature Communications*, 10(1):2857, jun 2019.
- [377] Przemysław Piekarczyk, Dominik Legut, Edoardo Baldini, Carina A. Belvin, Tomasz Kołodziej, Wojciech Tabiś, Andrzej Kozłowski, Zbigniew Kakol, Zbigniew Tarnawski, José Lorenzana, Nuh Gedik, Andrzej M. Oleś, Jürgen M. Honig, and Krzysztof Parlinski. Trimeron-phonon coupling in magnetite. *Physical Review B*, 103(10):104303, mar 2021.
- [378] Jung-Fu Lin, Junjie Wu, Jie Zhu, Zhu Mao, Ayman H. Said, Bogdan M. Leu, Jinguang Cheng, Yoshiya Uwatoko, Changqing Jin, and Jianshi Zhou. Abnormal Elastic and Vibrational Behaviors of Magnetite at High Pressures. *Scientific Reports*, 4(1):6282, may 2015.
- [379] E. Pachoud, J. Cumby, G. Perversi, J. P. Wright, and J. P. Attfield. Site-selective doping of ordered charge states in magnetite. *Nature Communications*, 11(1):1671, dec 2020.

Bibliography

- [380] Hebatalla Elnaggar, Silvester Graas, Sara Lafuerza, Blanka Detlefs, Wojciech Tabiś, Mateusz A. Gala, Ahmed Ismail, Ad van der Eerden, Marcin Sikora, Jurgen M. Honig, P. Glatzel, and Frank de Groot. Temperature-Driven Self-Doping in Magnetite. *Physical Review Letters*, 127(18):186402, oct 2021.
- [381] S. Borroni, E. Baldini, V. M. Katukuri, A. Mann, K. Parlinski, D. Legut, C. Arrell, F. van Mourik, J. Teyssier, A. Kozłowski, P. Piekarz, O. V. Yazyev, A. M. Oleś, J. Lorenzana, and F. Carbone. Coherent generation of symmetry-forbidden phonons by light-induced electron-phonon interactions in magnetite. *Physical Review B*, 96(10):104308, sep 2017.
- [382] Edoardo Baldini, Carina A. Belvin, Martin Rodriguez-Vega, Ilkem Ozge Ozel, Dominik Legut, Andrzej Kozłowski, Andrzej M. Oleś, Krzysztof Parlinski, Przemysław Piekarz, José Lorenzana, Gregory A. Fiete, and Nuh Gedik. Discovery of the soft electronic modes of the trimeron order in magnetite. *Nature Physics*, 16(5):541–545, may 2020.
- [383] Joaquín García and Gloria Subías. The Verwey transition—a new perspective. *Journal of Physics: Condensed Matter*, 16(7):R145–R178, feb 2004.
- [384] J. Paul Attfield. Magnetism and the Trimeron Bond. *Chemistry of Materials*, 34(7):2877–2885, apr 2022.
- [385] H. Y. Huang, Z. Y. Chen, R. P. Wang, F. M. F. de Groot, W. B. Wu, J. Okamoto, A. Chainani, A. Singh, Z. Y. Li, J. S. Zhou, H. T. Jeng, G. Y. Guo, Je-Geun Park, L. H. Tjeng, C. T. Chen, and D. J. Huang. Jahn-Teller distortion driven magnetic polarons in magnetite. *Nature Communications*, 8(1):15929, aug 2017.
- [386] H. Schwenk, S. Bareiter, C. Hinkel, B. Lüthi, Z. Kakol, A. Kosłowski, and J.M. Honig. Charge ordering and elastic constants in $\text{Fe}_{3-x}\text{Zn}_x\text{O}_4$. *The European Physical Journal B*, 13(3):491–494, jan 2000.
- [387] B Lüthi. *Physical acoustics in the solid state*. 2005.
- [388] L D Landau and E. M Lifschitz. *Statistical Physics*. Butterworth-Heinemann, third edit edition, 1980.
- [389] G. Perversi, J. Cumby, E. Pachoud, J. P. Wright, and J. P. Attfield. The Verwey structure of a natural magnetite. *Chemical Communications*, 52(27):4864–4867, 2016.
- [390] Hongsheng Liu and Cristiana Di Valentin. Band Gap in Magnetite above Verwey Temperature Induced by Symmetry Breaking. *The Journal of Physical Chemistry C*, 121(46):25736–25742, nov 2017.
- [391] S. K. Park, T. Ishikawa, and Y. Tokura. Charge-gap formation upon the Verwey transition in Fe_3O_4 . *Physical Review B*, 58(7):3717–3720, aug 1998.
- [392] I. Leonov, A. N. Yaresko, V. N. Antonov, M. A. Korotin, and V. I. Anisimov. Charge and Orbital Order in Fe_3O_4 . *Physical Review Letters*, 93(14):146404, sep 2004.
- [393] L. Perfetti, P. A. Loukakos, M. Lisowski, U. Bovensiepen, H. Eisaki, and M. Wolf. Ultrafast Electron Relaxation in Superconducting $\text{Bi}_2\text{Sr}_2\text{CaCu}_2\text{O}_{8+\delta}$ by Time-Resolved Photoelectron Spectroscopy. *Physical Review Letters*, 99(19):197001, nov 2007.
- [394] Fabrizio Carbone, Ding-Shyue Yang, Enrico Giannini, and Ahmed H. Zewail. Direct role of structural dynamics in electron-lattice coupling of superconducting cuprates. *Proceedings of the National Academy of Sciences*, 105(51):20161–20166, dec 2008.

- [395] Barbara Mansart, Mathieu J. G. Cottet, Thomas J. Penfold, Stephen B. Dugdale, Riccardo Tediosi, Majed Chergui, and Fabrizio Carbone. Evidence for a Peierls phase-transition in a three-dimensional multiple charge-density waves solid. *Proceedings of the National Academy of Sciences*, 109(15):5603–5608, apr 2012.
- [396] Barbara Mansart, José Lorenzana, Andreas Mann, Ahmad Odeh, Mariateresa Scaron-gella, Majed Chergui, and Fabrizio Carbone. Coupling of a high-energy excitation to superconducting quasiparticles in a cuprate from coherent charge fluctuation spectroscopy. *Proceedings of the National Academy of Sciences*, 110(12):4539–4544, mar 2013.
- [397] Hélène Seiler, Daniela Zahn, Marios Zacharias, Patrick-Nigel Hildebrandt, Thomas Vasileiadis, Yoav William Windsor, Yingpeng Qi, Christian Carbogno, Claudia Draxl, Ralph Ernstorfer, and Fabio Caruso. Accessing the Anisotropic Nonthermal Phonon Populations in Black Phosphorus. *Nano Letters*, 21(14):6171–6178, jul 2021.
- [398] Mark S. Senn, Jon P. Wright, James Cumby, and J. Paul Attfield. Charge localization in the Verwey structure of magnetite. *Physical Review B*, 92(2):024104, jul 2015.
- [399] W Tabis, J E Lorenzo, A Kozłowski, T Kolodziej, Z Tarnawski, Z Kakol, C Mazzoli, H C Walker, N Jaouen, D Mannix, C Marin, and J M Honig. Effect of surface polishing and oxidization induced strain on electronic order at the Verwey transition in Fe_3O_4 . *Journal of Physics: Condensed Matter*, 25(5):055603, feb 2013.
- [400] J. E. Lorenzo, C. Mazzoli, N. Jaouen, C. Detlefs, D. Mannix, S. Grenier, Y. Joly, and C. Marin. Charge and Orbital Correlations at and above the Verwey Phase Transition in Magnetite. *Physical Review Letters*, 101(22):226401, nov 2008.



Benoit Truc

📍 Avenue des Alpes 30 – 1006 Lausanne – Switzerland



+41 79 308 90 85



benoittruc@gmail.com



[benoittruc](#)

- Passion for science
- Founder of 4x committees in sport events
- People management and persuasion

“Try and fail, but never fail to try.”

Education

- **EPFL – Swiss Federal Institute of Technology – Institute of Physics** Switzerland
PhD degree in physics – Quantum materials, electron microscopy, and ultrafast photonics 2019-2023
2x published and 3x pending peer-reviewed publications
- **EPFL – Swiss Federal Institute of Technology – Institute of Physics** Switzerland
MSc. and BSc. degrees in physics – Quantum Magnetism 2012-2018
10-20h extra workload per week for events organization and representation
- **Gymnase of Morges** Switzerland
Federal maturity, advanced physics, mathematics and chemistry 2009-2012
Exceptional authorization requiring specific grades for sport competition (missing over 100 lectures per year)

Main projects

Founder and Head of the Student Sport Department PESE (2013-2020) – Students’ Games & PolySports

- PESE is a student volunteer-based unit embedded in the EPFL/UNIL sport facility aiming to organize sports events and represent EPFL and UNIL abroad.
- Foundation, recruitment (+100 students), management and coaching of 4 committees with +50 active members.
- Foundation of 5 sport events gathering +3000 participants from 20 universities, annual budget 200'000CHF with 30% fund raising from sponsors.

PhD project (2019-2023) – Ultrafast control of Emergent Quantum Matter probed by electron microscopy

- Extreme science (cryo-temperature, atomic and femtosecond resolutions) combing two cutting edge techniques; ultrafast photonics and 4D electron microscopy.
Investigating strongly-correlated systems for next generation technologies and fundamental understanding.
- Conception including safety and risk evaluation and implementation from scratch of an entire advanced laboratory room (only 2 operational labs with such capabilities worldwide).
- Forming international collaborations (Europe, USA & China), 10 conferences attended (Europe & USA)
- Elaboration of a physics doctoral course *“Ultrafast nonlinear optics and spectroscopy”* and a seminar given by an international renowned professor supported by the swissuniversities program.
+200 students and professors from 9 institutions (EPFL, ETHZ, MIT, PSI, Milano, ...) have attended.

Competencies

Transferable skills

Teamwork
Leadership & coaching
People and projects management
Risk evaluation
Time management

Technical skills

4D Electron Microscopy
Ultrafast photonics
FTIR spectroscopy
Thin film and nanocrystal
crystal growth

Programming

Matlab
R
C/C++
Microsoft Office
Latex

Professional experiences

- **Researcher, teacher assistant, safety coordinator** 2018-2023
EPFL – Swiss Federal Institute of Technology – Institute of Physics, Lausanne - CH
supervision of 6 master students, responsible and evaluation of 30 projects (2-3 people per project) *full time*
- **Teacher assistant** 2014-2018
EPFL – Swiss Federal Institute of Technology – Institute of Physics, Lausanne - CH
advanced physics and chemistry for Bachelor program, +300 students *1 day/week*
- **Project manager** – internship August 2017- February 2018
Rolex SA, Geneva - CH
Audit and optimization of a strategic production protocol using big data analysis with self-made R based diagnostic scripts. *full time*
- **Sailing coach** 2009-2018
Club Nautique de Morges & Rolle, CH
Coaching from beginners to international level competitors and a world champion (*N. Rolaz 2014*) *4h/week*
- **Researcher** – internship August - September 2016
KTH – Royal Institute of Technology – Micro and Nanotechnology Department, Stockholm - SWE
Design of an autonomous ELISA test using capillary driven microfluidics. *full time*
- **Ski instructor** 2012-2014
Ecole Suisse de Ski, Crans-Montana - CH
winter season

Personal situation and languages

date of birth : 16.02.1994

nationalities : Swiss and French

driving license : B (car), A&D (boat)



French

mother tongue



English C1

professional environment



German A2

basic knowledge

Association and representation

- **Scientific staff representant at the faculty and institute of physics councils** 2019-2023
EPFL – Swiss Federal Institute of Technology – Institute of Physics, Lausanne - CH
2x monthly meeting
- **Founder of the Student Sport Department & sport events manager** 2015-2020
UNIL/EPFL – University Sports Departments, Lausanne - CH
President of the Students' Games, 20 sports competition, +500 participants, 20 universities, 65'000CHF annual budget
Strategic coordinator of 3 committees (+50 students) *10h-20h/week*
- **Direction board, Founder & Head of Sport Department** 2013-2017
AGEPoly - General Association of EPFL Students - 10'000 students, 1.2Mio CHF annual budget, Lausanne - CH
President of PolySports (2014) and Students' Games (2015-2020) *10h-20h/week*
- **Environment and sustainability manager, board member** 2012-2013
Festival Balélec - Largest European student festival with 15'000 attendees, Lausanne - CH
3h/week
- **Founder and event manager** Since 2010
BT's Events, Lausanne - CH
Events ranging from parties, wedding, ski weekend to rock and roll lessons, and educational visits (20 to 1'200 people).
variable

Awards and Competition

- **Best scientific presentation** – NGSCES conference (Italy) 2022
- **Honorary member** – AGEPoly 2019
- **Best teacher assistant** – EPFL – Physics Practical work 3rd year of Bachelor 2017
- **Sport merits** – Rolle and Morges 2012, 2013, 2017
- **Sailor competitor – International level** 2001-2012
Club Nautique de Morges, Worldwide
Swiss Olympic talent, Swiss champion of Team Race
Selected for 2x World and 2x European championships (Europe & Brazil) *3-5 day/week*
- **Team leader Hackathon** <https://devpost.com/benoittruc> April – May 2020
- 48h YES-Europe Climathon, 2nd place – Economic Impact
- 72h VersusVirus Hackathon, top 6 – Economics and Policy
- **International Physicist Tournament** 2016
- *Team member*, winner of the national selection, 7th over the best 15 countries worldwide, Edition 2016, Paris - France.
- *Jury member* during the 2019 edition at EPFL.

New Generation in Strongly Correlated Electron Systems

5 - 9 Sept. 2022 | Iseo, Italy

NGSCES 2022 - 12th edition

lincolmostudio

Login

MAIN MENU

Home

Invited speakers

Program

Organizers and Partner Institutions

Sponsors and Contributors

Important dates

Registration

Venue

How to get there

Conference dinner

Abstract submission

Lunch menu

HELP

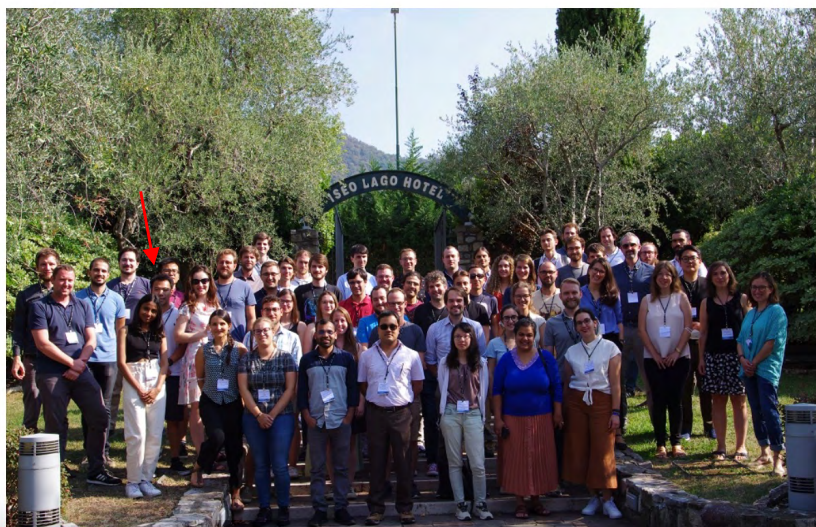
@ Contact

NGSCES2022 CONFERENCE DESCRIPTION

**Thank you to all participants and sponsors!
It has been a great week of science and networking at the NGSCES 2022!**

Our warmest congratulations to the prize winners:

- Mr. Frédéric Chassot, Université de Fribourg, Switzerland - best poster
- Mr. Benoît Truc, École Polytechnique Fédérale de Lausanne, Switzerland - best talk (experiment)
- Ms. Yi-Tsing Teng, Friedrich-Alexander-Universität Erlangen-Nürnberg, Germany - best talk (theory)



**communications
materials**

New Generation in
Strongly Correlated Electron Systems

Presentation Award

sponsored by Communications Materials

for

Benoît Truc

for outstanding **experimental** work presented as an **oral presentation** at
the NGSCES 2022 in Iseo, Italy, 5. – 9. September 2022

Elsa Abreu
Elsa Abreu

Dante Kennes
Dante Kennes

Selene Mor
Selene Mor

Christopher Nicholson
Christopher Nicholson

Publication lists

Overview

OrcID: 0000-0002-1350-7332

Google Scholar: Benoit Truc

Lead author

1. Phoebe Tengdin*, **Benoit Truc***, Alexey A. Sapozhnik*, Lingyao Kong, Nina delSer, Simone Gargiulo, Ivan Madan, Thomas Schönenberger, Priya R. Baral, Ping Che, Arnaud Magrez, Dirk Grundler, Henrik M. Rønnow, Thomas Lagrange, Jiadong Zang, Achim Rosch, and Fabrizio Carbone. Imaging the Ultrafast Coherent Control of a Skyrmion Crystal. *Physical Review X*, 12(4):041030, dec 2022. *These authors contributed equally to this work.
2. **Benoit Truc**, Paolo Usai, Francesco Pennacchio, Gabriele Berruto, Rémi Claude, Ivan Madan, Vittorio Sala, Thomas LaGrange, Gabriele Berruto, Siham Benhabib, and Fabrizio Carbone. Ultrafast generation of hidden phases via energy-tuned electronic photoexcitation in magnetite. *arXiv:2210.00070*, oct 2022. *under review*.
3. Alexey A. Sapozhnik*, **Benoit Truc***, Phoebe Tengdin*, Emil Vinas Boström, Thomas Schönenberger, Simone Gargiulo, Ivan Madan, Thomas LaGrange, Arnaud Magrez, Claudio Verdozzi, Angel Rubio, Henrik M. Rønnow, and Fabrizio Carbone. Observation of a new light-induced skyrmion phase in the Mott insulator Cu_2OSeO_3 . *arXiv.2212.07878*, dec 2022. *under review* *These authors contributed equally to this work.
4. **Benoit Truc**, Priya Ranjan Baral, Arnaud Magrez, Magnetization reversal and Synthesis of $\text{ZnFe}_2(\text{SeO}_3)_4$, *in preparation*.
5. **Benoit Truc**, Wen Hua Bi, Noémie Maamouri, Arnaud Magrez, Synthesis and characterization of the novel Kagome antiferromagnet hydronium selenate Jarosite, *in preparation*.

Significant contribution

1. Simone Gargiulo, Ivan Madan, **Benoit Truc**, Paolo Usai, Veronica Leccese, Giovanni Maria Vanacore, and Fabrizio Carbone. Nuclear excitations in optical laser-generated plasma from a solid target: design and implementation of a table-top setup, *in preparation*
2. Priya Ranjan Baral, **Benoit Truc**, Arnaud Magrez, A recipe for growing Cu_2OSeO_3 size-controlled nanocrystals , *in preparation*.

Supervision contribution

1. Alla. Arakcheeva, Noémie Maamouri, Wen Hua Bi, **Benoit Truc**, A. Magrez. Synthesis, Crystal Structure of $\text{Fe}[\text{SeO}_4]\text{OH}$ and Prediction of Polytypes in the extended $R[\text{MO}_4]Z$ Family, *CrystEngComm*, **25**, 1608, Feb 2023.

International conferences and schools

Conferences

- GRC - Advances in the Dynamics and Control of Quantum Materials
Ventura, United States of America, 9-14.10 2022
- New Generation in Strongly Correlated Electron Systems
Iseo, Italy, 5-9.09 2022
Contribution: Contributed talk, best presentation award
- VII Ultrafast Dynamics and Metastability & Ultrafast Bandgap Photonics
Heraklion, Greece, 6-10.06.2022
Contribution: Invited talk
- Joint Annual Meeting of ÖPG and SPS,
Fribourg, Switzerland, 27-30.08 2022.
Contribution : Contributed talk
- Joint Annual Meeting of ÖPG and SPS,
Innsbruck, Austria, 30.08-3.09 2021.
Contribution: Poster (4th place)
- NCCR MUST Annual Meeting,
Grindelwald, Switzerland, 13-15.09 2021.
Contribution: Poster

School

- Emergent Phenomena in Correlated Quantum Matter - Summer School
Cargèse, France, 5-17.08 2019
Contribution: Poster

Workshops

- GRS - Collective Dynamics in Complex Phases of Bulk and 2D Materials
Ventura, United States of America, 8-9.10 2022
Contribution : Poster
- Coherence and Entanglement in Quantum Systems - Summer Camp
Zuoz, Switzerland, 8-12.08 2022
Contribution : Poster
- Time domain control of atomic shell for nuclear excitation,
Lerici, Italy, 7th-9th October 2019.
Contribution: Poster

Academic involvement

Organization of a new doctoral course

During the COVID pandemic, I took the initiative to organize an online course aiming at learning ultrafast optics.

Ultrafast nonlinear optics and spectroscopy

EPFL - PHYS-813, 2-4 June, Online

by Prof. Cerullo from Politecnico di Milano (Italy)

in collaboration with the EPFL Doctoral Program in Physics and swissuniversities program.

+130 registrations from 15 universities (Switzerland, France, Germany, Italy, Netherlands, Romania, Russia, USA)

Organization of a seminar

Right after the block course, I host an online seminar given by Prof. Cerullo.

Ultrafast carrier and spin dynamics in two-dimensional semiconductors

12 June, Online, by Prof. Cerullo from Politecnico di Milano (Italy)

Teaching Activities and Supervision

I supervised five master students at the crystal growth facility and one master student in our laboratory (LUMES). Furthermore, as teacher assistant, I supervised 60 third-year physics bachelor students during the practical work.

The projects I was taking care of were: *Quantum effects, optical interferences, deterministic chaos, Magneto-optic effects*, each having four sub-projects.

Representation and Safety delegate

Faculty and Institute of physics councils

In 2020, I was elected to take one of the four available places to represent the scientific staff body at the basic science faculty council and the institute of physics council. The scientific staff body includes PhD students, Postdocs, and scientific collaborators.

Safety coordinator

At EPFL, each laboratory has a dedicated safety delegate. I took this responsibility at the beginning of my contract in 2019. In particular, I had to deal with laser, cryogenics, and radiation hazards. Furthermore, during developing the new laboratory I installed, I coordinated electricians, plumbers, and mechanics, ensuring the best security.